On the Effect of Texture on Kinking Non-Linear Elasticity of MAX Phases and MAX-reinforced Mg Matrix Composites

A thesis

Submitted to the Faculty

of

Drexel University

by

Shahram Amini

in partial fulfillment of the

requirements for the degree

of

Doctor of Philosophy

Summer 2009

Dedication

To my classy wife Sara, and our unborn daughter, Hannah,
by whom I was immensely inspired.

Acknowledgements

It gives me great pleasure to take this opportunity to acknowledge all the people who graciously supported me in the last several years during my Ph.D. programme here at Drexel University.

Firstly, and most importantly, I would like to thank my immediate thesis supervisor, Professor Michel W. Barsoum, for his gracious support, and confidence in me in every step of the way, his patience, kindness, generosity and all the time he spent with me and for numerous critical and stimulating discussions and constructive suggestions. Certainly, these words are not sufficient and will not reflect my deepest gratitude for him. Without his motivation and enthusiasm, the completion of this thesis would not have been possible. He always inspired me by thinking positively and independently, in order to become an independent researcher. I am greatly indebted to him for all my achievements. At this point, all I can say is THANK YOU. I was truly honored to work with him.

I would also like to acknowledge my internal thesis committee members, Professor Roger Doherty, Professor Antonios Zavaliangos, Professor Yury Gogotsi, and also my external committee member, Professor Ronald Armstrong from the University of Maryland College Park, for all the illuminating and fruitful discussions throughout the course of my research and for carefully reading my thesis and examining my results.

Interestingly and to my utter surprise, Professor Ronald Armstrong, who graciously accepted my invitation to serve as my external committee member, as it turned out, was former Ph.D. supervisor of my M.Sc. Thesis supervisor, Dr. Sirus Javadpour. This truly unique incident proved to us that the world of materials is indeed a nano-world.

I am also grateful to all the members of the MAX Phase Research Group and Earth Cement Group. To name a few, I would like to thank Drs. Dmitry S. Filimonov, Surojit Gupta, Aiguo Zhou, Sandip Basu, Peter Finkel, Ori Yeheskel, Eva Jud Sierra, and also Mr. Alex Moseson, Ted Scabarozi, Charles Spencer, Ismail Albayrak and Babak Anasori, for their help and support since the very beginning to the end, for numerous

stimulating discussions and for being great friends. Without their friendships, supports, and efforts, this thesis would not have reached this far.

I am grateful to all my friends and colleagues and staff in the Department of Materials Science and Engineering at Drexel University specifically Judith Trachtman, Crystal White, Dorilona Rose, Keiko Nakazawa, Yenneeka Long, Andrew Marx, Shirin Karsan, Dee Breger, Holy Burnside, Ed Basgall and Craig Johnson for extending their unconditional help whenever needed.

It also gives me great pleasure to thank my colleagues and collaborators, Drs. Jose M. Cordoba Gallego, Luke Daemen, Andrew R. McGhie, Chaoying Ni, Lars Hultman, Magnus Oden and Miladin Radovic at Nanostructured Materials, Department of Physics (IFM), Linkoping University, Linkoping, Sweden, Lujan Neutron Scattering Center, Los Alamos National Laboratory, Los Alamos, New Mexico, Laboratory for Research on the Structure of Matter, University of Pennsylvania, Philadelphia, Department of Materials Science and Engineering, University of Delaware, Newark, Delaware, Thin Film Physics Division, Department of Physics (IFM), Linkoping University, Linkoping, Sweden and Texas A&M University, respectively.

I would like to thank my parents Reza and Novid, and my brothers, Arash and Shaahin, from the bottom of my heart. I could not have come this far without their unconditional love, support and inspiration.

Last but not least, I would like to thank my wife, Sara and our unborn daughter, Hannah, whose love, existence, inspiration and motivation encouraged me throughout the course of my Ph.D.; I will be, forever, indebted to you.

Shahram Amini

Philadelphia

August 2009

Table of Contents

List of Tables ix

List of Figures xi

Chapter 1 : MAX Phases and KNE Solids 1

1.1. Introduction to MAX Phases 1

1.2. Kinking Nonlinear Elastic Solids 9

1.3. Kinking Nonlinear Elasticity in Hexagonal Metals 14

1.4. Kinking Nonlinear Elasticity and Nanoindentation 18

1.5. Goals and Motivations 21

Chapter 2 : Kinking Nonlinear Elasticity Microscale Model 23

Chapter 3 : MAXMETs; a New Class of Metal Matrix Composites Reinforced with MAX Phases 32

3.1. Introduction 32

3.2. Experimental Details 38

3.3. Results and Discussion 45

3.3.1. Density Measurements 45

3.3.2. Microstructural Results 46

3.3.3. X-ray Diffraction Results 58

3.3.4. Overview of Mechanical Properties 74

3.4. Summary and Conclusions 78

Chapter 4 : On the Effect of Texture on Mechanical Properties of "MAXMET"s 79

4.1. Introduction 79

4.2. Experimental Details 82

4.3. Results 83

4.4. Discussion 98

4.4.1. Kinking Nonlinear Elasticity 98

4.4.2. Ultimate Compressive Strength 103

4.4.3. Offset Yield Strength 105

4.4.4. Effective Young's Moduli 105

4.4.5. Vickers Microhardness, V_H 106

4.5. Summary and Conclusions 108

Chapter 5 : On the Effect of Texture on the Mechanical Properties of MAX Phases 110

5.1. Introduction 110

5.2. Experimental Details 111

5.3. Results 113

5.4. Discussion 129

5.4.1. Kinking Nonlinear Elasticity 129

5.4.2. Ultimate Compressive Strengths 135

5.4.3. Effective Young's Moduli 135

5.5. Conclusions 136

Chapter 6 : On the Thermal Stability of Mg nanograins to Coarsening after Repeated Melting 137

6.1. Introduction 137

6.2. Experimental Details 141

6.3. Results and Discussion 143

6.4. Summary and Concluding Remarks 152

Chapter 7 : Summary, Conclusions and Proposed Research Work 153

7.1. Summary 153

7.2. Concluding Remarks 154

7.3. Proposed Research Work 157

7.3.1. Crystallographic Texture Measurements 157

7.3.2. Development of KNE Model for MAX-metal composites 158

7.3.3. Fabrication and Mechanical Properties of AZ31B-Ti_2AlC composites 160

7.3.4. Nano- and Macro- Mg Crystal Growth 162

Appendix A : On the Synthesis and Mechanical Properties of Ti_2SC 170

AA.1. Introduction 170

AA.2. Experimental Procedures 171

AA.3. Results and Discussion 173

AA.4. Summary and Conclusions 190

Appendix B : On the Isothermal Oxidation of Ti_2SC in Air 192

AB.1. Introduction 192

AB.2. Experimental Procedures 194

AB.3. Results and Discussion 195

AB.4. Summary and Conclusions 209

Appendix C : On the Synthesis and Mechanical Properties of Cr_2GeC 210

AC.1. Introduction 210

AC.2. Experimental Procedure 211

AC.3. Results and Discussion 213

AC.3.1. X-Ray Diffraction and Microstructural Results 213

AC.3.2. Machinability 217

AC.3.3. Vickers Hardness 218

AC.3.4 Compression Test Results 222

AC.3.5 Elastic properties 226

AC.4. Summary and Conclusions 227

References 228

VITA 241

List of Tables

Table 2-1: Summary of measured and calculated parameters of KNE microscale model for: (a) several MAX phase materials assuming $M = 3$, $k_1 = 2$, $b = 3$ Å, and $\upsilon = 0.2$ [28, 45] except Cr_2GeC for which $\upsilon = 0.29$ and $b = 2.95$ Å [28]; (b) Hexagonal metals (HMs) assuming $M = 3$ and $k_1 = 2$. For Co, $b = 2.7$ Å, and $\upsilon = 0.31$ [58], for Mg, $b = 3.2$ Å, and $\upsilon = 0.35$ [59]; for Ti, $b = 3.3$ Å, and $\upsilon = 0.32$ [58]..... 31

Table 3-1: Mechanical properties of select Mg matrix composites fabricated with different techniques and various volume fractions of reinforcement (E is Young's Modulus; UTS is Ultimate Tensile Strength). 34

Table 3-2: The ratio of XRD peak intensities of (002) basal planes to (103) planes in Ti_2AlC and (002) basal planes to (104) planes in Ti_3SiC_2, respectively, obtained from their corresponding starting powders, XRD cards and those of the oriented preforms; in the latter case, XRD was performed on the surface of the preforms, wherein the majority of the basal planes were normal to the cold-pressing direction during preform preparation. Note that this direction, as described herein for the composites materials, is analogous to the MI-P composite sample. 60

Table 4-1: Effective Young's modulus, $\overline{E}$, for MI-P, MI-R, MI-N, HP50, HP40, Mg-312, Mg-SiC, Ti_2AlC and Ti_3SiC_2 samples tested herein. Also listed are the values for the *upper* and *lower* bounds of E [E(u) and E(l)], G [G(u) and G(l)] and Poisson's ratio, ν, [ν(u) and ν(l)], respectively. 91

Table 4-2: List of measured stress (σ), nonlinear strain (ε_{NL}), and dissipated energy (W_d) for MI-P, MI-R, MI-N, HP50, HP40, Mg-SiC, Mg-312 and randomly oriented Ti_2AlC and Ti_3SiC_2 samples tested herein. Also listed are the m_1, m_2 and their ratio and $3k_1\Omega/b$ values obtained from the slopes of ε_{NL} vs. σ^2, W_d vs. σ^2 and W_d vs. ε_{NL} plots, respectively. 92

Table 4-3: List of experimentally measured σ_t values obtained from the W_d vs. σ^2 plots (Figure 4.5a and d) and 2α values calculated using the σ_t values in column 1 and Eq. 1 assuming M=3. Also listed are calculated values of Ω/b obtained from Eqs. 4 & 5 and 6 (columns 4 and 5, respectively), N_k, $2\beta_{av,c}$, ε_{IKB} calculated from the third term of Eq. 4 and ε_{NL} measured directly by the extensometer. The $2\beta_{av}$ and ρ_{rev} values at the stress levels listed in the last column are also included. For all cases, b = 3.0 Å, M = 3, w = 5b, $k_1 = 2$; G and ν of the Mg-Ti_2AlC, Mg-Ti_3SiC_2 and Mg-SiC composites were assumed to be ~ 51 GPa and 0.26, ~ 58 GPa and 0.26, and ~ 70 GPa and 0.22 (Table 4.1). Those of Ti_2AlC [57], Ti_3SiC_2 [88], SiC [132], and Mg [58] are *118* GPa and *0.2*, *144* GPa and *0.2*, *192* GPa and *0.142*, and *19* GPa and *0.35*, respectively. 97

Table 5-1: Effective Young's moduli, $\overline{E}$, G and ν for FG-P, FG-R, FG-N, CG-P and CG-N samples tested herein and those of Mg-Ti_2AlC (P), Mg-Ti_2AlC (R) and Mg-Ti_2AlC (N) samples. Also included are the C_{11} and C_{33} values of Ti_2AlC reported by Wang *et al.* [152]. 122

Table 5-2: List of measured stress (σ), nonlinear strain (ε_{NL}), and dissipated energy (W_d) for FG-P, FG-R, FG-N, CG-P and CG-N samples tested herein. Also listed are the m_1, m_2 and their ratio and $3k_1\Omega/b$ values obtained from the slopes of ε_{NL} vs. σ^2,W_d vs. σ^2 and W_d vs. ε_{NL} plots. Also in column 5, ε_{IKB} values calculated from the third term of Eq. 2.5 for the sake of comparison with those measured directly by the extensometer (ε_{NL}) are listed. 123

Table 5-3: List of the experimentally measured M and the σ_t values obtained from the W_d vs. σ^2 plots and 2α values calculated from the σ_t values given in column 2 using Eq. 2.2. Also listed are the experimentally measured 2α values and calculated values of Ω/b obtained from Eqs. 2.5 & 2.6 and 2.7 (columns 4 and 5, respectively), N_k and $2\beta_{av,c}$. The $2\beta_{av}$ and ρ_{rev} values at the stress levels listed in the last column are also included. For all cases, b = 3.0 Å, $w = 5b$, $k_1 = 2$. The result of Ti_2AlC sample from previous work [45] is included for the sake of comparison. 124

Table 6-1: Summary of experimental and calculated parameters. The r_{av} of the Mg grains in the MI-sample was assumed to be 17±8 nm. The value of σ_{sl} was then used to estimate the average particle size for the HP sample. The standard deviation reported for the ΔH_i values are with respect to the three cycles. The actual uncertainty in the ΔH_i values, reflected in the differences between runs, is significantly larger since the exact amount of Mg – assumed to be 50 vol.% - in the composite is not known. 146

List of Figures

Figure 1-1: Unit cells of, (a) 211, (b) 312, and (c) 413 phases. M (red) is the early transition metal, A is A groups element, usually IIIA and IVA (dark blue), and X either nitrogen or carbon (black). The phases shown above the unit cells are some examples.... 1

Figure 1-2: The MAX phases are made up of an early transition metal M (red) in the periodic table, an element from the A groups, usually IIIA and IVA (dark blue), and a third element, X, which is either nitrogen or carbon (black), in the composition $M_{n+1}AX_n$, where n is 1, 2 or 3. MAX phases characterized to date fall into three groups, based on the number of atoms of M, A and X in each unit cell; these groups are known as 211, 312 and 413. Those marked with asterisks have been successfully synthesized so far [12, 19, 20, 28-35]. 3

Figure 1-3: MAX Phases are superbly machinable ternary carbides and nitrides (Photos by courtesy of 3-one-2 LLC) and can be machined with ease to net-shape components... 4

Figure 1-4: Thermal expansion vs. temperature for selected MAX phases. Curves are shifted vertically for clarity [15]. 5

Figure 1-5: c_{44} vs. c/a for a number of solids, some of which are known to kink and others that are not [60]. Based on this map it is clear that KNE solids lie to the right of the vertical line and hence constitute a huge class of solids. 9

Figure 1-6: Schematic of a typical stress-strain curve for a KNE solid. The various parameters needed to describe the curve are labeled. 11

Figure 1-7: Schematic of an IKB with length 2α and diameter 2β. D is the distance between the horizontal dislocation loops. 11

Figure 1-8: Typical stress-strain curves of Ti_3SiC_2; the loops are shifted horizontally for clarity (see Chapters 4 and 5 for more detail). 13

Figure 1-9: Stress-strain curves of uniaxial cyclic compression result of, (a) dense, and, (b) porous Ti_2AlC samples. The samples were first compressed to 350 MPa, unloaded and then reloaded to progressively higher stresses [78]. 13

Figure 1-10: (a) Stress-strain curve of Mg with a yield point σ_y, 52 MPa. Even below σ_y, there are hysteretic loops. (b) Stress-strain curves of Mg show some hysteretic loops below σ_y. The left one was obtained from a progressively-increasing-stress test (↑). The right one was obtained from a progressively-decreasing-stress test (↓). (c) Stress-strain curves of Co (d) Stress-strain curves of coarse grained Ti (CG) and fine grained Ti (FG). (e) Stress-strain curves of Zn [58, 69]. 17

Figure 1-11: Schematic of kinking mechanism. a) IKBs (Figure 1.7) devolve into mobile dislocation walls (MDW). Note that a new IKB may form inside two MDWs. c) Formation of permanent kink bands (KBs), which is an irreversible process [54]. 18

Figure 1-12: Cyclic nanoindentation results obtained when a 1.4 μm radius sphere is indented into the same location of a sapphire *C* (0001) crystal surface. (a) Load displacement for five cycles to 50 mN, followed by eight cycles at 100 mN. Inset is a schematic of an IKB. (b) Magnified view of the center of selected loops for an area indented 24 times to 100 mN. The reproducibility of the loops is noteworthy. In both a and b only a fraction of the data points collected are plotted [55]..... 20

Figure 1-13: Nanoindentation stress–strain curves obtained when a 13.5 μm radius hemisphere is indented five times into the same location, to the same maximum stress, on a ZnO surface. Note the fully reversible and reproducible nature of the loops. 20

Figure 2-1: Dislocation walls and dislocation loops of an IKB. D is the distance between two dislocation loops. $2\beta_x$ is the length of the edge dislocation segment; $2\beta_y$ is the length of the screw dislocation segment [69, 73]. 25

Figure 2-2: Plots of, (a) W_d vs. σ^2, (b) ε_{NL} vs. σ^2 and, (c) W_d vs. ε_{NL} obtained from uniaxial compression stress-strain curves of fully dense and 10 vol.% porous Ti_2AlC (Figure 1.9) [57]..... 28

Figure 2-3: Stress-strain curves of polycrystalline, (a) fine-grained and, (b) coarse-grained Ti_3SiC_2 tested under uniaxial cyclic compression. Note that the stress-strain curves of the coarse-grained sample were not strain rate dependent, at least in the 10^{-3} to 10^{-5} S^{-1} strain rate regime [53, 56]..... 29

Figure 3-1: (a) Chamber of the graphite-heated vacuum-atmosphere HP, (b) schematic of the HPing system utilized to fabricate Mg-Ti_2AlC composites using the Mg and Ti_2AlC powders' blend..... 39

Figure 3-2: Schematic of the MI system utilized to fabricate Mg-Ti_2AlC composites. ... 40

Figure 3-3: Front view of the hydraulic testing machine used for cyclic compression tests; also shown are the sapphire extension rods attached to the surface of the sample to measure its strain during loading. 44

Figure 3-4: Evolution of density versus Mg metal content in HPed and melt-infiltrated composites..... 45

Figure 3-5: Secondary electron SEM image of polished surface of, a) HP50 and, b) MI-R, c) MI-P and, d) MI-N composites..... 48

Figure 3-6: SEM image of fractured surface of, a) HP50; inset shows the facetted Mg single crystals at higher magnifications, and b) MI50 composites; c) and d) Facetted Mg single crystals formed during MI on the surface of the alumina lids..... 50

Figure 3-7: TEM images of HP50 composite showing the presence of areas where Mg matrix appears to have wet the Ti_2AlC matrix, very small amounts of porosity and areas where Mg single crystals were formed in the open spaces and porosities of the microstructure. 54

Figure 3-8: TEM images of MI50 composite wherein the molten matrix has wet and fully infiltrated the preform. Compared to Fig. 3.7 (HP50 composite) less porosity and limited regions filled with Mg single crystals are observed..... 56

Figure 3-9: Formation of kink bands with very sharp radii of curvature in, a) a single grain of Ti_2AlC on the polished surface of the HP50 composite sample and, b and, c) fractured surfaces of MI50 composite sample. 58

Figure 3-10: a) X-ray diffraction pattern of Mg-50 vol.% Ti_2AlC composite fabricated by HPing and MI; b) X-ray diffraction pattern of Mg-50 vol.% Ti_2AlC composite fabricated by HPing and MI before and after annealing (carried out at 550º C for 6 h in flowing Ar of a tube furnace), containing peaks for Ti_2AlC, Mg, TiC (~ 5 vol. % impurity in the starting Ti_2AlC powder) and MgO. In all cases Si was added as an internal standard..... 59

Figure 3-11: Optical micrographs of fully dense, polished and etched, a) Ti_2AlC, and b) Ti_3SiC_2. Both samples were fabricated by cold isostatically pressing (CIPing) to ~ 250 MPa for ~ 5 min followed by hot isostatic pressing (HIPing) at 1400 ºC and ~ 175 MPa for 2 h followed by furnace-cooling to room temperature..... 61

Figure 3-12: FWHM of Mg and MgO vs. peak intensity; three of the high intensity peaks were used in each case and compared with those of Si standard, pure Mg powder and Mg single crystal peaks. 62

Figure 3-13: TEM images of, (a) and (b), the MI50 composite and, (c) and (d), the HP50 composite showing the presence and morphology of the nc-Mg matrices within the composites..... 64

Figure 3-14: FWHM of Mg peaks in Mg-Ti_2AlC (MI50) composite before and after annealing; included in the same figure, for the sake of comparison, is the FWHM of the Mg ingot and the Mg in Mg-Ti_3SiC_2 (Mg-312) composite before and after annealing; the three highest intensity peaks were used in each case..... 65

Figure 3-15: a) Concentration in *at.%* of Mg and Ti within the Ti_2AlC grains verifying the formation of a $(Ti_{1-x}Mg_x)_2AlC$ solid solution, with an x as high as 0.2; b) Variation of *a* and *c* lattice parameters in as-received Ti_2AlC and that within the MI composite..... 67

Figure 3-16: Variation of *a* and *c* lattice parameters of as-received, (a) Ti_2AlC, (b) Ti_3SiC_2, and (c) Nb_2AlC and those within their MI composites after soaking for 1 hr and 4 hrs in the Mg melt. 71

Figure 3-17: TEM images of Mg-50 vol.% Ti_3SiC_2 composite fabricated by MI at 750º C for 1 h, showing the absence of nanocrystalline Mg matrix within the composite. 73

Figure 3-18: (a) Fully reversible hysteretic loops in MI Mg-50 vol. % Ti_2AlC composite. The sample was compressed to ~ 75% of its failure stress; the strains are shifted horizontally for clarity; (b) Plot of W_d and ε_{NL} vs. σ^2 from uniaxial compression stress-strain curves. 75

Figure 3-19: Plots of effective Young's moduli vs. volume fraction of the Mg-MAX composites in, (a) Mg-Ti_2AlC and, (b) Mg-Ti_3SiC_2. 77

Figure 4-1: Effect of indentation loads on the V_H values of the HP, MI-R, MI-P and MI-N samples, together with those of fully dense Ti_2AlC, pure Mg, Mg-312 and Mg-SiC for comparison. 84

Figure 4-2: SEM micrographs of Vickers indentations at 10 N on a) HPed and b) MI Mg-Ti_2AlC composites. 85

Figure 4-3: (a) Plot of UCS values of all materials tested in this work; compressive stress-strain curves indicating offset yield strength and fracture point for, (b) HP50 and, (c) MI50 composites. 87

Figure 4-4: Typical compressive stress-strain curves for a) MI-N, b) MI-P, c) MI-R, d) Mg-SiC and Mg-312, e) HP40 and, f) HP50 composites. Only the fifth cycle is shown and the curves are shifted horizontally for clarity. 90

Figure 4-5: Plots of, a) W_d vs. σ^2, b) ε_{NL} vs. σ^2, and c) W_d vs. ε_{NL} for all Mg-Ti_2AlC composites tested in this work and those of fully dense Ti_2AlC. Plots of, d) W_d vs. σ^2, e) ε_{NL} vs. σ^2, and, f) W_d vs. ε_{NL} for Mg-Ti_3SiC_2 and Mg-SiC composites. 96

Figure 4-6: Plot of Ω/b as a function of $\frac{1}{\sqrt{2\alpha}}$ for the average Ω/b values obtained herein and those reported in [57] for fully dense and 10 vol. % porous Ti_2AlC. 101

Figure 5-1: Optical micrographs of polished and etched surfaces of, a) FG and b) CG Ti_2AlC; Secondary electron SEM image of fractured surface of, c) FG and, d) CG Ti_2AlC. Note arrows showing the thickness of the grains along their *c*-axis (2α); Secondary electron SEM image of the fractured surface of CG sample showing, e) the formation of multiple kink bands with very sharp radii of curvature; f) extent of contortion in a single Ti_2AlC grain without fracture, which is a characteristic of the MAX phases. 117

Figure 5-2: Typical compressive stress-strain curves of, a) FG-P and, b) FG-N; only one cycle (last) per load is shown and the curves are shifted horizontally for clarity. 119

Figure 5-3: Typical compressive stress-strain curves of, a) CG-P and, b) CG-N; only one cycle (last) per load is shown and the curves are shifted horizontally for clarity. 120

Figure 5-4: Comparison of stress-strain loops for FG and CG Ti_2AlC samples and those of random and oriented Mg-Ti_2AlC composites at comparable stress levels, for the sake of comparison. The latter are much larger than the former. All loops are shifted horizontally for clarity. 121

Figure 5-5: Plots of, a) W_d vs. σ^2, b) ε_{NL} vs. σ^2, and c) W_d vs. ε_{NL} for all FG and CG Ti_2AlC samples and Mg-Ti_2AlC (P) composite for the sake of comparison. 126

Figure 5-6: Strains measured by neutron diffraction along the *a* and *c*-directions of the *majority* and *minority* grains in, a) CG-N and b) CG-P samples by measuring the longitudinal and transverse lattice parameter shifts denoted by *a* and *c* strains of the majority and minority grains. Also included is the macroscopic stress-strain plots obtained simultaneously using an extensometer denoted by open triangles..... 128

Figure 6-1: DSC results; a) Three cycles of MI-Ti_2AlC composite, b) Three cycles of HP-Ti_2AlC composite, c) Comparison of melting troughs and, d) solidification peaks for 5 samples tested herein. 145

Figure 6-2: FDS spectra of a 40 mm high, 10 mm diameter, MI Mg-Ti_2AlC composite solid cylinder. Red line is the neutron vibrational spectrum of the composite before H_2 annealing. Blue line is the spectrum after annealing in H_2 at 250 ^oC, 68 bar for 20 h. The hashes mark the locations of anatase (yellow) and rutile (green) peaks. The rest of the peaks, with the exception of those at 240 and 270 cm^{-1} are presumed to be those belonging to Ti_2AlC. Note that these peaks do *not* decrease in intensity with the H_2 anneal; the ones associated with rutile and anatase do, indirectly confirming their nature. 147

Figure 6-3: Plots of weight loss (%) as a function of time for 5 samples tested herein, showing, within the resolution of our TGA unit, almost naught weight loss in MI-Ti_2AlC and HP-Ti_2AlC samples. 151

Figure 7-1: Schematic of, (a) isostrain, and, (b) isostress conditions in Mg-Ti_2AlC composites showing strain and stress continuity across the constituent phases. 159

Figure 7-2: Plot of ultimate compressive strength (UCS) values of all materials tested in this work compare to Mg-Ti_2AlC AZ31B alloy composite. 161

Figure 7-3: Typical compressive stress-strain curves of Mg-Ti_2AlC AZ31B alloy composite; only one cycle per load is shown and the curves are shifted horizontally for clarity. 161

Figure 7-4: Schematic of the evaporation-condensation technique to make Mg single crystals and nano-Mg coatings on the surface of (a) alumina, (b) metallic films..... 164

Figure 7-5: Mg crystals grown on a) alumina, b) titanium foil, c and d) vanadium foil; e and f) 3D starfish Mg nanocrystals grown on vanadium foil; g) nanocrystalline Mg formed on the surface of Nb film. 168

Figure 7-6: Time dependence of nano-indentation strain at stresses shown for ZnO single crystals. Horizontal arrow points to a run that was interrupted for 50 s, 200 s into the creep run [204]. 168

Figure 7-7: Spherical nanoindentation stress-strain results on Mg single crystals. 169

ABSTRACT

On the Effect of Texture on Kinking Non-Linear Elasticity of
MAX Phases and MAX-reinforced Mg Matrix Composites

Shahram Amini
Ph.D. Supervisor: Prof. Michel W. Barsoum

The MAX phases and hexagonal metals, among many other plastically anisotropic solids with c/a ratios > 1.5, have been recently classified as kinking nonlinear elastic (KNE) solids – the signature of which is the formation of fully reversible, hysteretic stress-strain loops during cyclic loadings.

Herein, a unique and novel class of Mg matrix composites reinforced with Ti_2AlC was fabricated, for the first time, by spontaneous melt infiltration. The ~ 35 *nm* Mg grains that constituted the matrix of these composites were exceptionally stable: repeatedly heating the composite to 700 °C – 50 °C above the melting point of Mg – remarkably did not lead to any coarsening. At 380±20 MPa, 700±10 MPa and 1.5±0.5 GPa, the ultimate tensile and compressive strengths and Vickers hardness of these composites, respectively, are significantly greater than other pure Mg-composites reported in the literature, a fact attributed to nanocrystalline nature of the Mg-matrix. The advantages of melt infiltration as a processing technique are affordability and ease of scalability. To make these composites, all one needs to do is melt bulk Mg above a porous preform of Ti_2AlC; nature does the rest.

Because kinking is a form of plastic instability, orienting the Ti_2AlC grains, prior to infiltration, with their basal planes parallel to the loading direction led to exceptionally high values of dissipated energy per unit volume per cycle, W_d. At 450 MPa, W_d of these

composites with this texture was found to be ≈ 0.6 MJ/m^3, believed to be the highest ever reported for a crystalline solid. Counterintuitively, the W_d's of bulk Ti_2AlC samples, in which the basal planes are normal to the applied load were higher than those in which the basal planes were loaded parallel to the loading axis. In the case of the composites, the relatively softer Mg phase in between the Ti_2AlC grains allows the latter to kink, while in the Ti_2AlC bulk samples the majority of the plate-like grains of Ti_2AlC seem to be constrained by the minority grains. In-situ neutron diffraction experiments suggest that the minority grains are kinking significantly more than the majority grains. The KNE microscale model – previously developed to explain kinking nonlinear elasticity – is in excellent agreement with the experimental results obtained in this work. The model is capable of calculating the critical resolved shear stresses, CRSS, of basal plane dislocations making up the incipient kink bands – the reversible micro-constituent responsible for the nonlinearity and W_d. The model can also estimate the Taylor factor that, as far as we are aware, is the first time that factor has been measured experimentally. The Taylor factor – that ranged from 1.8 to 3.0 – was found to be a function of texture and grain size.

In summary, this work shows that the MAX-metal composites and their monolithic MAX phase counterparts fabricated herein are all KNE solids and their KNE behavior is a strong function of texture, and characterized by the formation of fully reversible hysteretic stress-strain loops under uniaxial cyclic compression.

Chapter 1 : MAX Phases and KNE Solids

1.1. Introduction to MAX Phases

The inspiration behind this work was the unique deformation behavior of the $M_{n+1}AX_n$ (MAX) phases as described in this chapter and Ch. 2. The MAX phases are layered hexagonal solids, with two formula units per unit cell, in which near close-packed layers of M are interleaved with layers of pure A-group elements, with the X-atoms filling the octahedral sites between the M layers (Figure 1.1). The A-group elements are located at the center of trigonal prisms that are larger than the octahedral sites and thus better able to accommodate the larger A-atoms. The M_6X octahedra are edge sharing and are identical to those found in the rock salt structure of the corresponding binary carbides. The main difference between the structures shown in Figure 1.1 is in the number of M layers separating the A-layers: in the 211's there are two; in the 312's three, and in the 413's four. This layered nature is of fundamental importance in understating the mechanical deformation discussed in most parts of this thesis.

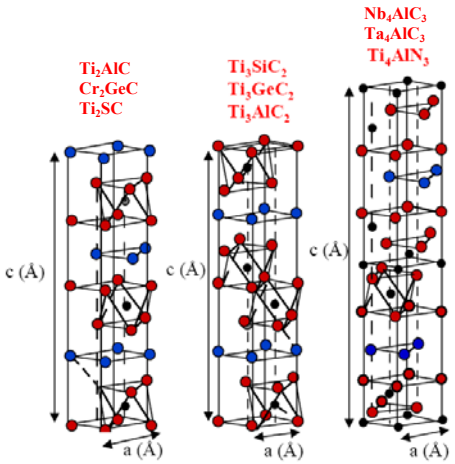

Figure 1-1: Unit cells of, (a) 211, (b) 312, and (c) 413 phases. M (red) is the early transition metal, A is A groups element, usually IIIA and IVA (dark blue), and X either nitrogen or carbon (black). The phases shown above the unit cells are some examples.

The MAX phases, numbering over 50 (Figure 1.2), are ternary carbides and nitrides that have received considerable attention in the past decade [1-6]. The most studied and best understood of the MAX phases are Ti_3SiC_2 and Ti_2AlC. In 1996, Barsoum and El-Raghy made a breakthrough [3] in the synthesis of bulk, dense samples of Ti_3SiC_2 and performed extensive characterization of its properties. Barsoum and his research group at Drexel University soon identified more than 50 closely related compounds (Ti_3AlC_2, Ti_2AlC, Ti_4AlN_3, Ti_2AlN, etc.) and named them the MAX phases. Most known MAX phases are listed in Figure 1.2 [7]. As a class, the MAX phases are best described as a unique class of thermodynamically stable polycrystalline nano-laminated solids [8].

At this time it is fairly well established that these phases have an unusual and sometimes unique combination of properties. They are excellent electrical and thermal conductors, thermal shock and chemical attack resistant, damage tolerant [9-14] and have relatively low thermal expansion coefficient (TEC) [15, 16]. Moreover, some of them are fatigue, creep and oxidation resistant [8, 13, 14, 17-26]. At high temperatures, they go through a plastic-to-brittle transition. At room temperature, they can be compressed to stresses as high as 1 GPa and fully recover upon removal of the load, while dissipating 25% of mechanical energy [16].

Until the discovery of the MAX phases, the price paid for high specific stiffness values has been lack, or difficulty, of machinability. One of the most important characteristic properties of the MAX phases despite being elastically quite stiff is the ease by which they can be machined, with nothing more sophisticated than a manual hack saw (Figure 1.3) [11, 12, 27, 28]. Their excellent electrical conductivities [16] also allows

them to be readily electron-discharge machined (EDMed) [27, 28] to net-shape components.

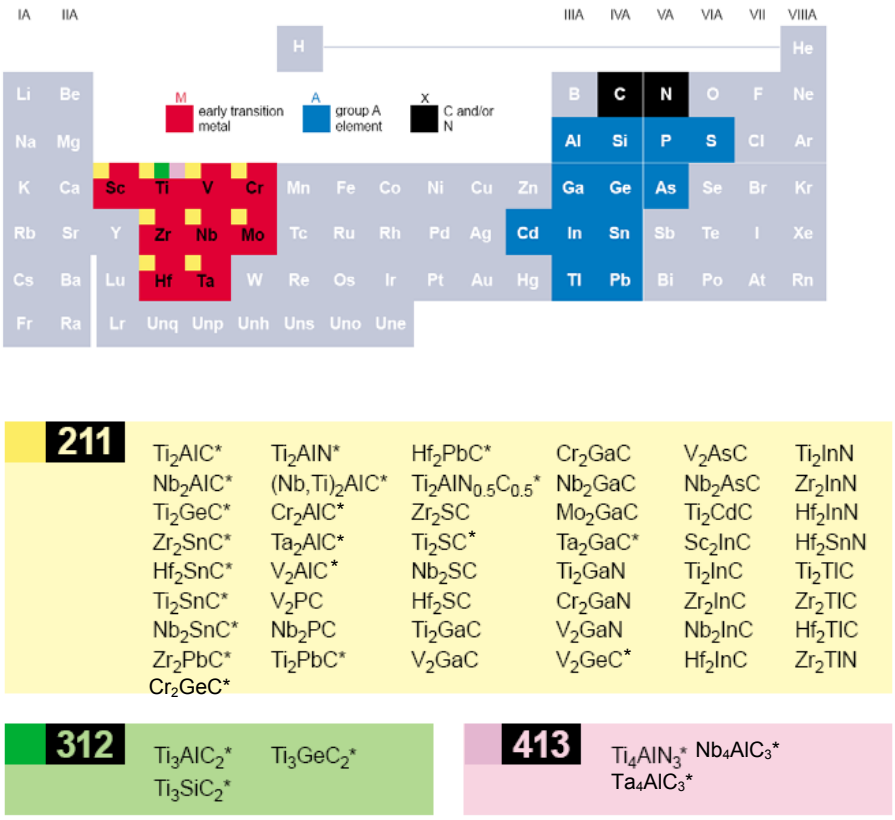

Figure 1-2: The MAX phases are made up of an early transition metal M (red) in the periodic table, an element from the A groups, usually IIIA and IVA (dark blue), and a third element, X, which is either nitrogen or carbon (black), in the composition $M_{n+1}AX_n$, where n is 1, 2 or 3. MAX phases characterized to date fall into three groups, based on the number of atoms of M, A and X in each unit cell; these groups are known as 211, 312 and 413. Those marked with asterisks have been successfully synthesized so far [12, 19, 20, 28-35].

Figure 1-3: MAX Phases are superbly machinable ternary carbides and nitrides (Photos by courtesy of 3-one-2 LLC) and can be machined with ease to net-shape components.

The MAX phases' electrical conductivities, like those of their M and MX, counterparts are metallic-like in that the resistivity increases linearly with increasing temperature, T [16].

The TECs of the MAX phases fall in the range of ≈ 5 to 13×10^{-6} K^{-1} (Figure 1.4) [15]. With two exceptions, being Cr_2GeC and Nb_2AsC, the agreement between the TEC values measured from dilatometry and those measured using high temperature diffraction [15], both XRD and neutron - are reasonable. Why Cr_2GeC and Nb_2AsC are such outliers is not clear at this time. A correlation exists between the TEC's of the ternaries and the corresponding MX binaries. For example, the TEC's of the Hf-containing MAX phases are lower than those containing Ti, which in turn are lower than Cr_2AlC. For comparison, the TEC's of HfC, TiC and Cr_3C_2 are 6.6, 7.4 and 10.5×10^{-6} K^{-1}, respectively [8, 15, 16].

The MAX phases do not melt congruently, but decompose peritectically according to $M_{n+1}AX_n \rightarrow M_{n+1}X_n + A$. Given the chemical stability of the $M_{n+1}X_n$ blocks and the fact that the A-layers are relatively loosely held, this result is not too surprising. The decomposition temperatures vary over a wide range from ≈ 850 °C for Cr_2GaN to above

2300 °C for Ti_3SiC_2. The decomposition temperatures of the Sn-containing ternaries range from 1200 to 1400 °C [8].

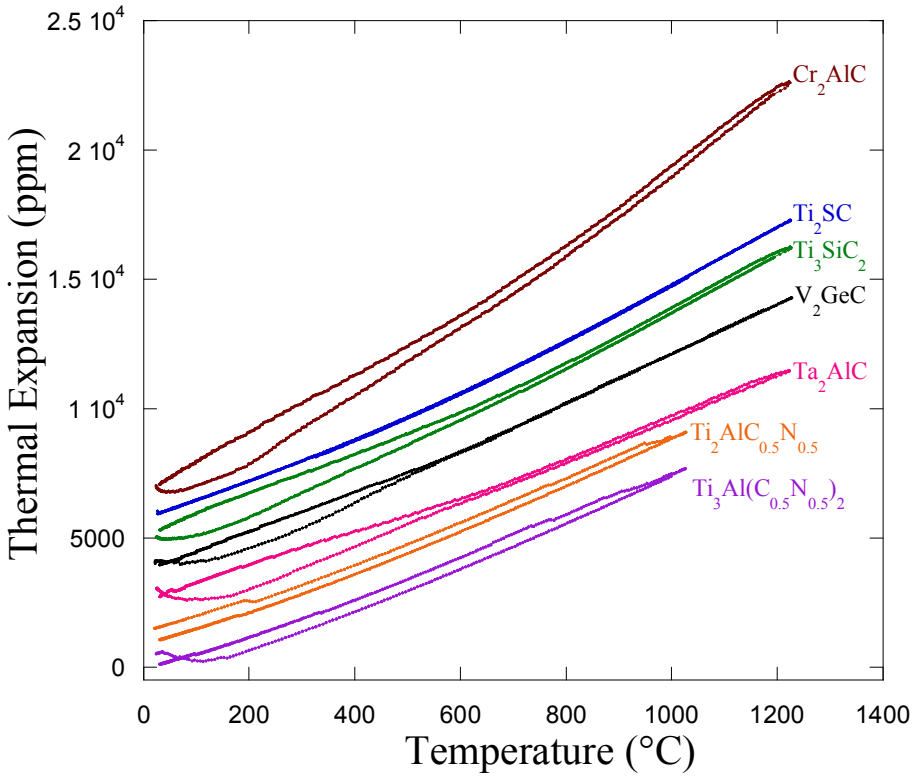

Figure 1-4: Thermal expansion vs. temperature for selected MAX phases. Curves are shifted vertically for clarity [15].

Given their excellent high temperature mechanical properties, some of the MAX phases are being considered for a number of high temperature applications, both structural and non-structural. To be used in air, however, their oxidation resistance is of paramount importance. Early, short term oxidation results on Ti_3SiC_2 [36] suggested it was oxidation resistant to temperatures as high as 1400 °C. A more recent long term oxidation study [37], on the same compound, however, indicate that, like for other rutile forming MAX-phases, the oxidation kinetics start out parabolic, but then switch to linear.

Based on that study, it now appears that the highest temperature at which Ti_3SiC_2 can be used continuously in air is ≈ 900 °C [37].

The most promising MAX phase to date, with superb oxidation resistance is Ti_2AlC [9, 38, 39]. After 10,000 cycles from 1350 °C to room temperature, only a thin, adherent protective 15 μm layer was found. The formation of Al_2O_3 is key to its high temperature oxidation protection. The oxidation resistance of Cr_2AlC is also quite good [40-43]. At 1000 and 1100 °C, the oxidation resistance is excellent because of the formation of a thin Al_2O_3 oxide layer with a narrow Cr_7C_3 underlayer. At 1200 and 1300 °C, an outer (Al_2O_3,Cr_2O_3)-mixed oxide layer, an intermediate Cr_2O_3 oxide layer, an inner Al_2O_3 oxide layer, and a Cr_7C_3 underlayer formed on the surface. At 1200 °C, scale cracking and spalling was observed; at 1300 °C, the cyclic oxidation resistance deteriorated due to the formation of voids and scale spallation [42]. It follows that despite its excellent oxidation resistance, it is unlikely that Cr_2AlC can be used at temperatures much higher than 1100 °C or even 1000 °C, because of this propensity for spallation that can be traced to the relatively high thermal expansion of this compound. In general, the oxidation of the MAX phases occurs according to the following reaction: [16]

$$M_{n+1}AX_n + b\ O_2 = n+1\ MO_{x/n+1} + AO_y + n\ XO_{2b-x-y}$$

More importantly, and contrary to Ti_2AlC and Ti_3SiC_2, in compounds such as Ti_2SC [44], wherein the oxidation products of both S and C are gases, the oxidation behavior is different from other Ti-containing MAX phases due to the formation of pores and microcracks in the rutile layer. For more details, see Appendix B.

The mechanical properties of the MAX phases are dominated by the fact that basal-plane dislocations multiply and are mobile at temperatures as low as 77 K and higher. The presence of basal slip is thus crucial to understanding their response to stress. This is true despite the fact that the number of independent slip systems is less than the 5 needed for ductility. In typical ceramics at room temperature, the number of independent slip systems is essentially zero. The MAX phases, thus occupy an interesting middle ground, in which in constrained deformation modes, highly oriented microstructures, and/or at higher temperatures they are pseudo-ductile. In unconstrained deformation, and especially in tension at lower temperatures, they behave in a brittle fashion. As noted above, basal plane, and only basal plane, dislocations are responsible for how the MAX phases respond to stress. There are no credible reports that twins and/or non-basal dislocations participate in any meaningful way in their deformation. It follows that at all times the number of slip systems active is < 5, needed for polycrystalline ductility. As will become apparent shortly, most of our understanding on the deformation of the MAX phases is based on early work carried out on Ti_3SiC_2, which is the most studied and best understood to date. However, there is little doubt, and more recent work [28, 45] confirms, that what applies to Ti_3SiC_2 applies to other MAX phases as well.

For the most part, the $M_{n+1}AX_n$ phases are elastically quite stiff. When combined with the fact that the densities of some of MAX phases are relatively low, ≈ 4.1 to 5 g/cm^3 [16] their specific stiffness values can be high [27]. For example, the specific stiffness of Ti_3SiC_2 is comparable to Si_3N_4, and roughly three times that of Ti. Also, with a Young's modulus of 316±2 GPa, Ti_2SC [27] is quite stiff and with a measured density of 4.59 Mg/m^3, its specific stiffness rivals that of Ti_2AlC, and Si_3N_4 (for more details, see

Appendix A). Poisson's ratios (υ) for all the MAX phases hover around 0.2 – with the exception of Cr_2GeC for which υ is 0.29 [16, 27, 28] – that in general are lower than the 0.3 of Ti, and closer to the 0.19 of near-stoichiometric TiC.

The MAX phases, unlike the MX carbides, are relatively soft and exceedingly damage tolerant [16, 28]. The Vickers hardness values of polycrystalline MAX phases fall in the range of 2-8 GPa [27, 28]. They are thus softer than most structural ceramics, but harder than most metals. The first hint that Ti_3SiC_2 was atypical came as early as 1972, when Nick1 et al. [46], working on chemically vapor deposited single crystals, showed that Ti_3SiC_2, was anomalously soft for an early transition metal carbide. The hardness was also quite anisotropic, with the hardness normal to the basal planes roughly 3 times than parallel to them. In 1987**,** Goto and Hirai [47], confirmed the results of Nick1 et al. Due to the difficulties in fabricating monolithic, bulk and dense Ti_3SiC_2, very little was known about this material until 1996 and some of what was known has been shown to be incorrect later.

Some MAX phases – most notably Ti_3SiC_2 and Ti_2AlC - are promising, lightweight candidates for high temperature structural and other applications. Their electrical and thermal conductivities are higher than those of Ti metal [3, 48]. Despite having a density (~4.5 gm/cm^3) comparable to Ti, their stiffness are roughly three times as high [49], and yet are most readily machinable. With a Vickers hardness of ≈ 3 GPa, they are relatively soft, unusually thermal shock resistant [3, 50] and highly damage tolerant [3, 51]. Unlike most brittle solids, edge cracks do not emanate from the corners of hardness indentations (e.g. see Appendices A and C). Rather, intensive kinking, buckling and bending of

individual grains take place in the vicinity of the indentations, resulting in pseudo-plastic behavior at room temperature [28, 51].

As discussed in more detail in the next section, one the most important properties of MAX phases, i.e. their so-called kinking non-linear elasticity, the key mechanism without which the deformation of MAX phases can not be understood.

1.2. Kinking Nonlinear Elastic Solids

Recently [52-54] it was postulated that most plastically anisotropic solids with *c*/*a* ratios > 1.5 (Figure 1.5) belong to the same class of solids labeled kinking nonlinear elastic (KNE) [28, 54-59].

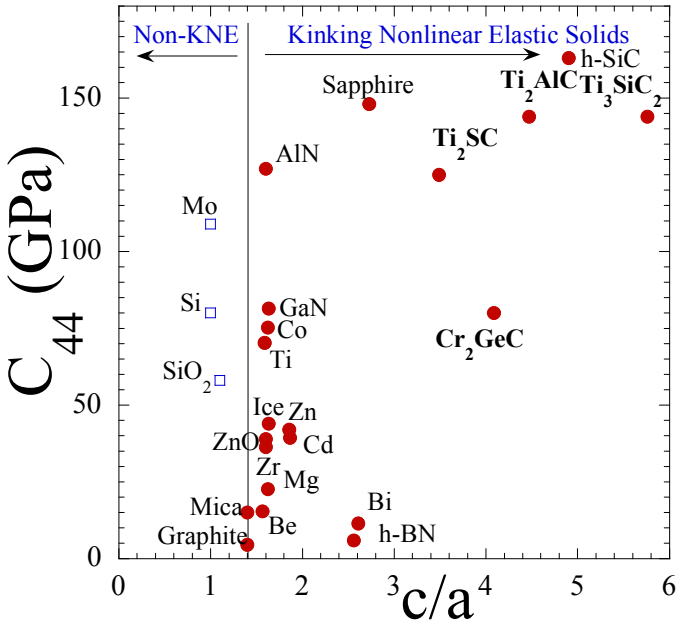

Figure 1-5: c_{44} vs. c/a for a number of solids, some of which are known to kink and others that are not [60]. Based on this map it is clear that KNE solids lie to the right of the vertical line and hence constitute a huge class of solids.

Kinking is a mechanism first reported by Orowan in single crystals of Cd loaded parallel to the basal planes [61]. Kink band formation is the key mechanism without which the deformation of KNE solids cannot be understood. Recently, it was established that a number of seemingly unrelated solids such as the MAX phases [28, 56, 57], graphite [62], mica [63], sapphire [64], ZnO [65], GaN [66], $LiNbO_3$ [67] and the hexagonal metals (Mg, Co, Ti, Zn etc.) [58, 59, 68-70], among many others, are KNE solids. Most recently, and as will be shown in this thesis, MAX-reinforced metal-matrix composites – what can be labeled MAXMETs – are KNE solids too [71, 72].

The signature of KNE solids is the formation of fully reversible, hysteretic stress-strain loops (Figure 1.6) during cyclic loadings [55, 56]. The various parameters needed to describe the stress-strain loops are as follows: measured stress (σ), nonlinear strain (ε_{NL}), linear strain (ε_{LE}), and dissipated energy per unit volume per cycle (W_d).

Full reversibility of such loops has been attributed to the formation of incipient kink bands (IKBs) that are comprised of multiple, parallel dislocation loops (Figure 1.7), whose shape ensures that when the load is removed they shrink significantly or are annihilated altogether [73]. In other words, solids that are highly plastically anisotropic deform at least initially by the formation of dislocation-based IKBs [54]. In addition to being fully reversible, the loading-unloading stress-strain curves of KNE solids are strain-rate independent and highly reproducible. Their shape, and the energy dissipated per unit volume in each cycle, W_d, are strongly influenced by grain size, with the former being significantly larger in coarse-grained solids [56]. At room temperature, some KNE solids such as Ti_3SiC_2 can be compressed to stresses as high as 1 GPa and fully recover upon removal of the load, while dissipating ≈ 25% of the mechanical energy [56, 74].

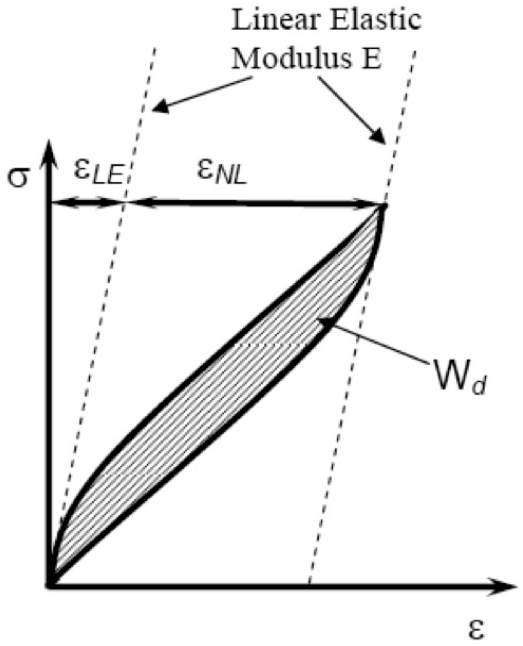

Figure 1-6: Schematic of a typical stress-strain curve for a KNE solid. The various parameters needed to describe the curve are labeled.

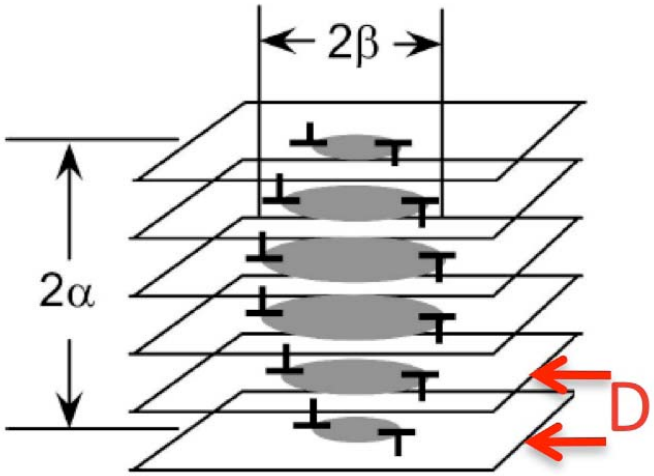

Figure 1-7: Schematic of an IKB with length 2α and diameter 2β. D is the distance between the horizontal dislocation loops.

Kinking nonlinear elasticity was first documented in Ti_3SiC_2 (Figure 1.8), a founding member of the MAX phases [52, 53, 56, 62, 75-77].

Recently, Zhou et al. reported on the mechanical response of fully dense and 10 vol. % porous Ti_2AlC bulk samples (Figure 1.9) to cyclic compressive loadings [57]. In that work, it was shown that the porous material dissipates more energy on an absolute scale, which is compelling evidence that we are dealing with a kink-based phenomenon as opposed to one that is dependent on the volume of the material, such as dislocation pileups.

More recently [28], it was also shown that Cr_2GeC samples compressively loaded from 300 MPa to ~ 570 MPa exhibited nonlinear, fully reversible, reproducible, hysteretic loops that dissipated ~ 20 % of the mechanical energy, due to the formation and annihilation of IKBs (for more details, see Appendix C).

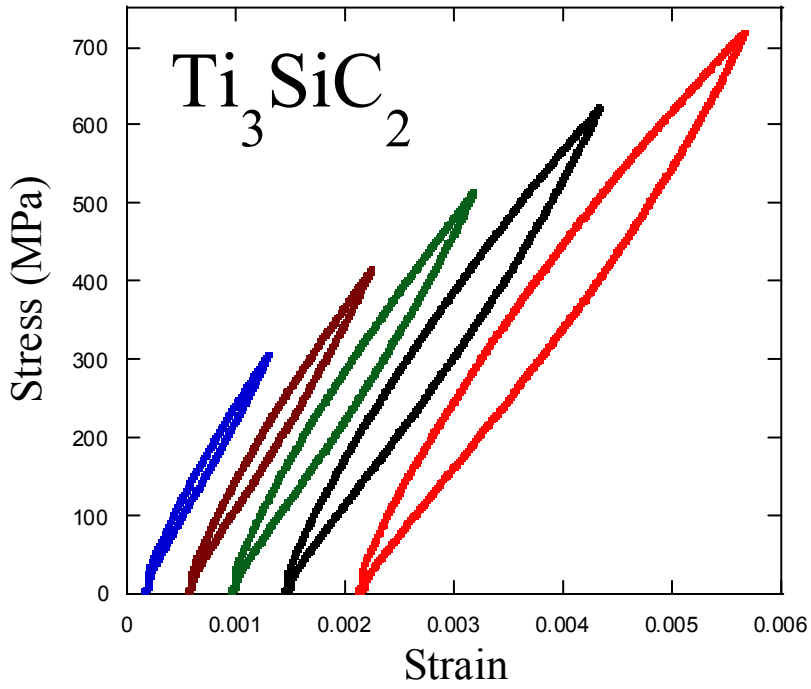

Figure 1-8: Typical stress-strain curves of Ti_3SiC_2; the loops are shifted horizontally for clarity (see Chapters 4 and 5 for more detail).

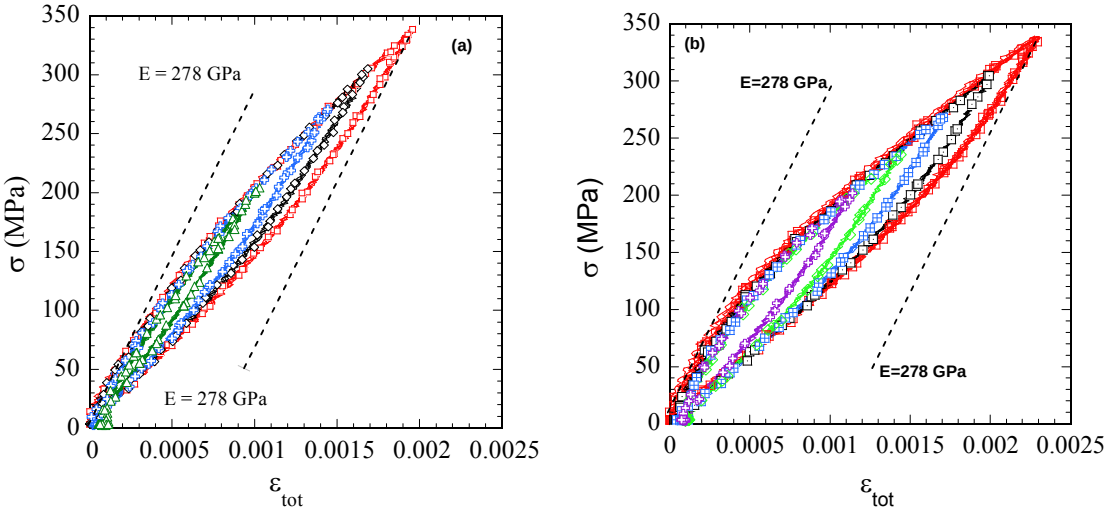

Figure 1-9: Stress-strain curves of uniaxial cyclic compression result of, (a) dense, and, (b) porous Ti_2AlC samples. The samples were first compressed to 350 MPa, unloaded and then reloaded to progressively higher stresses [78].

1.3. Kinking Nonlinear Elasticity in Hexagonal Metals

It was recently shown that the plastically anisotropic hexagonal metals (HMs), can be classified as KNE solids (Fig. 1.10) [45, 58, 59, 69, 70], thus explaining their microyielding and high damping [79, 80]. Because of their crucial technological importance, Ti, Zr, Mg, Zn and Co, among others, have been intensively studied over the past 70 years. Zr alloys used as cladding for nuclear reactor fuels and Ti alloys used in the aerospace and the aircraft industries are but a few examples. Mg is well known for its high damping capabilities [81, 82], lightweight, good castability and machinability [82-84] and its alloys are currently used in the automobile, computer, communication and consumer electronic applications. Therefore, the deformation mechanisms of these solids and their alloys to high strains are reasonably well understood. However, how these solids deform at low strains was not well understood until the crucial role kink bands (KBs) played in their early deformation was appreciated [58, 59, 69, 70, 80]. It was shown that their W_d and σ_t, being the threshold stress below which no kinking occurs, are a strong function of grain size, with larger grains resulting in lower σ_t and higher W_d values. As shown in the next chapter, W_d scales with the critical resolved shear stress (CRSS) of the easy slip dislocations. More importantly, by using the microscale model described in the next chapter, it was shown, how from a single uniaxial compression experiment, one can obtain a decent picture of the distribution and density of reversible dislocations at any stress, as well as extract the CRSS of the dislocations comprising the IKBs.

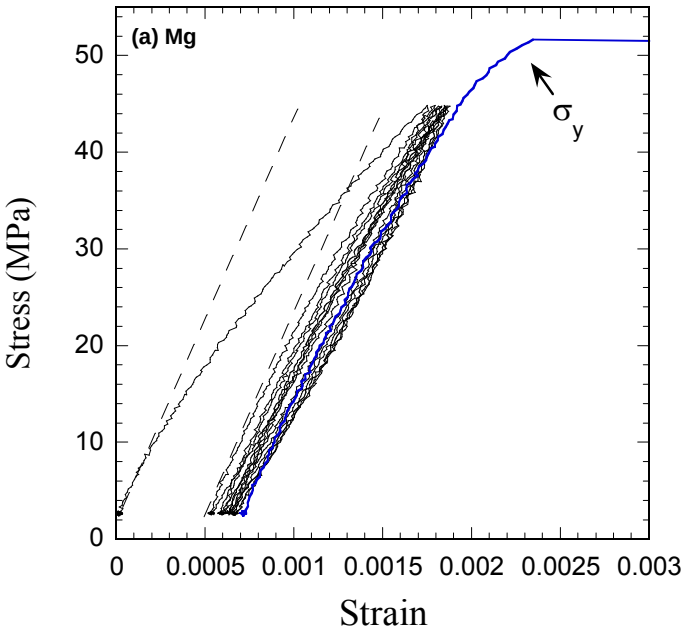
(a) Mg
σy
Stress (MPa)
Strain
0
10
20
30
40
50
0
0.0005
0.001
0.0015
0.002
0.0025
0.003

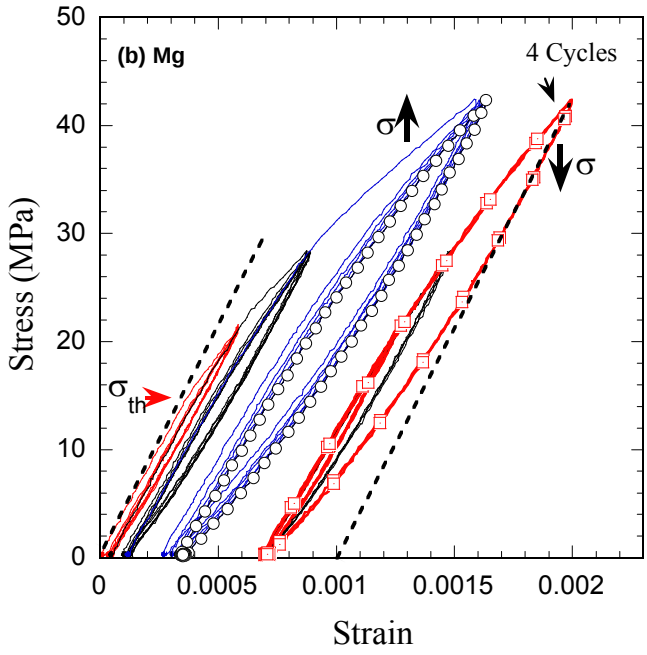
(b) Mg
4 Cycles
σ
σ
σth
Stress (MPa)
Strain
0
10
20
30
40
50
0
0.0005
0.001
0.0015
0.002

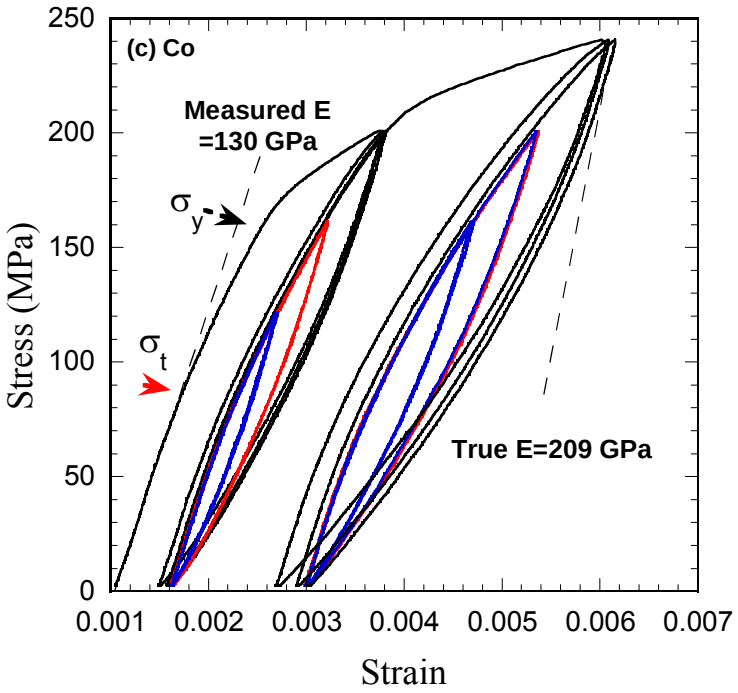
(c) Co
Measured E
=130 GPa
σy
σt
True E=209 GPa
Stress (MPa)
Strain
0
50
100
150
200
250
0.001
0.002
0.003
0.004
0.005
0.006
0.007

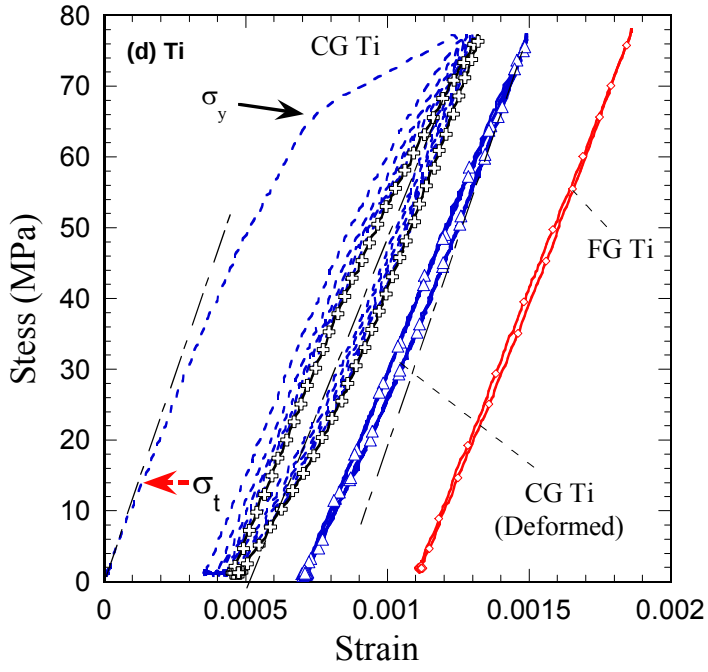
(d) Ti
CG Ti
σy
σt
FG Ti
CG Ti
(Deformed)
Stess (MPa)
Strain
0
10
20
30
40
50
60
70
80
0
0.0005
0.001
0.0015
0.002

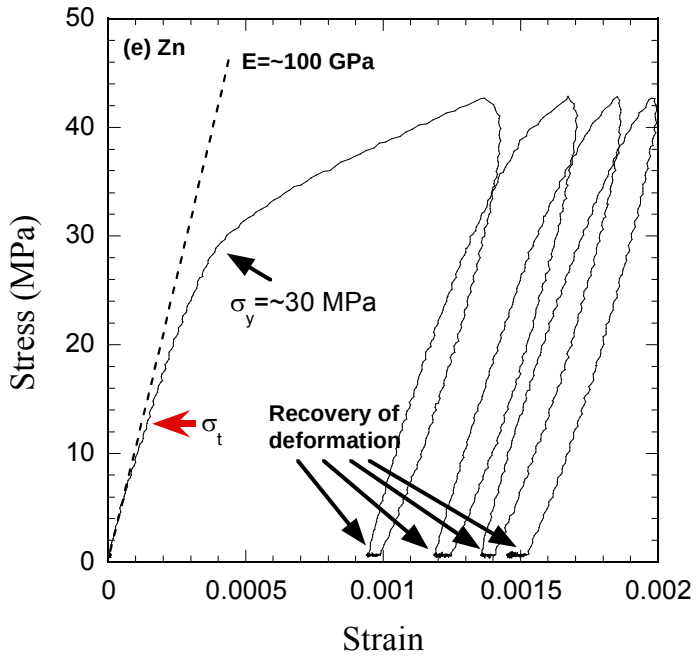

Figure 1-10: (a) Stress-strain curve of Mg with a yield point σ_y, 52 MPa. Even below σ_y, there are hysteretic loops. (b) Stress-strain curves of Mg show some hysteretic loops below σ_y. The left one was obtained from a progressively-increasing-stress test (↑). The right one was obtained from a progressively-decreasing-stress test (↓). (c) Stress-strain curves of Co (d) Stress-strain curves of coarse grained Ti (CG) and fine grained Ti (FG). (e) Stress-strain curves of Zn [58, 69].

It must be noted that IKBs are nature's solution to plastic anisotropy because their formation results in the dissipation or storage of substantial amounts of energy at low strains. Based on the previous works [28, 45, 55, 57-59, 65, 70, 71, 85], it is fair to conclude that IKBs constitute the last piece in the deformation-of-solids puzzle, without which it is not possible to understand the early deformation of plastically anisotropic solids, whether they are held together by covalent, ionic, metallic or secondary bonds.

1.4. Kinking Nonlinear Elasticity and Nanoindentation

At significantly higher stresses, however, under a nanoindenter, the IKBs (Figure 1.7) are sundered and devolve, first into mobile dislocation walls (MDW) (Figure 1.11a) and then ultimately into kink boundaries (KBs) (Figure 1.11b). The latter are irreversible [54].

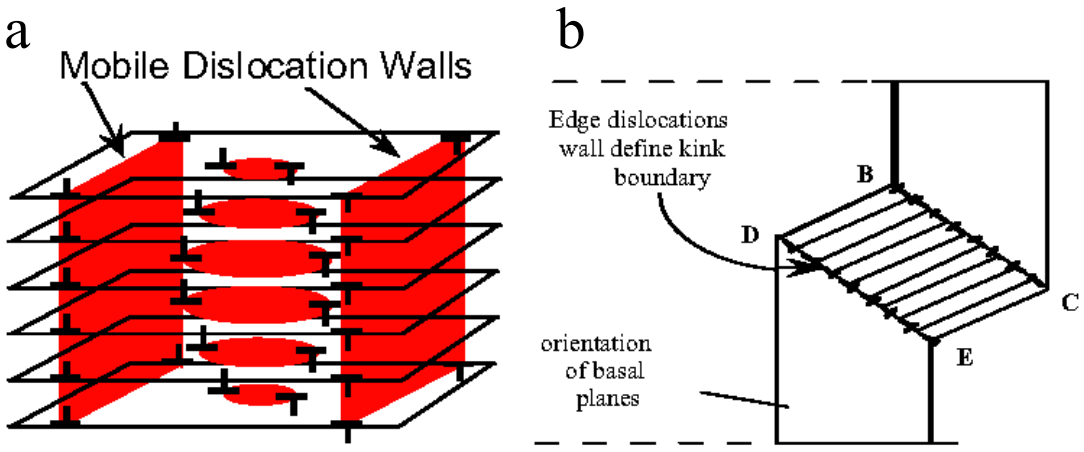

Figure 1-11: Schematic of kinking mechanism. a) IKBs (Figure 1.7) devolve into mobile dislocation walls (MDW). Note that a new IKB may form inside two MDWs. c) Formation of permanent kink bands (KBs), which is an irreversible process [54].

Barsoum et al. [62] reported on the response of graphite single crystals – loaded parallel to their c-axis with a 13.5 μm radius spherical diamond nanoindenter. Fully reversible hysteresis loops were observed up to stresses of ~ 0.5 GPa. At stresses > 0.5 GPa, the initial loops are slightly open; but subsequent loops, in the same location, are fully reversible and harder than the first. More interestingly, simple compression

experiments on polycrystalline samples yielded qualitatively similar results. These results can be explained by invoking the formation of IKBs.

Due to the high *c*/*a* ratio of sapphire (2.73) it was postulated that it should be a KNE solid. Basu *et al*. [55] showed that sapphire is a KNE solid by repeatedly loading (Figure 1.12) the same location on a sapphire single crystals with a 1 μm radius spherical nanoindenter, followed by atomic force microscopy. After pop-ins of the order of 100 *nm*, the repeated loadings gave rise to fully reversible, reproducible hysteresis loops wherein the W_d was of the order of 0.5 GJ/m^3. These results strongly suggest that similar to graphite, kink bands play a critical role in the constrained room temperature deformation of sapphire.

Basu *et al.* [65] also used nanoindentation experiments with two spherical tips, with radii of 13.5 and 1.4 μm, to explore the deformation behavior of ZnO single crystals with two orientations, C (basal) (Figure 1.13) and A (prism). In the C orientation repeated indentations to the same stress resulted in fully reversible hysteretic loops that were attributed to the formation and annihilation of IKBs.

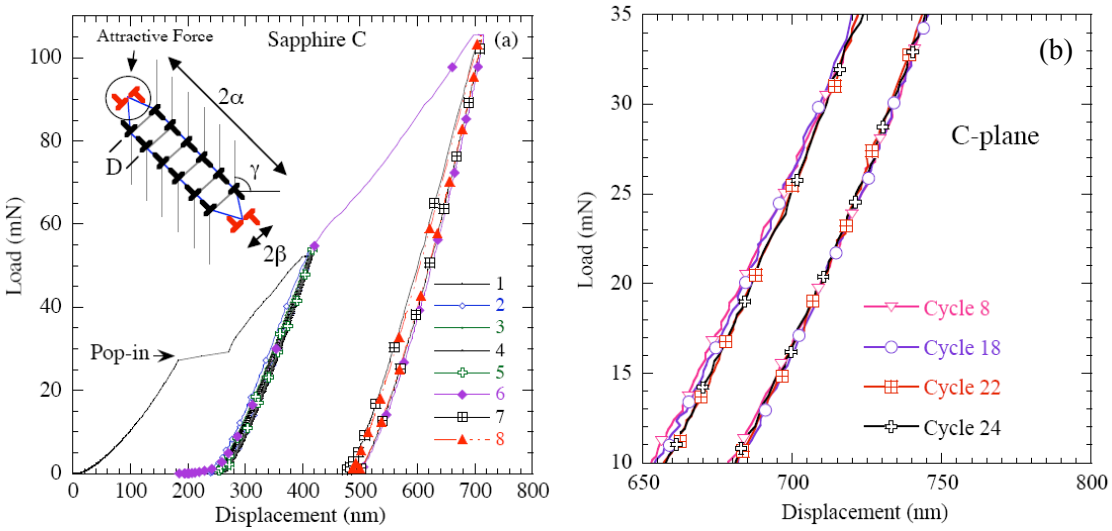

Figure 1-12: Cyclic nanoindentation results obtained when a 1.4 μm radius sphere is indented into the same location of a sapphire *C* (0001) crystal surface. (a) Load displacement for five cycles to 50 mN, followed by eight cycles at 100 mN. Inset is a schematic of an IKB. (b) Magnified view of the center of selected loops for an area indented 24 times to 100 mN. The reproducibility of the loops is noteworthy. In both a and b only a fraction of the data points collected are plotted [55].

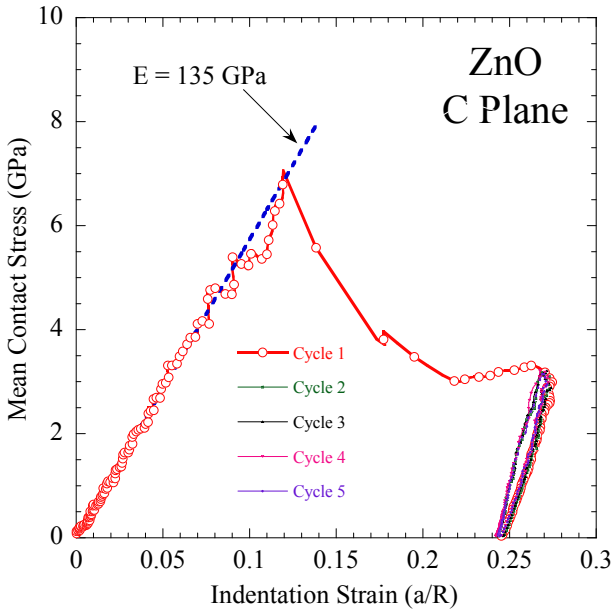

Figure 1-13: Nanoindentation stress–strain curves obtained when a 13.5 μm radius hemisphere is indented five times into the same location, to the same maximum stress, on a ZnO surface. Note the fully reversible and reproducible nature of the loops.

1.5. Goals and Motivations

Given the unique properties of Ti_2AlC [29] and its high damping [57], and the advantages of Mg, specifically its high damping [58, 59, 82-84], it was postulated that Mg-Ti_2AlC composites should result in solids that are not only machinable, stiff and light, but would also exhibit exceptional damping capabilities. More importantly, it was postulated that the response of MAX phases to cyclic loadings should depend on the orientation of the basal planes relative to the loading direction. Consequently, the primary motivation of this work was to explore the effect of texture on kinking nonlinear elasticity and damping capacity of these composites. Their mechanical response under compressive loadings will be reported using the recently developed microscale model to analyze the cyclic compressive stress-strain curves. Their response to micro-hardness indentation will be reported too.

The Mg-Ti_2AlC composites were fabricated using simple and cost-effective spontaneous infiltration fabrication technique that can be easily and readily scaled up. Therefore, before their mechanical behavior can be understood, it is necessary to report on the processing and microstructural characterization of these composites.

The second motivation of this thesis is to report on the mechanical response of bulk single phase Ti_2AlC to cyclic compressive loads and in-situ neutron diffraction, wherein the effect of texture and grain size on kinking nonlinear elasticity are investigated. Similar to Mg-Ti_2AlC composites, the KNE model – described in the next chapter – will be used to analyze the compressive cyclic stress-strain curves and compare them with those of the Mg-Ti_2AlC composites.

Last but not least, the cyclic thermal behavior of the aforementioned composites from room temperature to temperatures above the melting point of the nanocrystalline Mg phase – that constitute the matrix of the Mg-Ti_2AlC composites – will be reported. We will also investigate whether the thermal behavior of the nanocrystalline Mg matrix differs from that in the bulk state. It is hereby acknowledged that this chapter might be a diversion from the main theme of this thesis, but they are thought to be important enough to warrant inclusion here.

Chapter 2 : Kinking Nonlinear Elasticity Microscale Model

The deformation of KNE solids, as we have shown in Figure 1.8 for polycrystalline Ti_3SiC_2, essentially results in the formation of fully reversible, hysteretic stress-strain loops during cyclic loadings, under compression [28, 56] and tension [86]. According to Figure 1.6, the total strain, ε_{tot}, at a certain stress, σ, is constituted of a linear elastic strain ε_{LE} and a non-linear strain, ε_{NL} (Eq. 2.1), wherein E is the Young's modulus:

$$\varepsilon_{tot} = \frac{\sigma}{E} + \varepsilon_{NL} = \frac{\sigma}{E} + \varepsilon_{IKB} + \varepsilon_{DP} \qquad \text{(Eq. 2.1)}$$

In the most general case, ε_{NL} is composed of two components. The first, ε_{IKB}, is due to IKBs; the second, ε_{DP}, is due to basal slip that leads to dislocation pileups. In the entire thesis, we assume $\varepsilon_{NL} = \varepsilon_{IKB}$ and in essence ε_{DP} will be ignored for the most part. Therefore, the various parameters needed to describe the stress-strain loops are as follows: σ, ε_{NL}, ε_{LE}, and the dissipated energy per unit volume per cycle, W_d.

Frank and Stroh, F&S, [73] considered an elliptic kink band, KB, with length, 2α, and width, 2β, such that $\alpha >> \beta$ (Figure 1.7) and showed that the remote shear stress, τ, needed to render such a subcritical KB unstable is given by [87]:

$$\tau_t \approx \frac{\sigma_t}{M} \approx \sqrt{\frac{4G^2 b\gamma_c}{2\alpha\pi^2} \ln\left(\frac{b}{\gamma_c w}\right)} \qquad \text{(Eq. 2.2)}$$

where τ_t is the critical shear stress at the grain level and σ_t is the remote critical axial stress; *M* is the Taylor factor relating them; *G* is the shear modulus and *b* is the Burgers vector; *w* is related to the dislocation core width [73].

In our MAX phase work to date [28, 45, 72] as we will show in Chs. 4 and 5, we have equated the grain dimension along the [0001] direction – i.e. normal to the direction of easy slip – with 2α. The most reliable and precise technique to measure 2α is to measure the thickness of the grains by SEM from a fractured surface and OM micrographs (see Ch. 5).

σ_t, that is experimentally determinable, is essentially a threshold stress below which no kinking occurs or in other words when W_d is naught. Hence, if σ_t is known, then 2α can be estimated from Eq. 2.2; γ_c is a critical kinking angle calculated assuming [73]:

$$\gamma_c = \frac{b}{D} \approx \frac{3\sqrt{3}(1-\nu)}{8\pi e}\left(\frac{b}{w}\right) \qquad \text{(Eq. 2.3)}$$

where ν is Poisson's ratio, and D is the distance between dislocation loops along 2α (Figure 1.7). Because an IKB supposedly consists of multiple parallel dislocation loops (Figure 1.7), as a first approximation we assume each loop is comprised of two edge and two screw dislocation segments with lengths, $2\beta_x$ and $2\beta_y$, respectively (Figure 2.1). The latter are related to the applied stress, σ, and 2α assuming: [73]

$$2\beta_x \approx \frac{2\alpha(1-\nu)}{G\gamma_c}\frac{\sigma}{M} \qquad \text{and} \qquad 2\beta_y \approx \frac{2\alpha}{G\gamma_c}\frac{\sigma}{M} \qquad \text{(Eq. 2.4)}$$

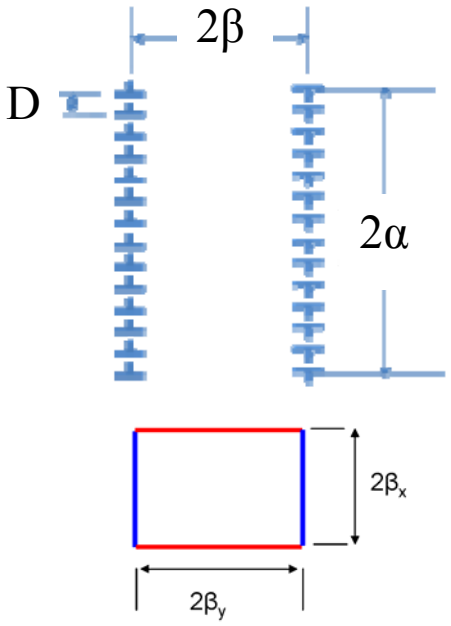

Figure 2-1: Dislocation walls and dislocation loops of an IKB. D is the distance between two dislocation loops. $2\beta_x$ is the length of the edge dislocation segment; $2\beta_y$ is the length of the screw dislocation segment [69, 73].

The formation of an IKB can be divided into two stages: nucleation and growth [59]. Since the former is not well understood, this model only considers IKB growth from $2\beta_{xc}$ and $2\beta_{yc}$ to $2\beta_x$ and $2\beta_y$, respectively. The dislocation segment lengths of an IKB nucleus, $2\beta_{xc}$ and $2\beta_{yc}$, are presumed to pre-exist, or are nucleated during pre-straining. The values of $2\beta_{xc}$ and $2\beta_{yc}$ are estimated from Eqs. 2.4, assuming $\sigma = \sigma_t$, where the latter is experimentally obtained (see below).

It follows that for $\sigma > \sigma_t$, the IKB nuclei grow and the IKB-induced axial strain resulting from their growth is assumed to be given by [59]:

$$\varepsilon_{IKB} = \frac{\Delta V N_k \gamma_c}{k_1} = \frac{N_k \gamma_c 4\pi\alpha(\beta_x\beta_y - \beta_{c,x}\beta_{c,y})}{3k_1} = \frac{4\pi(1-\nu)N_k\alpha^3}{3k_1 G^2\gamma_c M^2}(\sigma^2 - \sigma_t^2) = m_1(\sigma^2 - \sigma_t^2) \qquad \text{(Eq. 2.5)}$$

where m_1 is the coefficient before the term in brackets in the fourth term; N_k is the number of IKBs per unit volume; ΔV is the volume change due to the growth of one IKB as the stress is increases from σ_t to σ. It follows that the product $V \times N_k = v_f$, is the volume fraction of the material that is kinked. The factor k_1 relates the volumetric strain due to the IKBs to the axial strain along the loading direction, assumed to be 2.

The energy dissipated per unit volume per cycle, W_d, (shaded area in Figure 1.6) resulting from the growth of the IKBs from $\beta_{i,c}$ to β_i is given by [59]:

$$W_d = \frac{4\Omega\pi N_k\alpha}{D}(\beta_x\beta_y - \beta_{xc}\beta_{yc}) = \frac{4\pi(1-\nu)N_k\alpha^3}{G^2\gamma_c M^2}\frac{\Omega}{b}(\sigma^2 - \sigma_t^2) = m_2(\sigma^2 - \sigma_t^2) \qquad \text{(Eq. 2.6)}$$

Ω is the energy dissipated by a dislocation line sweeping a unit area. Thus, Ω/b should be proportional, if not equal, to the critical resolved shear stress, CRSS, of an IKB dislocation loop. In previous works it has been shown that to be the case [59, 68].

Combining Eqs. 2.5 and 2.6 yields:

$$W_d = 3k_1\frac{\Omega}{b}\varepsilon_{IKB} = \frac{m_2}{m_1}\varepsilon_{IKB} \qquad \text{(Eq. 2.7)}$$

Since $3k_1\frac{\Omega}{b}$ can be experimentally determined, the estimation of Ω/b only requires knowledge of k_1 in Eq. 2.7. When the stress-strain curves such as those in Figure 1.8 and 1.9 [57] are obtained and the parameters mentioned above measured experimentally, and

the plots of ε_{NL} and W_d vs. σ^2 and W_d vs. ε_{NL} shown in Figures 2.2 a-c are plotted [57], then the second term in Eq. 2.7 can be used to estimate Ω/b, assuming $k_1 = 2$.

On the other hand, m_1 and m_2 can be determined independently from the slopes of ε_{NL} vs. σ^2 and W_d vs. σ^2 plots (Figure 2.2). Hence, if our assumptions are valid and if the micromechanism that is causing the dependence of ε_{NL} on σ (i.e. Eq. 2.5) is the *same* as the one responsible for W_d (Eq. 2.7), then the *ratio* m_2/m_1 should equal $3k_1\Omega$/b as shown in Chs. 4 and 5 and in previous work [28, 57-59, 69-72, 88].

Lastly, for simplicity, assuming the IKBs are cylinders with radii β_{av}, then the *reversible* dislocation density, ρ_{rev}, due to the IKBs is given by:

$$\rho_{rev} = \frac{2\pi N_k 2\alpha\beta_{av}}{D} = \frac{4\pi N_k \alpha\beta_{av}\gamma_c}{b} \qquad \text{(Eq. 2.8)}$$

where β_{av} is the average of β_{xc} and β_{yc}.

The strongest evidence to date that shows the validity of the IKB model is shown in Figure 2.2 a-c, wherein it is obvious that a 10 % porous Ti_2AlC sample (loops in Figure 1.9 b) dissipates *more* energy per unit volume per cycle on an *absolute* scale than its fully dense counterpart (loops in Figure 1.9a). This compelling evidence essentially eliminates all mechanisms, such as dislocation pileups and/or twinning that scale directly with the volume of the material tested. It is, however, in agreement with the IKB model that kinking is a form of plastic instability, or buckling, and thus a less rigid or porous solid is more prone to kinking than a fully dense one [57]. This idea is a running theme in this thesis.

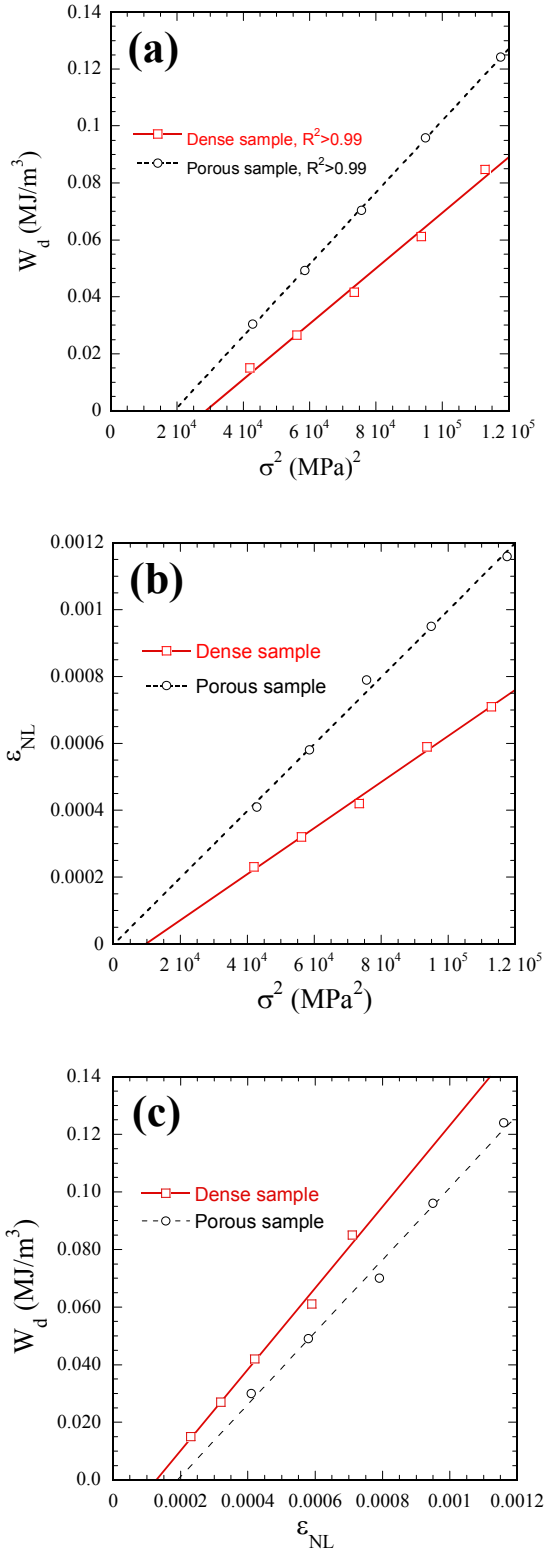

Figure 2-2: Plots of, (a) W_d vs. σ^2, (b) ε_{NL} vs. σ^2 and, (c) W_d vs. ε_{NL} obtained from uniaxial compression stress-strain curves of fully dense and 10 vol.% porous Ti_2AlC (Figure 1.9) [57].

More importantly, from Eq. 2.2, it follows that σ_t is a function of grain size, and the higher 2α, the lower σ_t. This means that nucleation and growth of IKBs occur at lower stresses in larger grains than in finer ones as we have shown in Refs. [53, 56] and in Figure 2.3, where the loop at 260 MPa in the fine-grained Ti_3SiC_2 sample (narrow, red loop on the left of Figure 2.3) is considerably smaller than the loop at 150 MPa of a coarse-grained sample of the same material, Ti_3SiC_2 (wide, blue on the right of Figure 2.3).

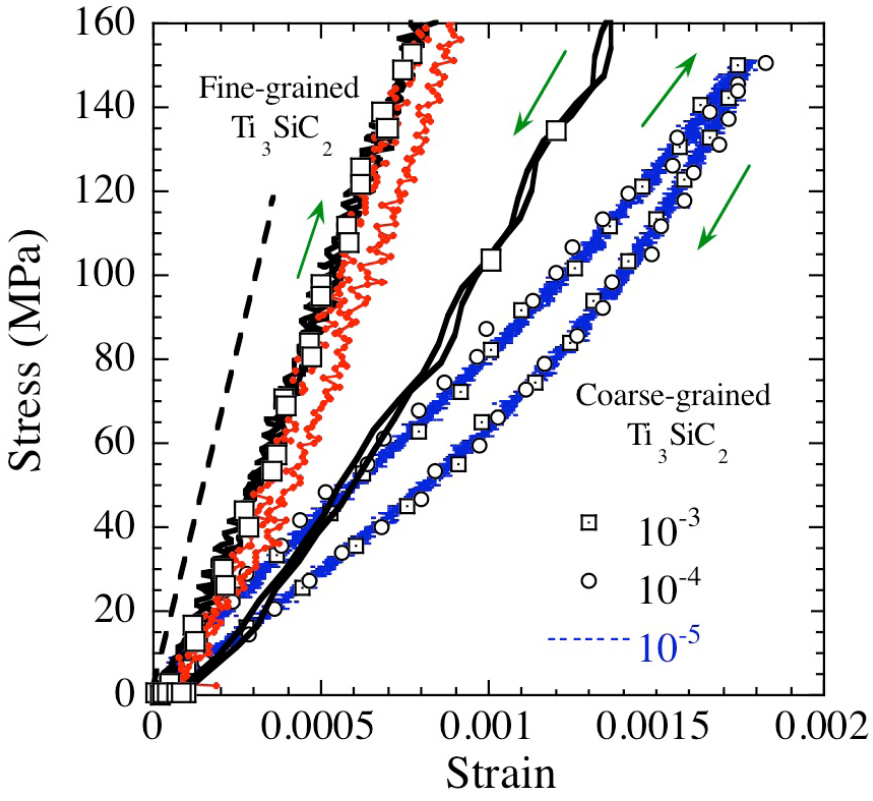

Figure 2-3: Stress-strain curves of polycrystalline, (a) fine-grained and, (b) coarse-grained Ti_3SiC_2 tested under uniaxial cyclic compression. Note that the stress-strain curves of the coarse-grained sample were not strain rate dependent, at least in the 10^{-3} to 10^{-5} S^{-1} strain rate regime [53, 56].

In addition to the good agreement between the various parameters and their interrelationships and consistency with the KNE model, probably the most important result is that the values of CRSS calculated from the model are in good agreement with the ones reported previously in the literature. For example the CRSS values in Mg and Co [58, 59] and the MAX phases, e.g. 36 MPa for Ti_3SiC_2 measured experimentally [13] are in good agreement with those calculated from the model.

Based on the work carried out so far, it is also remarkable that values of ρ_{rev}, all listed in Table 2.1, estimated from the model, vary by less than an order of magnitude in most MAX phases and only by a factor of 2 in hexagonal metals, with the exception of Mg, despite the fact that, i) the maximum applied stresses vary over a factor of 2 in some cases, ii) *G* varies by at least a factor of 2 and, ii) the N_k values vary by over 3 orders of magnitude. As we have stated in Refs. [28, 45, 59, 72] and in Chs. 4 and 5 herein, this observation suggests that an equilibrium ρ_{rev} exists to which all systems migrate. Presumably, in solids with high *G* and small grains, many small IKBs form; for solids with low *G* many fewer, but larger, IKBs form.

To sum up, based on the work in the literature, there are several factors that have been distinctly shown to affect the size and shapes of the stress-strain loops of KNE solids, namely: (a) Grain size; the larger the grain size, the larger the 2α and hence the lower the threshold stress, which results in larger stress-strain loops or larger W_d values; (b) Shear moduli: The lower the values of *G*, the larger W_d. This is a strong factor since because W_d is inversely proportional to G^2 (Eq. 2.6), which explains why porous solids can dissipate more energy than fully dense solids; (c) Ω/b that is essentially a measure of

the CRSS of the IKB dislocations. All else being equal, KNE solids with higher CRSS will dissipate more energy than those with lower values; e) Texture: This factor is essentially the motivation behind this thesis as mentioned in Ch. 1 and fully examined in Chs. 4 and 5, wherein we will show that texture can and will affect W_d as well as the Taylor factor, M.

Table 2-1: Summary of measured and calculated parameters of KNE microscale model for: (a) several MAX phase materials assuming $M = 3$, $k_1 = 2$, $b = 3$ Å, and $\upsilon = 0.2$ [28, 45] except Cr_2GeC for which $\upsilon = 0.29$ and $b = 2.95$ Å [28]; (b) Hexagonal metals (HMs) assuming $M = 3$ and $k_1 = 2$. For Co, $b = 2.7$ Å, and $\upsilon = 0.31$ [58], for Mg, $b = 3.2$ Å, and $\upsilon = 0.35$ [59]; for Ti, $b = 3.3$ Å, and $\upsilon = 0.32$ [58].

	G (GPa)	Ω/b (MPa)	2α (μm)	σ_t (MPa)	N_k (m^{-3})	$2\beta_{xc}$ (μm)	$2\beta_x$ (μm)	ρ_{rev} (m^{-2})	σ (MPa)
Ti_3AlC_2 Un-anneal. [45]	124	36	10	244	1.8×10^{16}	0.45	0.85	3.9×10^{13}	486
Ti_3AlCN [45]	137	53	10	270	1.4×10^{16}	0.5	1.0	3.5×10^{13}	629
Ti_3AlCN Annealed [45]	137	30	23	180	2.2×10^{15}	0.3	0.4	1.4×10^{13}	305
$Ti_2Al(C_{0.5},N_{0.5})$ [45]	124	62	4	376	2×10^{17}	0.1	0.9	8.7×10^{13}	610
Ti_2AlC [45]	118	24	19	170	7.3×10^{15}	0.6	1.2	4.2×10^{13}	336
Ti_3SiC_2 [45]	143	30	42	136	4.7×10^{14}	1	2.7	1.2×10^{13}	370
Cr_2GeC [28]	80	22	26	90	5.3×10^{14}	0.8	4.6	1.7×10^{13}	525
Mg [59]	19	6.5	28	14	7.8×10^{14}	0.7	1.7	4.9×10^{12}	42
Ti (FG) [58]	44	14	10±4	75	5×10^{14}	0.8	2	1×10^{8}	80
Ti(CG) [58]	44	16	100±30	47	2×10^{12}	2.5	15	0.5×10^{8}	80
Co [58]	75	18	200±70	84	8×10^{11}	3.7	50	0.5×10^{8}	240

Chapter 3 : MAXMETs; a New Class of Metal Matrix Composites Reinforced with MAX Phases

3.1. Introduction

As described in Ch. 1, the MAX phases are layered hexagonal solids, with two formula units per unit cell, in which near close-packed layers of M are interleaved with layers of pure A-group elements, with the X-atoms filling the octahedral sites between the M layers. At this time it is fairly well established that these phases have an unusual and sometimes unique combination of properties. They are excellent electrical and thermal conductors, thermal shock resistant and damage tolerant [9-14]. Despite being elastically quite stiff, they are all readily machinable with nothing more sophisticated than a manual hacksaw [11, 12]. Moreover, some of them are fatigue, creep and oxidation resistant [8, 13, 14, 17-26].

Also as explained in Ch. 2, more recently [52, 53, 56, 62, 75, 76], the MAX phases were classified as kinking nonlinear elastic (KNE) solids because they deform primarily by kinking, and the formation of kink bands. Kinking – a mechanism first reported in crystalline solids by Orowan in single crystals of Cd loaded parallel to the basal planes [61] – has also been identified as the physical origin of the hysteretic, nonlinear elastic behavior exhibited by these solids. Kink band formation is the key mechanism without which the deformation of KNE solids, in general, and MAX phases in particular, cannot be understood. When cyclically loaded, KNE solids form fully reversible, hysteretic stress-strain loops (Figure 1.6 and 1.8). This full reversibility has been attributed to the formation of IKBs that are comprised of multiple, parallel dislocation loops, whose shape

ensures that when the load is removed they shrink significantly or are annihilated altogether (Figure 1.7).

Ever since the development of the Volkswagen Beetle magnesium, Mg, engines and transmission in 1946 until the Mercedes-Benz 300 SLR Le Mans disaster in 1955, Mg parts had been seen as candidates for automotive components [89]. More importantly, however, Mg, and its alloys have also been recently used extensively in various industries – such as automotive – due to their lightweight, good castability and machinability [82-84]. Mg is also well known for its high damping capabilities [81, 82]. The reasons for this high damping had to date not been well understood. Most recently, it was shown by Zhou et al. that the high damping can be traced to the formation of IKBs [58, 59]. In other words, they showed that Mg - and other hexagonal metals, including Ti, Co and Zn - can be classified as KNE solids.

Compared to other structural metals, Mg alloys have relatively low strength, especially at elevated temperatures that limits their applications to temperatures lower than ≈ 120 ºC. The need for high-performance and lightweight materials for some demanding applications has led to the development of Mg-matrix composites [82, 90]. Despite their advantages, a major drawback of Mg matrix composites is their relative high cost of fabrication. It follows that cost-effective processing would expand their applications [82]. To manufacture composites with optimum properties, the manufacturing process must assure a uniform distribution of the reinforcing phase in the matrix. A variety of Mg-matrix composites have been fabricated through powder metallurgy [91-93]. Stir casting has been used for manufacturing composites, with up to 30% vol. fraction of reinforcement. Further extrusion to reduce porosity, refine the

microstructure, and homogenize the distribution of the reinforcement has also been used [82, 94-97]. Squeeze infiltration [82, 83, 98-103] and spontaneous infiltration [82, 104-106], have also been used. The mechanical properties of some of these composites are summarized in Table 3.1.

Table 3-1: Mechanical properties of select Mg matrix composites fabricated with different techniques and various volume fractions of reinforcement (E is Young's Modulus; UTS is Ultimate Tensile Strength).

Matrix	**Reinforcement**	**Fabrication Technique**	**E (GPa)**	**UTS (MPa)**	**Ref.**
AZ91*	-	As-cast	40	150-200	[91, 98]
AZ80**	50 vol.% SiC	Pressure infiltration	103	550	[103]
AZ91	20 vol.% alumina	Infiltration	70	240-290	[98]
AZ91	10 vol.% SiC	Mechanical alloying	50	150	[92]
AZ91	10 vol.% SiC	Powder metallurgy	45-50	135	[91, 92]
Mg	30 vol.% SiC	Powder metallurgy	59	250	[96]
Mg	30 vol.% SiC	Stir cast and extruded	60	258	[96]
Mg	50 vol.% SiC	Hot pressing (HPing)	120±20	-	This work
Mg	50 vol.% Ti_3SiC_2	HPing	75±5	-	This work
Mg	50 vol.% Ti_2AlC	Melt infiltration (MI)	72±6	350±40	This work

* (Cast Mg alloy; 9 % Al, 1 % Zn and 0.2 % Mn) ** (Cast and wrought Mg alloy; 8 % Al, 0.5 % Zn and 0.2 % Mn) [107]

Among all feasible fabrication techniques, the advantages of melt infiltration, MI, include the capability of incorporating a relatively high volume fraction of reinforcement and the fabrication of composites with matrix alloys and reinforcement systems that are otherwise not easily fabricated by other techniques. The MI technique utilized herein, not only resulted in homogenous microstructures but, more importantly, is a low cost technique that can be readily scaled up.

Given the unique properties of Ti_2AlC [29], its high damping [57], and the advantages of Mg [58], it was postulated that Mg-Ti_2AlC composites should result in solids that are not only machinable, stiff and light, but would also exhibit exceptional damping capabilities.

In general there has *not* been much work on MAX-metal composites – what can be labeled MAXMETs. Recently, Gupta et al. [108] fabricated Ta_2AlC and Cr_2AlC Ag-based composites. These composites are new solid lubricant materials for use over a wide temperature range against Ni-based superalloys and alumina. There are also a few papers in the literature on Ti_3SiC_2-Cu composites [109-111] and Ti_3SiC_2-SiC and TiC composites [37, 112]. Warm compaction, which is a simple and economical forming process to prepare high density powder metallurgy materials, was employed by Ngai *et. al* [110, 111] to fabricate Ti_3SiC_2 particulate reinforced Cu matrix composite with high strength, high electrical conductivity and good tribological behaviors. Ti_3SiC_2-Cu composites, with 1.25, 2.5 and 5 wt. % Ti_3SiC_2 were prepared by compacting powder with a pressure of 700 MPa at 145°C followed by sintering at 1000 °C. Their density, electrical conductivity and UTS decrease with increase in particulate concentration, while the hardness increases with the increase in particulate concentration. A small addition of Ti_3SiC_2 particulate increased the hardness of the composite without losing much of the electrical conductivity. The composite containing 1.25 wt. % Ti_3SiC_2 has an UTS of 158 MPa and an electrical resistivity of 3.91×10^{-8} Ωm [111]. Cu-Ti_3SiC_2 composite powders have also been fabricated using an electroless plating technique [109].

Wu *et al.* [113] reported on Ti_2SnC dispersion-strengthened Cu matrix composites fabricated by hot-pressing (HPing). The change of microstructure, mechanical properties, and electrical resistivity as a function of Ti_2SnC volume fraction were studied. Their results demonstrated that the grain size of Cu decreased pronouncedly from 27 μm in bulk Cu to ~ 1 μm by incorporating Ti_2SnC particulates, and the strengthening effect was significant. Improvements in yield strength of up to four times that of pure Cu were found

in Cu-1 vol.% Ti_2SnC, however, the conductivity of the composite was 85.6% of pure Cu. The high strength and low electrical resistivity of Cu-Ti_2SnC composites indicated that Ti_2SnC is a promising reinforcement for Cu.

For many years the use of Mg alloys as the matrix phases in metal matrix composites (MMCs) has been of interest as alternatives to Al-based composites for advanced structural applications and for components in engines, with the advantage of high specific strength and stiffness. Mg MMCs have mechanical properties basically similar to those of Al MMCs and can be used for similar lightweight structural and functional parts. The main advantage of Mg MMCs in comparison to Al MMCs is weight savings of about 20 to 25 %. In general, they also provide better machinability in comparison to Al MMCs [103, 114, 115]. Although cast Mg alloys and their composites have dominated the market, interest in the use of wrought Mg alloys and composites with greater strength and ductility is continuously growing [116].

Early development of Mg MMCs concentrated on continuous-fiber reinforced composites, especially graphite fibers due to the low thermal expansion of the composites fabricated. More recently, discontinuously reinforced composites have combined alumina, boron carbide and silicon carbide in the form of whiskers, particles and short fibers with a variety of Mg alloys through different manufacturing processes such as rheo-, compo-, stir- and squeeze-casting, and various MI processes, as well as, powder metallurgy [103].

Due to its extensive fluid-flow capabilities and lower melting temperature than Al, Mg is an ideal material for processing via the molten or semi-solid metal processing.

Among all, MI processes have numerous advantages, mainly due to the reactivity and low viscosity of Mg that speeds up the production of Mg MMCs. Another important advantage is that selectively reinforced components, within which the metal is reinforced only where needed, can be produced [117].

Two broad variants of infiltration processes have been devised for the fabrication of Mg MMCs: (1) pressureless infiltration (i.e. spontaneously, in the absence of an external pressure) which can be used when good wetting conditions exist, and, (2) pressure infiltration, in which pressure is required to drive the molten metal into the preform. Pressureless infiltration is simple, cost-effective and can result in near-net shape parts with a more homogenous distribution of particulate reinforcements. Easy tailoring of reinforcement volume fraction between 35-70 vol. % or higher is also possible [103, 117].

Spontaneous MI of Mg-based alloys into preforms is usually performed in an oxygen-free, nitrogen-containing atmosphere, where in the initial stages of the processing, Mg reacts with nitrogen to form thin Mg_3N_2 coatings on the reinforcement surfaces, which in turn renders the system wettable and eliminates the need for pressure. The MI can also be carried out in vacuum [103, 117]. We show here that composites can be fabricated successfully in a vacuum atmosphere.

To manufacture composites with optimum properties, the manufacturing process has to assure a uniform distribution of the reinforcing phase in the matrix. Both techniques utilized herein namely melt infiltration (MI) and HPing (HP), result in a homogenous microstructure, with a uniform distribution of the reinforcement.

In this chapter, processing and microstructural characterization of Mg-Ti_2AlC composites [71] will be reported. Their response to cyclic compressive loads is briefly discussed; their mechanical properties are discussed in the next chapters. This is the first work on the fabrication and characterization of Mg-Ti_2AlC composites.

3.2. Experimental Details

The composites tested herein were made using two different techniques: HPing and MI. The former was used initially on the assumption – later proven incorrect – that Mg, like Al, would not spontaneously infiltrate a Ti_2AlC preform. Both techniques are described in detail below.

Hot pressing: The starting powders of Ti_2AlC (-325 mesh, 3-ONE-2, Voorhees, NJ) and Mg (-325 mesh, 99.8 % pure, Alfa Aesar, Ward Hill, MA) were ball-milled for 12 h and dried in a mechanical vacuum furnace at 150 °C for 24 h. The dried powder mixtures were poured and wrapped in graphite foil, that, in turn, were placed in a graphite die and HPed in a graphite-heated vacuum-atmosphere HP (Figure 3.1), (Series 3600, Centorr Vacuum Industries, Somerville, MA), heated at 10°C/min to 750°C and held at the target temperature for 1 h, after which the HP was turned off and the samples were furnace cooled. A load, corresponding to a stress of ~ 45 MPa, was applied when the temperature reached 500 °C and maintained thereafter. The samples were removed from the dies and the graphite foil was removed. These samples will be referred to as the "HP" samples.

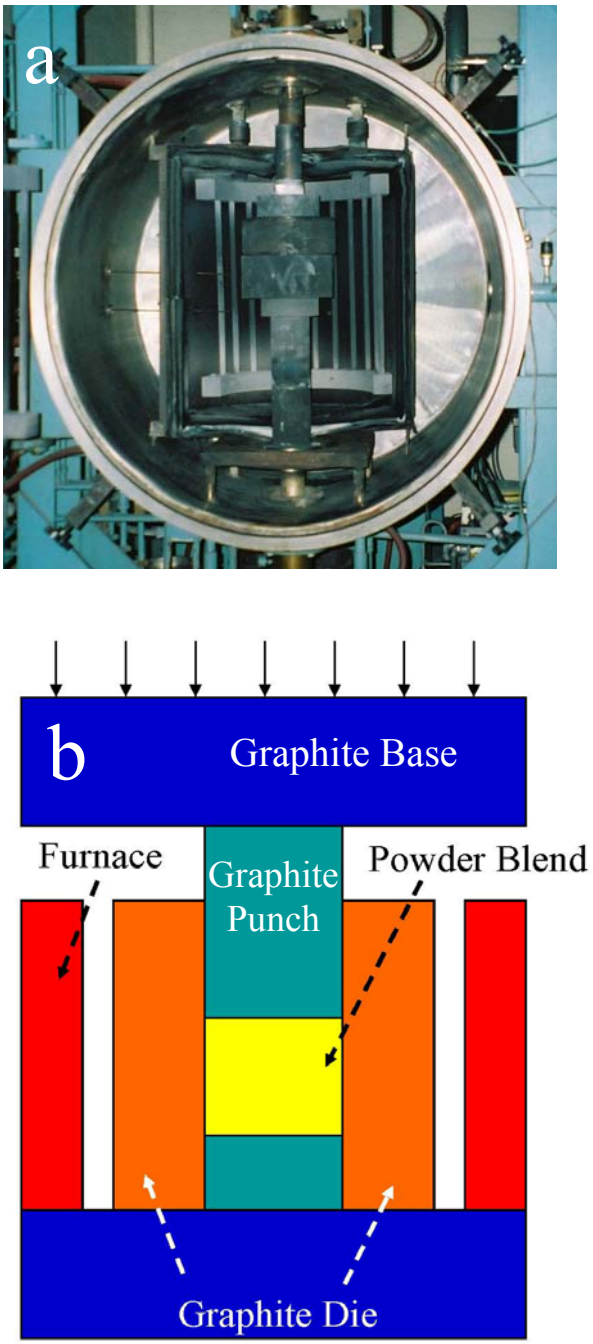

Figure 3-1: (a) Chamber of the graphite-heated vacuum-atmosphere HP, (b) schematic of the HPing system utilized to fabricate Mg-Ti_2AlC composites using the Mg and Ti_2AlC powders' blend.

Melt Infiltration: for the second set of samples, ≈ 50 vol.% porous preforms in the form of rectangular bars (1.2×1.2×70 cm^3) or cylinders (40 mm in diameter and 40 mm or 70 mm high) were fabricated by cold pressing the same Ti_2AlC powder together with ~ 1 wt. % polyvinyl alcohol as a binder at 45 MPa. Two microstructures were fabricated, random and oriented. The former were made by simply pouring, and cold pressing the Ti_2AlC-binder mixture into a steel die. To fabricate the latter, the Ti_2AlC-binder mixture was first poured into the die and manually vibrated for ~ 15 minutes in an attempt to orient the flaky Ti_2AlC powders perpendicular to the pressing direction [118]. The preforms' densities were calculated by dividing their weight by their volume because they were regularly shaped. For consistency, only those preforms that were 50±1% dense were used for the infiltration process (Figure 3.2).

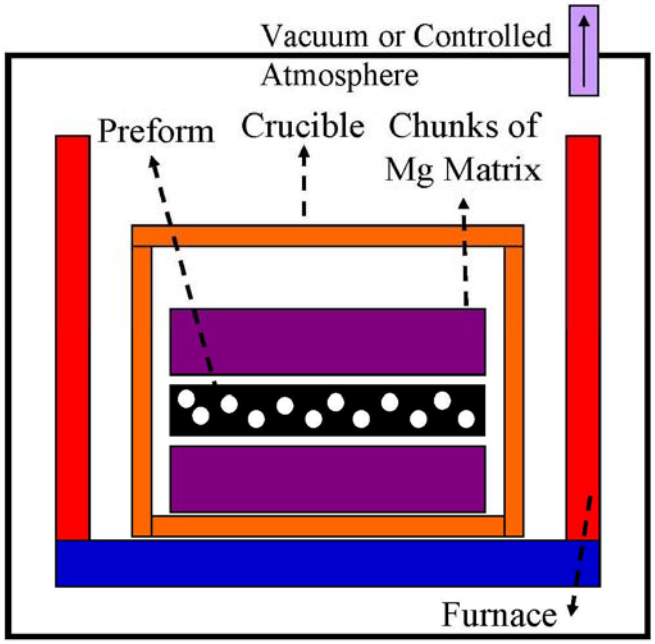

Figure 3-2: Schematic of the MI system utilized to fabricate Mg-Ti_2AlC composites.

The performs were then placed in a graphite-heated vacuum furnace and heated at 5°C/min to 900°C, held at the target temperature for 5 h, after which the furnace was turned off and the preforms were furnace cooled. More recent work showed that this heat treatment step is not necessary and can be eliminated.

To carry out the infiltration step, pure Mg chunks (99.8 % pure, Alfa Aesar, Ward Hill, MA) were used to surround the preforms that, in turn, were placed in alumina, Al_2O_3, crucibles (AdValue Technology, Tucson, AZ). The crucibles were covered with Al_2O_3 lids and placed in the same vacuum furnace used for sintering the preforms, heated at 10°C/min to 750°C, held at that temperature for 30 min, after which the furnace was turned off and the samples were furnace cooled. In all cases, the excess Mg surrounding the infiltrated preforms was machined off. These samples will henceforth be referred to as MI.

The composite samples were then annealed at 550º C for 6 h in flowing Ar in a tube furnace in order to investigate the thermal stability of the Mg matrices in the various composites.

Cylinders for compression tests *parallel* and *normal* to the cold-pressing direction were EDMed from the same oriented infiltrated preforms. Under compression, the basal planes in the former are *normal*, or edge-on, to the loading direction, which is why these samples will be referred to as "MI-N". When the basal planes are parallel to the loading direction, the samples will be referred to as "MI-P". This nomenclature is also valid for the Vickers hardness measurements because in the MI-N sample, the indenter is *normal* to the basal planes, etc. The randomly oriented samples will be referred to as MI-R. For

clarity's sake, in most of the stress-strain figures, a small schematic of the relationship of the basal planes to the applied load is shown as an inset.

Also for the sake of comparison, Mg-50 vol.% Ti_3SiC_2 and Mg-50 vol. % SiC composites were fabricated by HPing. In this case, the starting powders were Ti_3SiC_2 (- 325 mesh, 3-ONE-2, Voorhees, NJ), SiC (- 325 mesh, Alfa Aesar, Ward Hill, MA) and the same Mg powder used above. The processing details were identical to those of the Mg-Ti_2AlC (HP) composites described above. These samples will henceforth be referred to as "Mg-312" and "Mg-SiC", respectively.

Bulk Ti_2AlC and Ti_3SiC_2 samples were also made by hot isostatic pressing (HIPing). The starting powders were sealed in rubber bags under a mechanical vacuum and then cold isostatically pressed (CIPed) to ~ 250 MPa for ~ 5 min. The samples were then placed in crushed borosilicate glass and then in a hot isostatic press (HIP), heated to 750 ºC at a rate of 5 ºC/min, at which time the chamber was pressurized with Ar gas to ~ 100 MPa. The heating was then resumed at a rate of 10 ºC/min to 1400 ºC at which time the chamber was further pressurized to ~ 175 MPa and the samples were held for 2 h followed by furnace-cooling to room temperature.

The composite samples' microstructures were observed in a field emission scanning electron microscope, SEM, (Zeiss Supra 50VP, Germany) after cross-sectioning, mounting and polishing with a diamond solution down to 1 μm. The bulk Ti_3SiC_2 and Ti_2AlC samples were polished and etched for ~ 10 s with a 1:1:1 (volume) H_2O:HNO_3:HF etchant solution and their microstructures were then observed with an optical microscope, OM, (Olympus PMG-3, Tokyo, Japan). The oriented composite

samples were cross-sectioned parallel and normal to the plate-like-grains in order to image the morphology in both directions (MI-P and MI-N).

X-ray diffraction (XRD) was carried out on bulk composites, powders and preforms in a diffractometer (Model 500D, Siemens, Karlsruhe, Germany) and the spectra were collected using step scans of 0.01º in the range of 10º to 90º 2 theta (2θ) and a step time of 2 s. Scans were made with Cu Kα radiation (40 KV and 30 mA). The XRD results obtained from the preforms will be discussed in Ch. 4.

The Vickers microhardness values, V_H, – measured using a microhardness indenter (LECO-M400, LECO Corp. St. Joseph, MI) – were determined by averaging at least 10 measurements at 1, 2, 3, 5 and 10 N. The hardness measurements were carried out on the MI (MI-R, MI-P and MI-N) and HP composites, pure polycrystalline Mg, dense Ti_2AlC, Ti_3SiC_2, Mg-SiC and Mg-312 composites.

The room temperature UCSs were measured using a hydraulic testing machine (MTS 810, Minneapolis, MN) (Figure 3.3) on small 4×4×4 mm^3 EDMed cubes. Six samples were tested. Tensile bars were EDMed from the random and oriented infiltrated preforms according to ASTM E8-04. Three samples were tested. EDMed cylinders 9.7 mm in diameter and 31 mm high were used to measure the Young's moduli in compression and to carry out the cyclic uniaxial compression tests. In all cases, the strains were measured by a capacitance extensometer (MTS, Minneapolis, MN) – attached to the samples (Figure 3.3) – with a range of 1 % strain. All the loading-unloading compression tests were performed in load-control mode at a loading-unloading rate of 15 MPa/s, respectively, which corresponds to a strain rate of ~ 2×10^{-4} s^{-1}.

The offset yield strength (Y_s) of the composites – being the stress required to produce a plastic deformation strain of 0.2 %, was determined by the stress corresponding to the intersection of the stress-strain curves offset by 0.2 %. These measurements were carried out at room temperature on small 4×4×4 mm^3 EDMed cubes, in displacement-control mode at a displacement rate of 0.005 mm/s. These results are fully discussed in Ch. 4.

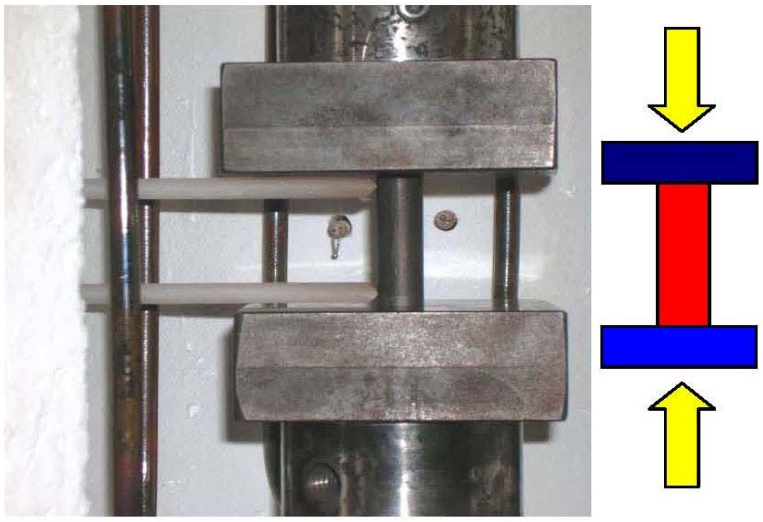

Figure 3-3: Front view of the hydraulic testing machine used for cyclic compression tests; also shown are the sapphire extension rods attached to the surface of the sample to measure its strain during loading.

TEM foils were prepared by a conventional TEM sample preparation process: 0.5 mm-thick slices were first cut from bulk samples using a low-speed diamond saw and further thinned with a disc-grinder to a thickness of about 20 μm. Final perforation was made by an ion mill operating at 5 kV. TEM characterization was performed using a field emission TEM (JEOL JEM-2010F) operating at 200kV. Images were collected with a multi-scan CCD digital camera. EDS analysis was carried out with an attached EDAX ultra-thin window X-ray energy dispersive spectrometer.

3.3. Results and Discussion

3.3.1. Density Measurements

The highest density of 2.87±0.03 Mg/m^3 (~ 98.5 % of theoretical) in the HP composites was only obtained when the Mg content was 50 vol. % (HP50). At 40 vol. % Mg the density was ~ 85 % of theoretical (HP40). Lower Mg contents resulted in more porous samples that were not studied further (Figure 3.4). The theoretical density was calculated assuming the densities of Mg and Ti_2AlC to be 1.74 Mg/m^3 and 4.11 Mg/m^3 respectively [8]. At 2.87±0.05 Mg/m^3, the densities of the Mg-50 vol.% Ti_2AlC MI samples were also ~ 98.5 % of theoretical.

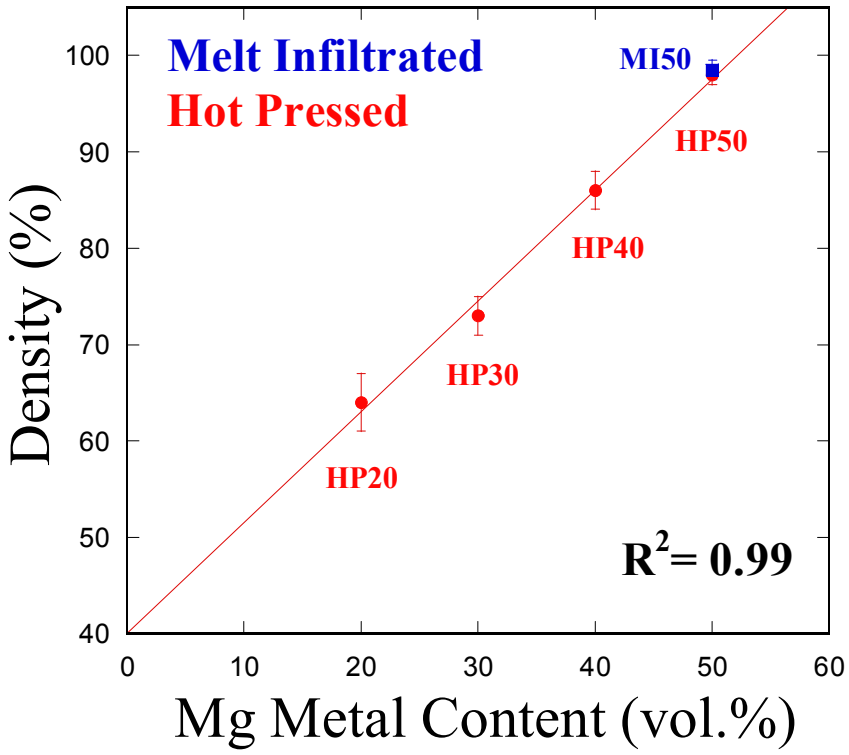

Figure 3-4: Evolution of density versus Mg metal content in HPed and melt-infiltrated composites.

3.3.2. Microstructural Results

The microstructure of the HP50 and MI50 samples was quite homogeneous (Figure 3.5 a and b). As expected, the microstructure of the MI50-oriented sample, however, was different in the two different directions (Figure 3.5 c and d) being MI-P and MI-N, respectively. It is readily observed that manual vibration of the powder prior to cold pressing oriented most of the plate-like-grains with their basal planes exposed to the surface in MI-P sample (Figure 3.5 c). In contradistinction, most of these grains' basal planes are perpendicular to the surface in MI-N sample (Figure 3.5 d). The width and the thickness of the average Ti_2AlC grains were, respectively, 30±10 and 5±3μm (see Chs. 4 and 5).

Figures 3.6 a and b show the fractured surfaces of HP50 and MI50 composites, respectively. Very few facetted Mg single crystals were formed throughout the entire microstructure of both MI50 and HP50 composites. Interestingly enough, similar, but much larger, facetted single crystals were formed on the surface of the Al_2O_3 lids during MI (Figures 3.6 c and d) used to keep the Mg from evaporating. It follows that they were formed by an evaporation/condensation process. Further work, as described in Ch. 7, shows that the morphology of the Mg crystals formed on various substrates is significantly different and is a strong function of the type of substrate used. It is hereby acknowledged that more work is needed to understand the mechanisms by which these crystals form.

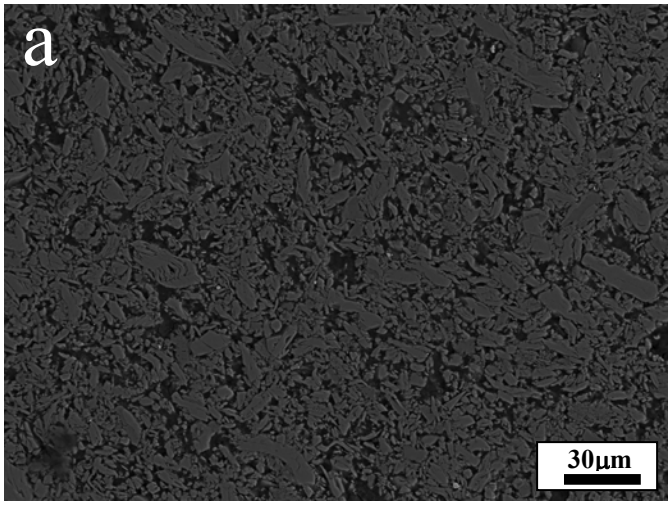
a
30µm

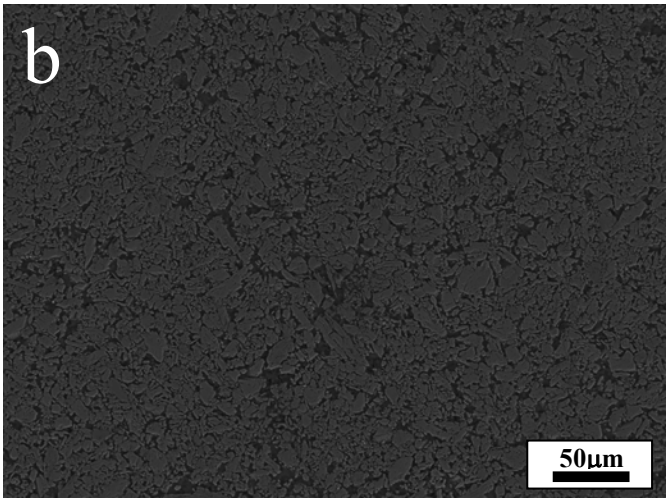
b
50µm

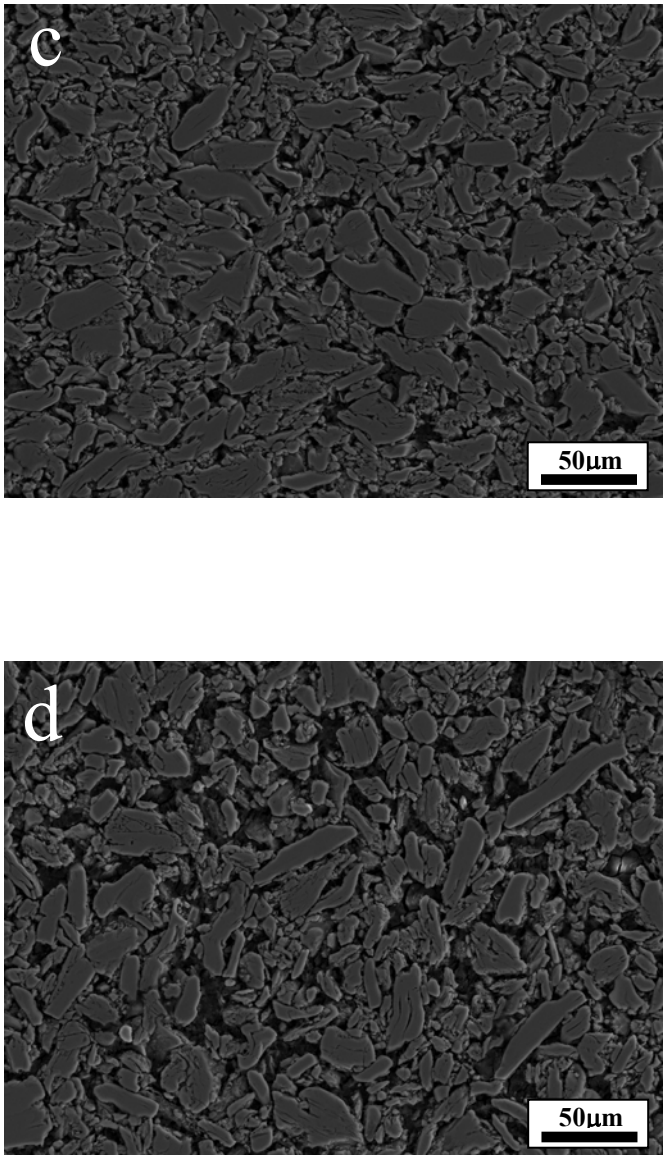

Figure 3-5: Secondary electron SEM image of polished surface of, a) HP50 and, b) MI-R, c) MI-P and, d) MI-N composites.

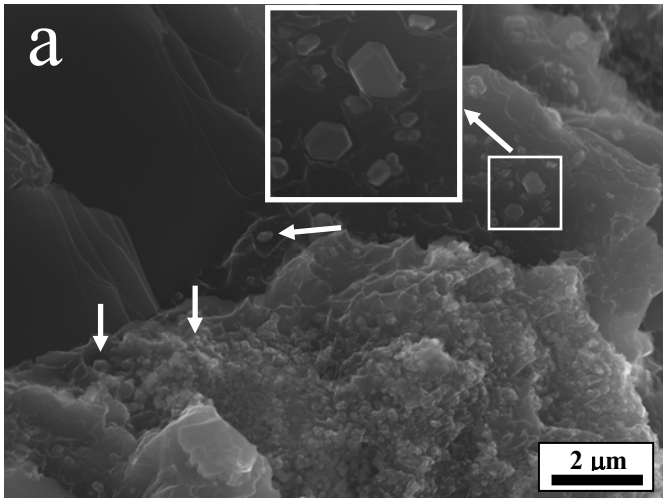
a
2 µm

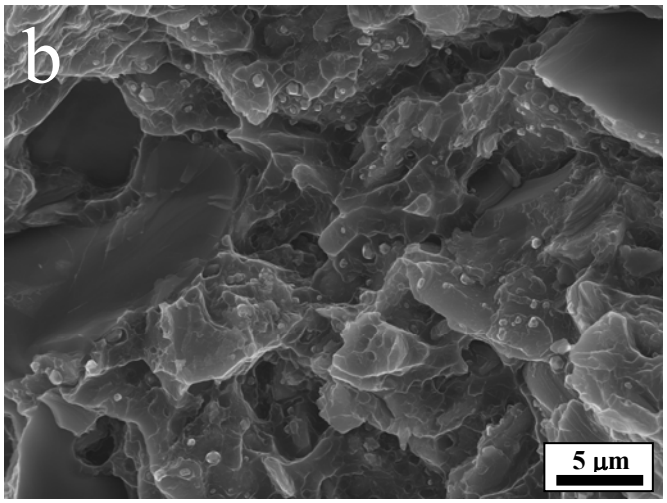
b
5 µm

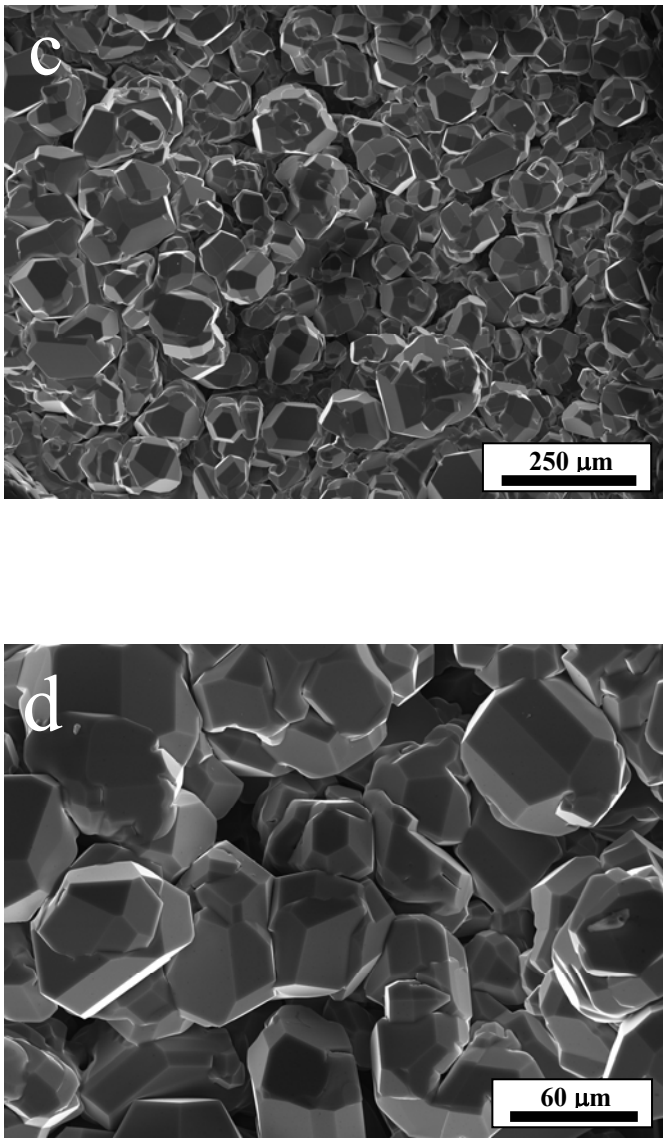

Figure 3-6: SEM image of fractured surface of, a) HP50; inset shows the facetted Mg single crystals at higher magnifications, and b) MI50 composites; c) and d) Facetted Mg single crystals formed during MI on the surface of the alumina lids.

Figure 3.7 show several TEM images of a HP50 composite sample, where the Mg matrix appeared to have completely wet the Ti_2AlC. In some areas some porosity was observed. Presence of areas where the Mg matrix appears to have formed as particles, most likely similar to those single crystals that were shown on the fractured surfaces in Figure 3.6, is also evident.

Figures 3.7 c to f show TEM images taken at higher magnifications from regions similar to those shown in Figure 3.5. They all show areas where Mg matrix appears to have wet the Ti_2AlC matrix and areas where Mg single crystals were formed in the open spaces and porosities of the microstructure. Note that these finite porosities were only observed in TEM images. It is thus reasonable to assume that the single crystals observed on the fractured surfaces are similar to those observed in the TEM images.

Figures 3.8 a to d show TEM images of the MI50 composite. Similar to the HP50 composite, the molten matrix wet and fully infiltrated the preform. There is, however, less porosity in this microstructure and thus limited regions filled with Mg single crystals. Again, this is in good agreement with the fractured surface meaning that the Mg single crystals observed on the fractured surfaces are similar to those in the TEM images shown in Figure 3.7.

Figure 3.9 a shows the formation of kink bands (the governing phenomenon in the deformation of KNE solids) in a single grain of Ti_2AlC on the polished surface of a HP50 composite. Figures 3.9 b and c depict the formation of kink bands with very sharp radii of curvature on a fractured surface of a MI50 composite. Based on these micrographs, and

the evidence shown below and in Ch. 4, it is reasonable to assume that these kink bands were preceded by IKBs.

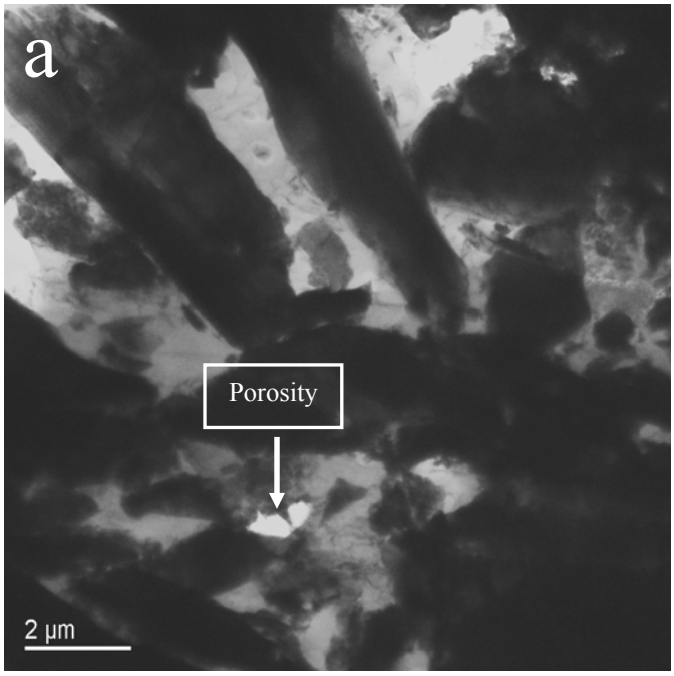

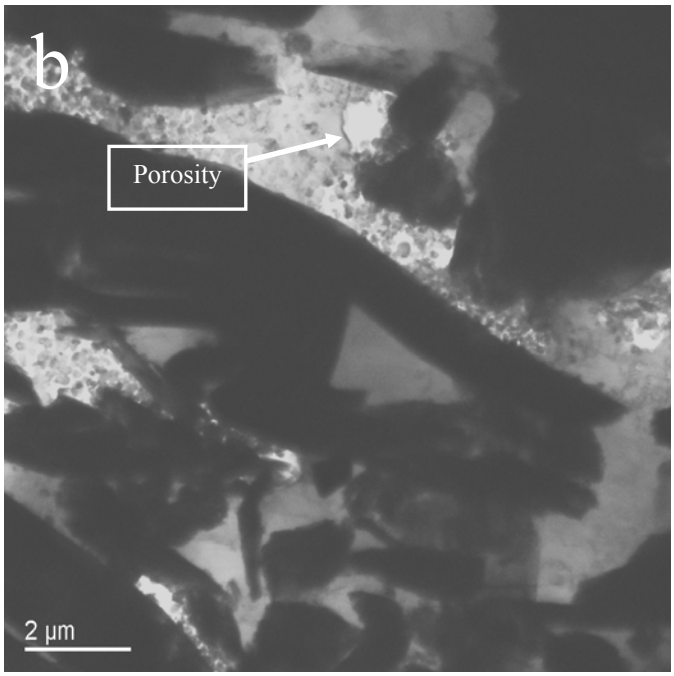

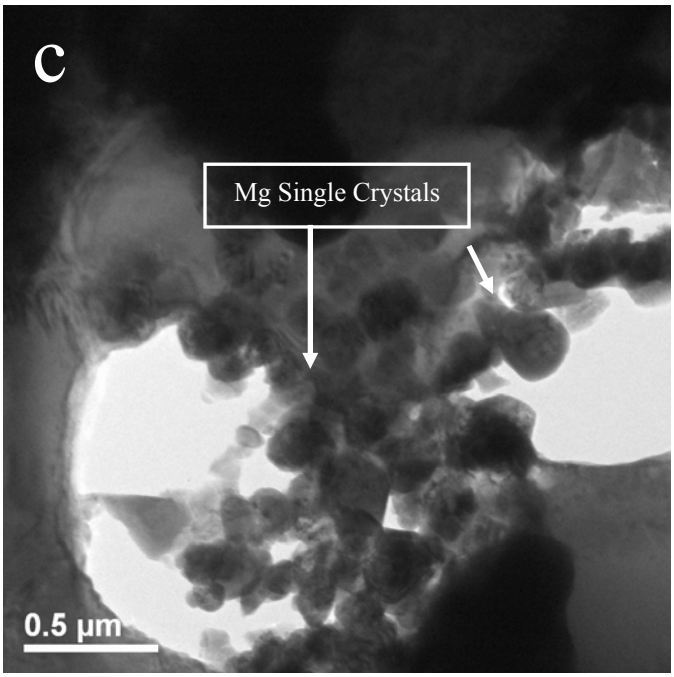
c
Mg Single Crystals
0.5 µm

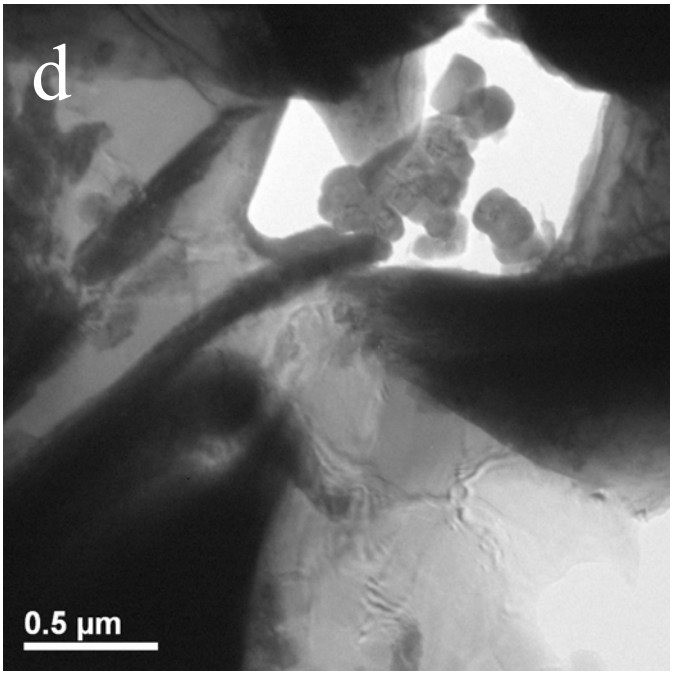
d
0.5 µm

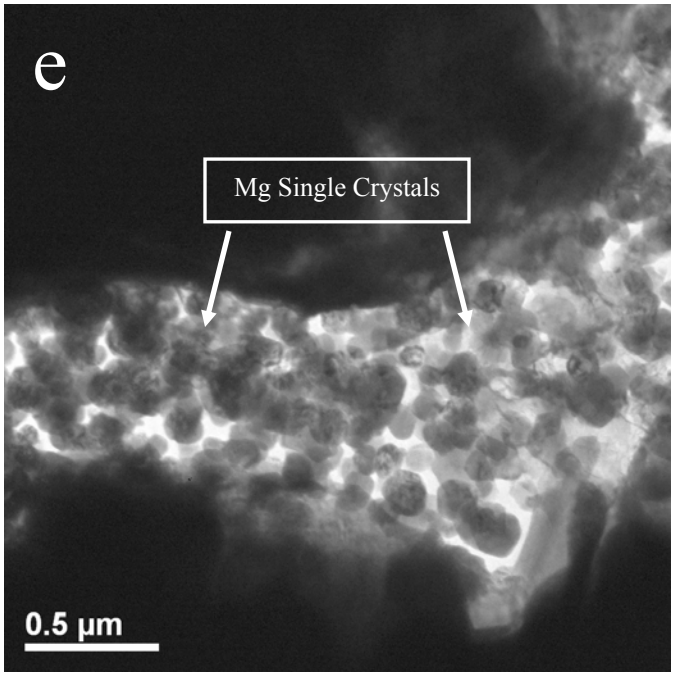

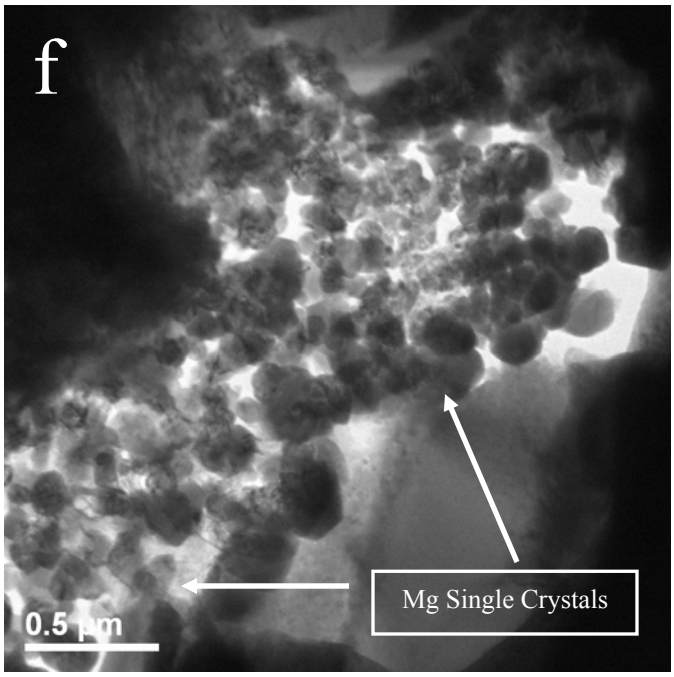

Figure 3-7: TEM images of HP50 composite showing the presence of areas where Mg matrix appears to have wet the Ti_2AlC matrix, very small amounts of porosity and areas where Mg single crystals were formed in the open spaces and porosities of the microstructure.

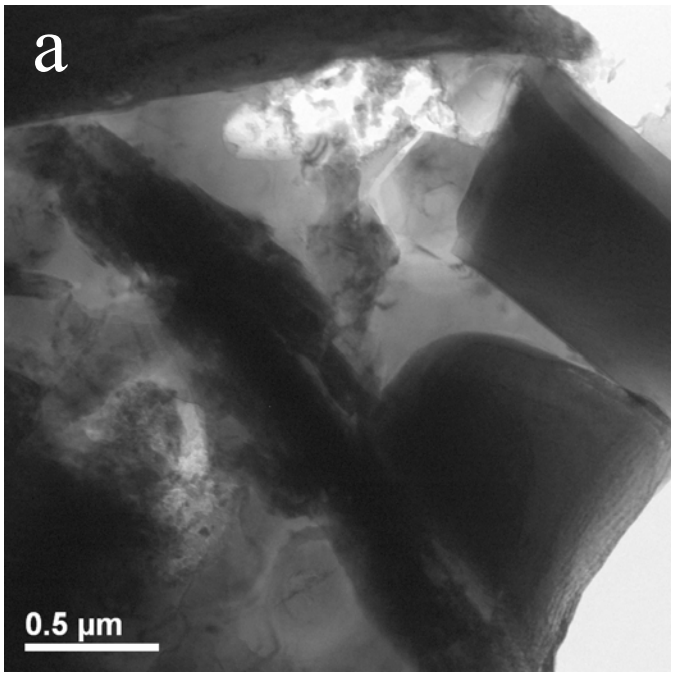
a
0.5 µm

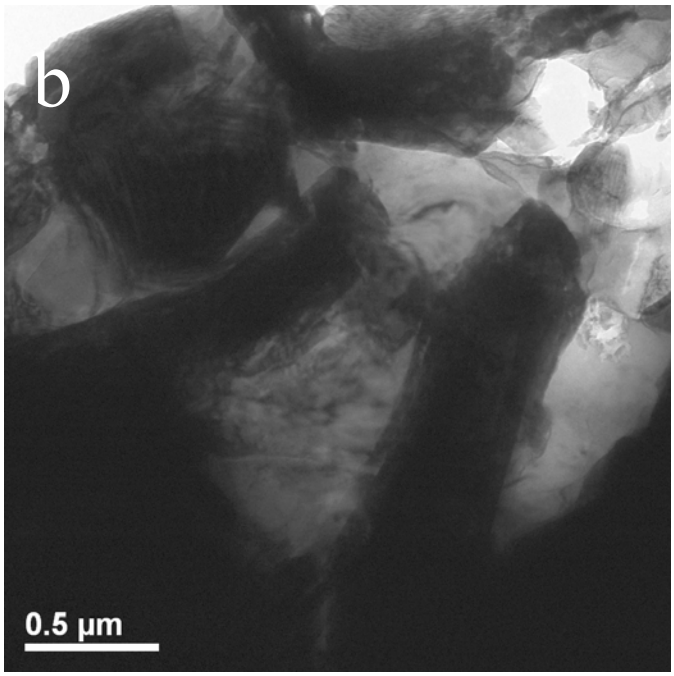
b
0.5 µm

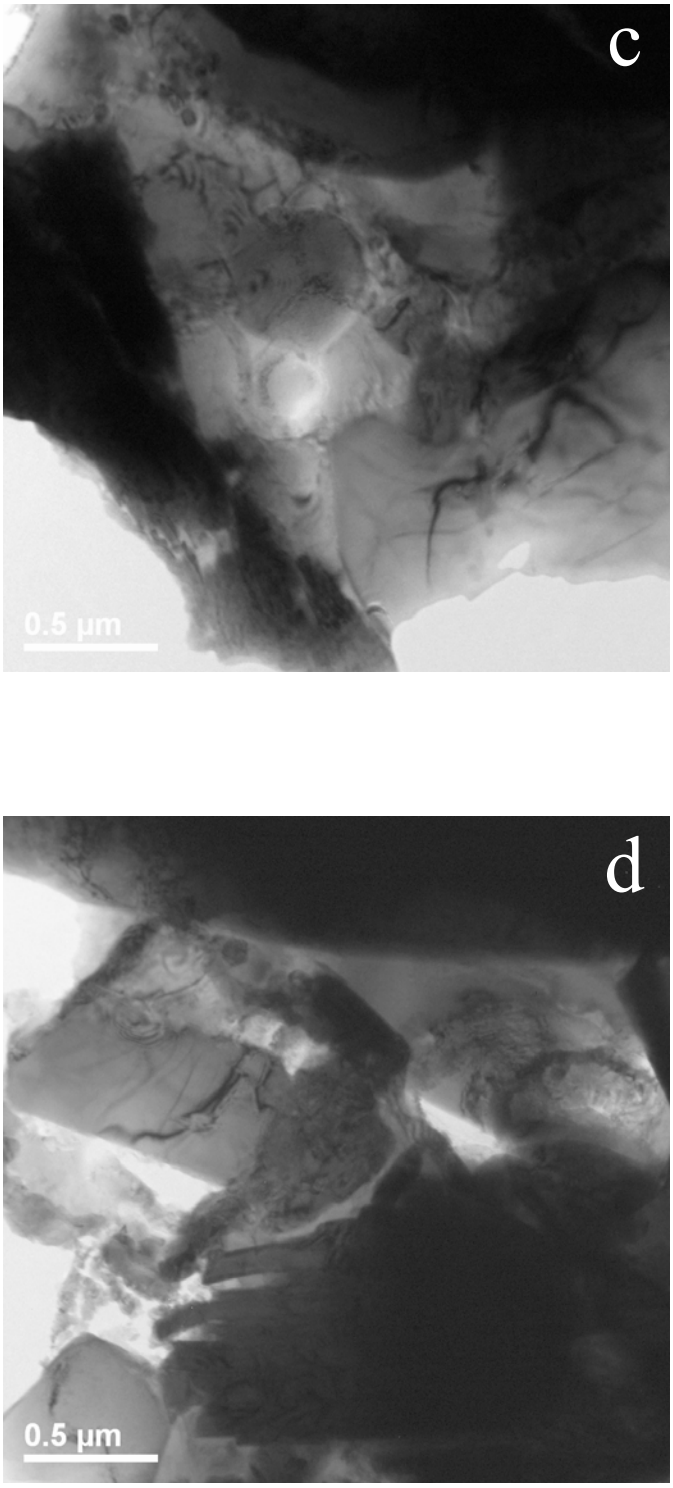

Figure 3-8: TEM images of MI50 composite wherein the molten matrix has wet and fully infiltrated the preform. Compared to Fig. 3.7 (HP50 composite) less porosity and limited regions filled with Mg single crystals are observed.

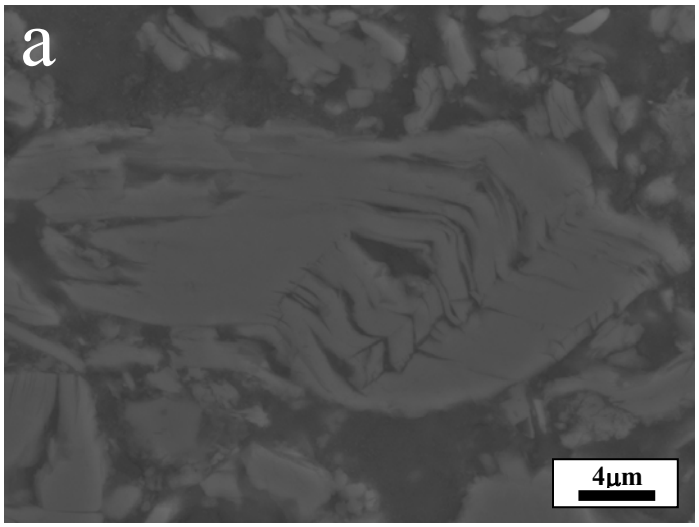
a
4μm

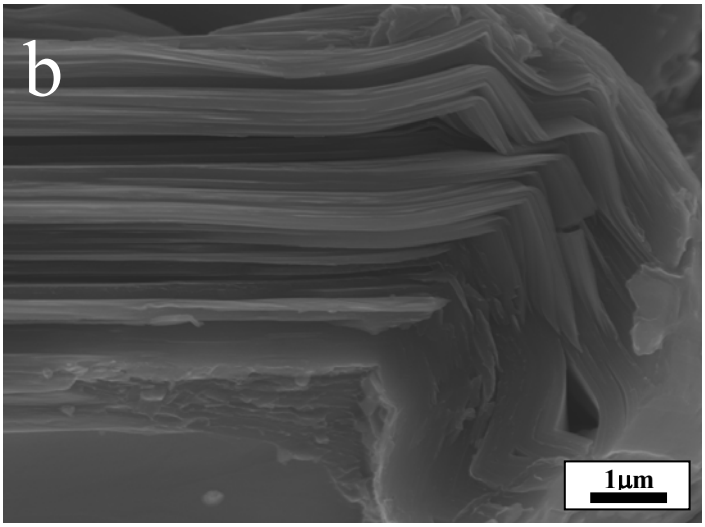
b
1μm

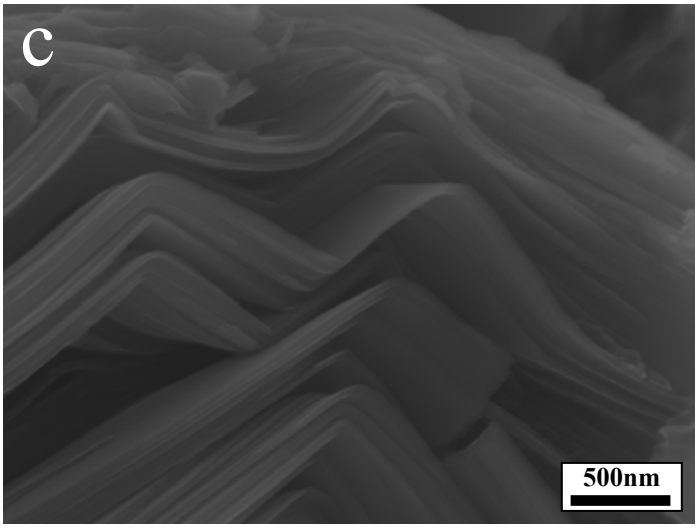

Figure 3-9: Formation of kink bands with very sharp radii of curvature in, a) a single grain of Ti_2AlC on the polished surface of the HP50 composite sample and, b and, c) fractured surfaces of MI50 composite sample.

3.3.3. X-ray Diffraction Results

Typical XRD patterns of the HP50 and MI50 composites (Figure 3.10 a) contained peaks for Ti_2AlC, Mg, TiC (~ 5 vol. % impurity in the starting Ti_2AlC powder), MgO and Si (the latter added as an internal standard). Figure 3.10 b also shows the XRD pattern of HP50 and MI50 samples before and after annealing, for the sake of comparison, containing peaks for Ti_2AlC, Mg, TiC (~ 5 vol. % impurity in the starting Ti_2AlC powder) and MgO.

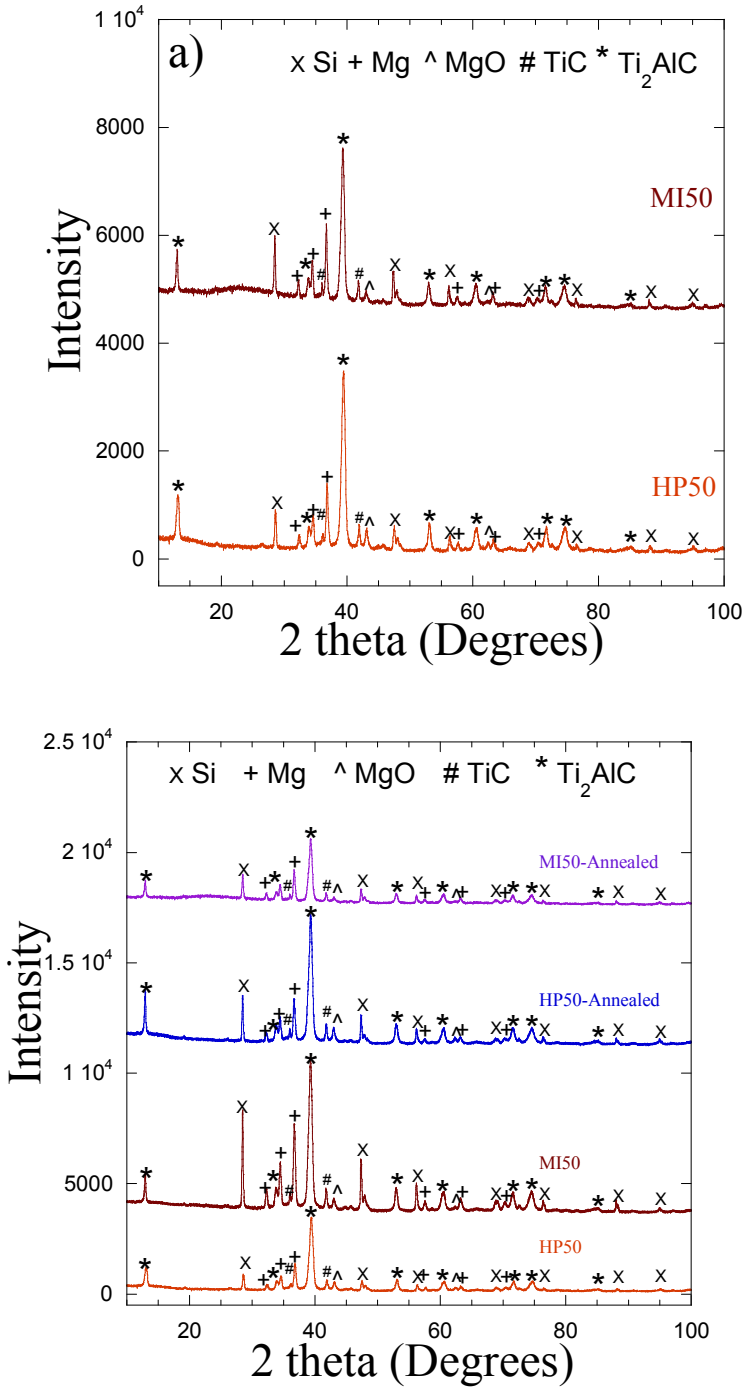

Figure 3-10: a) X-ray diffraction pattern of Mg-50 vol.% Ti_2AlC composite fabricated by HPing and MI; b) X-ray diffraction pattern of Mg-50 vol.% Ti_2AlC composite fabricated by HPing and MI before and after annealing (carried out at 550º C for 6 h in flowing Ar of a tube furnace), containing peaks for Ti_2AlC, Mg, TiC (~ 5 vol. % impurity in the starting Ti_2AlC powder) and MgO. In all cases Si was added as an internal standard.

The ratio of XRD peak intensities of the (002) basal planes to (103) planes in Ti_2AlC and the (002) basal planes to (104) planes in Ti_3SiC_2, respectively, were obtained from the XRD spectra of their corresponding starting powders, XRD cards [119, 120] and, oriented preforms. The data is summarized in Table 3.2. A perusal of this table makes it clear that the ratios of the 002/10l intensities in the oriented Ti_2AlC and Ti_3SiC_2 preforms are several multiples of what they are in the as-received powder or according to the XRD cards [119, 120]. We note in passing that one reason for the ease by which these powders can be aligned is their flake-like nature (Figure 3.11a) [118]. Also note the equiaxed morphology of the Ti_3SiC_2 grains (Figure 3.11b). We will explain in Ch. 4 how the difference in grain morphology of Ti_2AlC and Ti_3SiC_2 grains, best manifested by comparing the OM micrographs of Figure 3.11, will render the latter relatively less amenable to kinking as compared to the plate-like grains of the former.

Table 3-2: The ratio of XRD peak intensities of (002) basal planes to (103) planes in Ti_2AlC and (002) basal planes to (104) planes in Ti_3SiC_2, respectively, obtained from their corresponding starting powders, XRD cards and those of the oriented preforms; in the latter case, XRD was performed on the surface of the preforms, wherein the majority of the basal planes were normal to the cold-pressing direction during preform preparation. Note that this direction, as described herein for the composites materials, is analogous to the MI-P composite sample.

↓*Intensities–Material*→	Ti_2AlC powder	Ti_2AlC (XRD card [119])	Oriented Ti_2AlC preform
I (002) / I (103)	0.5	0.4	1.3
↓*Intensities–Material*→	Ti_3SiC_2 powder	Ti_3SiC_2 (XRD card [120])	Oriented Ti_3SiC_2 preform
I (002) / I (104)	0.4	0.2	1.7

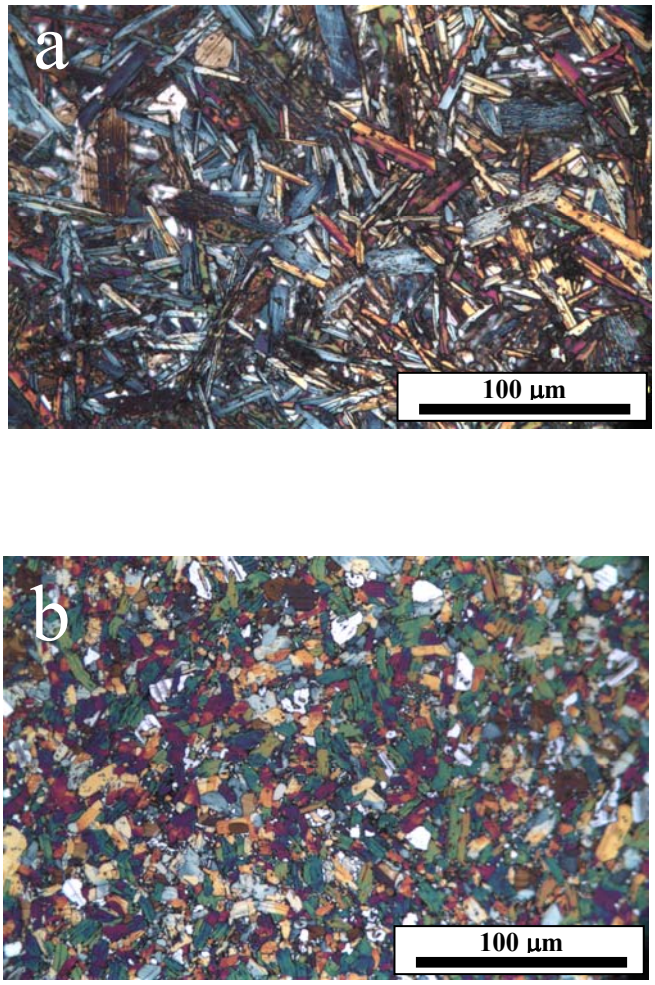

Figure 3-11: Optical micrographs of fully dense, polished and etched, a) Ti_2AlC, and b) Ti_3SiC_2. Both samples were fabricated by cold isostatically pressing (CIPing) to ~ 250 MPa for ~ 5 min followed by hot isostatic pressing (HIPing) at 1400 ºC and ~ 175 MPa for 2 h followed by furnace-cooling to room temperature.

When the full-widths at half maximum, FWHM, of the Mg peaks in the HP50 and MI50 composites are compared with those of the pure Mg powder ($d_{av} \approx 150$ µm), Mg single crystals or Si (Figure 3.12) it is apparent that the former are significantly broader. Using the Scherrer formula [121] the Mg particle size was estimated to be ~35±15*nm* in both HP50 and MI50 composites.

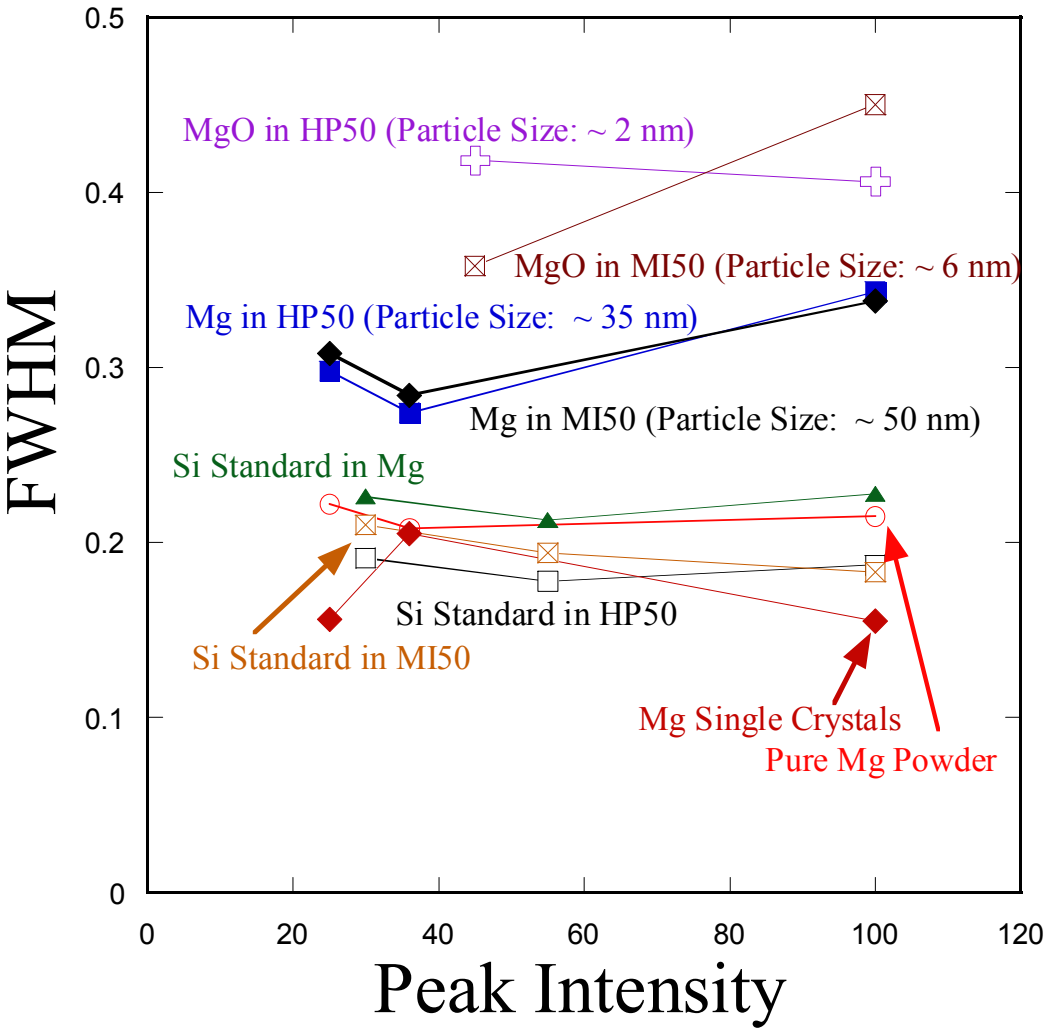

Figure 3-12: FWHM of Mg and MgO vs. peak intensity; three of the high intensity peaks were used in each case and compared with those of Si standard, pure Mg powder and Mg single crystal peaks.

More TEM images from the Mg matrix of the MI50 (Figure 3.13 a and b) and HP50 (Figure 3.13 c and d) composites were taken at higher magnifications in order to confirm the presence of nano-crystalline Mg matrix. From these micrographs it is evident that the molten Mg matrix solidified in the form of nano-crystals (≈20 nm in MI50 and ≈10 nm in HP50).

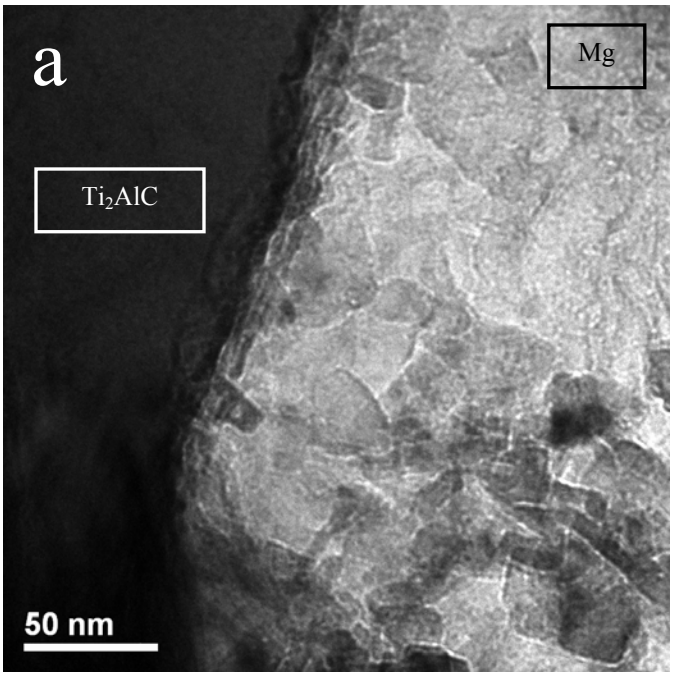
a
Mg
Ti2AlC
50 nm

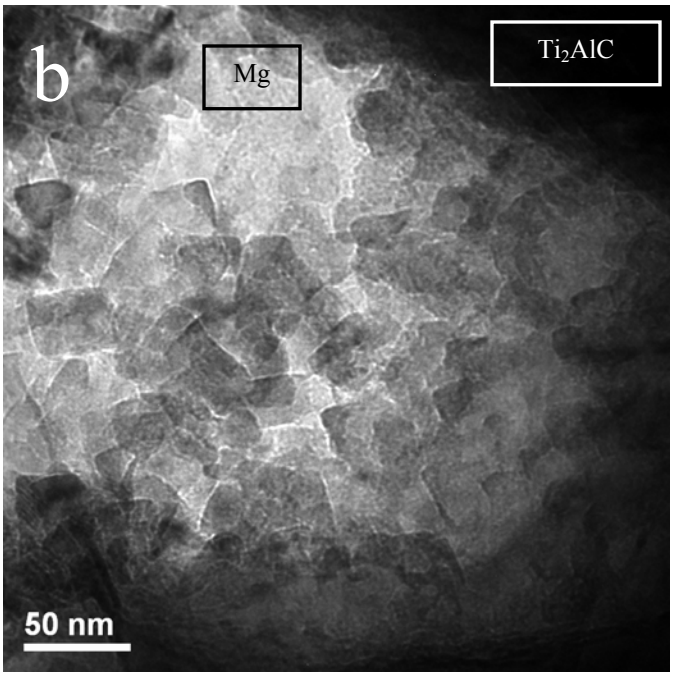
b
Mg
Ti2AlC
50 nm

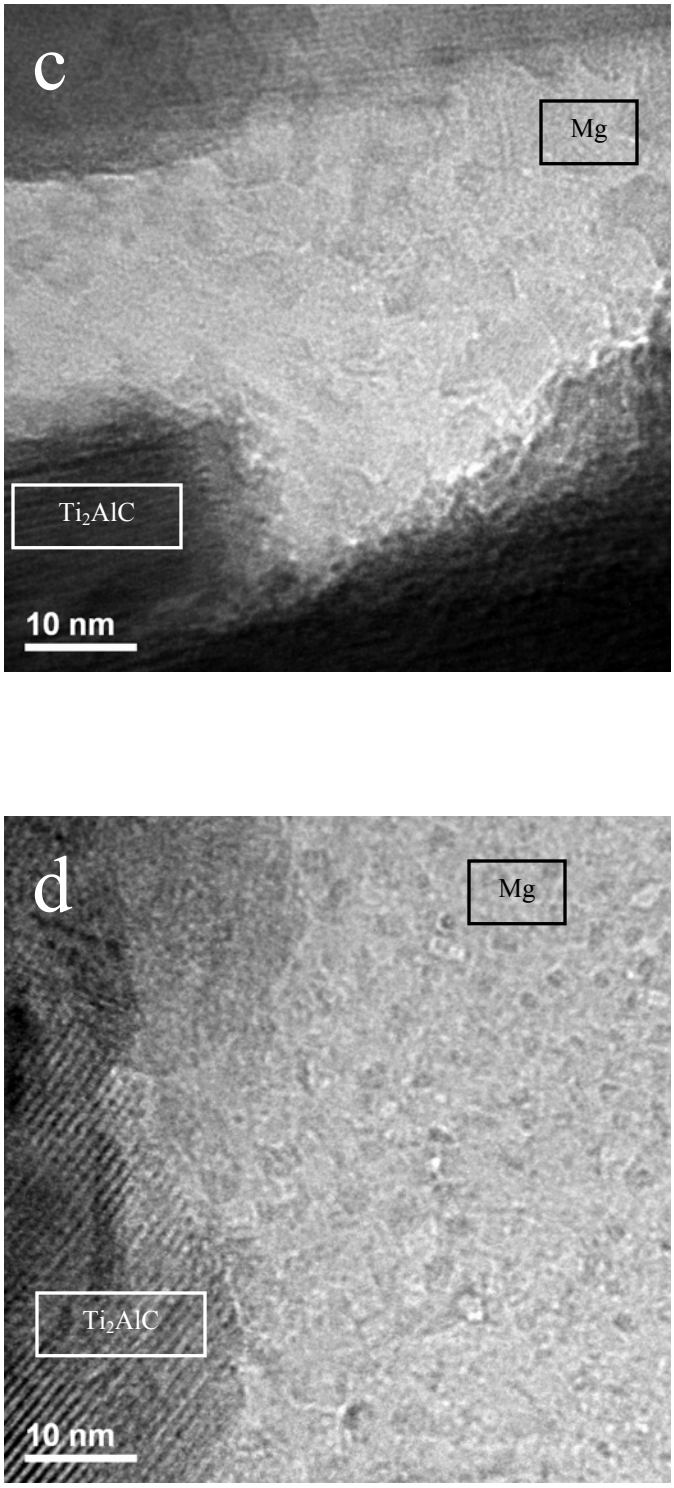

Figure 3-13: TEM images of, (a) and (b), the MI50 composite and, (c) and (d), the HP50 composite showing the presence and morphology of the nc-Mg matrices within the composites.

Survival of these Mg nanocrystals after 1 h at 750°C in the HP vacuum implies the presence of a potent grain-growth inhibitor. The presence of MgO peaks in the XRD spectra strongly suggests that MgO plays that role. Based on the FWHM of the MgO peaks its grain size is estimated to be of the order of ~ 3±1 *nm* in both the HP50 and MI50 composites.

These microstructures were also *remarkably stable*: annealing at 550 °C for 6 h did *not* result in grain growth as evidenced by the FWHM of the Mg-peaks after annealing (Figure 3.14). This remarkable result – most probably associated with the presence of MgO at the grain boundaries as a potent grain-growth inhibitor – bodes well for possible applications of this composite at elevated temperatures.

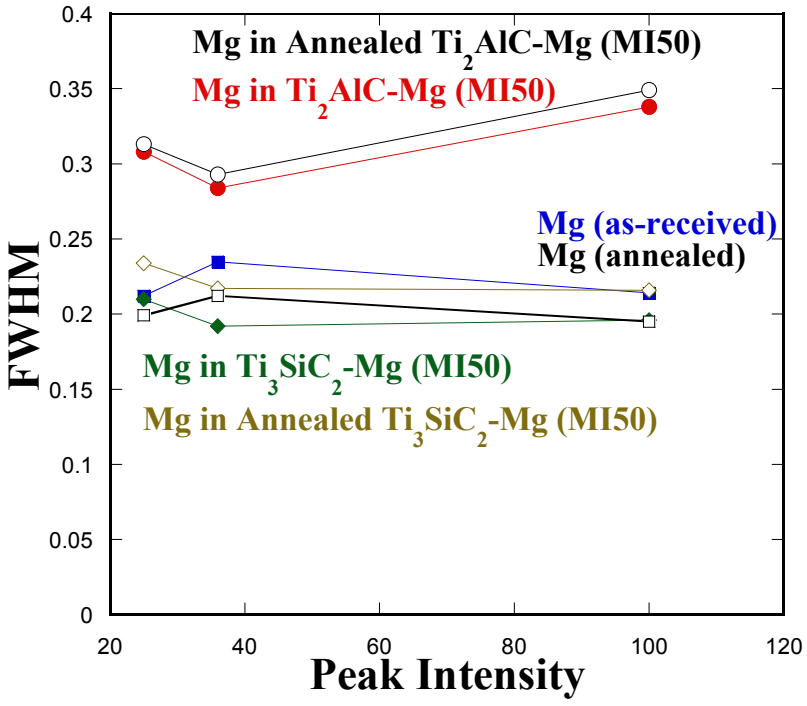

Figure 3-14: FWHM of Mg peaks in Mg-Ti_2AlC (MI50) composite before and after annealing; included in the same figure, for the sake of comparison, is the FWHM of the Mg ingot and the Mg in Mg-Ti_3SiC_2 (Mg-312) composite before and after annealing; the three highest intensity peaks were used in each case.

Energy dispersive X-Ray Spectroscopy (EDS) in the TEM of the Mg matrix in several regions similar to those shown in Figure 3.13 confirmed the presence of Mg, Ti and O. EDS microanalysis of the Mg matrix in the SEM revealed the presence of ~ 3±1 at. % Ti. It is likely that Ti diffuses out of the Ti_2AlC grains into the Mg matrix and Mg diffuses in.

It is important to note, however, that according to the Mg-Ti binary phase diagram [122] the solubility of Ti in Mg at 750°C is almost nil. The absence of pure Ti regions in the TEM, however, suggests that the Ti is supersaturated in the Mg matrix. Further work (see Ch. 6 for details) suggests that Ti may be also present in the form of rutile and/or anatase.

Interestingly and consistent with what is known about how strongly bound the C is in the MAX phases [123] the C does not appear to diffuse out of the Ti_2AlC grains. This conclusion is also in agreement with the fact that the MAX phases do not melt congruently, but dissociate into $M_{n+1}X_n$ and an A-rich liquid [16, 19]. It is also consistent with how Ti_3SiC_2 reacts with other reactive liquids. For example, when Ti_3SiC_2 is immersed in molten Al or crolyite, the Si diffuses out leaving behind a TiC-rich phase [124, 125]. In other words, in neither case does the C-diffuse out.

EDS microanalysis of the Ti_2AlC grains in the TEM and SEM revealed the presence of Mg within them (Figure 3.15a). The sum of Mg and Ti concentrations at various distances from the grain edges was ~ 50 at. %; it follows that the solubility of Mg in Ti_2AlC is non-negligible. In other words, the solid solution $(Ti_{1-x}Mg_x)_2AlC$, in which x is at least as high as 0.2, might exist.

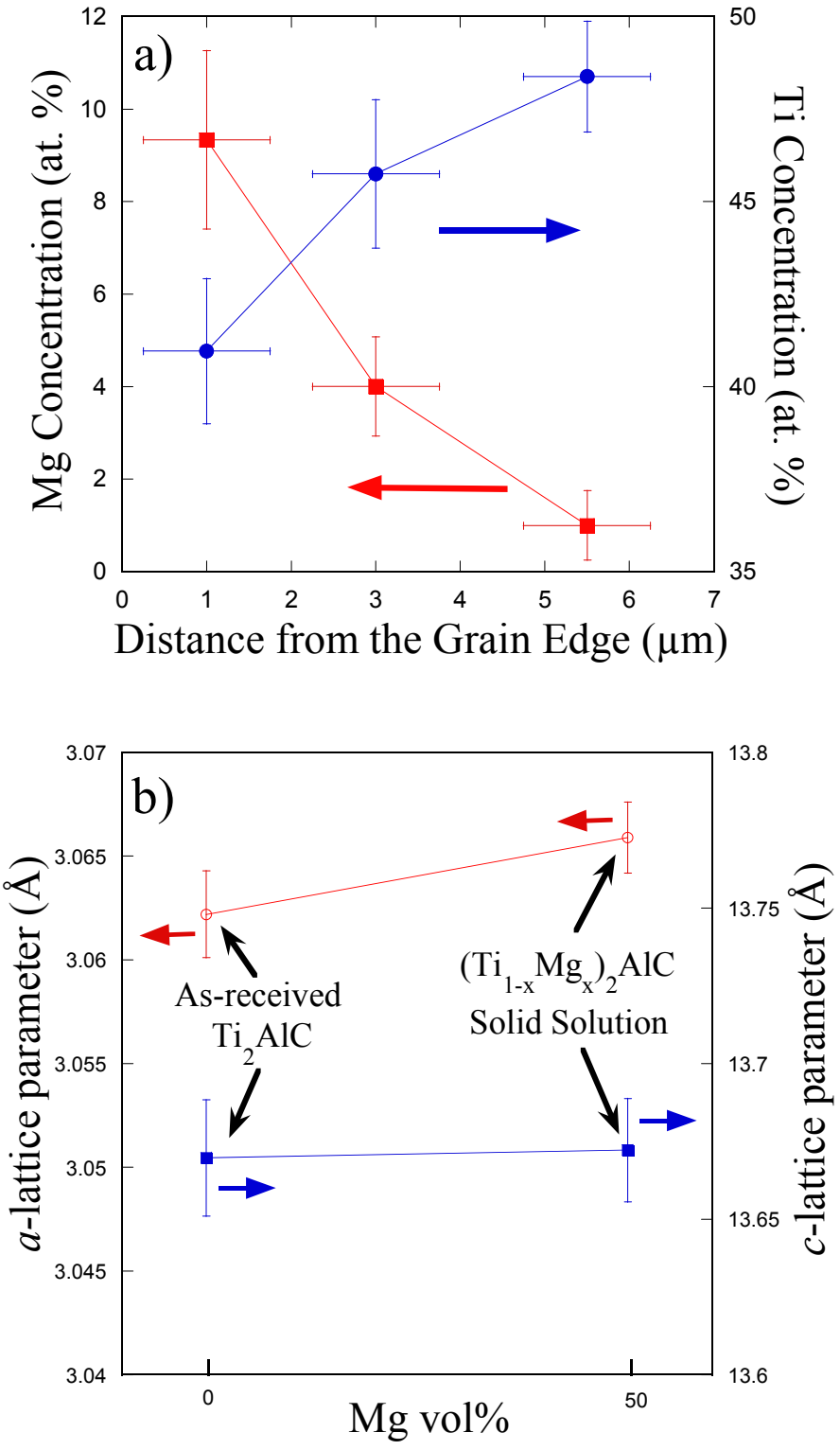

Figure 3-15: a) Concentration in *at.%* of Mg and Ti within the Ti_2AlC grains verifying the formation of a $(Ti_{1-x}Mg_x)_2AlC$ solid solution, with an x as high as 0.2; b) Variation of *a* and *c* lattice parameters in as-received Ti_2AlC and that within the MI composite.

Due to the fairly low Mg-content, its effect on the *c*-lattice parameter of Ti_2AlC grains is small and, within experimental scatter, identical to the as-received powders (Figure 3.15b). The increase in *a*-lattice parameter, on the other hand can be attributed with the larger radius of Mg in comparison with Ti. More work is needed here to confirm some of these conclusions. Note the values reported herein are, most probably, *not* equilibrium values. The diffusion coefficient of Mg in Ti_2AlC at 750 °C is estimated (x^2/Dt, where x is the distance from Mg/Ti_2AlC interface and t is the diffusion time) to be $\approx 3\times10^{-16}$ m^2/s.

In order to further investigate the variation of lattice parameters in several MAX phases when in contact with molten Mg, and to study the stability of MAX phases in the presence of Mg melt, we attempted to fabricate Mg-Ti_2AlC, Mg-Nb_2AlC and Mg-Ti_3SiC_2 composites by MI, similar to the manner explained in the experimental section above. In order to obtain equilibrium values, we fabricated the composites for two different soaking times: for the first set of samples, we soaked the porous MAX phase preforms for 1 h in the Mg melt at 750 ºC, followed by furnace cooling. The second set of samples were fabricated by soaking the preforms for 4 h at 750 ºC, also followed by furnace cooling. For each of the samples, the *a* and *c* lattice parameters of the MAX phase were calculated and plotted as a function of soaking time.

Figure 3.16a shows the *a* and *c* lattice parameters of Ti_2AlC. Within the experimental scatter, the *a* lattice parameter – as mentioned earlier – seem to be increasing with soaking time up to 1 hr and then apparently reaches an equilibrium value at 4 hrs. The *c* lattice parameter seems to remain unchanged and equal to its value in the starting powders.

On the other hand, Figure 3.16b and c show the *a* and *c* lattice parameters of Ti_3SiC_2 and Nb_2AlC, respectively. Apparently, within the experimental scatter, both *a* and *c* lattice parameters of Ti_3SiC_2 and Nb_2AlC, within their composites, seem to be constant as the soaking time increases.

These results show the stability of Ti_3SiC_2 and Nb_2AlC MAX phases when in contact with Mg melt, which is probably why the Mg matrix did not appear to be in nanoscale in Mg-Ti_3SiC_2 and Mg-Nb_2AlC composites. Figure 3.17 shows the TEM images obtained from the Mg-Ti_3SiC_2 composites, showing the absence of a nanocrystalline Mg matrix, corroborating the results shown in Figure 3.16.

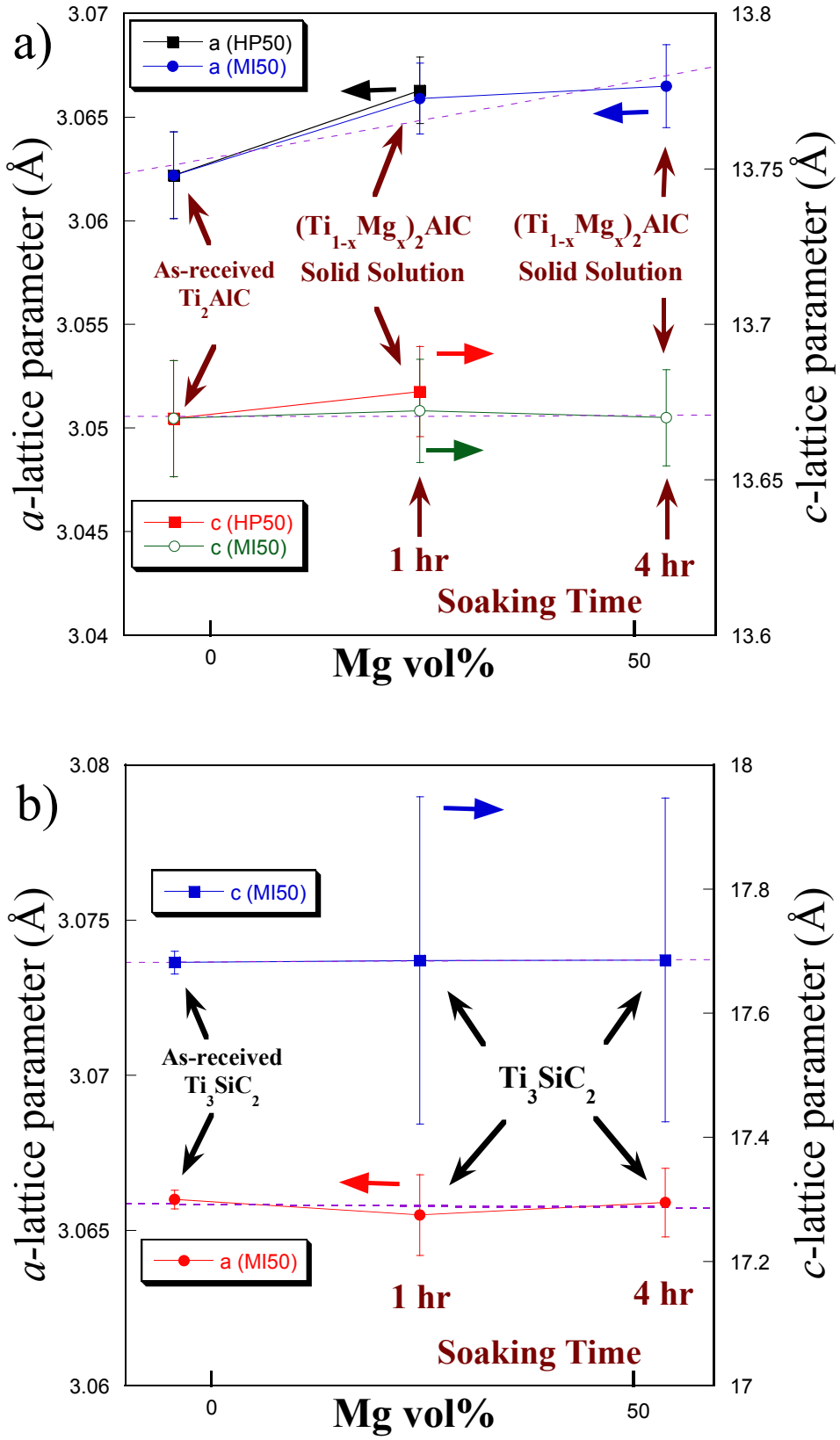
a)
a (HP50)
a (MI50)
c (HP50)
c (MI50)
As-received Ti2AlC
(Ti1-xMgx)2AlC Solid Solution
(Ti1-xMgx)2AlC Solid Solution
1 hr
4 hr
Soaking Time
a-lattice parameter (Å)
c-lattice parameter (Å)
Mg vol%
3.07
3.065
3.06
3.055
3.05
3.045
3.04
13.8
13.75
13.7
13.65
13.6
0
50
b)
c (MI50)
a (MI50)
As-received Ti3SiC2
Ti3SiC2
1 hr
4 hr
Soaking Time
a-lattice parameter (Å)
c-lattice parameter (Å)
Mg vol%
3.08
3.075
3.07
3.065
3.06
18
17.8
17.6
17.4
17.2
17
0
50

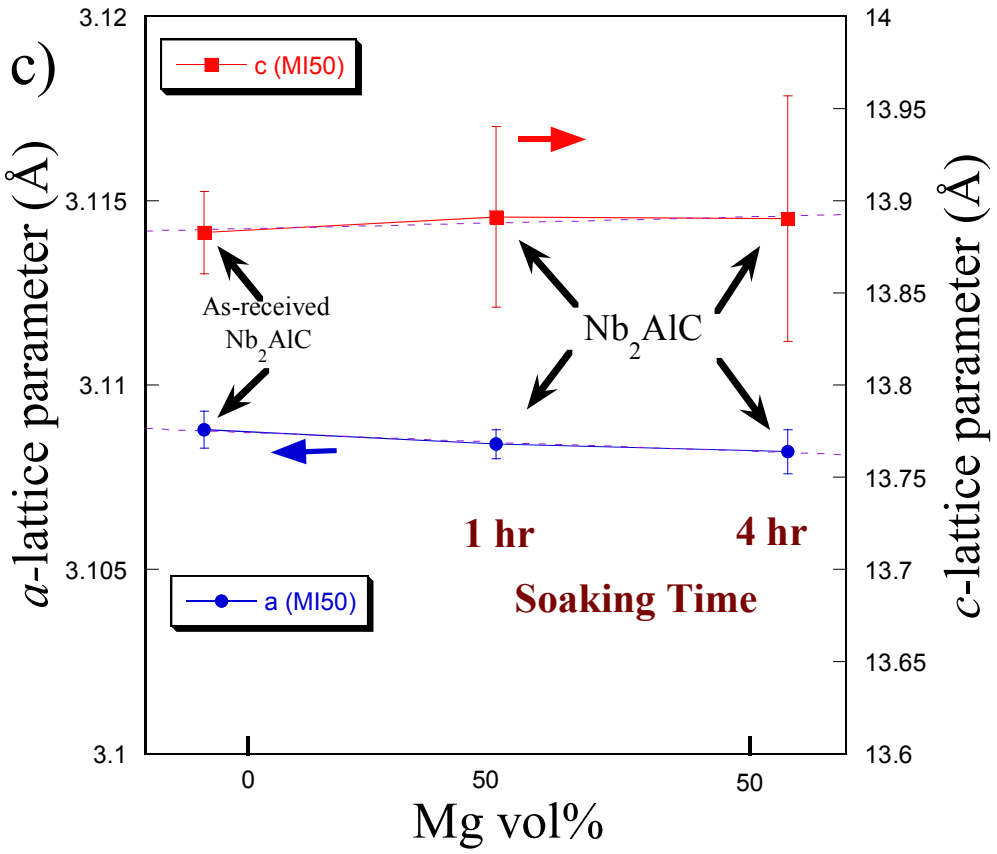

Figure 3-16: Variation of *a* and *c* lattice parameters of as-received, (a) Ti_2AlC, (b) Ti_3SiC_2, and (c) Nb_2AlC and those within their MI composites after soaking for 1 hr and 4 hrs in the Mg melt.

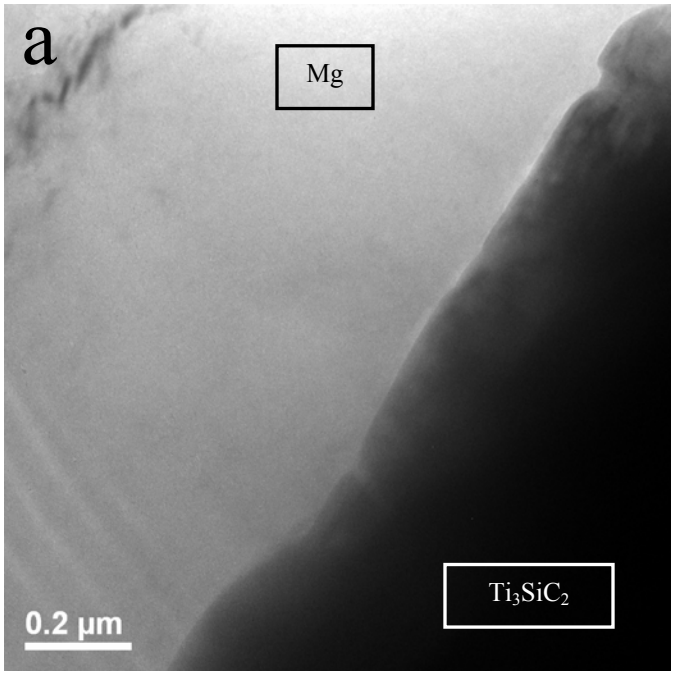
a
Mg
Ti_3SiC_2
0.2 μm

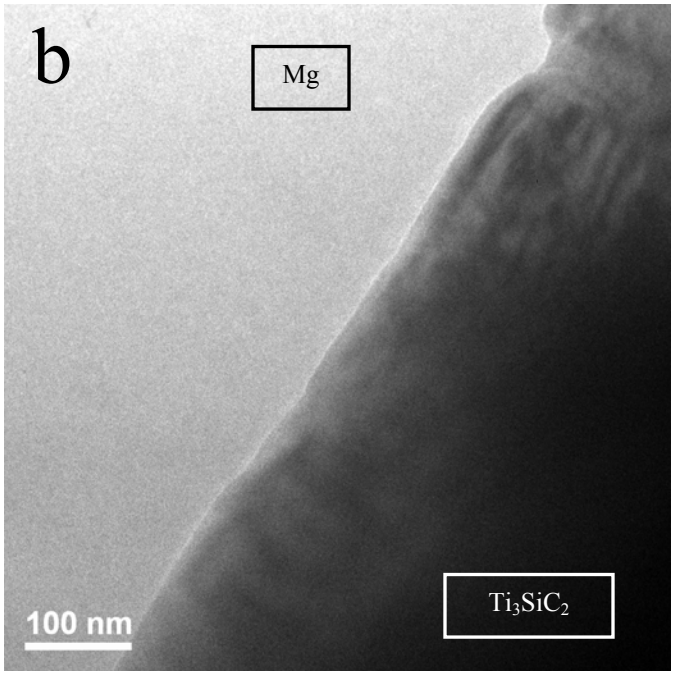
b
Mg
Ti_3SiC_2
100 nm

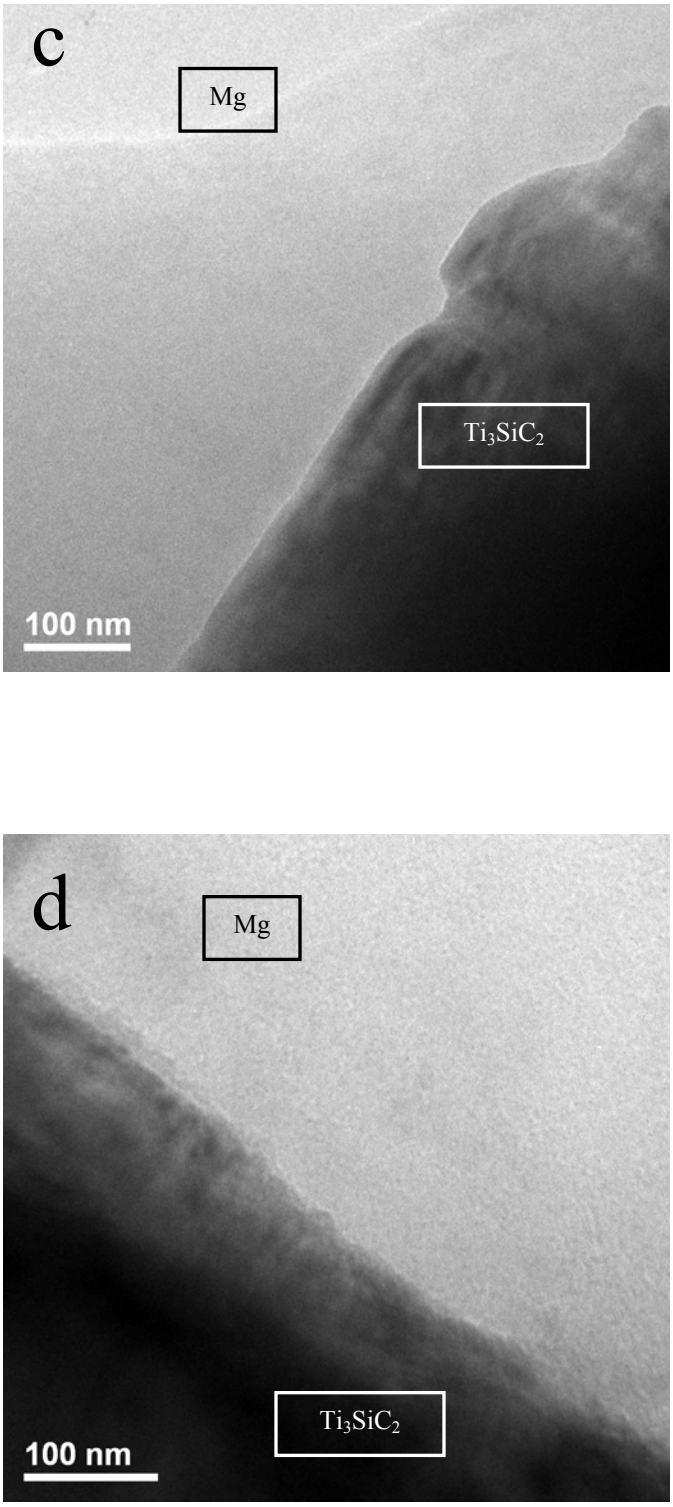

Figure 3-17: TEM images of Mg-50 vol.% Ti_3SiC_2 composite fabricated by MI at 750º C for 1 h, showing the absence of nanocrystalline Mg matrix within the composite.

3.3.4. Overview of Mechanical Properties

Herein, the mechanical properties of the Mg-Ti_2AlC and Mg-Ti_3SiC_2 composites are briefly discussed. A more complete discussion can be found in Chs. 4 and 5.

The UTS of the randomly oriented (MI-R) composite was measured to be 345±40 MPa. This value is noteworthy since it is significantly higher than pure Mg matrix composites reinforced with 10-30 vol. % SiC_P (particulate) (217 to 280 MPa) [96]. This strength is in line with Mg-*alloy* matrix composites, such as AZ91 reinforced with SiC (320 MPa), Al_2O_3 (310 MPa) or TiB_2 (340 MPa) [82]. The UTS of Mg-Ti_2AlC composites measured herein is comparable with Al-40%SiC_P composites (390 MPa) [126].

At 700±10 MPa the ultimate compressive strengths (UCS) of the Mg-Ti_2AlC composites were lower than the 865±55 MPa of fully dense Ti_2AlC. However, to confirm that the nanometer scale of the Mg grains was responsible for the high strengths observed, we HPed Mg-50 vol.% SiC and Mg-50 vol.% Ti_3SiC_2 composites. In the latter two composites the Mg-grains were not in the nanometer scale and their UCSs – at 500±25 and 460±10 MPa, respectively – were significantly lower than those of the MI Mg-Ti_2AlC composites.

Typical stress-strain curves in compression at four different loads, shifted horizontally for clarity, up to ~ 75% of the failure stress are shown in Figure 3.18a. Based on these curves, and the fact that the energy dissipated per cycle per unit volume, W_d, and the nonlinear strain, ε_{NL} , at a stress, σ, both scale as σ^2 (Figure 3.18b) as predicted from the KNE model are consistent with the fact that IKBs are responsible for both.

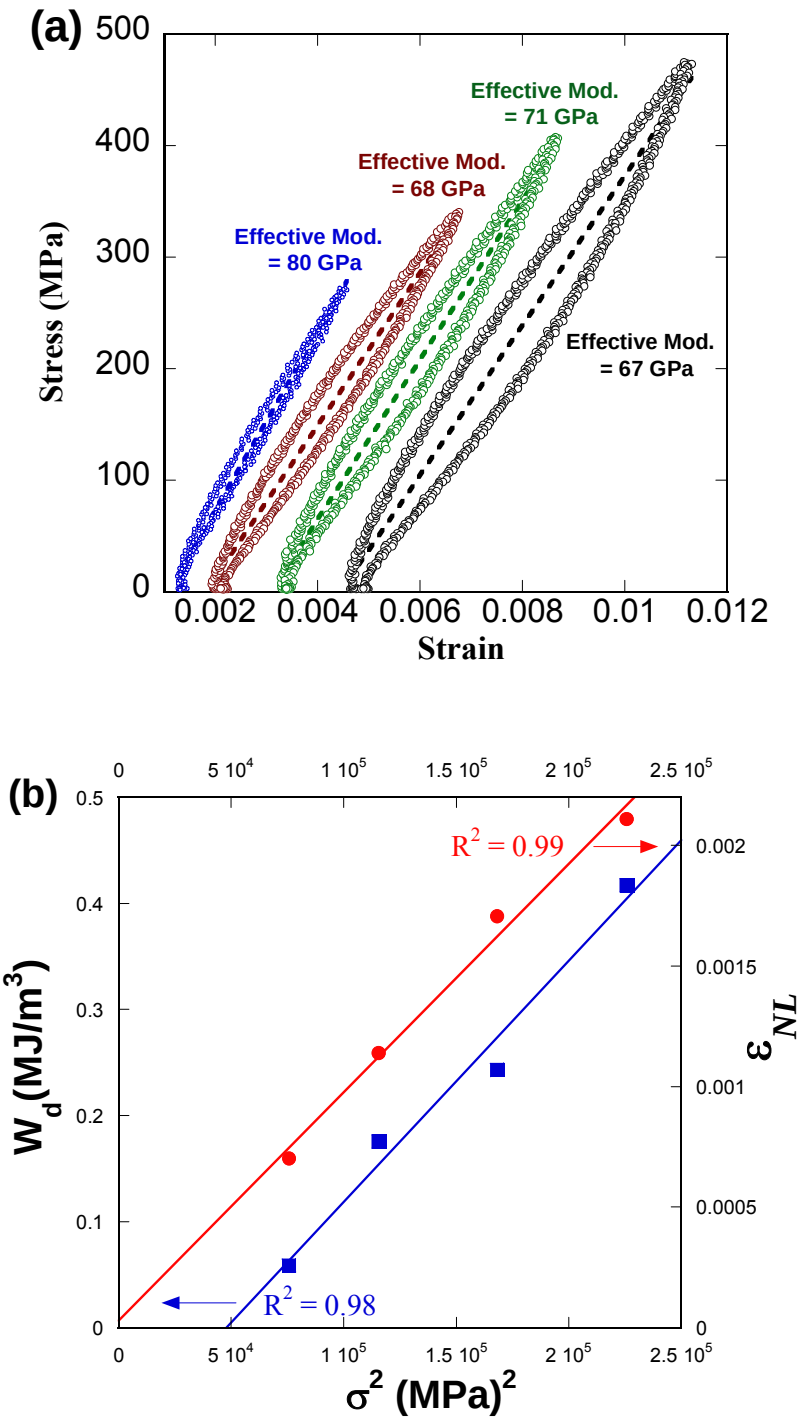

Figure 3-18: (a) Fully reversible hysteretic loops in MI Mg-50 vol. % Ti_2AlC composite. The sample was compressed to ~ 75% of its failure stress; the strains are shifted horizontally for clarity; (b) Plot of W_d and ε_{NL} vs. σ^2 from uniaxial compression stress-strain curves.

In other words, it is reasonable to conclude that W_d and ε_{NL} are due to the formation and annihilation of IKBs. As far as we are aware, the value of W_d measured herein (0.58 MJ/m^3) is the highest ever reported at a stress of ≈ 500 MPa. However, as shown in Ch. 4 this record was surpassed by a W_d value of 0.6 MJ/m^3 simply by orienting the basal planes of the Ti_2AlC grains along the loading direction. Based on the SEM micrographs of typical kink bands observed on the fractured surfaces of the MI composites (Figure 3.9), and the evidence shown above, it is not unreasonable to assume that they were preceded by IKBs.

The effective Young's moduli, $\overline{E}$, calculated from least squares fits of the entire data set – shown as diagonal lines bisecting the loops in Figure 3.18a – range from 67 to 80 GPa. The "rule-of-mixtures" for particulate composites for $\overline{E}$ was utilized herein for Mg-Ti_2AlC and Mg-Ti_3SiC_2 composites, respectively. The results are plotted in Figure 3.19; the $\overline{E}$ of Mg, Ti_2AlC and Ti_3SiC_2 were measured to be: 45 GPa, 218 GPa and 236 GPa (see Chs. 4 and 5 for details). For the most part, with the exception of MI-P sample (the reason for this is explained in Ch. 4.), $\overline{E}$ of the composites fall within the upper and lower bounds of the "rule-of-mixtures". We will explain in Ch. 4 that $\overline{E}$ is a function of kinking and the size and extent of the stress-strain loops.

And while there are many solids, for which damping is much higher, like elastomers for example, we believe that the combination of W_d, UTS, UCS and $\overline{E}$ values reported herein is unique. More importantly, at a density of 2.87±0.03 Mg/m^3 and UTS of 380 MPa, compared to that of 3.3 Mg/m^3 and 200 MPa for Mg-TiC composites [127], the specific tensile strength of Mg-Ti_2AlC composites is higher than those of Mg-TiC

composites by a factor of 2 (compare 130 vs. 60 kN.m/Kg). There results can not be overemphasized.

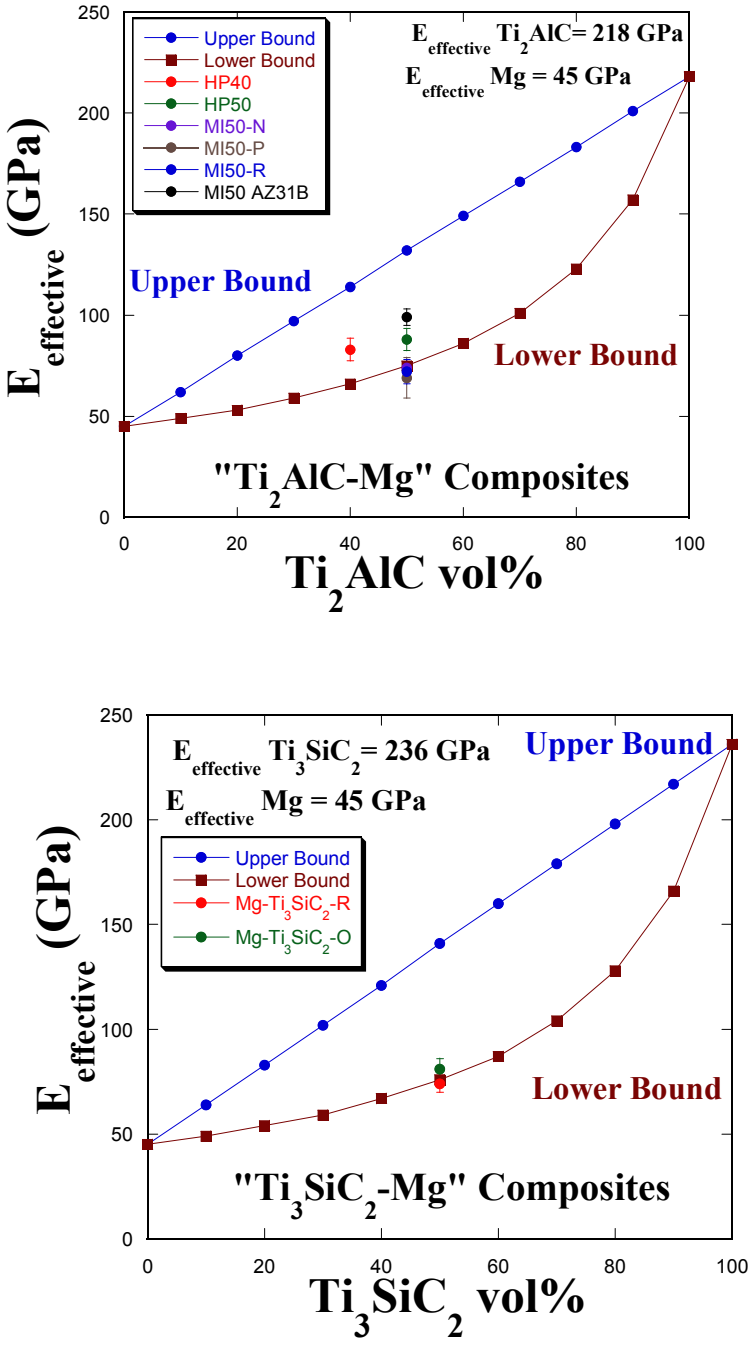

Figure 3-19: Plots of effective Young's moduli vs. volume fraction of the Mg-MAX composites in, (a) Mg-Ti_2AlC and, (b) Mg-Ti_3SiC_2.

3.4. Summary and Conclusions

The primary focus of this chapter was to report on the processing and microstructural characterization of 50 vol. % Ti_2AlC/nanocrystalline (nc) Mg-matrix composites fabricated by pressureless MI at 750 °C for 1 h. X-ray diffraction and transmission electron microscopy both confirmed that the Mg grain size was ~10-20 *nm*. The microstructure was also exceptionally stable; annealing for 6 h at 550 °C did *not* alter the size of the Mg-grains. Some Mg was dissolved in the Ti_2AlC which suggest the existence of a $(Ti_{1-x}Mg_x)_2AlC$ solid solution, with x as high as 0.2. Several experiments were performed to understand how and why the matrix of the Mg-Ti_2AlC composite form nanocrystalline Mg, but the major scientific question still remains partially unanswered. It is hereby acknowledged that more work is needed to understand the formation of the nanocrystalline Mg.

At 350±40 the UTS, and more importantly, the specific strength, are significantly greater than other pure Mg-composites reported in the literature. At 700±10 MPa, the ultimate compressive stresses of these composites were ≈ 40% higher than those of a 50 vol.% Ti_3SiC_2-Mg or a 50 vol.% SiC-Mg, in which the Mg-matrix grains were not at the nanoscale. The Ti_2AlC/nc-Mg composites are readily machinable, stiff (≈ 70 GPa), strong, light (2.9 g/cm^3) and exhibited exceptional damping capabilities.

Chapter 4 : On the Effect of Texture on Mechanical Properties of "MAXMET"s

4.1. Introduction

Recently [52-54, 56] it was postulated that most hexagonal solids with *c*/*a* ratios > 1.5 are plastically anisotropic and thus belong to the same class of solids that we labeled kinking nonlinear elastic (KNE). Kinking is a mechanism first reported in metals by Orowan in single crystals of Cd loaded parallel to their basal planes [61]. Kink band formation is the key mechanism without which the deformation of KNE solids cannot be understood. Recently, we have established that a number of seemingly unrelated solids such as graphite [128], mica [63, 129], sapphire [64], ZnO [130], GaN [66], $LiNbO_3$ [85] and hexagonal metals (Mg, Co, Ti, Zn etc.) [59, 68], among many others, are also KNE solids. More importantly, we also showed that MAX-reinforced metal-matrix composites – what can be labeled MAXMETs – are KNE solids [71].

Kinking nonlinear elasticity was first documented in Ti_3SiC_2, a founding member of the MAX phases [56, 75]. We also recently showed that the plastically anisotropic hexagonal metals can be classified as KNE solids, thus explaining their microyielding and high damping [59, 79]. Because of their crucial technological importance, Ti, Zr, Mg, Zn and Co, among others, have been intensively studied over the past 70 years. Zr alloys used as cladding for nuclear reactor fuels and Ti alloys used in the aerospace and the aircraft industries are but a few examples. Consequently, the deformation mechanisms of these solids and their alloys to high strains are reasonably well understood. However, how these solids deform at low strains was not well understood until the crucial role KBs play in their early deformation (see below) was appreciated [58, 59]. Mg is well known

for its high damping capabilities [81, 82], lightweight, good castability and machinability [82-84]. Mg alloys are currently used in the automobile, computer, communication and consumer electronic applications.

At room temperature, some KNE solids such as Ti_3SiC_2 can be compressed to stresses as high as 1 GPa and fully recover upon removal of the load, while dissipating ≈ 25% of the mechanical energy [56]. At much higher stresses, for example in case of $LiNbO_3$ single crystals under a nanoindenter, the IKBs are sundered and devolve, first into mobile dislocation walls (MDW) and then ultimately into kink boundaries; the latter are irreversible [56]. Recently, we showed that 10 vol. % porous Ti_2AlC samples dissipate more energy on an *absolute* scale than their fully dense counterpart, which was taken to be compelling evidence that we are dealing with a kink-based phenomenon as opposed to one that is dependent on the volume of the material, such as dislocation pileups [57].

Given the various attributes of Mg and Ti_2AlC summarized above, it was postulated that Mg-Ti_2AlC composites should result in solids that are not only machinable, strong, stiff and light, but should also exhibit exceptional damping capabilities. In Ch. 3, we reported on the processing and microstructural characterization of 50 vol.% Ti_2AlC nanocrystalline (nc) Mg-matrix composites fabricated by pressureless MI. We established, using XRD and TEM images [71], that the Mg grains in the MI composites were in the 20-40 *nm* range. In another paper [131] and in Ch. 6, we showed that the average diameter of the Mg grains in hot pressed (HP) samples was ~ 26 *nm*. The microstructures were also exceptionally stable; heating the composites three times to 700°C – 50°C over the melting point of Mg – did not lead to any coarsening (see Ch. 6).

At 350±40 MPa, the UTS of the Ti_2AlC/nc-Mg composites is significantly greater than other pure Mg-composites reported in the literature [82, 96, 126, 127]; for example, Contreras *et al.* [127] reported UTS values of ~ 200 MPa in tension for their Mg-50 vol. % TiC composites made by pressureless MI at 950 ºC. Our Mg-Ti_2AlC composites were infiltrated at significantly lower temperatures (750 ºC) and yielded UTS values that were higher by a factor of ~ 2. At 700±10 MPa, the UCS of these composites were ≈ 40 % higher than those of a 50 vol.% Mg-Ti_3SiC_2 or a 50 vol.% Mg-SiC, in which the Mg-matrix grains were not at the nanoscale (Ch. 3). These Ti_2AlC/nc-Mg composites are readily machinable, stiff (≈ 70 GPa), strong, light (2.9 g/cm^3) and exhibited exceptional damping capabilities that increased as the square of the applied stress to stress levels of the order of ≈ 500 MPa. The W_d values at such stresses is believed to be the highest reported for a crystalline solid and to be due to the formation and annihilation of IKBs [71].

The objectives of this chapter are threefold: first, to report on the mechanical response of the aforementioned composites under microhardness indentation and compressive loadings; second, is to apply the KNE microscale model [59] (Ch. 2) to analyze the cyclic compressive stress-strain curves obtained. Lastly, because the MAX phases are layered hexagonal solids that deform by kinking, it was postulated that their response to cyclic loadings would depend on the orientation of the basal planes relative to the loading direction. The effect of texture was thus investigated.

4.2. Experimental Details

The composites tested herein were made using two different techniques: hot pressing (HPing) and melt infiltration (MI). The former was used initially on the assumption – later proven incorrect – that Mg, like Al, would not spontaneously infiltrate a Ti_2AlC perform; both techniques are fully described in Ch. 3.

Cylinders for compression tests *parallel* and *normal* to the cold-pressing direction were EDMed from the *same* oriented MI samples. Under compression, the basal planes in the former are *normal* to the loading direction, which is why these samples are referred to as "MI-N". When the basal planes are parallel to the loading direction, the samples will be referred to as "MI-P". This nomenclature is also valid for the Vickers hardness measurements because in the MI-N sample, the indenter is *normal* to the basal planes, etc. The randomly oriented samples will be referred to as MI-R. For clarity's sake, in most of the stress-strain figures, a small schematic of the relationship of the basal planes to the applied load is shown as an inset.

Also for the sake of comparison, Mg-50 vol.% Ti_3SiC_2 and Mg-50 vol. % SiC composites were fabricated by HPing. In this case, the starting powders were Ti_3SiC_2 (- 325 mesh, 3-ONE-2, Voorhees, NJ), SiC (- 325 mesh, Alfa Aesar, Ward Hill, MA) and the same Mg powder used above. The processing details were identical to those of the Mg-Ti_2AlC (HP) composites described above. These samples will henceforth be referred to as "Mg-312" and "Mg-SiC", respectively.

Bulk Ti_2AlC and Ti_3SiC_2 samples were also made by hot isostatic pressing (HIPing) for the sake of comparison. The starting powders were sealed in rubber bags under a

mechanical vacuum and were cold isostatically pressed (CIPed) to ~ 250 MPa for ~ 5 min. The samples were then placed in crushed borosilicate glass and then in a hot isostatic press (HIP), heated to 750 ºC at a rate of 5 ºC/min, at which time the chamber was pressurized with Ar gas to ~ 100 MPa. The heating was then resumed at a rate of 10 ºC/min to 1400 ºC at which time the chamber was further pressurized to ~ 175 MPa and the samples were held for 2 h followed by furnace-cooling to room temperature.

4.3. Results

Not surprisingly, and similar to all other MAX phases [12, 27, 28], and Mg, both HP and MI composites are readily machinable even with a manual hack-saw with no lubrication or cooling. They can also readily be EDMed with a significantly higher rate and ease than the MAX phases. According to our machinist, their machinability is similar to 7000 series Al alloys.

The effect of indentation loads on the V_H values of the HP, MI-R, MI-P and MI-N samples, together with those of fully dense Ti_2AlC, pure Mg, Mg-312 and Mg-SiC for the sake of comparison are plotted in Figure 4.1; Figure 4.2 shows secondary electron SEM images of Vickers indentation marks in the MI and HP composites.

Figure 4.3a compares the UCS of all materials tested in this work. Figures 4.3b and c show the compressive stress-strain curves to the point of fracture indicating offset yield strength and fracture point in HP50 and MI50 composites, respectively.

For cyclic compression tests, typically five cycles are obtained at each load. For the most part, the first cycles were very slightly open, registering a plastic strain of the order of ~ 0.05%.

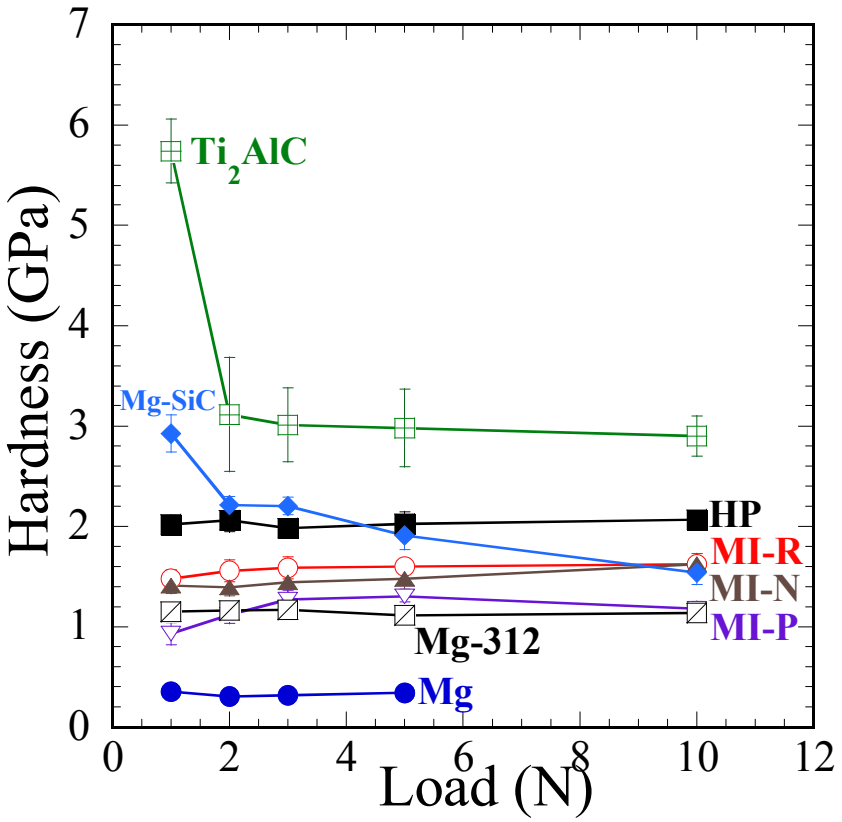

Figure 4-1: Effect of indentation loads on the V_H values of the HP, MI-R, MI-P and MI-N samples, together with those of fully dense Ti_2AlC, pure Mg, Mg-312 and Mg-SiC for comparison.

However, all subsequent cycles, to the same stress, were closed and exceptionally reproducible, which is why in Figure 4.4 only one loop at any given stress is plotted. Typical stress-strain loops at various stresses for the MI-P (Figure 4.4a), MI-N (Figure 4.4b) and MI-R (Figure 4.4c) – loaded to roughly ~ 75% of their UCS – at different stresses are all closed. Typical fully reversible stress-strain loops for the Mg-312 and Mg-SiC composites (Figures 4.4d) are, however, significantly smaller than the rest. Figures 4.4e and 4.4f show typical fully reversible stress-strain loops of HP50 and HP40 composites, respectively.

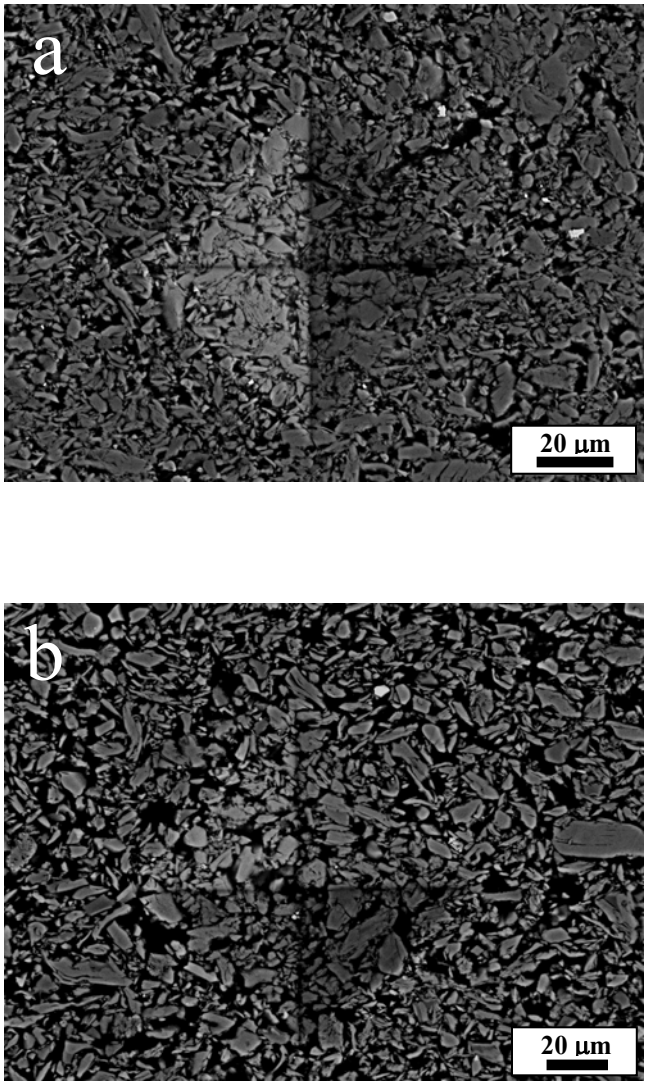

Figure 4-2: SEM micrographs of Vickers indentations at 10 N on a) HPed and b) MI Mg-Ti_2AlC composites.

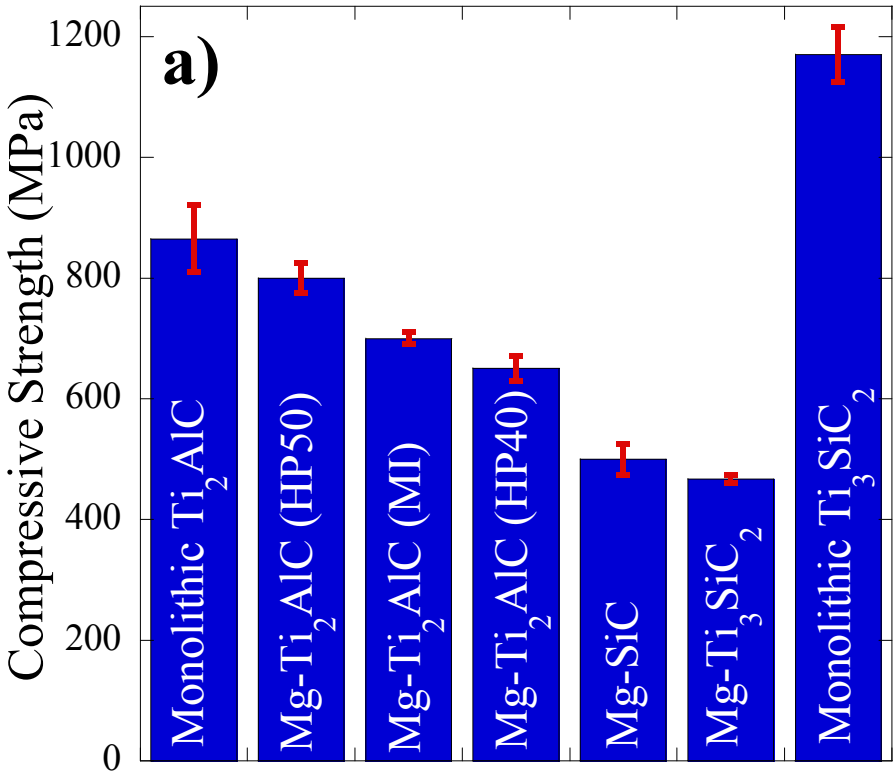
a)
Compressive Strength (MPa)
0
200
400
600
800
1000
1200
Monolithic Ti2AlC
Mg-Ti2AlC (HP50)
Mg-Ti2AlC (MI)
Mg-Ti2AlC (HP40)
Mg-SiC
Mg-Ti3SiC2
Monolithic Ti3SiC2

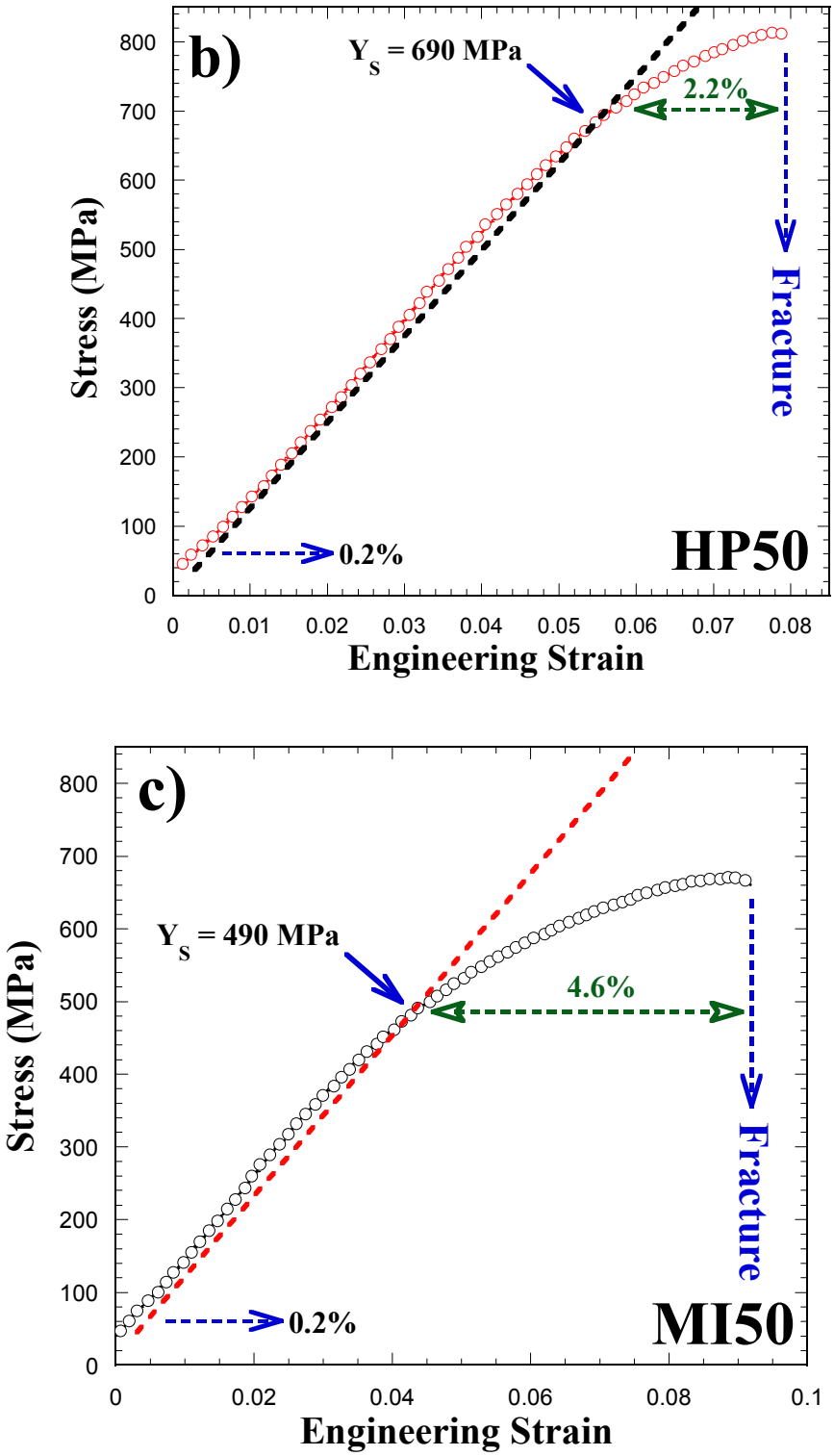

Figure 4-3: (a) Plot of UCS values of all materials tested in this work; compressive stress-strain curves indicating offset yield strength and fracture point for, (b) HP50 and, (c) MI50 composites.

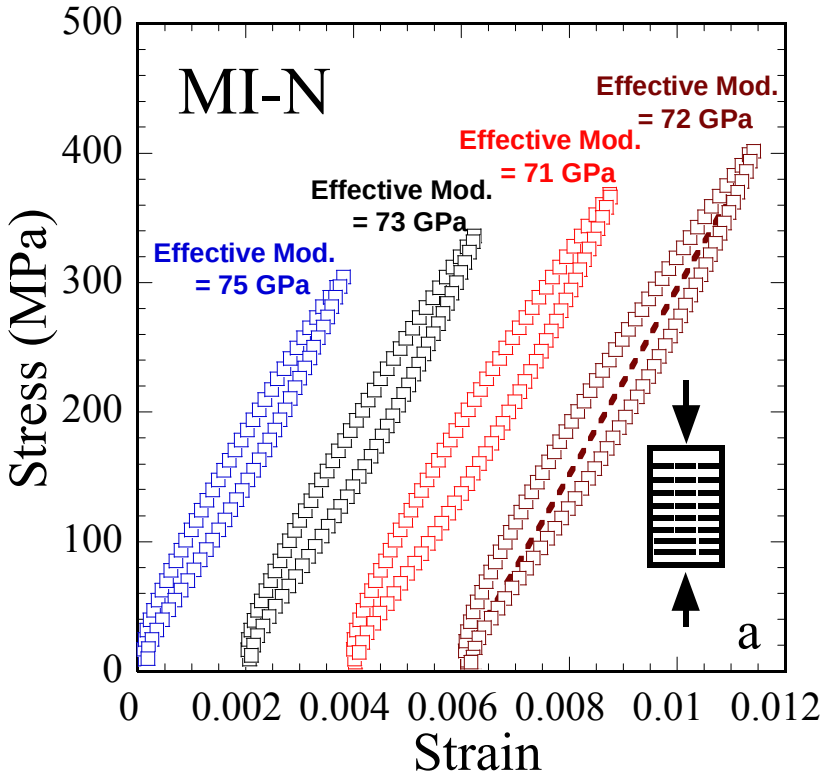
MI-N
Effective Mod.
= 72 GPa
Effective Mod.
= 71 GPa
Effective Mod.
= 73 GPa
Effective Mod.
= 75 GPa
a
Stress (MPa)
Strain
0
100
200
300
400
500
0
0.002
0.004
0.006
0.008
0.01
0.012

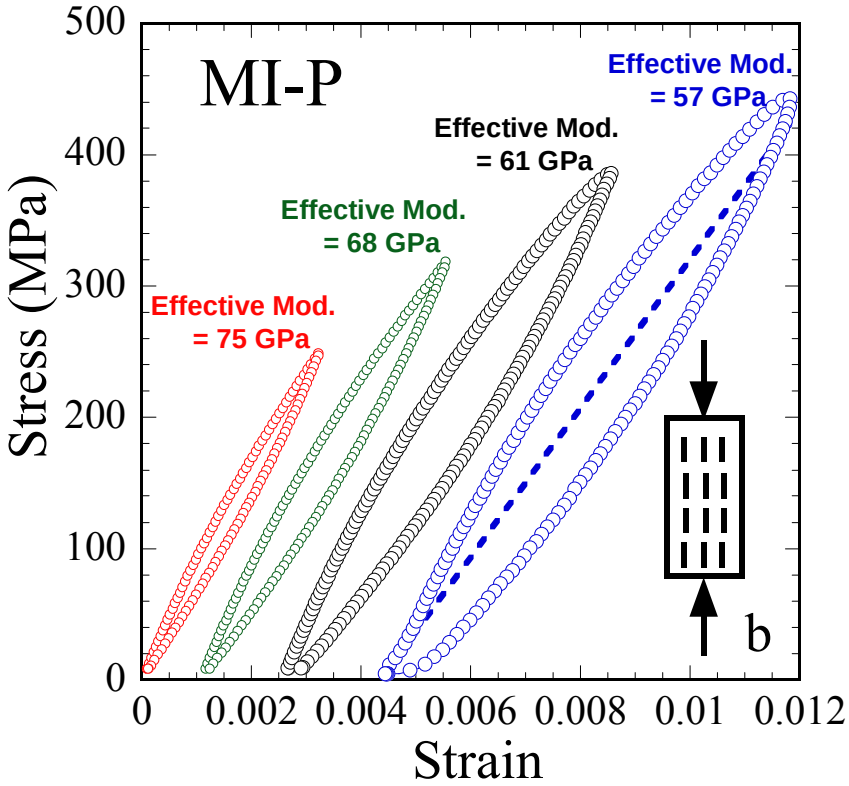
MI-P
Effective Mod.
= 57 GPa
Effective Mod.
= 61 GPa
Effective Mod.
= 68 GPa
Effective Mod.
= 75 GPa
b
Stress (MPa)
Strain
0
100
200
300
400
500
0
0.002
0.004
0.006
0.008
0.01
0.012

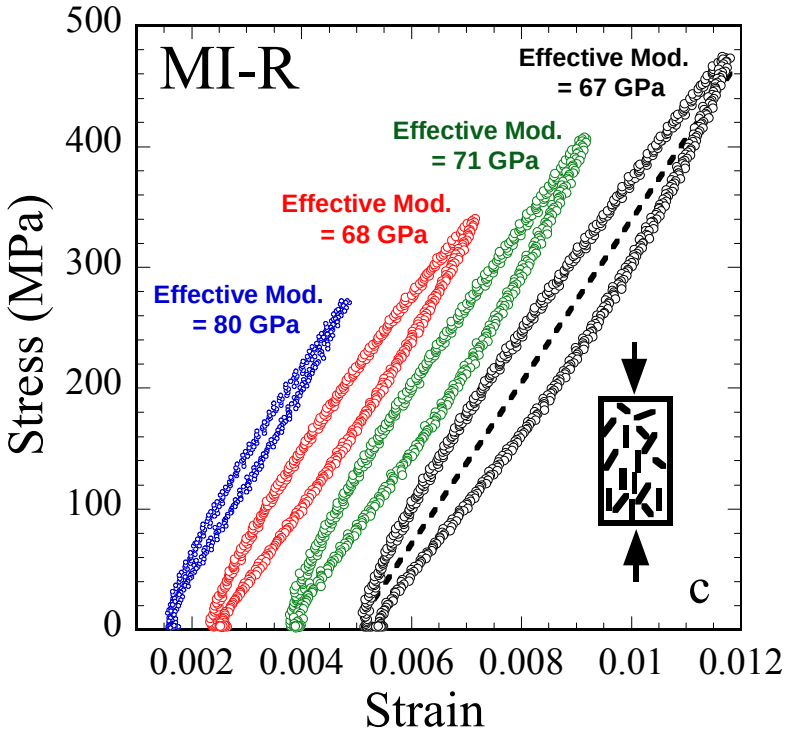
MI-R
Effective Mod.
= 67 GPa
Effective Mod.
= 71 GPa
Effective Mod.
= 68 GPa
Effective Mod.
= 80 GPa
c
Stress (MPa)
Strain
0
100
200
300
400
500
0.002
0.004
0.006
0.008
0.01
0.012

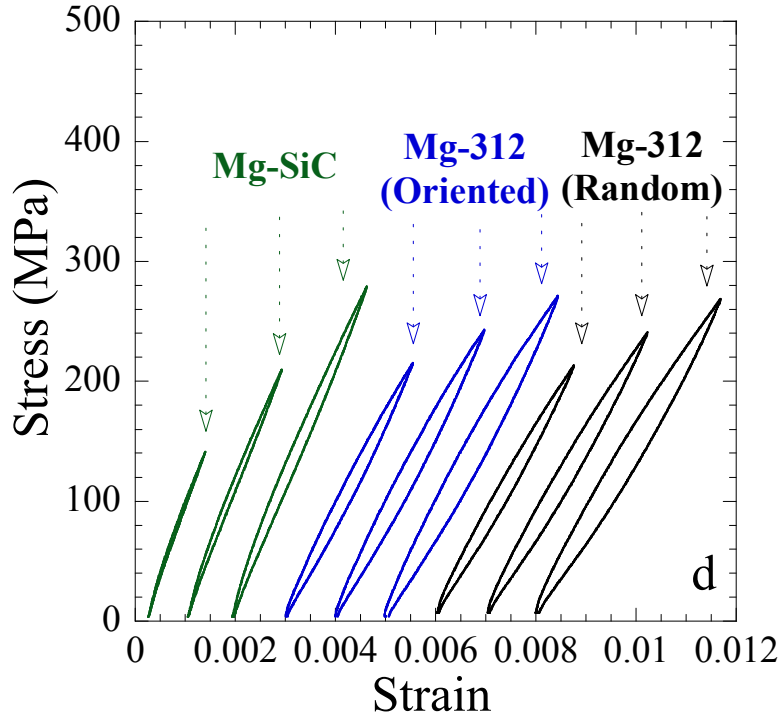
Mg-SiC
Mg-312
(Oriented)
Mg-312
(Random)
d
Stress (MPa)
Strain
0
100
200
300
400
500
0
0.002
0.004
0.006
0.008
0.01
0.012

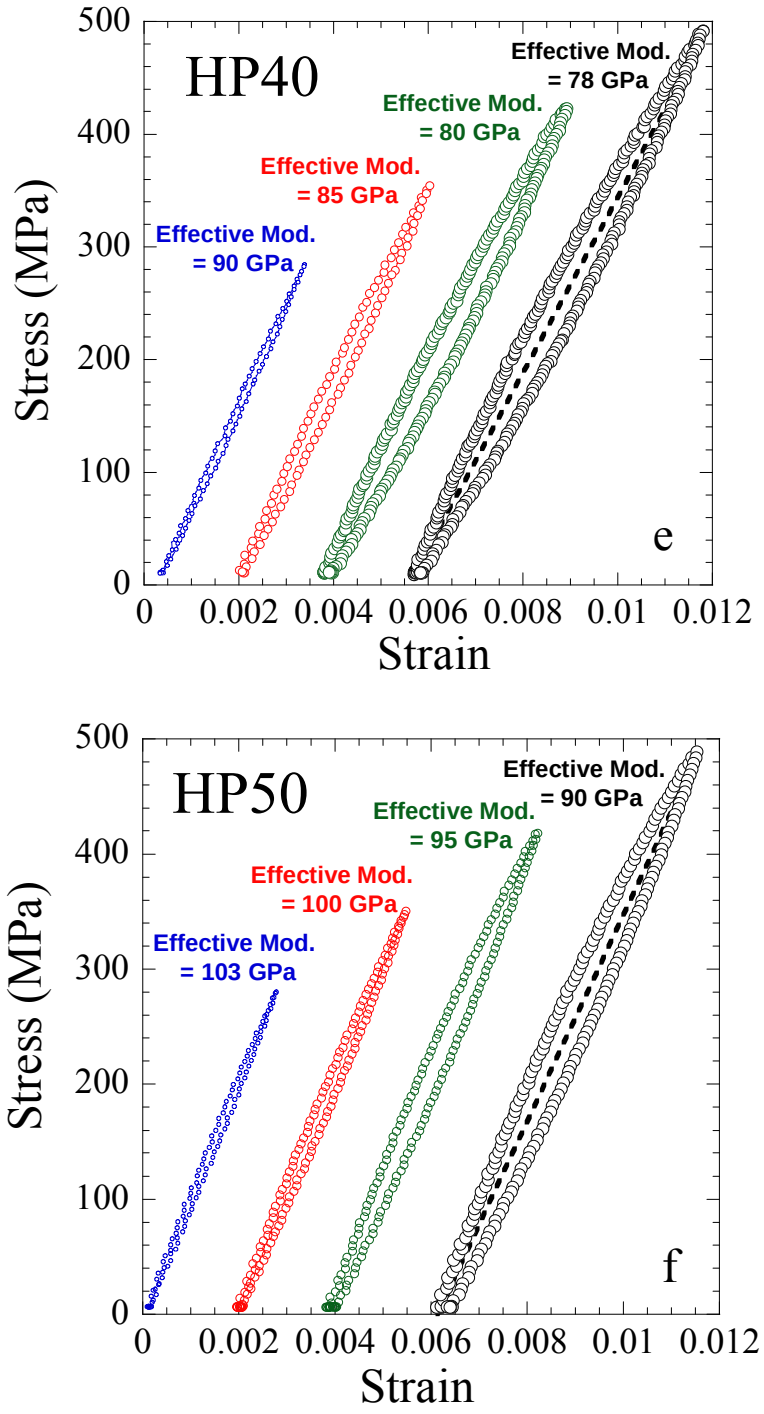

Figure 4-4: Typical compressive stress-strain curves for a) MI-N, b) MI-P, c) MI-R, d) Mg-SiC and Mg-312, e) HP40 and, f) HP50 composites. Only the fifth cycle is shown and the curves are shifted horizontally for clarity.

Defining a Young's modulus for loops such as those shown in Figure 4.4 is problematic. However, to obtain an *approximate* "effective" Young's modulus, $\overline{E}$, least squares fits of the entire data set that resulted in diagonal lines bisecting the loops (only those at the highest loads are shown in figures) were carried out at each stress. The results are summarized in Table 4.1.

Table 4-1: Effective Young's modulus, $\overline{E}$, for MI-P, MI-R, MI-N, HP50, HP40, Mg-312, Mg-SiC, Ti_2AlC and Ti_3SiC_2 samples tested herein. Also listed are the values for the *upper* and *lower* bounds of E [E(u) and E(l)], G [G(u) and G(l)] and Poisson's ratio, ν, [ν(u) and ν(l)], respectively.

Material	MI-P	MI-R	MI-N	HP50	HP40
$\overline{E}$ (GPa)	69±10	72±6	74±3	88±5	83±5
E (u)	130±3	130±3	130±3	130±3	127±3
E (l)	74±1	74±1	74±1	74±1	-
G (u)	69	69	69	69	67
G (l)	33	33	33	33	-
ν (u)	0.27	0.27	0.27	0.27	0.24
ν (l)	0.25	0.25	0.25	0.25	-

Table 4.1: continued.

Material	Mg-312	Mg-SiC	Ti_2AlC	Ti_3SiC_2
$\overline{E}$ (GPa)	74±4	117±17	218±6	237±22
E (u)	140±10	260	-	-
E (l)	75±1	82	-	-
G (u)	82	106	-	-
G (l)	34	35	-	-
ν (u)	0.27	0.25	-	-
ν (l)	0.25	0.20	-	-

Based on our model, the mechanical hysteresis of a KNE solid can be characterized by three parameters, σ, ε_{NL} and W_d – all obtainable from the hysteretic stress-strain curves shown in Figure 4.4 – listed in Table 4.2 for the samples tested herein.

Table 4-2: List of measured stress (σ), nonlinear strain (ε_{NL}), and dissipated energy (W_d) for MI-P, MI-R, MI-N, HP50, HP40, Mg-SiC, Mg-312 and randomly oriented Ti_2AlC and Ti_3SiC_2 samples tested herein. Also listed are the m_1, m_2 and their ratio and $3k_1\Omega/b$ values obtained from the slopes of ε_{NL} vs. σ^2, W_d vs. σ^2 and W_d vs. ε_{NL} plots, respectively.

	σ MPa	ε_{NL}	W_d MJ/m^3	m_1 (MPa)$^{-2}$	m_2 (MPa)$^{-1}$	m_2/m_1 (MPa)	$3k_1\Omega/b$ (MPa)
MI-P	250	0.0007	0.0832	1.5×10^{-8}	3.4×10^{-6}	230	229
	319	0.0012	0.1922				
	388	0.0021	0.3443				
	445	0.0027	0.5850				
MI-R	275	0.0007	0.0795	9.8×10^{-9}	2.2×10^{-6}	225	223
	340	0.0011	0.1755				
	410	0.0017	0.2752				
	475	0.0021	0.4171				
MI-N	305	0.0005	0.1101	9.0×10^{-9}	2.0×10^{-6}	225	224
	338	0.0007	0.1440				
	370	0.0009	0.1962				
	405	0.0011	0.2573				
HP50	280	0.0001	0.0324	7.7×10^{-9}	1.8×10^{-6}	235	237
	350	0.0003	0.0705				
	420	0.0006	0.1352				
	490	0.0013	0.2862				
HP40	285	0.0002	0.0398	6.4×10^{-9}	1.5×10^{-6}	231	232
	355	0.0004	0.0848				
	423	0.0008	0.1498				
	492	0.0012	0.2775				
Ti_2AlC	342	0.0002	0.0166	1.0×10^{-9}	2.4×10^{-7}	230	229
	445	0.0003	0.0359				
	537	0.0004	0.0557				
	628	0.0005	0.0794				

Table 4.2: continued.

	σ MPa	ε_{NL}	W_d MJ/m^3	m_1 (MPa)$^{-2}$	m_2 (MPa)$^{-1}$	m_2/m_1 (MPa)	$3k_1\Omega/b$ (MPa)
Mg-SiC	70	0.0001	0.0005	1.3×10^{-8}	4.2×10^{-7}	32	32
	140	0.0004	0.0045				
	210	0.0006	0.0168				
	280	0.0009	0.0459				
Mg-312 (Random)	159	0.0001	0.0178	1.8×10^{-8}	1.7×10^{-6}	94	93
	186	0.0002	0.0304				
	213	0.0003	0.0457				
	241	0.0005	0.0671				
Mg-312 (Oriented)	159	0.0003	0.0179	1.7×10^{-8}	1.7×10^{-6}	102	99
	188	0.0004	0.0274				
	215	0.0006	0.0432				
	243	0.0008	0.0660				
Ti_3SiC_2	307	0.0001	0.0208	2.8×10^{-9}	5.2×10^{-7}	193	192
	417	0.0003	0.0516				
	514	0.0006	0.0988				
	623	0.0009	0.1732				

According to Eqs. 2.5-7, plots of W_d vs. σ^2, ε_{NL} vs. σ^2 and W_d vs. ε_{NL} should all yield straight lines. With the notable exception of the Mg-SiC composite (see below), that is what was observed (Figures 4.5 a-f). The lowest correlation coefficient, R^2, obtained from least squares analysis of the results, with again the exception of the SiC-containing system, was > 0.95. Table 4.3 lists the threshold stresses, σ_t, obtained from the W_d vs. σ^2 plots, viz. Figure 4.5 a and d. Also, based on the results shown in Figure 4.5a-f, the model presented in Ch. 2, and the constants listed in Table 4.3, the values of 2α, Ω/b, N_k, $2\beta_{av,c}$, $2\beta_{av}$, ρ_{rev} and ε_{IKB} were calculated. It is important to note that the values of 2α in Table 4.3 are calculated from the σ_t values (Table 4.3) and Eq. 1, assuming M=3. The latter is a good first assumption. In Ch.4 we refine our methodology and show that M varies

slightly with texture. The ε_{NL} values labeled "*measured*" are those measured by the extensometer directly attached to the samples' surface.

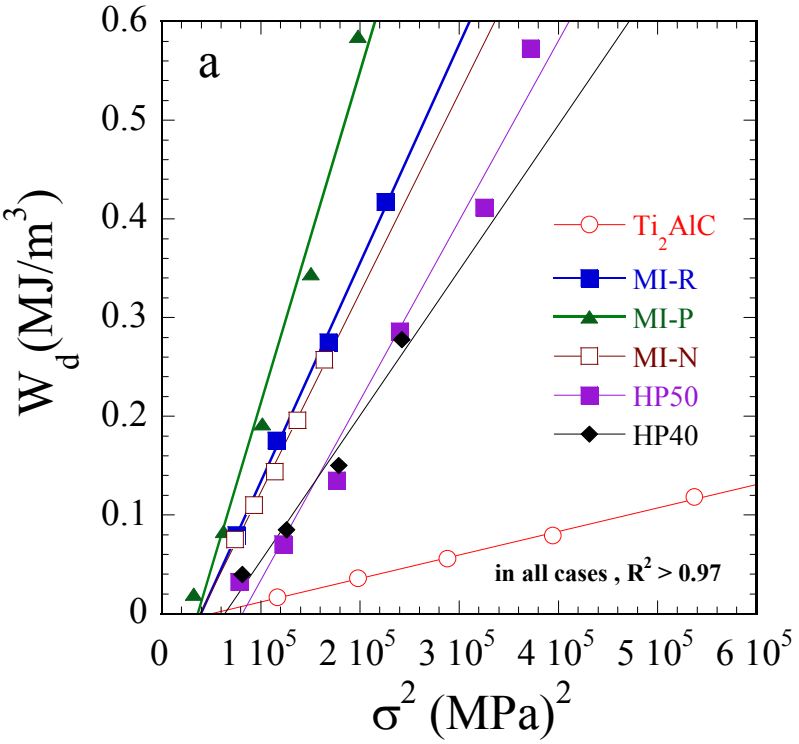

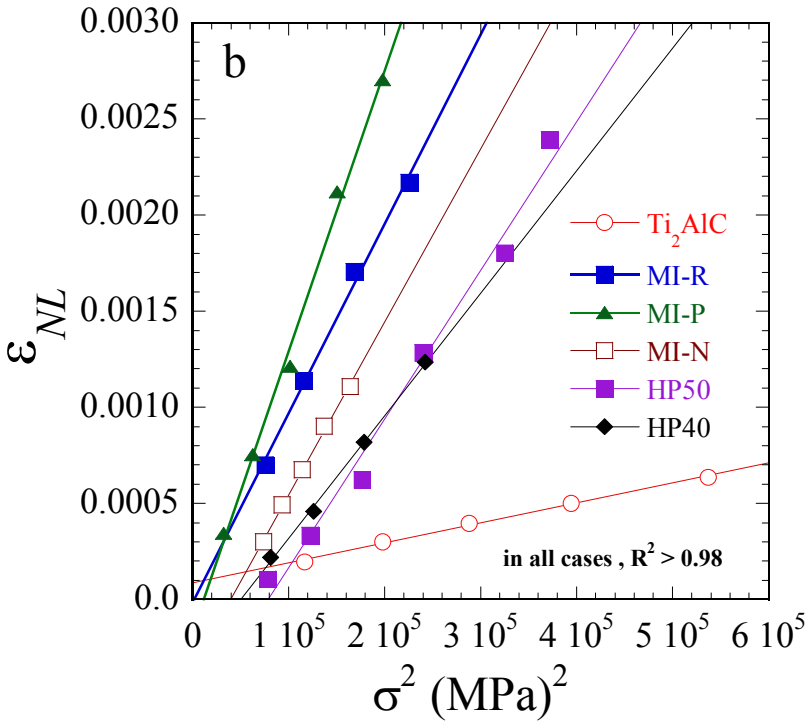

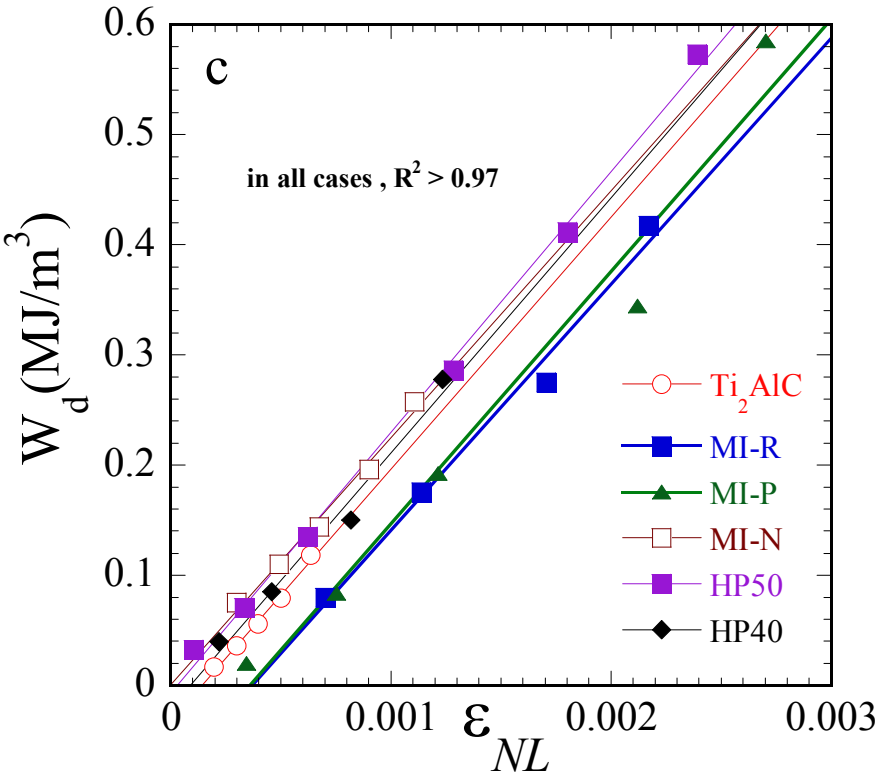
c
in all cases , R² > 0.97
Ti2AlC
MI-R
MI-P
MI-N
HP50
HP40
W_d (MJ/m³)
ε_NL
0
0.1
0.2
0.3
0.4
0.5
0.6
0.001
0.002
0.003

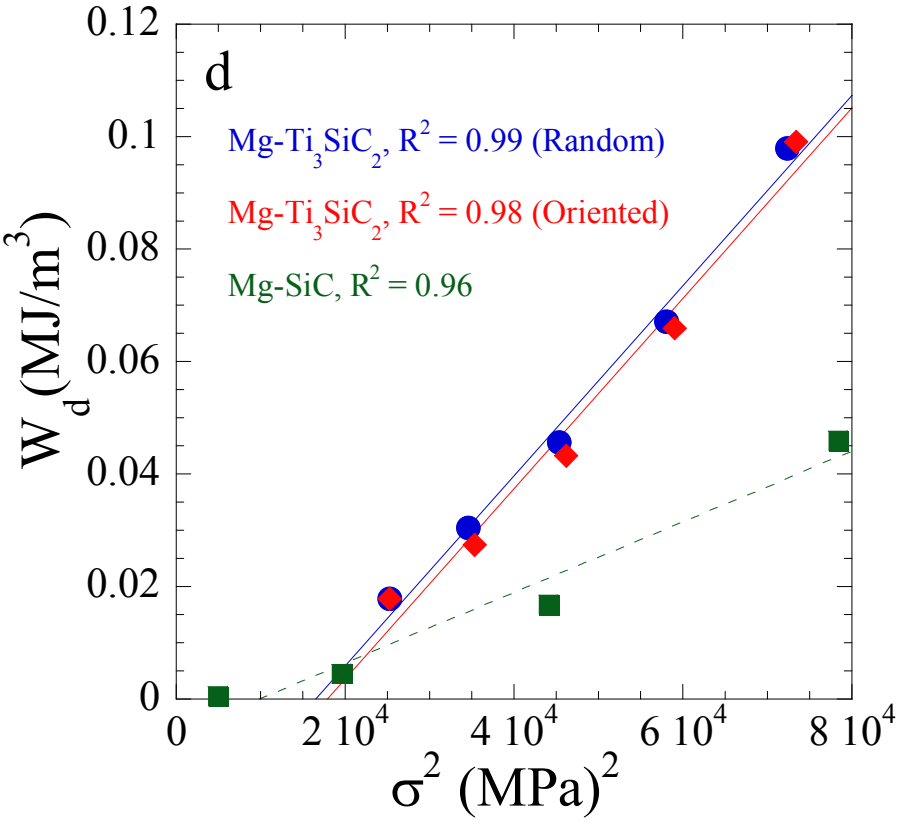
d
Mg-Ti3SiC2, R² = 0.99 (Random)
Mg-Ti3SiC2, R² = 0.98 (Oriented)
Mg-SiC, R² = 0.96
W_d (MJ/m³)
σ² (MPa)²
0
0.02
0.04
0.06
0.08
0.1
0.12
2 10⁴
4 10⁴
6 10⁴
8 10⁴

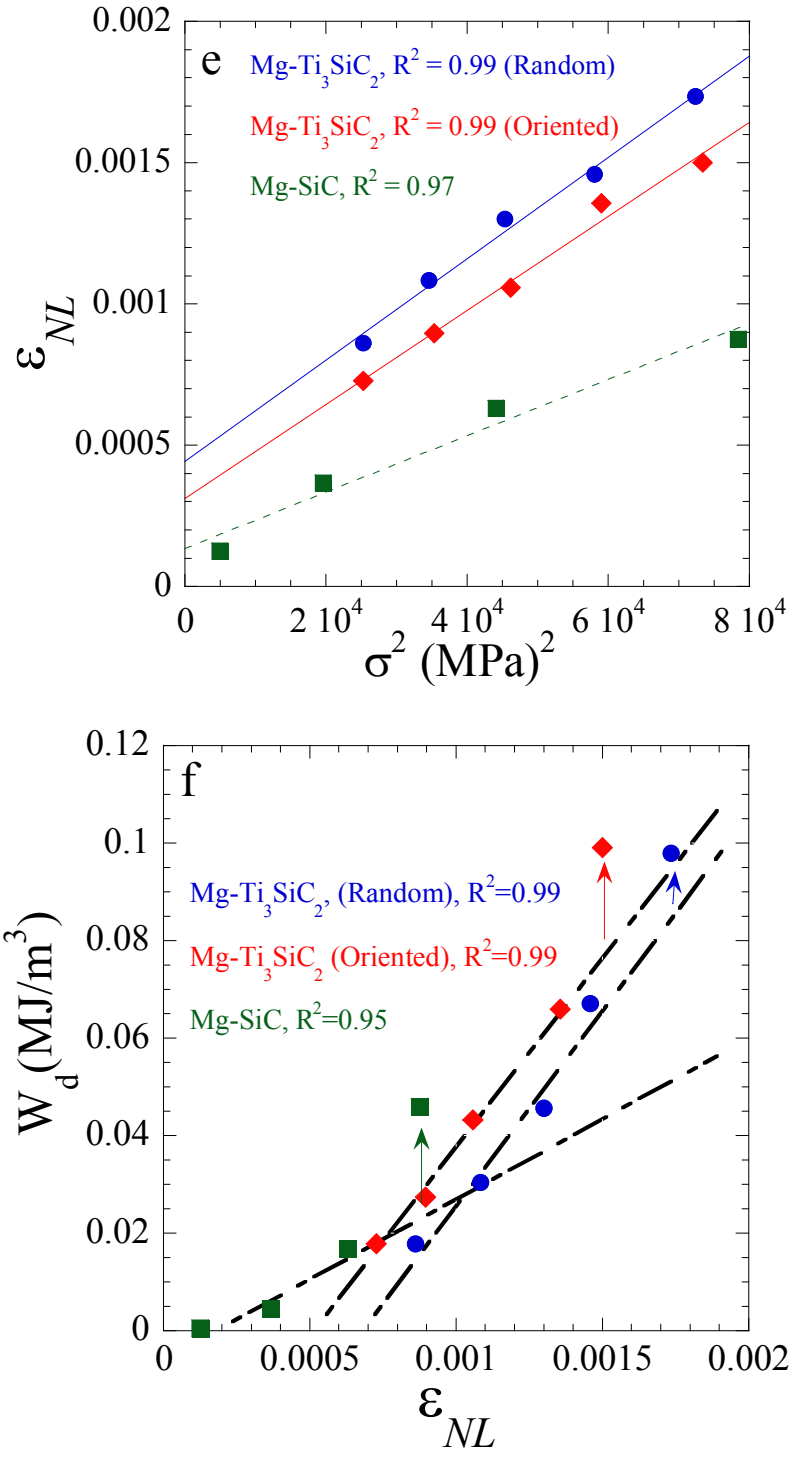

Figure 4-5: Plots of, a) W_d vs. σ^2, b) ε_{NL} vs. σ^2, and c) W_d vs. ε_{NL} for all Mg-Ti_2AlC composites tested in this work and those of fully dense Ti_2AlC. Plots of, d) W_d vs. σ^2, e) ε_{NL} vs. σ^2, and, f) W_d vs. ε_{NL} for Mg-Ti_3SiC_2 and Mg-SiC composites.

Table 4-3: List of experimentally measured σ_t values obtained from the W_d vs. σ^2 plots (Figure 4.5a and d) and 2α values calculated using the σ_t values in column 1 and Eq. 1 assuming M=3. Also listed are calculated values of Ω/b obtained from Eqs. 4 & 5 and 6 (columns 4 and 5, respectively), N_k, $2\beta_{av,c}$, ε_{IKB} calculated from the third term of Eq. 4 and ε_{NL} measured directly by the extensometer. The $2\beta_{av}$ and ρ_{rev} values at the stress levels listed in the last column are also included. For all cases, b = 3.0 Å, M = 3, *w* = 5b, k_1 = 2; G and ν of the Mg-Ti_2AlC, Mg-Ti_3SiC_2 and Mg-SiC composites were assumed to be ~ 51 GPa and 0.26, ~ 58 GPa and 0.26, and ~ 70 GPa and 0.22 (Table 4.1). Those of Ti_2AlC [57], Ti_3SiC_2 [88], SiC [132], and Mg [58] are *118* GPa and *0.2*, *144* GPa and *0.2*, *192* GPa and *0.142*, and *19* GPa and *0.35*, respectively.

	σ_t (MPa)	2α (μm)	Ω/b (MPa) Eqs. 4&5	Ω/b (MPa) Eq. 6	N_k (m^{-3})	$2\beta_{av,c}$ (μm)	$2\beta_{av}$ (μm)	ρ_{rev} (m^{-2})	ε_{IKB} calculated	ε_{NL} measured	σ (MPa)
MI-P	162	3	38.4	38.2	4.7×10^{17}	0.29	0.79	1.5×10^{14}	0.0025	0.0027	445
MI-R	198	2	37.5	37.2	1.1×10^{18}	0.23	0.56	1.6×10^{14}	0.0018	0.0021	475
MI-N	198	2	37.5	37.3	9.7×10^{17}	0.23	0.48	1.3×10^{14}	0.0011	0.0011	405
HP50	225	2	39.2	39.5	1.8×10^{18}	0.20	0.45	1.7×10^{14}	0.0015	0.0013	490
HP40	219	2	38.5	38.7	1.3×10^{18}	0.21	0.48	1.3×10^{14}	0.0012	0.0012	492
Ti_2AlC (Random)	226	8	38.3	38.2	7.1×10^{15}	0.48	0.95	8.8×10^{12}	0.0003	0.0002	445
Mg-SiC	99	18	5.6	5.4	5.2×10^{15}	0.65	1.85	2.2×10^{13}	0.0009	0.0009	280
Mg-312 Random	128	7	15.7	15.5	8.7×10^{16}	0.41	0.77	5.5×10^{13}	0.0007	0.0005	241
Mg-312 Oriented	134	7	16.9	16.6	1.0×10^{17}	0.40	0.71	5.7×10^{13}	0.0007	0.0008	243
Ti_3SiC_2 (Random)	284	10	32.1	31.9	3.4×10^{16}	0.47	0.68	2.8×10^{13}	0.0003	0.0003	417

4.4. Discussion

4.4.1. Kinking Nonlinear Elasticity

The most important result of this work is the exceptional damping capability of the MI-P and HP50 composites (Figure 4.5a). The W_d's of the MI-P and HP50 composites are ~0.6 MJ/m^3, a value that surpasses the previous record of 0.42 MJ/m^3 at 450 MPa reported in Ch. 3 for MI-R composite, by almost 50 % [71]. Note that the MI-P value was achieved at 450 MPa, whereas the HP50 value was achieved at 610 MPa.

When the W_d results of MI-P composite are compared with those of fully dense single-phase Ti_2AlC with comparable grain size, it is evident that the former are higher by at least one order of magnitude. Also when the W_d results of MI-P composite are compared with those of fully dense and 10 vol.% porous Ti_2AlC [57] with significantly larger grains (d_{av}=113±60μm and 2α=14±7μm for the dense sample and d_{av}=133±70 μm and 2α=16±7μm for the porous sample [57]), at ~ 350 MPa, W_d of the composites fabricated herein are larger by at least a factor of ~ 2 and 4, respectively. Note that W_d is a strong function of grain size and that the grains in the previous work [57] were considerably larger than the ones explored herein. Furthermore, as argued elsewhere [88], and confirmed herein, the relationship between Ω/b and grain size is essentially Hall-Petch like (see below).

The response of the Mg-Ti_2AlC composites strongly depended on the orientation of the basal planes relative to the loading direction (Figure 4a-c) in a way that is consistent with a kinking phenomenon. Recall that kinking is a plastic instability and should be greatly enhanced if the basal planes are loaded edge-on, compared to when they are

loaded along the c-axis. It is this simple intuitive conjecture that explains why the W_d's of MI-P samples are roughly double those of the MI-N samples, with those associated with MI-R in between (Figure 4.5a).

The main role of the nc-Mg matrix is to increase the strength of the composite, which in turn greatly enhances W_d, since the latter scales with σ^2 (Eq. 5). The nc-Mg matrix is, *however*, still soft enough to allow the Ti_2AlC grains to kink. Along the same lines, the influence of the Mg-matrix here is somewhat the opposite of the small equiaxed grains in the $Ti_2Al(C_{0.5},N_{0.5})$ solid solutions, wherein the "hard" small grains appear to constrain the majority grains from kinking [88].

The fact that at $\sigma < 420$ MPa, the HP40 porous sample dissipates more energy than the dense HP50 sample on an absolute scale (Figure 4.5a), is in line with previous results [57]. This observation, together with the fact that the MI-P composites produce the largest loops yet, is compelling evidence that what is observed is most likely due to IKBs because, as noted previously [57], it essentially eliminates deformation mechanisms that scale with the volume of the material, and/or depend on shear alone, such as dislocation pileups. Said otherwise, had dislocation pileups been responsible for the loops, the W_d values would have probably been expected to be highest for the random, fully dense, microstructure. This conclusion cannot be overemphasized.

In contrast to Mg-Ti_2AlC samples, the W_d vs. σ^2 plots of the randomly oriented Mg-312 composite and those of the oriented Mg-312 sample (Figure 4.5d) seem to be, within experimental scatter, identical, although the XRD results showed that the Mg-312 sample was highly oriented too. The reason for this state of affairs is not *entirely* clear at

this point but can be related to the equiaxed morphology of the Ti_3SiC_2 grains that are relatively less amenable to kinking as compared to the plate-like grains of Ti_2AlC. This is best manifested by comparing the OM micrographs of Figure 3.11. As shown in Fig 4.5 d, for the Mg-312 and Mg-SiC composites, the linear curves of ε_{NL} vs. σ^2 plots extrapolate back to a finite ε_{NL} at zero applied loads. Apparently, these linear plots fail at low applied stresses in these composite samples, while not in the Mg-Ti_2AlC composites.

The results shown in Table 4.3 are important for several reasons. First, the fact that the values of Ω/b – calculated from Eqs. 5 and 6, and listed in columns 4 and 5 in Table 4.3, respectively – are almost identical in all cases is, as noted above, strong evidence that the micromechanism that is causing the strain nonlinearity is the same as that resulting in W_d. Hence, for example, we can exclude microcracking as a possible mechanism for W_d. Second, at 37.7±0.5 MPa, the Ω/b values obtained here for both the Mg-Ti_2AlC composites, as well as the bulk Ti_2AlC, are quite comparable. This is important because it implies that most of the energy dissipated is occurring in the Ti_2AlC phase. These values are ≈ 50 % larger than those reported previously for Ti_2AlC [57, 88]. The reason(s) for this discrepancy is most probably the differences in grain size. We have recently shown that at least for the $Ti_{n+1}AlX_n$ phases the CRSS follows a Hall-Petch type relationship [88]; this is further corroborated by Figure 4.6 in which Ω/b is plotted as a function of $\frac{1}{\sqrt{2\alpha}}$ for the average of Ω/b values obtained herein from Mg-Ti_2AlC composites and fully dense Ti_2AlC samples. Those of the fully dense and 10 vol. % porous Ti_2AlC [57] are also included. A least squares analysis of the data results in an $R^2 = 0.99$. Note that Ω/b is a function of grain size in Ti_3SiC_2 as well [53].

In contrast to the aforementioned case where the Ti_2AlC phase is responsible for most of the energy dissipated per cycle, the situation for the Mg-312 composites is substantially different. At 16 MPa, the Ω/b value appears to be an average of that of Ti_3SiC_2 (32 MPa obtained here and 30 MPa reported in [88]) and Mg (3 MPa [58, 80]). This suggest that both of the Mg and Ti_3SiC_2 contribute to Ω/b, and hence W_d.

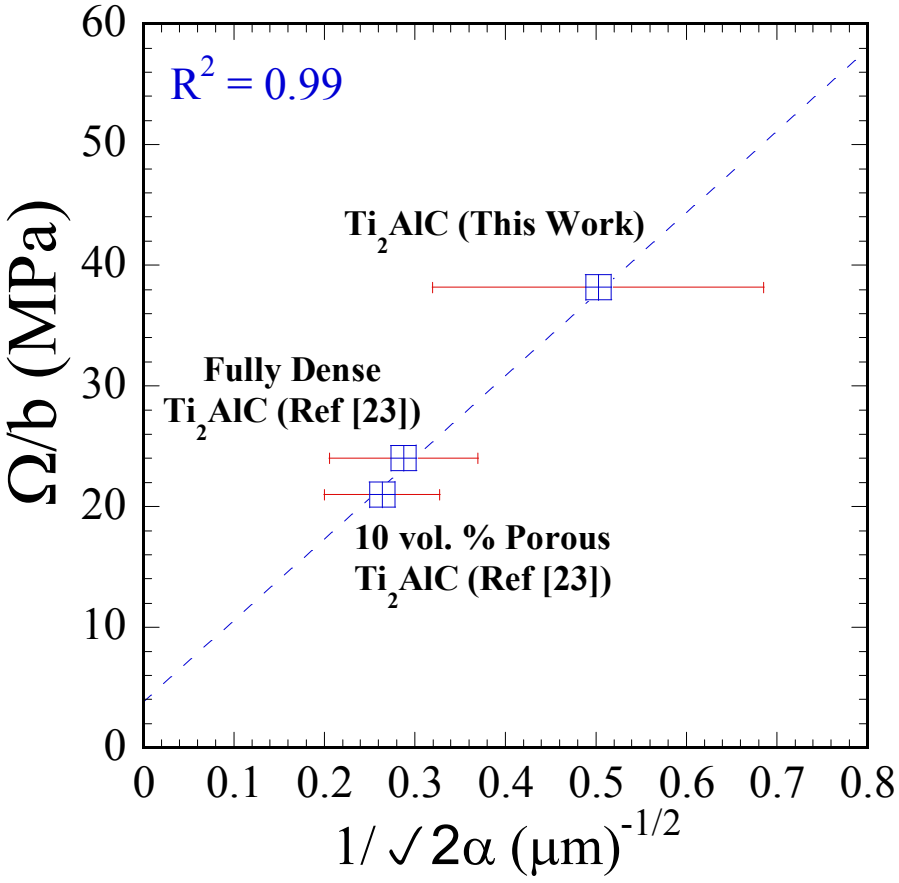

Figure 4-6: Plot of Ω/b as a function of $\frac{1}{\sqrt{2\alpha}}$ for the average Ω/b values obtained herein and those reported in [57] for fully dense and 10 vol. % porous Ti_2AlC.

Indirectly confirming this notion is the fact that Ω/b for Mg-SiC composite (5.5±0.1 MPa) is the lowest value obtained in this work and in good agreement with the 3-4 MPa reported for pure Mg [58, 59]. This implies that SiC does not contribute to the strain

nonlinearities or W_d's observed herein. Note that to obtain the 5.5 MPa value, the last datum point in Figure 4.5f, was not included for reasons discussed elsewhere, but related to the breakdown of our model in Mg at higher strains [58, 59].

To obtain the aforementioned Ω/b values, k_1 was assumed to be 2 in all cases. This result is somewhat surprising, since we expected k_1 to be texture dependent. Why that is the case is not entirely clear, but suggests that if k_1 is a function of texture, that dependence is weak.

At $\approx 1.3\times10^{14}$ to 1.7×10^{14} m^{-2}, the values of ρ_{rev}, at comparable stress levels listed in the last column of Table 4.3 for all Mg-Ti_2AlC composites tested here fall in a very narrow range despite the large differences in size and shape of the original loops from which these values were extracted. Recall that ρ_{rev} is *not* the dislocation density in the sample when the load is removed, but rather the one due solely to the IKBs, i.e. ρ_{rev} given by Eq. 2.8. The values of ρ_{rev} fall in a narrow range despite the fact that: i) the maximum applied stresses vary in some cases by a factor of 2, ii) the N_K values vary by ~ 3 orders of magnitude, and, iii) the variations in σ_t and 2α. The values of ρ_{rev} at the maximum (and comparable) stress levels (last column in Table 4.3) for Mg-SiC and the Mg-312 composites also fall in the narrow range of 1.7×10^{13} to 5.7×10^{13} m^{-2}.

The same is true for Ti_3AlC_2, Ti_2AlC, $Ti_3Al(C_{0.5},N_{0.5})_2$ and $Ti_2Al(C_{0.5},N_{0.5})$ (Table 2.1) where it was shown that despite large variations in the shapes and sizes of the hysteretic loops, ρ_{rev} varied by less than one order of magnitude (1×10^{13} to 9×10^{13} m^{-2}). The same is true for Mg [59] wherein N_k varied by almost 3 orders of magnitude, the *reversible* dislocation density, ρ_{rev}, varied by a factor of 3. Although not clearly

understood at this point, the results of this work, and those of Refs. [59, 88] suggest that a near-constant ρ_{rev} exists to which all systems migrate, regardless of their chemistry and/or microstructure.

Lastly, the choice of the value of w = 5b, needs to be addressed. The minimum value of w is b which cannot be correct since, from Eq. 2.1, results in 2α values in the order of ≈ 20 μm for the Mg-Ti_2AlC composites and ≈ 35 μm in Mg-Ti_3SiC_2 composites that are much larger than the experimentally measured 2α values. Recall, 2α is the thickness of the Ti_2AlC and Ti_3SiC_2 grains along the *c*-axis, which, are estimated to be ~ 5±3μm and ~ 8±2 μm, respectively. On the other extreme, assuming w = 20b, yields 2α values ≈ 1 μm for the Mg-Ti_2AlC composites and ≈ 2 μm in Mg-Ti_3SiC_2 composites, values that are again inconsistent with the OM micrographs. Assuming w = 5b results in 2α values of the *average* Ti_2AlC and Ti_3SiC_2 grains in their composites to be ≈ 3 μm and ≈ 7 μm, respectively, results in values that are in reasonable agreement with experimentally measured 2α values of bulk Ti_2AlC and Ti_3SiC_2 grains mentioned above.

4.4.2. Ultimate Compressive Strength

Typically the addition of soft metallic phases to binary carbides and nitrides decreases the strength of the composites [107]. The UCS of the HP and MI composites were measured to be 800±25 and 700±10, respectively. These values are slightly lower than the 865±55 MPa, of fully dense Ti_2AlC, and are remarkably high for a 50 vol. %, essentially pure, Mg matrix composite. The reason for these extreme values is most likely attributable to the nano-grains of the Mg matrix. This is best evidenced by comparing the UCSs of the Ti_2AlC reinforced composites with those reinforced with SiC or Ti_3SiC_2, in

which case the Mg-grains were *not* in the nanometer scale. At 500±25 and 460±10 MPa, respectively, their UCSs were significantly lower than the Mg-Ti_2AlC composites with comparable volume fractions. These values were also less than *half* the strengths of bulk Ti_3SiC_2 (Figure 4.2). Said otherwise, when the Mg-matrix grains were *not* in the nanometer scale, the UCS values obtained were significantly lower than those obtained from their monolithic binary or ternary carbide counterparts.

The UCS values achieved here – e.g. in the HP composites – by the addition of 50 vol. % commercially pure Mg to Ti_2AlC – are , as far as we are aware, the highest ever reported for a pure Mg-matrix composite with 50 vol.% Mg. The lower UCS of the HP40 composite compared to fully dense HP50 is due to the porosity in the former. It is important to note that despite the non-linear IKB induced strains and also the permanent plastic strains (Figure 4.3 b and c) observed, the samples failed by shear banding at 45° to the loading axis. Given the limited number of slip systems in Mg, Ti_2AlC and Ti_3SiC_2 and the high UCS, this is not too surprising. These findings are consistent with those reported elsewhere in other Mg-matrix composites reinforced with *large* reinforcement particles [133, 134]. Interestingly, when sub-micron ceramic particles such as nano-Al_2O_3 [135-137] and nanosized Y_2O_3 particulates [138, 139] are used, the fracture behavior of the Mg matrix changed from brittle to ductile. It would be therefore worthwhile to try and make and test composites in which both the Mg-matrix *and* the reinforcing phases are both at the nanoscale.

4.4.3. Offset Yield Strength

As shown in the monotonic stress-strain plots to the point of fracture in HP50 and MI50 samples (Figures 4.3 b and c), the 0.2% offset yield strength (Y_S) of HP50 and MI50 composites were measured to be ~ 690 and 490 MPa, respectively. The irreversible permanent plastic strains were also measured to be ~ 2.2 and 4.6%, respectively. The reason for these differences between the two microstructures can, most likely, be attributed to the finer grain size of the nanocrystalline Mg matrix in the HP50 sample. These results are directly corroborated by the microhardness results shown below (see section 4.4.5).

4.4.4. Effective Young's Moduli

As shown in Table 4.1, $\overline{E}$ is a function of kinking and depends on the size and extent of the hysteresis stress-strain curves. The MI-N composites exhibited slightly higher $\overline{E}$ values compared to MI-P. The $\overline{E}$'s of the Mg-Ti_3SiC_2 composites seem to be close to the Mg-Ti_2AlC ones, despite the fact that Ti_3SiC_2 is slightly stiffer than Ti_2AlC (~ 343 vs. 277 GPa reported in Ref. [140], respectively). The fact that $\overline{E}$ in their corresponding composites is most likely due to the lack of kinking of the Mg nanograins in the Mg-Ti_2AlC system and their kinking in the Mg-312 composites. The Mg-SiC composite, on the other hand, exhibited the largest $\overline{E}$ values believed to be due to the higher modulus of elasticity of SiC (~ 475 GPa [132]) and the small size of the stress-strain loops associated with Mg-SiC composite (Figures 4.4d and 4.5d).

With the exception of MI-P sample, the average $\overline{E}$ values for Mg-Ti_2AlC, Mg-Ti_3SiC_2 and Mg-SiC composites (listed in Table 4.1 and shown in Figure 3.19), within

experimental scatter, fall in between the rule of mixtures' upper and lower bounds given by $E_c(u) = E_m V_m + E_p V_p$ and $E_c(l) = E_m E_p / (V_m E_p + V_p E_m)$, respectively [141], wherein $E_c(u)$ and $E_c(l)$ are the composites' moduli obtained from upper and lower bounds; E_m, E_P, V_m and V_P are the moduli and volume fractions of the Mg matrix and reinforcement particles, respectively. It follows that, G and ν of the Mg-Ti_2AlC, Mg-Ti_3SiC_2 and Mg-SiC composites are assumed to be ~ the averages of rule-of-mixtures' lower and upper bounds [141] of the corresponding composites. All values are listed in Table 4.1. The G and ν values of Ti_2AlC [57], Ti_3SiC_2 [88], SiC [132], and Mg [58] are *118* GPa and *0.2*, *144* GPa and *0.2*, *192* and *0.142*, and *19* GPa and *0.35*, respectively.

4.4.5. Vickers Microhardness, V_H

At 2.0±0.1 and 1.5±0.1 GPa, the V_H obtained herein for HP and MI composites are again remarkably high for a 50 vol.% Mg composite. The hardness enhancement in the HP sample compared to its MI counterpart can be attributed to the smaller nc-Mg matrix in the former. This is also directly corroborated by the higher Y_S and lower permanent plastic strains measured for the HP sample.

The MI-N orientation is also ~ 25 % harder than its counterpart, MI-P. Since both samples were obtained from the same billet, it is fair to conclude that the orientation of the basal planes is responsible for the difference. Image analysis of the MI-P and MI-N indented surfaces, showed that the area covered by the "harder" Ti_2AlC grains was ≈ 7±1% larger in the former than the latter. This probably, partially, explains the differences in hardness.

This is true despite the results of Kooi *et al.* [142] who showed, using a nanoindenter and orientation image microscopy, that the Berkovich hardness was lower in Ti_3SiC_2 grains that were indented perpendicular to the basal planes, i.e. when loaded along the c-direction. Kooi *et al.* performed their nano-indentations on individual Ti_3SiC_2 grains with their basal planes either oriented parallel or perpendicular to the surface. The results reported here are for Mg-Ti_2AlC composites, where the Mg-grains are responsible for most of the deformation strain, which is presumably why the volume fraction of Mg is more important than the orientation of the Ti_2AlC grains.

The V_H values of the nc Mg-Ti_2AlC composites tested herein are comparable to those of Mg-matrix composites in which the reinforcing phase is significantly harder. For example, at 2.0±0.1 GPa our HP50 results are comparable to those of the Mg-SiC samples tested here (Figure 4.1), or Mg-TiC composites, with 56 vol. % TiC, reported by Contreras *et al.* [127]. This value is also higher than, i) the Mg-312 samples (Figure 4.1) tested here, ii) > ~ 1.1 GPa values reported in Mg-TiC composites fabricated by powder metallurgy [143], iii) the ~ 1 GPa values reported for Mg-alloy matrix composites reinforced with TiC [144]. In all cases, the large hardness differences between SiC (V_H ~ 28 GPa [132]), TiC (V_H ~ 35 GPa [132, 145]) and Ti_3SiC_2 (steady state V_H = 4.0±1.0 GPa) [21], on the one hand, and Ti_2AlC (steady state V_H = 3.0±0.1 GPa), on the other, is compensated by the nano-crystalline nature of the Mg-matrix in the Mg-Ti_2AlC composites.

Like most MAX phases [27, 28, 146], the hardness values of monolithic Ti_2AlC are initially high, decrease with increasing load, and then asymptote at higher loads Figure 4.1. Interestingly, the composites' hardness values are not a function of load and fall in

between those of pure Mg and monolithic Ti_2AlC. Like the vast majority of MAX phases [17, 28, 146], no cracks are observed to emanate from the corners of the Vickers indentations of the composite samples. This damage tolerance is a hallmark of the MAX phases and results from the activation of basal slip which allows the material to absorb energy locally by various energy absorbing mechanisms such as microcracking, delamination, grain buckling and grain pull-out [17, 28]. The plastic deformation of the Mg matrix must also play an important role. The desirability of such high damage tolerance in potential applications cannot be overemphasized.

4.5. Summary and Conclusions

The MAXMETs fabricated herein are all KNE solids characterized by the formation of fully reversible hysteretic stress-strain loops under uniaxial cyclic compression. The microscale model developed to analyze and explain kinking nonlinear elasticity in KNE solids is in excellent agreement with the experimental results obtained in the composites and their monolithic counterparts. The results obtained here are important when designing solids with ultrahigh damping capabilities at high stresses and decent elastic moduli. Depending on the application, and the stress levels required during service, different MAX-Mg composites can be used. For relatively high stress applications, the basal planes of the MAX phases should be loaded edge-on to yield the highest W_d values.

The Ω/b values obtained from the model are a function of their constituents and whether or not they kink. Because for the Mg-Ti_2AlC composites, the Ω/b values are almost identical to those of bulk Ti_2AlC, it is reasonable to assume that the latter is doing most of the kinking. In contradistinction, because the Mg matrix of the Mg-312

composites are *not* at the nanoscale and are thus more prone to kinking, the Ω/b values obtained are considerably less than those of the Mg-Ti_2AlC system, and seem to be the average of the Ω/b values of Mg and Ti_3SiC_2. The Mg-SiC, in which only the Mg matrix is presumably *kinking*, showed the lowest Ω/b values that are in line with those of pure Mg.

The ρ_{rev} values calculated herein, and in several other materials, fall in a narrow range, suggesting that an equilibrium state, to which all the systems migrate, exists.

Despite a 50 vol.% loading of essentially pure Mg, the highest UCS and V_H values of the composites fabricated here were 800±25 MPa and 2.0±0.1 GPa. These extreme values are related to the nano-size of the Mg grains. The fact that these composites are also readily fabricated by MI, machinable, light-weight and stiff, as well as highly damping, should render them useful materials for a host of applications.

Chapter 5 : On the Effect of Texture on the Mechanical Properties of MAX Phases

5.1. Introduction

We reported in Ch. 4 on the effect of texture on kinking nonlinear elasticity, damping capability and Vickers microhardness of nanocrystalline (nc) Mg-matrix composites reinforced with 50 vol. % Ti_2AlC.

In all composites, and despite very different loop shapes and sizes, the critical resolved shear stresses of basal plane dislocations in Ti_2AlC, calculated from the model fell in the narrow range of 37.7±0.5 MPa. The same was true for the reversible dislocation density that fell in the quite narrow range of $1.1\pm0.3\times10^{14}$ m^{-2}, suggesting the presence of an equilibrium state to which all the systems migrate.

Because kinking is a form of plastic instability, it was hypothesized that orienting the Ti_2AlC grains, prior to infiltration, with their basal planes parallel to the loading direction should lead to exceptionally high values of W_d. Indeed, at 450 MPa, W_d of a composite with this texture was found to be ≈ 0.6 MJ/m^3, the highest ever reported for a crystalline solid due to the formation and annihilation of IKBs. The main role of the nc-Mg matrix was to enhance the ultimate compressive and tensile stresses of the composites. At 700±10 and 380±20 MPa, the ultimate compressive and tensile strengths of the composites were higher than any reported in the literature for pure Mg matrices.

The presence of a relatively "*softer*", but nc-Mg phase, in between Ti_2AlC grains allowed the latter "*room*" to kink. In that situation, the influence of nc-Mg grains was the

opposite of the small equiaxed grains in $Ti_2Al(C_{0.5},N_{0.5})$ solid solutions, [45] wherein the "*hard*" small grains constrained the larger grains from kinking.

Because the MAX phases are layered hexagonal solids that deform by kinking, it was postulated that the response of *monolithic* MAX phases to cyclic loadings, similar to Mg-Ti_2AlC composites, should depend on the orientation of the basal planes relative to the loading direction. Thus, the objectives of this chapter are threefold: First, to report on the mechanical response of single phase Ti_2AlC samples to cyclic compressive loads as a function of texture. The results are then compared to those of the Ti_2AlC reinforced nc-Mg matrix composites alluded to above. The second is to report on in-situ neutron diffraction results obtained while the samples were cyclically loaded. The third objective is to apply the KNE model to analyze the compressive cyclic stress-strain curves.

5.2. Experimental Details

The starting powder of Ti_2AlC (-325 mesh, 3-ONE-2, Voorhees, NJ) was poured and wrapped in graphite foil, placed in a graphite die and hot pressed in a graphite-heated vacuum-atmosphere hot press, HP, (Series 3600, Centorr Vacuum Industries, Somerville, MA), heated at 10°C/min to 1400°C and held at that temperature for 2 h, after which the HP was turned off and the samples were furnace cooled. A load, corresponding to a stress of ~ 45 MPa, was applied when the temperature reached 500°C and maintained thereafter. The samples were removed from the dies and the graphite foil was removed. Two samples were fabricated, random and oriented. The former were made by simply pouring, and hot pressing the Ti_2AlC powder into the graphite die. To fabricate the latter, the Ti_2AlC powder was first poured into the die and manually vibrated for ~ 15 minutes

in an attempt to orient the flaky Ti_2AlC powders perpendicular to the pressing direction. We note in passing that one reason for the ease by which these powders can be aligned is their flake-like nature.

The samples were further annealed for 12 h at 1450 °C under an Ar atmosphere in a tube furnace in order to increase their grain size. The Mg-Ti_2AlC composites samples were fabricated using MI fully described in Ch. 4.

The samples' microstructures were observed in a field emission SEM. Samples were also cross-sectioned, mounted and polished with a diamond solution down to 1 μm and etched for ~ 10 s with a 2:1:1 (volume) H_2O:HNO_3:HF etchant solution and their microstructures were then observed with an optical microscope.

Cylinders for compression tests *parallel* and *normal* to the pressing direction were EDMed from the bulk of the fine grain (FG) and coarse grain (CG) oriented samples. Under compression, the basal planes in the former are *normal* to the loading direction, which is why these samples are referred to as "FG-N" and "CG-N". When the basal planes are *parallel* to the loading direction, the samples are referred to as "FG-P" and "CG-P". The *randomly* oriented samples will be referred to as "FG-R" and "CG-R". For clarity's sake, in the stress-strain figures, a small schematic of the relationship of the basal planes to the applied load is shown as an inset.

The room temperature ultimate compressive stresses, UCS, were measured on FG and CG samples using a hydraulic testing machine (MTS 810, Minneapolis, MN) on small 4×4×4 mm^3 EDMed cubes. Ten samples were tested in each case.

EDMed cylinders 9.7 *mm* in diameter and 31 *mm* in height were used to measure the Young's moduli in compression and to carry out the cyclic uniaxial compression tests. In all cases, the strains were measured by a capacitance extensometer (MTS, Minneapolis, MN) – attached to the samples – with a range of 1 % strain. All the loading-unloading compression tests were performed in load-control mode at a loading-unloading rate of 15 MPa/s, respectively, which corresponds to a strain rate of $\approx 2\times10^{-4}$ s^{-1}.

To better understand the deformation of the bulk samples, they were subjected to neutron diffraction as they were loaded. CG-N and CG-P samples, was placed in the neutron beam and compressed in the spectrometer for materials research at temperature and stress (SMARTS) to various loads and unloaded, while diffraction patterns were taken. For more details refer to any of the followings Refs. [147-151]. The compression direction was either along the basal planes in the case of CG-P sample and along the c-axis for the CG-N sample. The texture of the samples was measured using neutron diffraction in the high-pressure preferred orientation neutron diffractometer (HIPPO). For more details see for e.g. Ref. [147].

5.3. Results

OM and SEM micrographs of polished and fractured surfaces of FG (Figures5.1a and c) and CG (Figures 5.1 b and d) samples, respectively, clearly indicate the difference in their grain size. At 30±10 μm in diameter and 5±3 μm in thickness, the FG Ti_2AlC grains are plate-like. Annealing at 1450°C for 12 h increased the average grain diameter to 60±40 μm and its thickness to 25±10 μm (Figures 5.1b and d). Arrows in Figures 5.1c and d point to the widths of the average grains along the c-axis, viz. 2α.

Figure 5.1e shows SEM micrograph of multiple kink bands with very sharp radii of curvature in individual grains observed on the fractured surfaces of a CG sample. Figure 5.1f exemplifies the extraordinary extent by which some grains can contort and bend without fracture. Based on these SEM micrographs, and the evidence presented below, it is not unreasonable to assume that these permanent kink bands were preceded by IKBs.

The room temperature UCS of the FG and CG Ti_2AlC samples tested herein were measured to be 1.0±0.1 GPa and 640±50 MPa, respectively.

As discussed in detail in Chs. 3, the ratios of XRD peak intensities of the (002) basal planes to the (103) planes were obtained from the XRD spectra of the corresponding starting powder, XRD card [119] and the oriented preforms prior to hot pressing. The ratio in the preforms was several multiples of what it was in the as-received powders or according to the XRD card [119] due to the flake-like nature of the starting Ti_2AlC powder [72, 118]. Note that the XRD results mentioned above are those obtained from the preforms instead of the hot-pressed samples because the latter may not reflect the true information pertaining to the texture, due to the sensitivity of the XRD results to the angle at which the hot-pressed samples were cross-sectioned and prepared. Therefore, we only report the XRD results obtained from the virgin preforms.

Similar to all other MAX phases [12, 27, 28], the random and oriented Ti_2AlC samples and Mg-Ti_2AlC composites [71, 72] are readily machinable even with a manual hack-saw, with no lubrication or cooling. They are also readily EDMed.

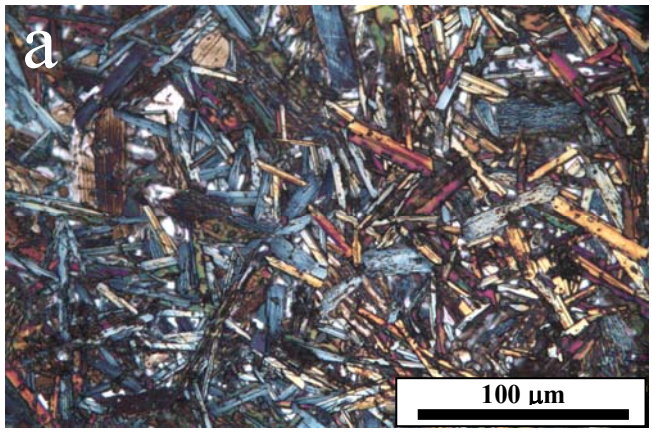
a
100 μm

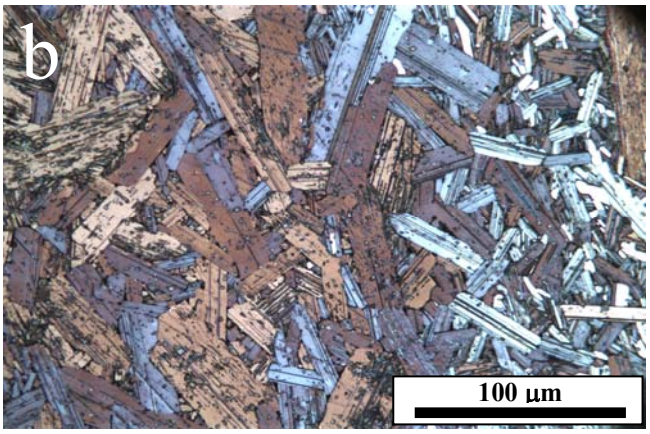
b
100 μm

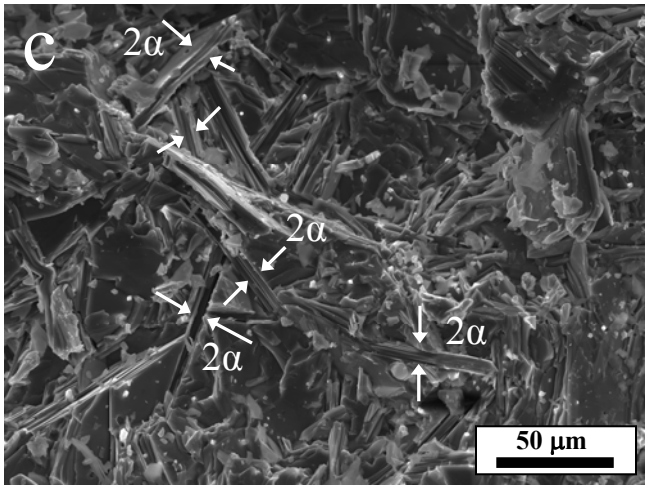
c
2α
2α
2α
2α
50 μm

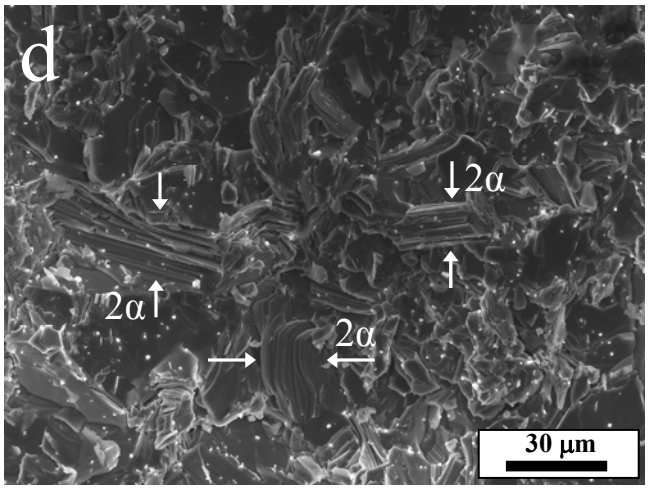
d
2α
2α
2α
30 μm

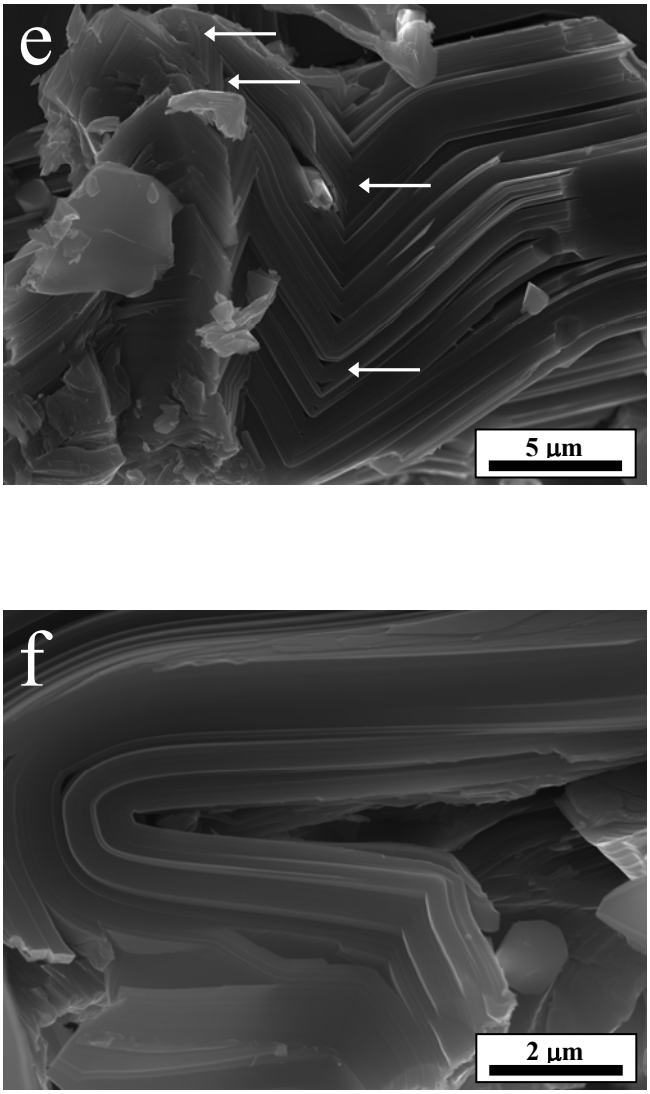

Figure 5-1: Optical micrographs of polished and etched surfaces of, a) FG and b) CG Ti_2AlC; Secondary electron SEM image of fractured surface of, c) FG and, d) CG Ti_2AlC. Note arrows showing the thickness of the grains along their *c*-axis (2α); Secondary electron SEM image of the fractured surface of CG sample showing, e) the formation of multiple kink bands with very sharp radii of curvature; f) extent of contortion in a single Ti_2AlC grain without fracture, which is a characteristic of the MAX phases.

For the cyclic compression tests, typically five cycles were obtained at each load. For the most part, the first cycles were very slightly open, registering a plastic strain of the order of ~ 0.01 % in the Ti_2AlC samples and 0.05 % in the Mg-Ti_2AlC samples [72]. However, all subsequent cycles, to the same stress, for both set of samples were closed and exceptionally reproducible, which is why in Figure 5.2 only one loop (typically the last cycle) at any given stress is plotted. Typical stress-strain loops at various stresses for the FG-P (Figure 5.2a), FG-N (Figure 5.2b), CG-P (Figure 5.3a), and CG-N (Figure 5.3b) – loaded to roughly ~ 75% of their UCS – at different stresses are all fully closed.

Figure 5.4 compares typical loops for the single phase Ti_2AlC and Mg-Ti_2AlC composites [72] at similar stress levels. For reasons that are not entirely clear, the stress-strain loops of the CG-R sample were different than all the others. This anomalous shape renders the nonlinear strain calculations nontrivial. More importantly, unlike the oriented samples that were EDMed from the *same* billet, the random sample was fabricated in a separate hot-press run. Therefore, and with the exception of the W_d calculations, we will *not* include this sample in the discussion of Taylor factor (M).

Defining a Young's modulus for loops such as those shown in Figures 5.2 to 5.4 is somewhat problematic. However, to obtain an approximate "effective" Young's modulus, $\overline{E}$, least squares fits of the entire data set that resulted in diagonal lines bisecting the loops were carried out at each stress level and the corresponding $\overline{E}$ for each loop is shown in Figures 5.2 and 3. The average of these results, are summarized in Table 5.1. For both FG and CG microstructures, the samples in which the basal planes are parallel to the loading direction are effectively stiffer than the ones in which the basal planes are normal to the loading direction.

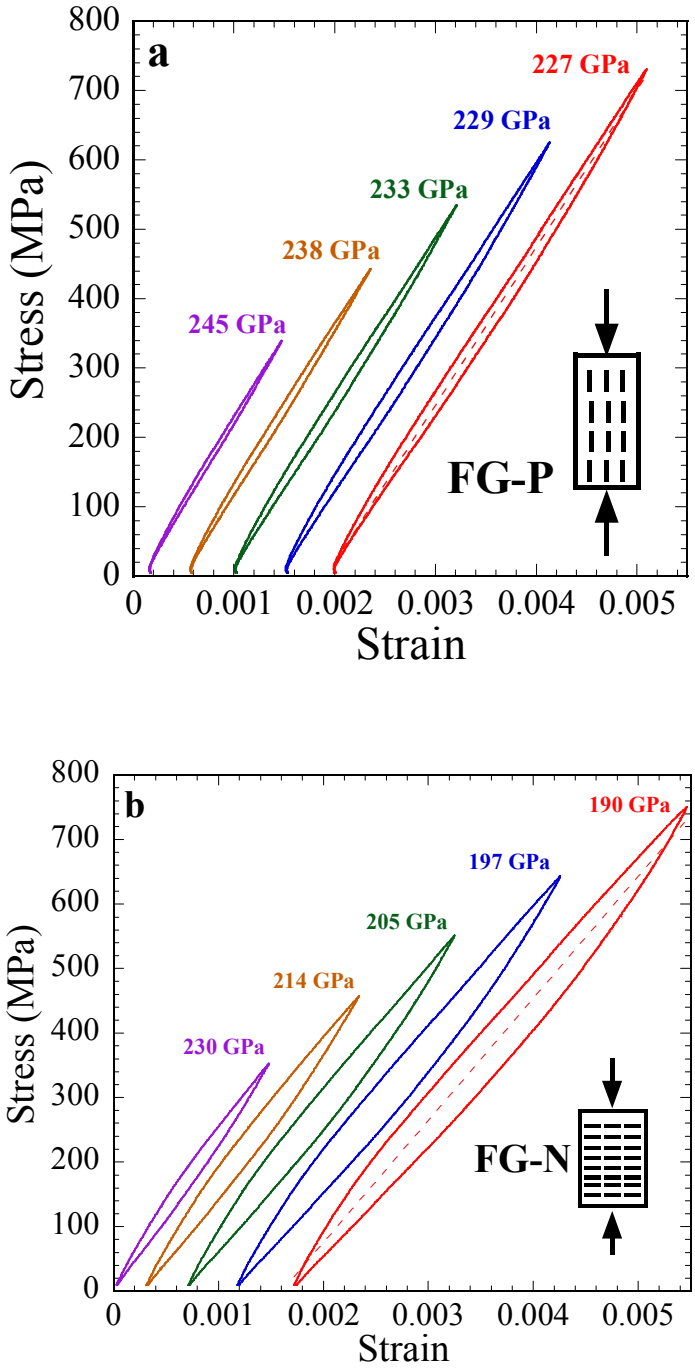

Figure 5-2: Typical compressive stress-strain curves of, a) FG-P and, b) FG-N; only one cycle (last) per load is shown and the curves are shifted horizontally for clarity.

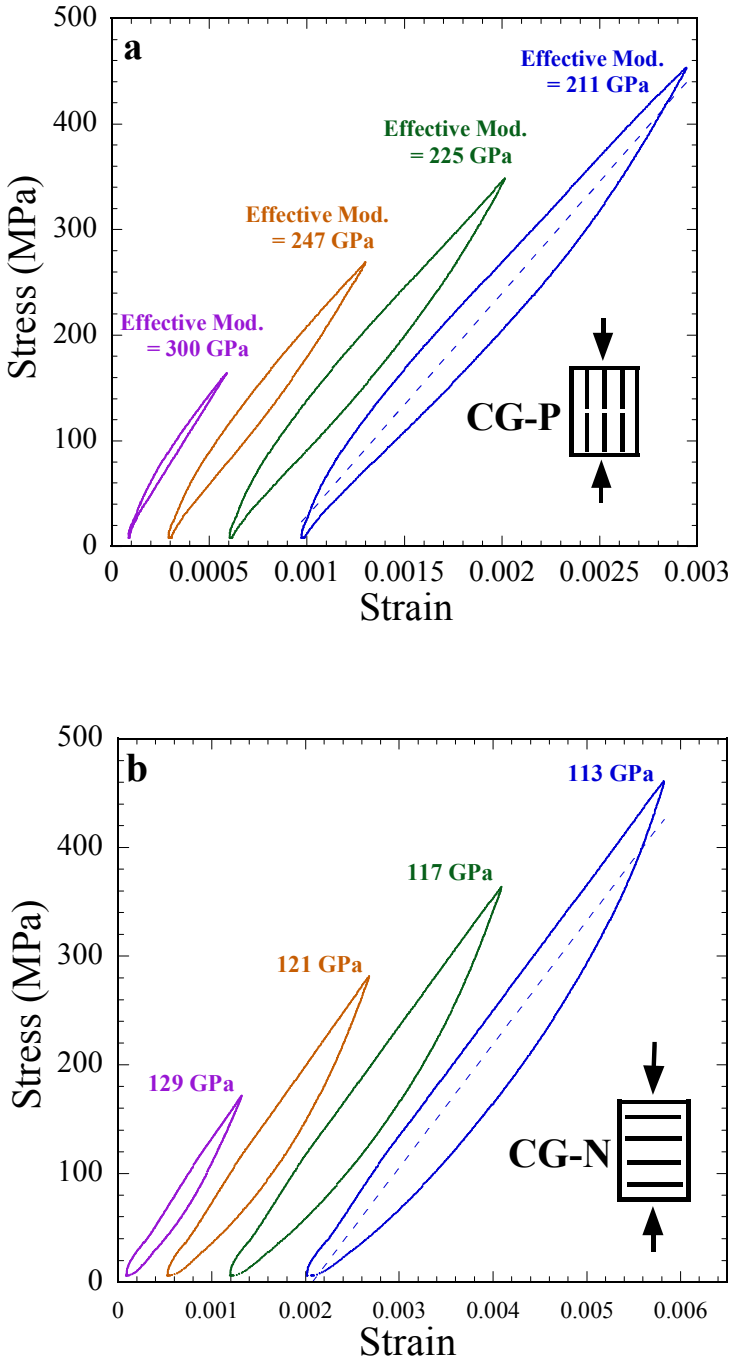

Figure 5-3: Typical compressive stress-strain curves of, a) CG-P and, b) CG-N; only one cycle (last) per load is shown and the curves are shifted horizontally for clarity.

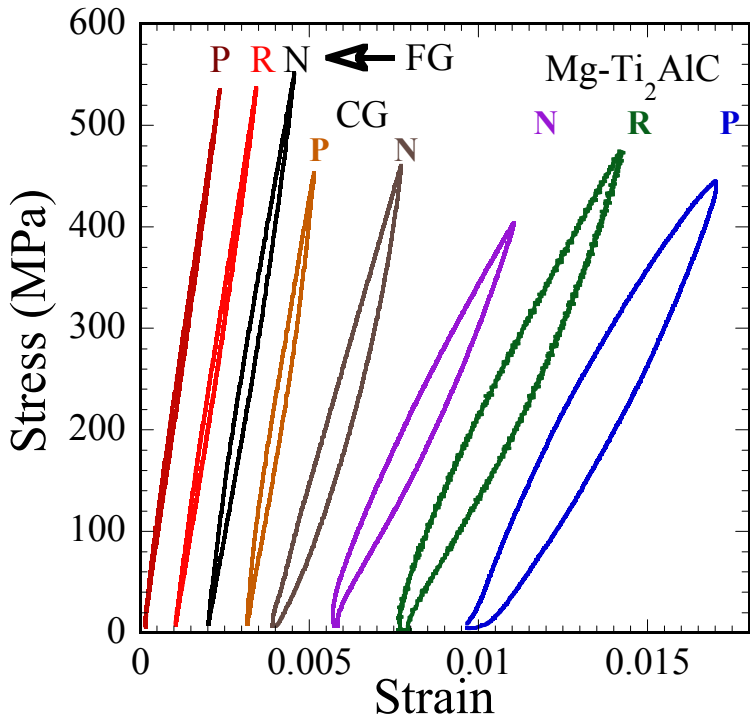

Figure 5-4: Comparison of stress-strain loops for FG and CG Ti_2AlC samples and those of random and oriented Mg-Ti_2AlC composites at comparable stress levels, for the sake of comparison. The latter are much larger than the former. All loops are shifted horizontally for clarity.

Table 5.1 lists the G and ν values, as well as, the elastic constants c_{11} and c_{33} values for Ti_2AlC, reported by Wang *et al.* [152]. Not surprisingly, the presence of ~ 50 vol. % Mg in the composite sample reduces $\overline{E}$ as compared to the non-Mg containing samples.

The values σ, ε_{NL} and W_d obtained from the corresponding hysteretic stress-strain curves (Figures 5.2 and 3) - are listed in Table 5.2. Also listed in Table 5.2 are m_1, m_2, their ratio, and $3k_1\Omega/b$ values directly obtained from the slopes of W_d vs. ε_{NL} plots (Figure 5.5a). According to our model, plots of W_d vs. σ^2, ε_{NL} vs. σ^2 and W_d vs. ε_{NL}

should yield straight lines, as observed in Figures 5.5a-c. The lowest correlation coefficient, R^2, obtained from least squares analysis of the results was > 0.97.

Table 5-1: Effective Young's moduli, $\overline{E}$, G and ν for FG-P, FG-R, FG-N, CG-P and CG-N samples tested herein and those of Mg-Ti_2AlC (P), Mg-Ti_2AlC (R) and Mg-Ti_2AlC (N) samples. Also included are the C_{11} and C_{33} values of Ti_2AlC reported by Wang *et al.* [152].

Material→ ↓ *Physical Constants*	FG-P	FG-R	FG-N
$\overline{E}$ (GPa), G (GPa), ν	235±8, 118 [57], 0.2 [57]	218±6, 118, 0.2	207±15, 118, 0.2
Material→ ↓ *Physical Constants*	CG-P	CG-R	CG-N
$\overline{E}$ (GPa), G (GPa), ν	245±40, 118, 0.2	-	120±7, 118, 0.2
Material→ ↓ *Physical Constants*	Mg-Ti_2AlC (P)	Mg-Ti_2AlC (R)	Mg-Ti_2AlC (N)
$\overline{E}$ (GPa), G (GPa), ν	69±10, 51 [72], 0.26 [72]	72±6, 51, 0.26	74±3, 51, 0.26
Material→ ↓ *Physical Constants*	Ti_2AlC (C_{11})	Ti_2AlC (C_{33})	
c_{ij} (GPa)	308 [152]	270 [152]	

Table 5.3 lists the calculated Taylor factor (M) and σ_t values obtained from the W_d vs. σ^2 plots (Figure 5.5a) and 2α values calculated from the σ_t values given in column 2 using Eq. 2.2. Also listed are the experimentally measured 2α values from the various micrographs and the calculated values of Ω/b obtained from Eqs. 2.4 & 2.5 and 2.6 (columns 4 and 5, respectively), N_k and $2\beta_{av,c}$. The $2\beta_{av}$ and ρ_{rev} values at the stress levels listed in the last column are also included; note that for all cases, b = 3.0 Å, w = 5b, k_1 = 2. Also listed are the ε_{IKB} values calculated from the third term of Eq. 2.5 for the sake of comparison with those measured directly by the extensometer, ε_{NL}.

Table 5-2: List of measured stress (σ), nonlinear strain (ε_{NL}), and dissipated energy (W_d) for FG-P, FG-R, FG-N, CG-P and CG-N samples tested herein. Also listed are the m_1, m_2 and their ratio and $3k_1\Omega/b$ values obtained from the slopes of ε_{NL} vs. σ^2, W_d vs. σ^2 and W_d vs. ε_{NL} plots. Also in column 5, ε_{IKB} values calculated from the third term of Eq. 2.5 for the sake of comparison with those measured directly by the extensometer (ε_{NL}) are listed.

	σ MPa	W_d MJ/m^3	ε_{NL}	ε_{IKB}	m_1 (MPa)$^{-2}$	m_2 (MPa)$^{-1}$	m_2/m_1 (MPa)	$3k_1\Omega/b$ (MPa)
FG-N	352	0.0337	0.0003	0.0002	2.2×10^{-9}	4.7×10^{-7}	215	215
	458	0.0737	0.0005	0.0004				
	551	0.1148	0.0007	0.0006				
	643	0.1670	0.0009	0.0008				
	750	0.2506	0.0013	0.0011				
FG-R	342	0.0166	0.0002	0.0001	1.0×10^{-9}	2.4×10^{-7}	230	229
	445	0.0359	0.0003	0.0002				
	537	0.0557	0.0004	0.0002				
	628	0.0794	0.0005	0.0004				
	733	0.1181	0.0006	0.0005				
FG-P	340	0.0078	8×10^{-5}	3×10^{-5}	7.6×10^{-10}	1.8×10^{-7}	229	229
	443	0.0214	0.0002	0.0001				
	535	0.0367	0.0002	0.0002				
	626	0.0553	0.0003	0.0002				
	731	0.0812	0.0004	0.0004				
CG-P	165	0.0044	0.0002	2×10^{-5}	3.6×10^{-9}	5.2×10^{-7}	145	145
	270	0.0256	0.0004	0.0002				
	348	0.0511	0.0005	0.0004				
	453	0.097	0.0008	0.0007				
CG-N	172	0.0263	0.0004	0.0002	8.0×10^{-9}	1.2×10^{-6}	146	146
	282	0.0843	0.0009	0.0006				
	364	0.1485	0.0013	0.0010				
	460	0.2413	0.0019	0.0017				

Table 5-3: List of the experimentally measured M and the σ_t values obtained from the W_d vs. σ^2 plots and 2α values calculated from the σ_t values given in column 2 using Eq. 2.2. Also listed are the experimentally measured 2α values and calculated values of Ω/b obtained from Eqs. 2.5 & 2.6 and 2.7 (columns 4 and 5, respectively), N_k and $2\beta_{av,c}$. The $2\beta_{av}$ and ρ_{rev} values at the stress levels listed in the last column are also included. For all cases, b = 3.0 Å, $w = 5b$, $k_1 = 2$. The result of Ti_2AlC sample from previous work [45] is included for the sake of comparison.

	M	σ_t (MPa)	2α (μm)	$2\alpha_{exp}$ (μm)	Ω/b (MPa) Eq. 2.6	Ω/b (MPa) Eq. 2.7	N_k (m^{-3})	$2\beta_{av,c}$ (μm)	$2\beta_{av}$ (μm)	ρ_{rev} (m^{-2})	σ (MPa)
FG-N	2.0	214	5	5±3	35.8	35.8	5.7×10^{16}	0.34	0.72	2.6×10^{13}	458
FG-P	2.5	272	5	5±3	38.2	38.2	3.2×10^{16}	0.34	0.55	1.1×10^{13}	443
CG-N	1.8	87	25	24±10	24.3	24.3	1.4×10^{15}	0.75	3.98	1.7×10^{13}	460
CG-P	3.0	147	25	24±10	24.2	24.2	1.7×10^{15}	0.75	2.32	1.3×10^{13}	453
Ti_2AlC [45]	3.0	170	20	-	24	24	7.3×10^{15}	1.10	2.40	4.2×10^{13}	336

The neutron diffraction strains along the *a* and *c*-directions of the *majority* and *minority* grains for both the CG-N and CG-P samples are shown in Figures 5.6a and b. This was done by measuring the *longitudinal* (i.e. in the loading direction) and *transverse* (i.e. normal to the loading direction) lattice parameter shifts. These results are denoted by *a* and *c* strains of the *majority* and *minority* grains on Figures 5.6a and b, respectively, and are plotted with the macroscopic stress-strain plots obtained simultaneously using an extensometer (open triangles in Figure 5.6). Based on the results of Figure 5.6 it is obvious that:

1) In case of the CG-N sample, (Figure 5.6a) the *a*-strain of the *majority* grains behaves more or less in a linear fashion. The compressive loads applied normal to the basal plane of the *majority* grains result in lattice expansion along the *a*-direction. On the other hand, the *c*-strain of the *majority* grains seems to be behaving also, more or less

elastically, although a small hysteresis is observed. This result is not surprising because compressive loads on the *majority* grains cause lattice contraction along the *c*-direction. Similarly, the *a*-strain of the *minority* grains, is also behaving relatively linearly elastic, and without noticeable hysteresis. In contradistinction, the *c*-strain of the *minority* grains exhibited evident hysteresis.

2) In case of the CG-P sample, (Figure 5.6b) the *a*-strain of the *majority* grains appears to behave in a linear elastic fashion. No hysteresis is observed. Similarly, the *c*-strain of the *majority* grains behaves in a linear elastic manner. The strain is negative because of Poisson's effect. The *a*-strain of the *minority* grains also appears to behave in a linear elastic fashion. Again, and similar to CG-N sample, the *c*-strain of the *minority* grains exhibited evident hysteresis.

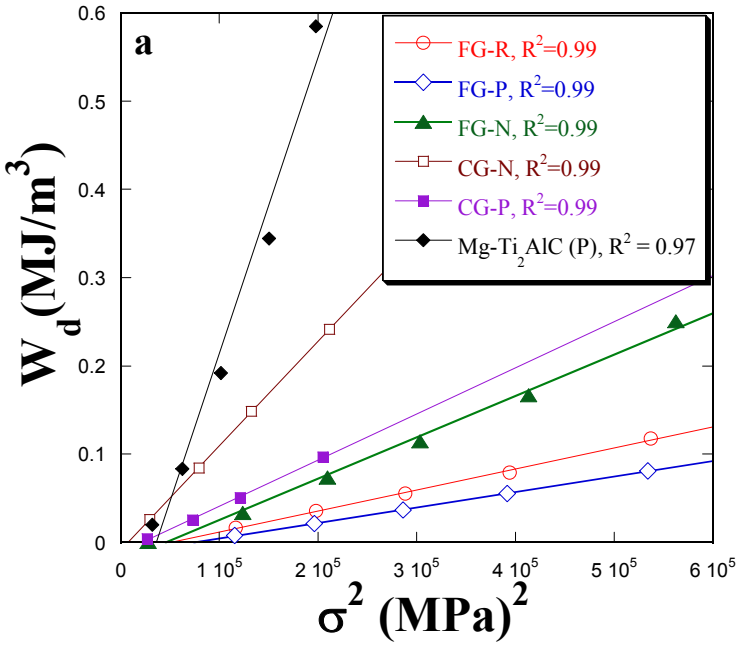

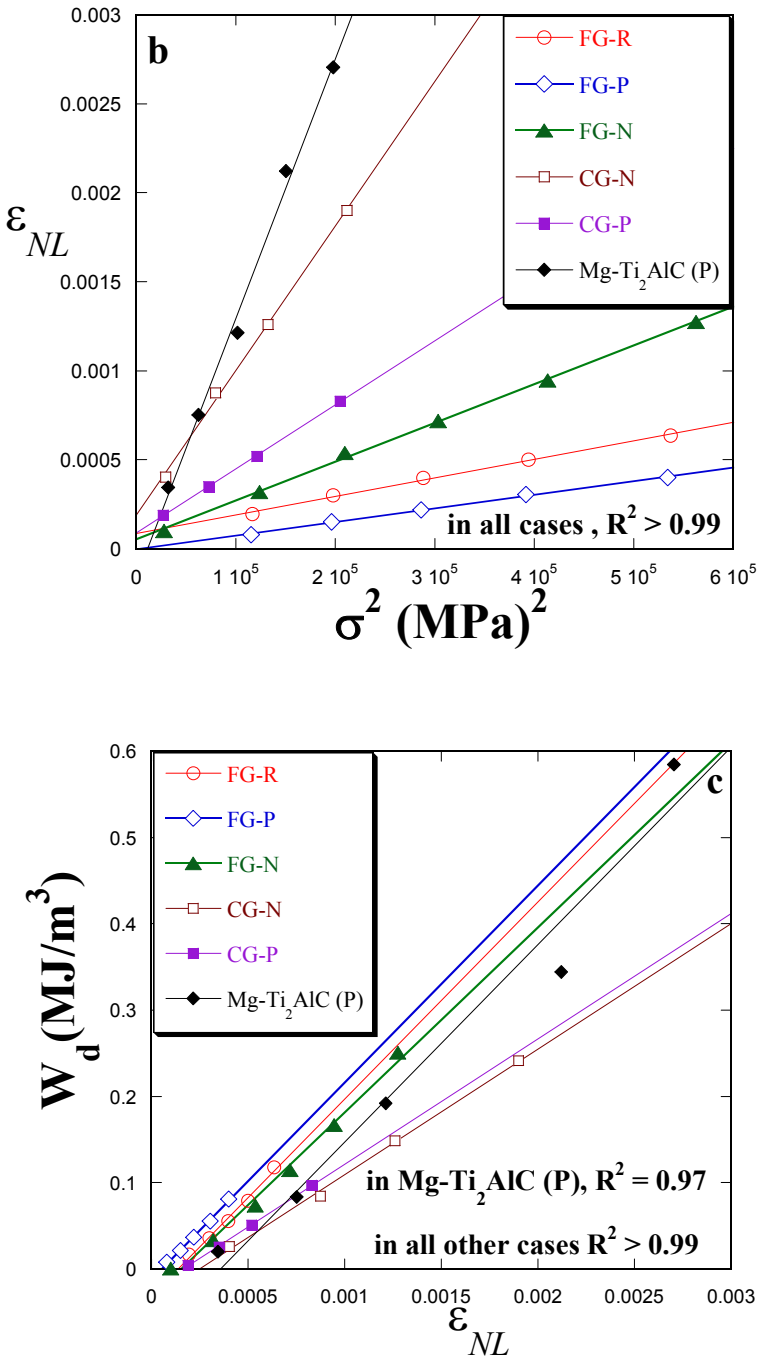

Figure 5-5: Plots of, a) W_d vs. σ^2, b) ε_{NL} vs. σ^2, and c) W_d vs. ε_{NL} for all FG and CG Ti_2AlC samples and Mg-Ti_2AlC (P) composite for the sake of comparison.

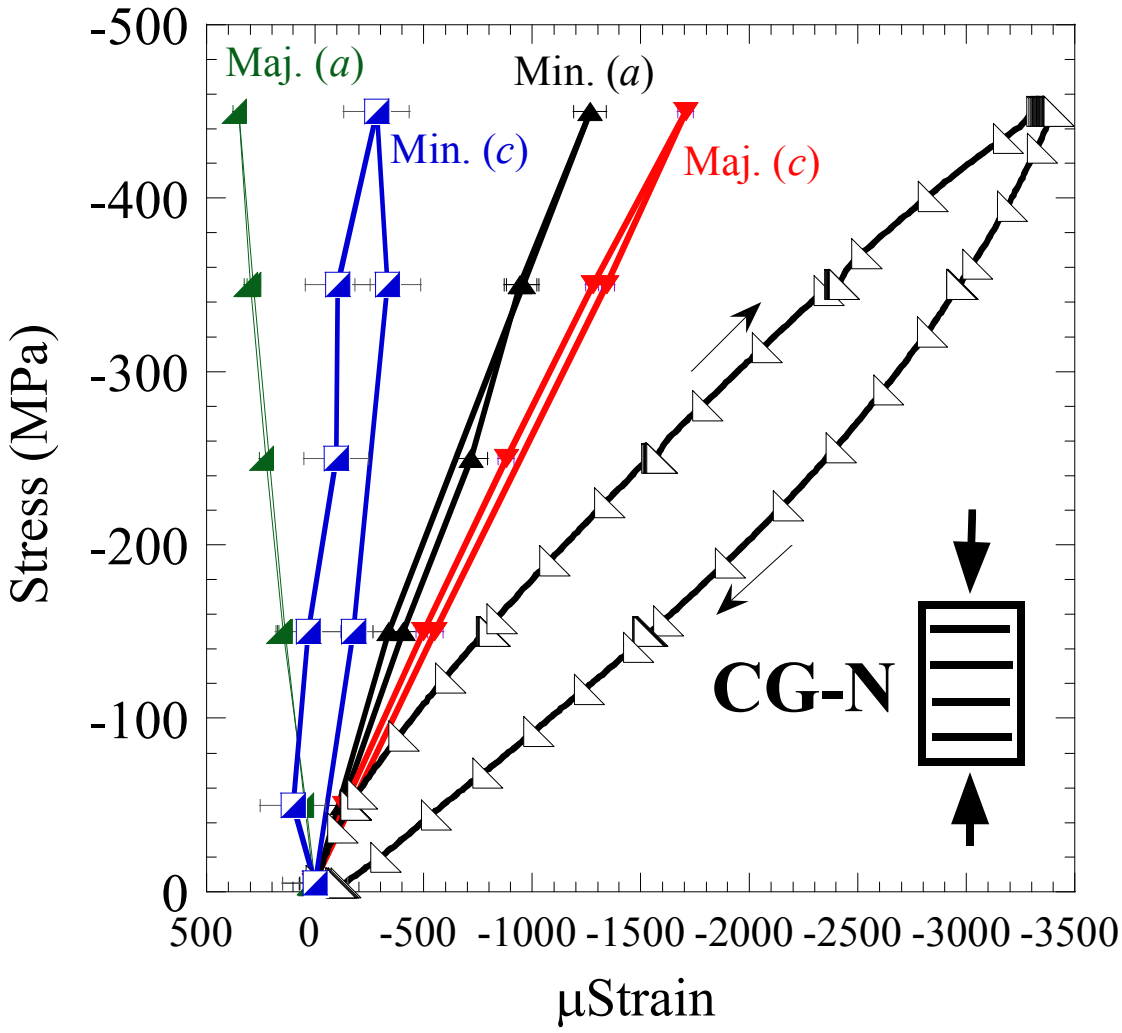
Maj. (a)
Min. (a)
Min. (c)
Maj. (c)
CG-N
Stress (MPa)
-500
-400
-300
-200
-100
0
500
0
-500
-1000
-1500
-2000
-2500
-3000
-3500
μStrain

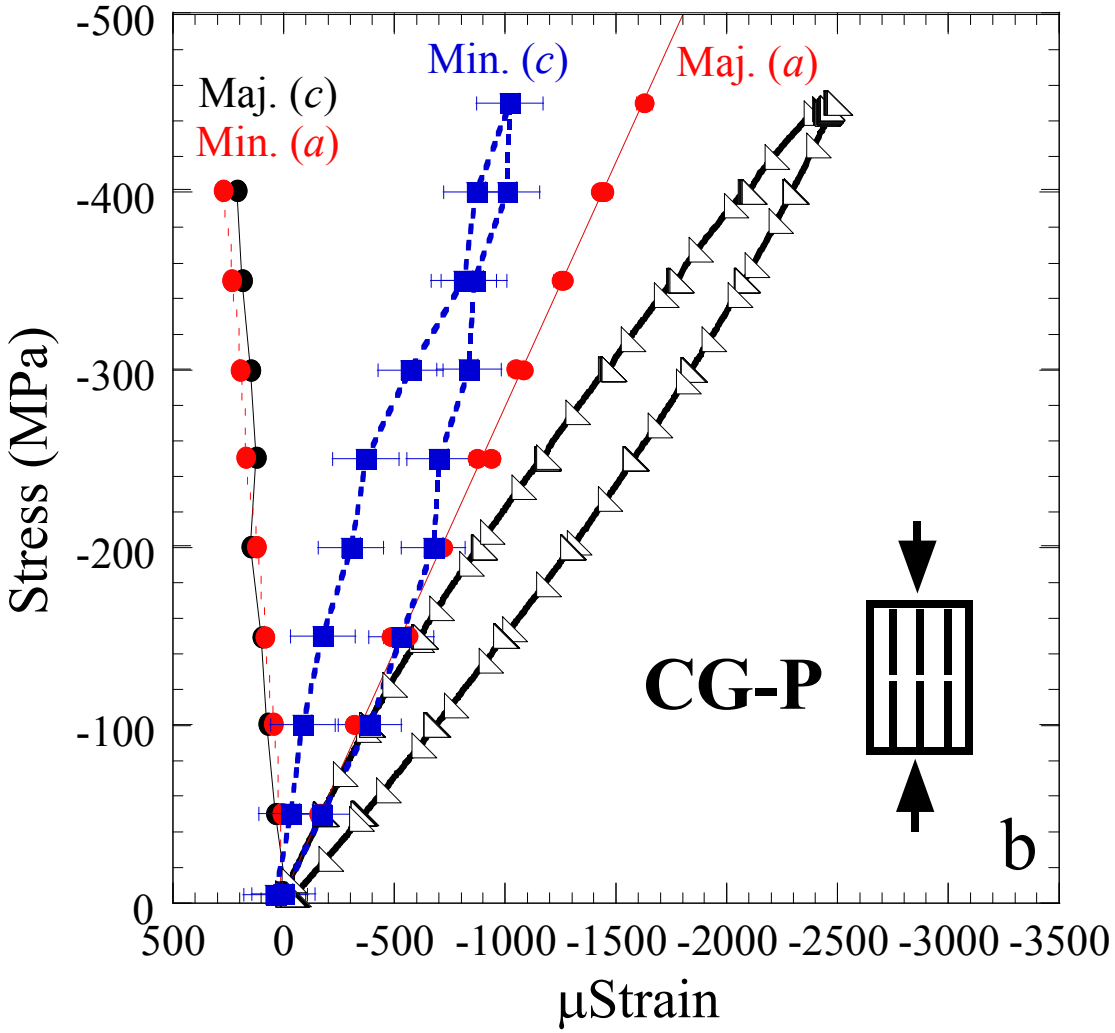

Figure 5-6: Strains measured by neutron diffraction along the *a* and *c*-directions of the *majority* and *minority* grains in, a) CG-N and b) CG-P samples by measuring the longitudinal and transverse lattice parameter shifts denoted by *a* and *c* strains of the majority and minority grains. Also included is the macroscopic stress-strain plots obtained simultaneously using an extensometer denoted by open triangles.

5.4. Discussion

5.4.1. Kinking Nonlinear Elasticity

The most surprising result of this chapter is the fact that the W_d's for the samples in which the basal planes are normal to the applied load are higher than those in which the basal planes are loaded parallel to the loading axis (Figure 5.5a). This result is counterintuitive; the opposite was expected because kinking is a form of plastic instability, and intuitively, one would expect more kinking when the loading direction is parallel to the basal planes.

This is particularly true given that the response of the Ti_2AlC-50 vol.% Mg composite was what was expected (compare last 3 loops on the right in Figure 5.4). However, based on the size of stress-strain curves shown in Figures 5.2 and 5.4 and the plots of W_d vs. σ^2 (Figure 5.5a), it is evident that at all stresses the FG-N and CG-N samples dissipate *more* energy compared to FG-P and CG-P samples, by a factor of ~ 3.

The questions raised are: why does the Mg-composite dissipate more energy and what is the origin of the counterintuitive effect observed? Both questions can be answered by appreciating that for kinking to occur, "room" is needed. As discussed in Ch. 4 in the case of the composite, the relatively *softer* Mg phase in between the Ti_2AlC grains allows the latter to kink, with little penalty [71, 72]. In the Ti_2AlC bulk samples, however, the majority of the plate-like grains seem to be constrained by the *minority* grains. We argued elsewhere [72] that the influence of Mg-matrix is the opposite of the small equiaxed grains in $Ti_2Al(C_{0.5},N_{0.5})$ solid solutions [45] wherein the "*hard*" small grains constrain the majority grains from kinking. This is also clearly manifested here by

comparing the size of the Ti_2AlC and Mg-Ti_2AlC stress-strain loops (Figure 5.4) that result in W_d values being higher by at least one order of magnitude in the latter (Figure 5.5a).

The ND results, however, are indispensable in understanding – at least partially – the counterintuitive nature of the results in Ti_2AlC. If the reasonable assumption is made that the extent of kinking is related to the area of the *elastic* hysteresis loops in Figures 5.6a and b, then it is immediately obvious that the *minority* grains in both microstructures are kinking significantly *more* than the majority grains. Based on the results shown in Figure 5.6, it is evident that the *minority* grains in both microstructures are responsible for most of the kinking and undergo hysteresis. Thus, it is fair to conclude that the *majority* grains in both samples are apparently constrained by the *minority* grains, wherein the latter inhibits kinking in the former. The role of *minority* grains here is essentially the opposite of the role the nanocrystalline Mg grains play in Mg-Ti_2AlC composites.

More importantly, in the CG-P sample, not only kinking in the *majority* grains is inhibited, but also the loading direction is supposedly normal to the basal planes of the *minority* grains that intuitively should suppress kinking. That is probably why the size of the stress-strain loops (Figures 5.2 and 5.4) and W_d (Figure 5.5a) in CG-P sample is smaller than CG-N. In the latter microstructure, the loading direction is parallel to the basal planes of the *minority* grains that in turn promotes kinking.

Remarkably – and fully consistent with its definition – the Ω/b values are a weak function of texture (Table 5.3). They are, however, a function of grain size. At 37.7±0.5

MPa, the Ω/b values obtained here for FG-P and FG-N bulk samples are almost identical to those obtained from Mg-Ti_2AlC composites with the same grain size (Ch. 4) [72]. Similarly, at 24.2±0.1 MPa, the values obtained from CG-P and CG-N samples are almost identical to those obtained for bulk Ti_2AlC with comparable grain size [45]. We recently showed that at least for the $Ti_{n+1}AlX_n$ phases the CRSS follows a Hall-Petch type relationship [45]. This is corroborated herein by plotting Ω/b as a function of $1/\sqrt{2\alpha}$ (Figure 5.7) for the average of the Ω/b values obtained from fully dense Ti_2AlC samples and Mg-Ti_2AlC composites and those of fully dense and 10 vol. % porous Ti_2AlC samples with larger grain sizes obtained in Ref. [57]. Least squares analysis of the data resulted in an $R^2 = 0.91$, a testament to the dependence of Ω/b on grain size.

The results shown in Table 5.3 are of paramount significance for several other reasons as well. The fact that the Ω/b values calculated from Eqs. 2.5 & 2.6 or Eq. 2.7 (columns 6 and 7 in Table 5.3) for both FG-P and FG-N samples are almost identical is strong evidence that the micromechanism causing the strain nonlinearity is most likely the same as that resulting in W_d [45, 57-59, 72].

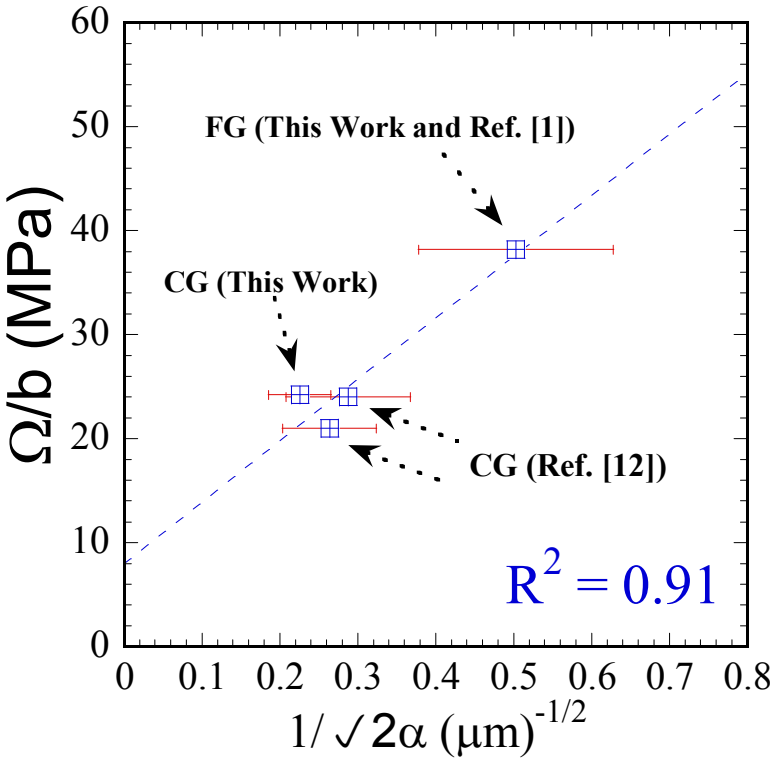

Figure 5.7: Plot of Ω/b as a function of $\frac{1}{\sqrt{2\alpha}}$ for the average Ω/b values of FG Ti_2AlC obtained herein and those of Mg-Ti_2AlC composites [72], with the same grain size, CG Ti_2AlC and those reported for fully dense and 10 vol. % porous Ti_2AlC [57].

Even more importantly, the fact that the Ω/b values are almost identical in the bulk Ti_2AlC and in the Mg-Ti_2AlC composites [72] with comparable grain sizes, most likely suggests that in both cases Ti_2AlC is kinking.

At ≈ 1.1×10^{13} to 2.6×10^{13} m^{-2}, the values of ρ_{rev}, at comparable stress levels, listed in Table 5.3 for FG and CG samples tested here fall in a narrow range despite the differences in size of the original loops from which these values were extracted, grain size and texture. Recall that ρ_{rev} is not the dislocation density in the sample when the load

is removed, but rather the one due solely to the IKBs, i.e. ρ_{rev} given by Eq. 2.9. As importantly, at ≈ 1.3×10^{14} to 1.7×10^{14} m^{-2}, the values of ρ_{rev} at comparable stress levels for Mg-Ti_2AlC composites also fall in a narrow range despite the large differences in size and shape of their original loops as we have discussed in Ch. 4 and shown here in Figures 5.2 and 5.4. It is noteworthy that even at 750 and 460 MPa being the highest stress levels tested in this work on the FG-N and CG-N samples, their corresponding ρ_{rev} did *not* exceed the values of 4.2×10^{13} and 1.7×10^{13} m^{-2} despite the significant increase in the stress, e.g. in FG-N sample by more than a factor of 2, compared to when the sample was loaded to 352 MPa, at which level the ρ_{rev} was only 2.0×10^{13} m^{-2}.

More importantly, as argued elsewhere [45, 58, 59, 71, 72] and above, the values of ρ_{rev} fall in this narrow range despite the fact that: i) the maximum applied stresses vary by a factor of 2 (see above), and ii) the N_K values vary from 1.4×10^{15} in the CG-N sample to 1.1×10^{18} in the Mg-Ti_2AlC composites. The same seems to be true for Ti_3AlC_2, Ti_2AlC, $Ti_3Al(C_{0.5},N_{0.5})_2$ and $Ti_2Al(C_{0.5},N_{0.5})$ [45], where it was shown that despite large variations in the shapes and sizes of the hysteretic loops, ρ_{rev} varied by less than one order of magnitude (1×10^{13} to 9×10^{13} m^{-2}). The same is true for Mg [59], wherein N_k varied by almost 3 orders of magnitude, but ρ_{rev} varied by a factor of 3.

Thus, the results of this chapter, Ch. 4 and those of Refs. [45, 59, 72] suggest that a near-constancy ρ_{rev} exists to which all systems migrate, regardless of their chemistry and/or microstructure.

Lastly, it is crucial to emphasize the significance of the Taylor factor (M) calculations, listed in Table 5.3 for the FG and CG samples tested herein for the two

different orientations with respect to the loading direction. M, which is a measure of plastic work in crystal plasticity [153], essentially relates the average local shear stress at the single grain level to the macroscale uniaxial stress [59, 154, 155] by $\tau_t \approx \frac{\sigma_t}{M}$. Evidently, at ~ 2.5 and 3, the M of FG-P and CG-P samples are ~ 25% and 65 % greater than those of the FG-N and CG-N samples. Note that the *majority* of basal planes in the former samples are *parallel* to the loading direction. These results unambiguously show that M is a function of texture and grain size and is larger when the basal planes are *parallel* to the loading direction as opposed to *normal* to the loading conditions. It follows that M - in general, nontrivial to measure - can be estimated for the MAX phases with the knowledge of 2α values by simply utilizing the KNE microscale model and carrying out simple uniaxial compression tests, from which one can easily measure σ_t, and hence M. Also, as we have shown in Ch. 4, the choice of the value of $w = 5b$ and M mentioned above results in 2α and σ_t values that are in reasonable agreement with experimentally measured 2α and σ_t (Table 5.3). The fact that oriented samples are EDMed from the same billet, implies that their 2α, *b* and *w* must be identical. Hence, the only remaining variant is M. And while one may quibble with the absolute values of M, the ratio of its values for various orientations is much less inexact. These conclusions cannot be overemphasized.

5.4.2. Ultimate Compressive Strengths

Elsewhere [29, 57], we reported UCS values of ~ 540, 393 and 600 MPa for Ti_2AlC samples with average grain sizes of 20-25, 100-200 and 113±60 μm, respectively. Also more recently we reported values of 865±55 MPa [72] for fully dense Ti_2AlC samples fabricated by hot isostatic pressing (HIPing) using similar processing parameters as used here. These values differ slightly from those fabricated by hot pressing. Although there has not been any systematic study to investigate the different parameters that influence the compressive strengths of Ti_2AlC, the reason(s) for such inequalities in our previous works [29, 57, 72] and those reported herein are believed to be due to the differences in grain size, grain morphology and quite possibly fabrication routes. Aside from the non-linear IKB induced strain, the samples failed in brittle mode; they shattered upon failure.

5.4.3. Effective Young's Moduli

As stated in Ch. 4, $\overline{E}$ depends on the both constituents and the size and extent of the hysteretic stress-strain curves. Not surprisingly, the presence of ~50 vol. % Mg in the composite sample reduces $\overline{E}$ two ways; because of the low modulus of Mg and the more kinking that is induced (Figure 5.4). $\overline{E}$ of the single phase Ti_2AlC samples is significantly higher than those of the former, by at least a factor of 3.

It is important to note that when the FG-P and FG-N samples were compressed up to ~ 160 GPa, their behavior was linear elastic, with a Young's modulus of 275±2 GPa, which is in excellent agreement with the value of 277 GPa [156, 157] for Ti_2AlC measured by resonant ultrasound spectroscopy. Note that C_{11} and C_{33} values of Ti_2AlC reported by Wang *et al.* [152] are 308 and 270 GPa, respectively. It turns out that the E

values measured experimentally herein and those by resonant ultrasound spectroscopy are in line with the C_{33} values reported by Wang *et al.* [152].

5.5. Conclusions

In summary, we showed that, surprisingly, the W_d's for the Ti_2AlC samples in which the basal planes are normal to the applied load are higher than those in which the basal planes are loaded parallel or edge-on. In the composite samples, the relatively *softer* Mg phase in between the Ti_2AlC grains allowed them to kink but in the Ti_2AlC bulk samples, the majority of the plate-like grains seem to be constrained by the *minority* grains. The neutron diffraction results were indispensable because they suggest that the *minority* grains in both microstructures are kinking significantly *more* than the majority grains.

We also showed that Ω/b is a strong function of grain size and a weak function of texture. The values of ρ_{rev} at comparable stress levels fell in a narrow range suggesting that an equilibrium state must exist to which all the systems migrate. Lastly, the results of this chapter unambiguously showed that how M is a function of texture and grain size and is larger when the basal planes are *parallel* to the loading direction as opposed to *normal* loading conditions.

Chapter 6 : On the Thermal Stability of Mg nanograins to Coarsening after Repeated Melting

6.1. Introduction

In the continuing quest for improved performance of materials - including lighter, stiffer and stronger - many approaches have been attempted; one of the more successful being composite materials [71, 158-162]. More recently, much emphasis has been given to nano-scaled solids for structural applications [163-166] because the unusual properties of nanometer-sized materials have generated tremendous interest in both scientific and technological communities [167]. While the advantages of nano-structured solids, in some applications, are clear, making them economically and on an industrial scale has been more of a challenge. Typically, nano-sized powders – that ideally have to remain non-agglomerated and mono-dispersed - are first synthesized and then consolidated [168]. Maintaining the nano-scale morphology during consolidation, of metals, in general, and low melting point metals in particular, is non-trivial [168, 169]. Even when such microstructures are fabricated, their use is typically limited to ambient or near ambient temperatures in order to prevent grain growth [163, 165, 166, 168, 169].

In Ch. 3, the processing and microstructural characterization of 50 vol.% Ti_2AlC nanocrystalline Mg-matrix composites fabricated by pressureless MI was described. XRD and TEM images established that the Mg grains in melt infiltrated (MI) composites were ~20-40*nm*. Most importantly, as described in Ch. 3, these microstructures were exceptionally stable because initial experimental results showed that annealing for 6 h at 550 °C in flowing Ar gas did *not* alter the Mg grain size [71].

Given the constraints and hurdles mentioned earlier in order to maintain the nano-scale morphology during processing and post-processing, owing to the fact that we can spontaneously infiltrate a ceramic preform, and obtain a superbly machinable – Ti_2AlC is most readily machinable like all other MAX phases [29, 156] – nano-structured composite, with high strength and stiffness, low density, and ultrahigh damping capacity, is noteworthy. However, understanding the factors that may affect the stability of the aforementioned nanocrystalline Mg-matrix composites is critical to identifying the best strategies for future technology developments. The thermal stability of the microstructures obtained herein, is an important and, quite possibly, crucial advantage that other nano-Mg powders developed for applications such as hydrogen storage – typically fabricated by mechanical alloying – do not posses because the high degree of internal stored energy leads to recrystallization with partial, or total, annihilation of the nanocrystalline structure [168, 169].

In addition, it is postulated that the nano-crystalline-Mg matrix would exhibit significant melting point depression and also depression in latent heat of fusion due to the nanocrystalline nature of the matrix compared to bulk Mg. As far as we are aware, there has not been any work on investigating the size effect on the melting temperature of nanocrystalline Mg.

The phenomenon of particle-size-dependent melting point depression of various materials in general that occurs when the particle size is of the order of nanometers [167, 170-173] and melting of small metal particles below the melting temperature of the corresponding bulk metal [170, 172, 174-176] in particular has received significant attention since the first detailed experiments were published by Takagi in 1954 [177]. His

thin metallic films were prepared in the electron diffraction camera by evaporating the metals on several kinds of crystals with an average thickness ranged from 10 to 1000 Å. The corresponding melting temperature was estimated from the change in appearance of diffraction rings. The electron diffraction camera has since been used by several other investigators in the study of the size-dependent melting effect. The author then concluded that the melting temperature is a function of crystal size [176, 177]. Although in some cases such as gold particles of 1 *nm* radius, the melting point depression can be as great as 500 K [174], the depression can be relatively small for metals such as Al nanoparticles; for example, a depression of only 13K is observed for a particle having a 10*nm* radius Al core with a passivation layer of approximately 10*nm* [178]. Allen *et al.* showed that submicron-sized crystallites of lead, tin, indium and bismuth melted *in situ* in a TEM exhibited melting points that decreased with decreasing particle size and a near-linear relationship was observed for the melting point as a function of the reciprocal of the radius [176]. Qi *et al.* [179] and Lai *et al.* [167] have shown particle-size-dependent melting point depression of free-standing nanosolids such as Sn and Pb nanoparticles and In nanowires and nanofilms where the melting point decreases with a decrease in size. Ben David *et al.* [180] have shown that melting and solidification of Pb ultra-fine particles are a strong function of the particle size. Semiconductor nanocrystals such as CdS [171, 181] show a large depression in the melting temperature with decreasing size.

It is well established that the thermal behavior of nanoparticles differ from that in the bulk state due to their increased surface-to-volume ratio and increased proportion of loosely bound surface atoms [178]. The surface atoms of a crystal usually have low

coordination numbers [182] and thus experience different bonding forces compared to the bulk atoms [182]. As a consequence, a depression in the melting temperature occurs when the fraction of surface atoms becomes significant. Thus, depending on size, enough for the surface to play a significant role [183], small crystallites of metals melt below the bulk melting point [167, 181].

Several models [181, 184-186] have been proposed that reveal the size dependence of melting point in nanocrystals. The predictions of these models have been consistent for the most part with both experimental results and other thermodynamic models for metallic nanocrystals. The melting point depression for small crystals can be simply described in a classical thermodynamic approach by the so-called Gibbs–Thomson equation: [187]

$$T_m(r) = T_m(\infty) - \frac{2T_m(\infty)\sigma_{sl}}{\Delta H_f(\infty)\rho_s r} \quad \text{(Eq.6.1)}$$

where $T_m(\infty)$, $\Delta H_f(\infty)$ and ρ_s are the bulk melting temperature, the bulk latent heat of fusion, and the solid phase density, respectively; r represents the radius of the spherical particle and $T_m(r)$ is the melting point of a particle with radius r; σ_{sl} is the solid–liquid interfacial energy.

Despite several phenomenological models in the literature addressing the melting point depression of small metal particles, a more comprehensive understanding of the thermodynamics of finite material systems has always been imperative to investigate the details of heat exchange during the melting process, in particular the latent heat of fusion

ΔH_f, e.g. computational simulation works in Au clusters have predicted a cluster-dependent depression of ΔH_f in addition to the depression of T_m [170]. For the first time, the latent heat of fusion ΔH_f and also melting point depression for Sn particles formed by evaporation on inert substrates with radii ranging from 5 to 50*nm* has been measured directly using a novel scanning nanocalorimeter by Lai *et al.* [167] and a particle-size-dependent reduction of ΔH_f has been observed. They showed that the heat of fusion decreases markedly from the bulk as much as 70% when the particle size is reduced.

The objectives of this chapter are twofold: First, to report on the cyclic thermal behavior of the aforementioned composites from room temperature to temperatures above the melting point of Mg utilizing differential scanning calorimetry and to explore the thermal stability of nanocrystalline Mg matrix. Second, is to establish, for the first time, whether the thermal behavior of nanocrystalline Mg matrix differ from that in the bulk state and investigate the phenomenon of grain-size-dependent melting point depression and to understand, quantify and relate the melting point reductions to the size of the Mg nano-particles.

6.2. Experimental Details

Three sets of composite samples were fabricated. The first by the spontaneous MI of a porous Ti_2AlC perform at 750 °C. The details can be found in Ch. 3. The second set of samples was fabricated by HPing the starting Ti_2AlC (3-ONE-2, Voorhees, NJ) and Mg powders (Alfa Aesar, Ward Hill, MA) at 750 °C while a load, corresponding to a stress of ~ 45 MPa, was applied. XRD established that the Mg grains in both cases were

~35±15 *nm* in diameter. TEM images confirmed the nano-scale of the grains (Ch. 3). A third set - Mg-50 vol.% Ti_3SiC_2 composite - was also fabricated by MI. In this case, the Mg grain size was *not* at the nanoscale. We also documented the behavior of pure bulk Mg. In all cases, the Mg was 99.8% pure (Alfa Aesar, Ward Hill, MA). The -325 mesh, Ti_2AlC and Ti_3SiC_2 powders were commercially obtained (3-ONE-2, Voorhees, NJ).

Differential scanning calorimetry, DSC, analysis was carried out, on bulk samples, in a simultaneous TGA/DSC unit (Netzsch STA 449C Jupiter, Selb, Germany) in ultra high pure Ar, in sintered Al_2O_3 crucibles. The temperature was cycled three times from room temperature to 973 K and back to 373 K, at 10 K/min. TEM foils were prepared by a conventional TEM sample preparation process and characterization was performed using a field emission TEM (JEOL JEM-2010F) operating at 200 kV. HRTEM was carried out in a JEOL JEM-2100 unit operating at 200kV.

A filter difference spectrometer (FDS) at Los Alamos National Laboratory was used to obtain a reference vibrational spectrum (red curve in Figure 6.2) of a MI-Ti_2AlC sample. The sample was then loaded in a stainless steel crucible and heated to 250 ^oC for 20 h. The crucible was evacuated and connected to a hydrogen cylinder supplying a constant pressure of H_2 of 68 bar. After cooling to room temperature and releasing the pressure, a second neutron vibrational spectrum (blue spectrum in Figure 6.2) was collected. For both FDS measurements, the sample was placed in a sealed cylindrical aluminum can under a He atmosphere. Data were collected at 10 K.

6.3. Results and Discussion

The DSC results (Figure 6.1a and b) are unambiguous: repeated melting of the composites did *not* lead to coarsening of the Mg-grains.

Table 6.1 summarizes the onsets of melting, T_m, and solidification, T_s, of the 4 samples tested. At 645 °C, the melting point of the 99.8% pure Mg (Figure 6.1c) compares favorably with the value of 649 °C reported in Refs. [107, 122]. The onset of solidification was also close to that of melting (Figure 6.1d).

At 638 °C, the onset of melting in the MI-Ti_3SiC_2 (Figure 6.1c) was slightly reduced as compared to pure Mg, a reduction that probably partially reflects the large Ti_3SiC_2/Mg interfacial area and/or the fact that the Mg is no longer pure.

The reductions in MP, as compared to the bulk Mg, for the MI- and HP-Ti_2AlC samples were 45 K and 58 K, respectively. The respective onsets of solidification were also suppressed by 12 K and 20 K relative to pure Mg. Most surprisingly, heating the samples to 700 °C three times, clearly did not affect these values. The reproducibility is noteworthy. Clearly, the microstructures formed during the fabrication of these composites are extremely stable.

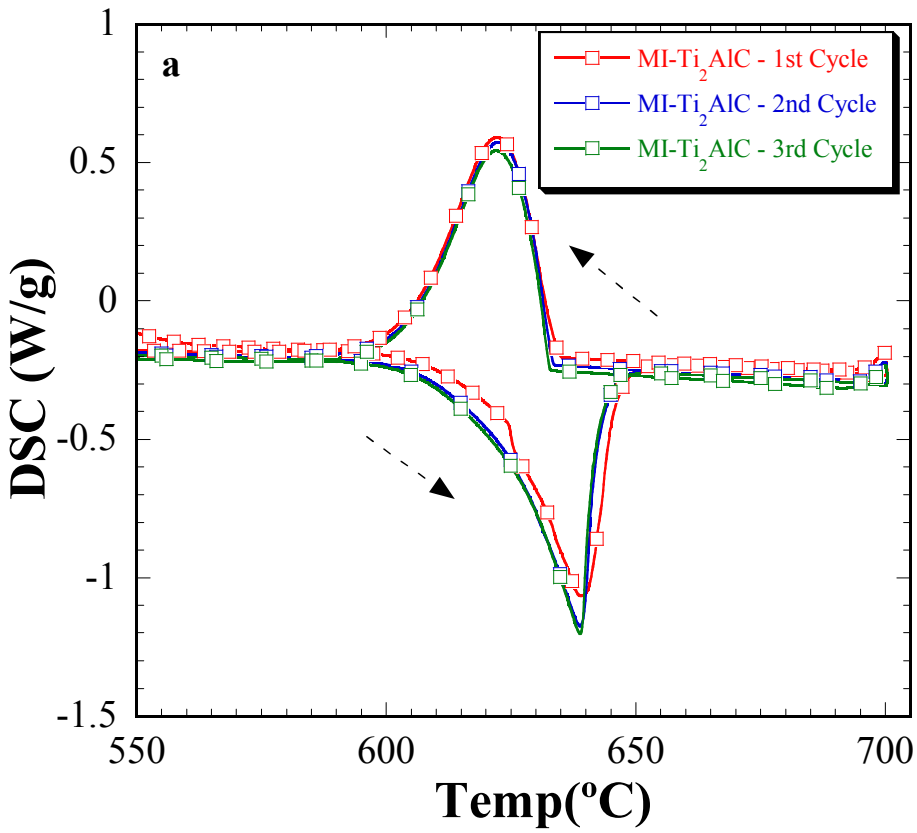
a
MI-Ti2AlC - 1st Cycle
MI-Ti2AlC - 2nd Cycle
MI-Ti2AlC - 3rd Cycle
DSC (W/g)
Temp(°C)
1
0.5
0
-0.5
-1
-1.5
550
600
650
700

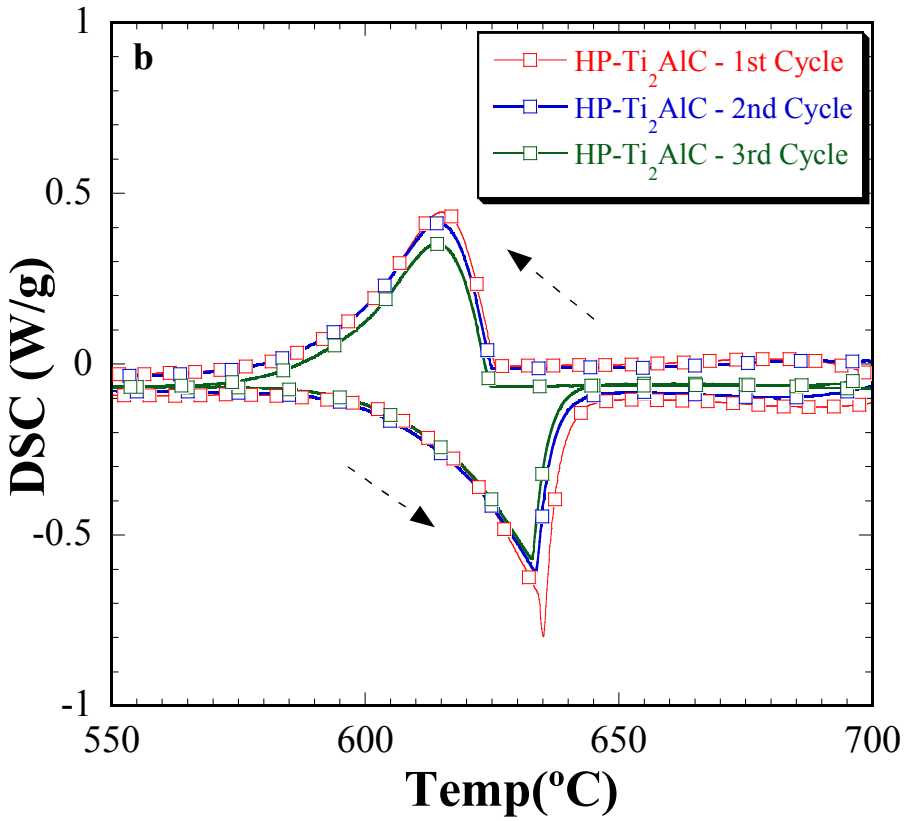
b
HP-Ti2AlC - 1st Cycle
HP-Ti2AlC - 2nd Cycle
HP-Ti2AlC - 3rd Cycle
DSC (W/g)
Temp(°C)
1
0.5
0
-0.5
-1
550
600
650
700

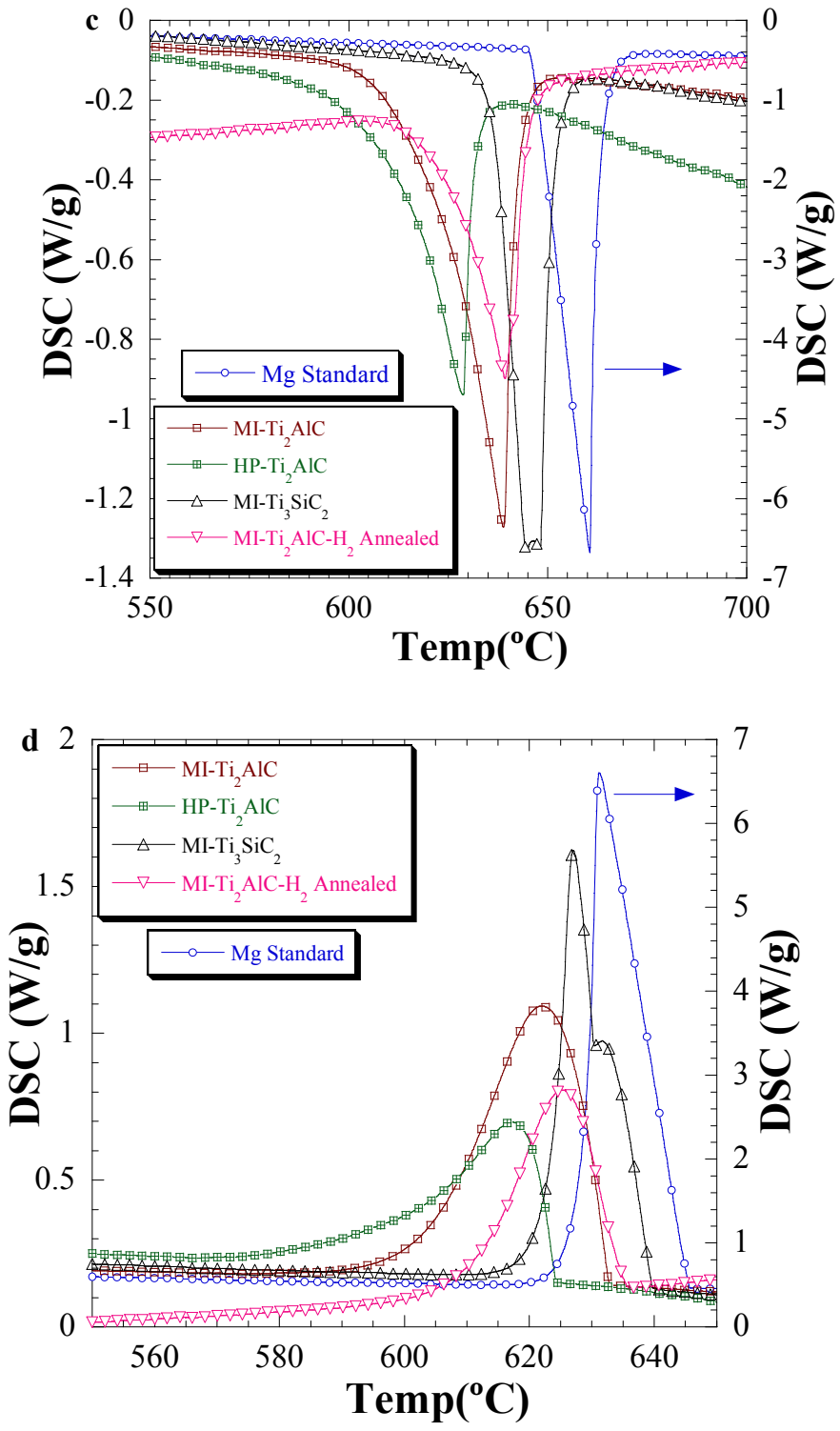

Figure 6-1: DSC results; a) Three cycles of MI-Ti_2AlC composite, b) Three cycles of HP-Ti_2AlC composite, c) Comparison of melting troughs and, d) solidification peaks for 5 samples tested herein.

Table 6-1: Summary of experimental and calculated parameters. The r_{av} of the Mg grains in the MI-sample was assumed to be 17±8 nm. The value of σ_{sl} was then used to estimate the average particle size for the HP sample. The standard deviation reported for the ΔH_i values are with respect to the three cycles. The actual uncertainty in the ΔH_i values, reflected in the differences between runs, is significantly larger since the exact amount of Mg – assumed to be 50 vol.% - in the composite is not known.

	T_m (ºC)	T_s (ºC)	r_{av} nm	σ_{sl} (mJ/m^2)	ΔH_f (kJ/mol) From DSC	ΔH_s (kJ/mol) from DSC
Pure Mg	646±1*	645±1	--	90 [188]	8.5±0.2**	8.6±0.1
MI-Ti_2AlC	601±2	633±1	17‡	252±120	8.6±0.1	8.3±0.4
MI-Ti_2AlC H_2 Annealed	603±1	635±1		–	5.2±0.1	5.1±0.3
HP-Ti_2AlC	588±1	625±1	13‡‡	252±120	5.7±0.3	5.4±0.8
MI-Ti_3SiC_2	638±1	640±1		–	6.9±0.1	6.8±0.4

‡ From XRD line broadening. ‡‡ Calculated assuming σ_{sl} =252 mJ/m^2.

It is fair to conclude that a sheath or skin – that did not melt – prevented the Mg grains from coarsening. The simplest assumption is that the nano-grains are encased in a very thin oxide jacket. The presence of such oxides was confirmed by both XRD and neutron spectroscopy. As reported elsewhere [71] and in Ch. 3, XRD spectra of the composites included small peaks that could be indexed to MgO. Closer examination of the reference spectrum (Figure 6.2) shows a number of vibrational modes consistent with the presence of rutile and anatase [189, 190]. However, according to Ellingham-Richardson diagram [191] of temperature dependence of the free energy of formation (ΔG_f°) in oxides, MgO is a more stable oxide than TiO_2 at temperatures below 2000 K. Thus, TiO_2 should have been reduced (under equilibrium conditions) by Mg metal. Why TiO_2 is still present is not entirely clear at this point.

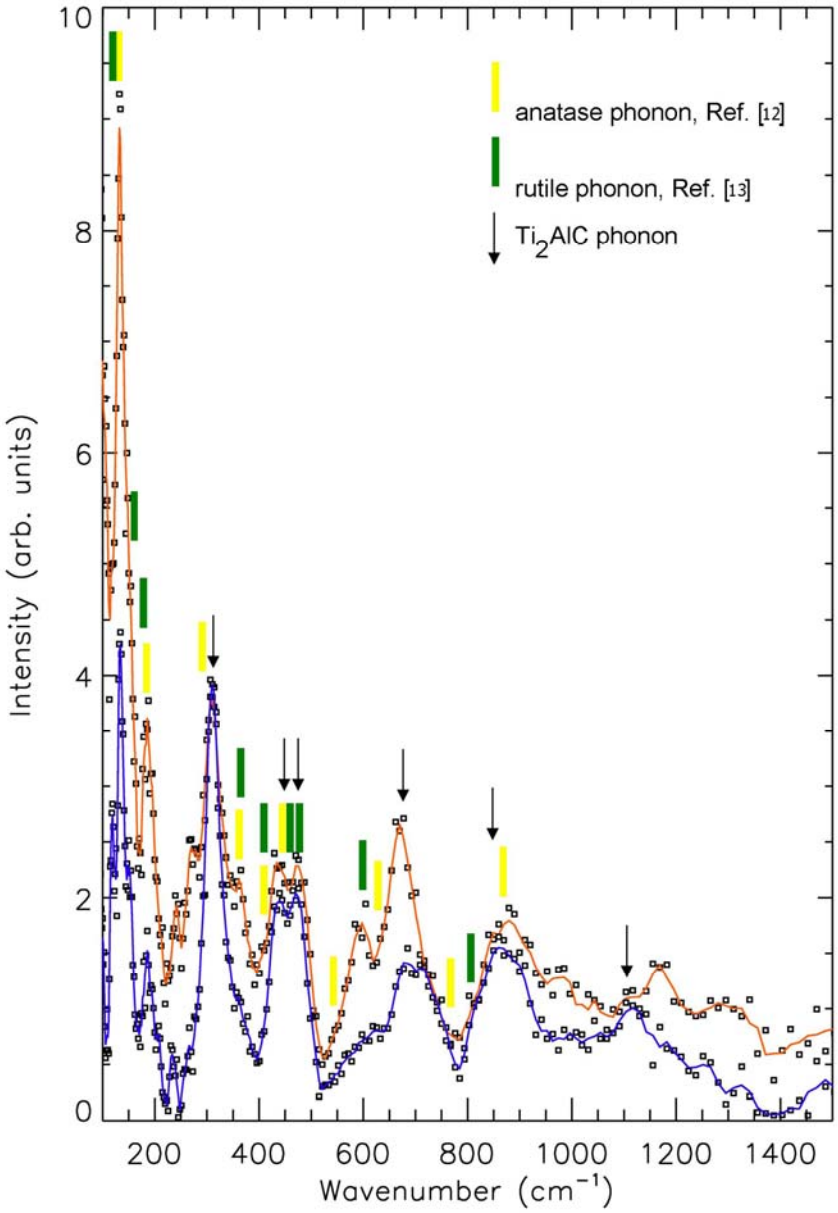

Figure 6-2: FDS spectra of a 40 mm high, 10 mm diameter, MI Mg-Ti_2AlC composite solid cylinder. Red line is the neutron vibrational spectrum of the composite before H_2 annealing. Blue line is the spectrum after annealing in H_2 at 250 ^oC, 68 bar for 20 h. The hashes mark the locations of anatase (yellow) and rutile (green) peaks. The rest of the peaks, with the exception of those at 240 and 270 cm^{-1} are presumed to be those belonging to Ti_2AlC. Note that these peaks do *not* decrease in intensity with the H_2 anneal; the ones associated with rutile and anatase do, indirectly confirming their nature.

Presence of TiO_2 was further confirmed by the weakening or disappearance of some of these modes in the vibrational spectrum after the H_2 annealing. The remaining modes we tentatively ascribe to Ti_2AlC since the intensities of the modes associated with Ti_2AlC remained unchanged after the H_2 anneal. It follows that much of the H_2 supplied to the sample was consumed in the reduction of the oxides - a reduction that may not have been complete at the time heating was stopped because some intensity remains in the vibrational spectrum where the lattice modes of TiO_2 appear. As a further testament of the stability of the microstructure, the major effect of the H_2 reduction was to skew the DSC baseline for reasons that are not clear. However, for the most part, the reductions in melting points and solidification temperatures were not that different to those of the MI-Ti_2AlC sample (Table 6.1). Interestingly, high-resolution TEM images of the Mg grains failed to unambiguously prove the presence of a grain boundary oxide phase.

We now turn our attention to the reduction in melting points. According to Eq. 6.1, if we make the following assumptions for the MI-Ti_2AlC sample: $\Delta T = 45$ K, $\Delta H_f = 8.6$ kJ/mole and r = 17 nm, then σ_{sl} is calculated to be 255 mJ/m^2. For the HP samples, with a $\Delta T = 58$ K, and the same values for the other parameters, yields $\sigma_{sl} = 327$ mJ/m^2. Given that we are dealing with the same system it is reasonable to assume the same value of σ_{sl}. The fact that they are not is most probably because of the uncertainty in the exact value of r; and while XRD line broadening yields the same average r value for both composites, the matrix in the HP samples in the TEM appeared finer compared to MI sample (Figure 6.3a and b). More importantly, the melting onset for the HP-samples occurs at a lower temperature. If one assumes σ_{sl} for the HP samples to be 252 mJ/m^2, then r for that sample would be 13.2 nm, which is not unreasonable. This is

independently, but indirectly, corroborated by the fact that the ultimate compressive stresses of the HP samples were slightly higher than the MI ones. Since as far as we are aware this is the first study on the effect of particle size on the melting of Mg nano-grains, there are no results to compare ours with. A recent molecular dynamic simulation study of Mg, calculated σ_{sl} to be 90 mJ/m^2 [188]. A direct comparison of these results with ours is problematic, however, due to the presence of an oxide skin in our case. Although it is reasonable to assume that the values calculated herein most probably reflect those of Mg and oxide skins. More work, both theoretical and experimental, is required to shed light on the matter.

The solidification onset temperatures of the nano-grains are also lower than those of the other two samples (Fig. 6.1 and Table 6.1). This most probably implies the absence of potent nucleating agents in the nano-particles and is consistent with particles that are sheathed in an oxide coating. The absence of nucleating agents is also manifested in the long solidification tails observed, especially for the HP-Ti_2AlC sample where some solidification is still occurring at 580 K. It is well known that in order for elemental metallic liquids to solidify homogeneously, it is necessary to supercool the melt to a characteristic undercooled temperature (T_{UC}) below the thermodynamic melting point, (T_{MP}) [192]. Turnbull, approximately 60 years ago [193], established an empirical rule that a $\Delta T^* = |T_{UC} - T_{MP}|$ approximately equal to $0.18T_{MP}$ for several elemental metallic liquids, among which Mg was not listed. Assuming Turnbull's theory is valid for Mg, and more importantly in this case, the Mg melt needs to be supercooled to temperatures around 485 ºC in order to solidify homogeneously. Evidently, in the most extreme case

here being for the HP-Ti_2AlC sample, solidification was completed at 580 ºC. Again, assuming Turnbull's theory is valid, the oxide films can thus be a somewhat effective heterogeneous nucleation catalyst for the Mg melt. Note that the oxide layers are clearly not only preventing the coarsening, but they must also be quite thin and thus flexible enough to withstand the repeated melting and solidification stresses.

It is worth noting that the chemical interaction of Mg with Ti_2AlC appears to be responsible for the formation of the nanocrystalline Mg. In case of Ti_3SiC_2, the Mg matrix does not exist at the nanoscale. How the chemical product of such interactions in the former results in a nanocrystalline Mg matrix with an oxide skin remains a mystery. It is also worth noting that in order to get a 35*nm* grain size upon solidification, one would require solidification rates significantly higher [194], by several orders of magnitude, than those experimentally carried out in this work.

Last but not least, we plotted the weight loss as a function of time (Figure 6.3) for all the materials tested here. The MI-Ti_2AlC and HP-Ti_2AlC samples showed, within the resolution of our TGA, no weight loss upon completion of three cycles from room temperature to 700 ºC, another strong testament to the thermal stability and inertness of the Mg-nanograins. While the pure Mg seems to have lost ~ 1.5 % weight, it is fair to conclude that the magnesia and/or rutile-anatase sheaths surrounding the Mg-nanograins, not only did *not* melt, but also prevented the Mg from evaporating.

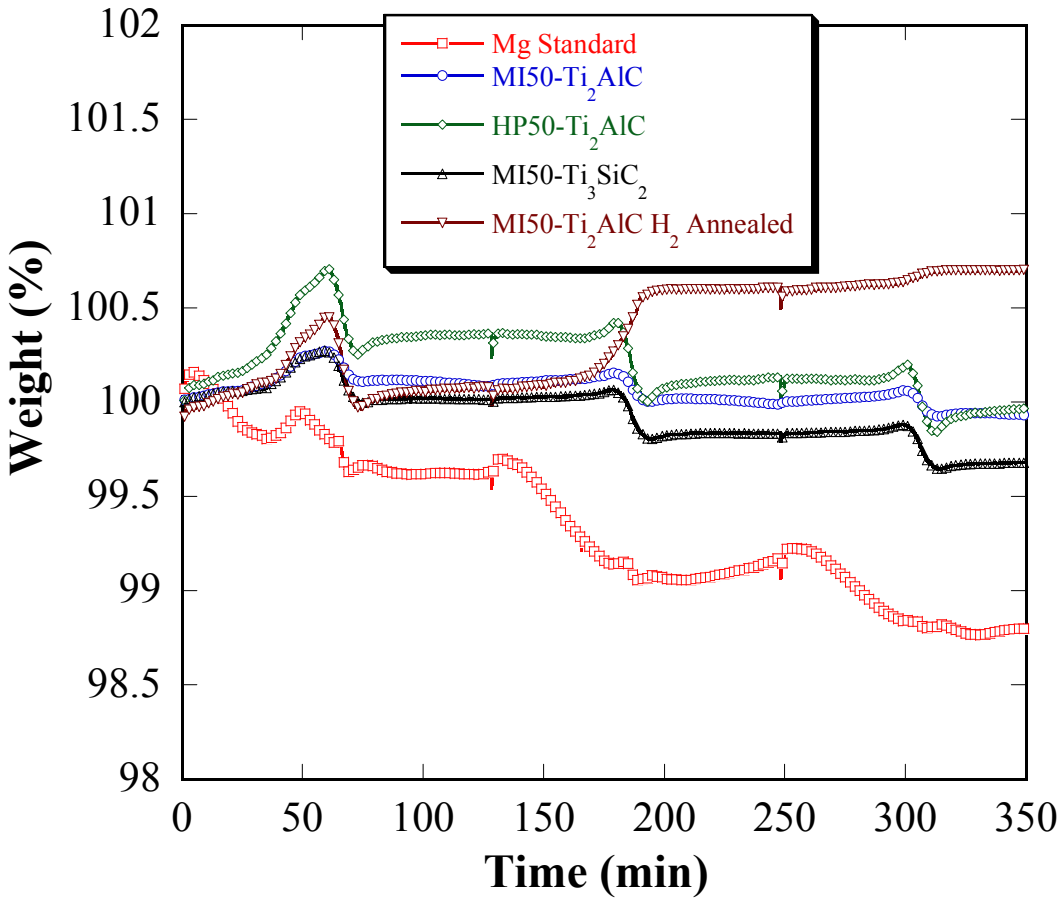

Figure 6-3: Plots of weight loss (%) as a function of time for 5 samples tested herein, showing, within the resolution of our TGA unit, almost naught weight loss in MI-Ti_2AlC and HP-Ti_2AlC samples.

6.4. Summary and Concluding Remarks

A unique, simple and cost effective technique to fabricate Ti_2AlC nanocrystalline Mg-matrix composites by pressureless MI was developed. These composites are readily machinable, relatively stiff (≈ 100 GPa), strong and light (2.9 g/cm^3) and exhibit ultrahigh damping [71]. These solids can be potentially technologically important because of their unusual thermal stability. One clear potential application is to use such nanostructures as hydrogen storage materials [168, 169]. One of the motivations of this work was to explore whether these composites can be used for hydrogen storage since there are several reports in the literature claiming that nano-grained Mg enhances the H_2 uptake and increases the kinetics [195-197]. It was thus somewhat of a surprise that the neutron spectra did not show *any* evidence for H in either Mg or Ti_2AlC. The reason for this state of affairs is unclear at this time, but could be related to the fact that the H was prevented from diffusion into the Mg and/or was consumed in reducing the oxide layers. We are planning to continue the neutron spectroscopy work in the near future to better understand the interaction of H with the composite samples. We note in passing that neutron diffraction is an almost ideal technique to study H. If the nano-grained microstructure can be maintained, during repeated H-loading and degassing this composite material may prove to be an excellent candidate for H-storage.

Chapter 7 : Summary, Conclusions and Proposed Research Work

7.1. Summary

In this work, a novel class of Mg matrix composites reinforced with Ti_2AlC was fabricated by spontaneous melt infiltration. The ~ 35 *nm* Mg grains that constituted the matrix of these composites were exceptionally stable because repeatedly heating the composite to 700 °C – 50 °C above the melting point of Mg – remarkably and surprisingly did not lead to any coarsening.

At 380±20 MPa, 700±10 MPa and 1.5±0.5 GPa, the ultimate tensile and compressive strengths and Vickers hardness of these composites, respectively, are significantly greater than other pure Mg-composites reported in the literature, a fact attributable to nanocrystalline Mg-matrix.

The results of this work showed that incorporation of Mg into Ti_2AlC increased the damping capability of the composites by at least one order of magnitude because the relatively *softer* Mg phase in between the Ti_2AlC grains allows the latter to kink, with little penalty. Also because kinking is a form of plastic instability, orienting the Ti_2AlC grains, prior to infiltration, with their basal planes parallel to the loading direction led to exceptionally high values of W_d. At 450 MPa, W_d of composites with such textures was found to be ≈ 0.6 MJ/m^3, believed to be the highest ever reported for a crystalline solid.

The effect of texture on W_d's of bulk Ti_2AlC samples was counterintuitive. In contradistinction to the composites, in the Ti_2AlC bulk samples the majority of the plate-like grains of Ti_2AlC seemed to be constrained by the minority grains. In-situ neutron diffraction experiments suggested that the minority grains are kinking significantly more

than the majority grains. The results of this work also unambiguously showed that the MAX phases and MAX-metal composites fabricated in this thesis can be classified as KNE solids characterized by the formation of fully reversible hysteretic stress-strain loops under uniaxial cyclic compression.

The KNE microscale model – previously developed to explain kinking nonlinear elasticity – was in excellent agreement with the experimental results obtained in this thesis. The results also showed that the Taylor factor, M, which to date has not been experimentally measurable, can be calculated from the KNE model and shown to be a function of texture and grain size. The critical resolved shear stress (CRSS) values obtained from the KNE model in case of Mg-Ti_2AlC composites were in line with those of their monolithic counterparts, Ti_2AlC, suggesting that the latter is doing most of the kinking. Furthermore, the relationship between CRSS and grain size in Ti_2AlC was shown to be essentially Hall-Petch like. Lastly, the ρ_{rev} values calculated herein fell in a narrow range, suggesting that an equilibrium state, to which all the systems migrate, exists.

7.2. Concluding Remarks

In the continuing quest for improved performance of materials – including lighter, stiffer and stronger – many approaches have been attempted; one of the more successful being the development of new composite materials. More recently, much emphasis has been given to nano-scaled solids for structural applications [163-166] and while the advantages of nano-structured solids, in some applications, are clear, making the latter economically and on an industrial scale has been more of a challenge. Typically, nano-sized powders – that ideally have to remain non-agglomerated and mono-dispersed - are

first synthesized and then consolidated [168]. Maintaining the nano-scale morphology during consolidation, of metals, in general, and low melting point metals in particular, is non-trivial [168, 169]. Even when such microstructures are fabricated, their use is typically limited to ambient or near ambient temperatures in order to prevent grain growth [163, 165, 166, 168, 169].

Given these constraints and hurdles, the fact that it was feasible to spontaneously infiltrate a ceramic preform, and obtain a superbly machinable – like all other MAX phases Ti_2AlC is most readily machinable [29, 156] – nano-structured composite, with strengths > 700 MPa in compression and > 350 MPa in tension, a stiffness of the order of 70 GPa, a density of 2.9 Mg/m^3, that can also dissipate 25 % of the mechanical energy during each cycle, is noteworthy. Note that since the wetting, and subsequent infiltration, are spontaneous, there should be, in principle, no limits to the sizes or shapes of the Ti_2AlC preforms, which in turn would allow for the production of large, net- or near net-shape parts or components. As important, when the reasons for the formation of the Mg nano-grains are better understood, and if they can be implemented without Ti_2AlC and/or at lower concentrations of the latter, then such understanding could lead to the casting of large, nc-Mg ingots economically and on an industrial scale with an infrastructure that is not too different than the one used in the casting of Mg nowadays.

Additionally, Mg is a promising hydrogen storage material due to its high storage capacity (~ 7.7 wt.%). However, the high absorption and desorption temperature (400ºC) and poor kinetics have restricted its potential [197, 198]. Efforts have been devoted to improve its hydrogen storage properties by forming Mg nano-composites by mechanical alloying [198-201] because it is well established that the hydrogen storage capacity, and

the kinetics of hydrogen absorption/desorption of Mg are strongly linked to its microstructure showing that when the Mg morphology is on the nanoscale, the storage kinetics are faster [197, 202, 203]. It has also been shown that by forming nano-composites of Mg with intermetallic compounds through mechanical alloying, the desorption temperature of Mg is lowered and the desorption kinetics improved. This is believed to be due to the large amount of interphase boundaries, and short hydrogen diffusion lengths [197]. Thus, understanding the factors that affect the stability of nanostructured materials is critical to identifying the best strategies for future technology developments. The thermal stability of the microstructure obtained herein, is an important and quite possibly crucial advantage that other nano-Mg powders developed for hydrogen storage – typically fabricated by mechanical alloying – do not posses because the high degree of internal stored energy in the latter invariably leads to recrystallization with partial or total annihilation of the nanocrystalline structure [168, 169]. Such knowledge could also be in principle used to thermally spray nano-grained powders that in turn can become an important, high-performance, safe and cost-effective hydrogen storage medium.

These comments notwithstanding, it is hereby acknowledged that before some of these potential applications can become a reality, much more work is needed (see below), some of which is being currently pursued by the MAX Phase Research Group at Drexel University. Even in the unlikely eventuality that this intriguing formation of a nc-Mg matrix from its melt, described herein, does not lead to new applications, its study should enhance our understanding of the behavior of a new class of composites with exceptional

properties that will certainly appeal to numerous constituencies, industries, technologies, and scientists.

7.3. Proposed Research Work

7.3.1. Crystallographic Texture Measurements

As stated in Chs. 3-5, texture measurement by use of a sample fixed in an XRD machine, is sensitive to the angle at which the sample is mounted in the XRD machine or more importantly, the angle at which the sample is cross sectioned with respect to the orientation of the basal planes. Hence, the texture measurement data described in this thesis is an initial observation and needs further in-depth research. In order to quantify the remarkable mechanical properties of the samples tested herein and also to analyze the lattice parameter strain measurements described in Ch. 5, full quantitative texture measurements is a critical step for further research. This can be obtained by several techniques such as texture goniometer, orientation imaging microscopy (OIM) and neutron diffraction (ND), providing data that can be used in the representation of crystallographic preferred orientation to determine the fraction of the material capable of kinking in oriented Mg-Ti_2AlC composites and also monolithic Ti_2AlC samples. Initial texture measurements were performed by ND in Los Alamos National Laboratory on Ti_2AlC samples. These important results need in-depth analysis, some of which is currently being pursued by the MAX Phase Research Group at Drexel University.

7.3.2. Development of KNE Model for MAX-metal composites

As described in Ch. 4, the KNE microscale model (see Ch. 2) – that was previously developed for monolithic KNE solids – was utilized herein to analyze the cyclic compressive stress-strain curves obtained from Mg-Ti_2AlC composites. Furthermore, at 37.7±0.5 MPa, the Ω/b values obtained in Chs. 4 and 5 for both the Mg-Ti_2AlC composites, as well as the bulk Ti_2AlC samples, with comparable grain sizes, were essentially comparable. This, as noted earlier, is important result because it implies that most of the energy dissipated is occurring in the Ti_2AlC phase. This is not unreasonable because Zhou et al. showed that W_d in Mg [59] and other HCP metals [58] is a function of grain size, wherein the fine-grained samples essentially exhibit less kinking as compared to the coarse-grained ones. Thus, it is fairly reasonable to assume that the contribution of the nanocrystalline Mg matrix of the Mg-Ti_2AlC composites towards W_d and ε_{NL} is almost nil.

In order to examine the validity of the KNE microscale model for composite materials, *isostrain* and *isostress* conditions were assumed to be the governing conditions for MI-P and MI-N composite materials, respectively (Figure 7.1). Under *isostrain* conditions, each component has a uniform deformation, while in *isostress* conditions each material has a uniform stress. The stress and strain, for isostrain and isostress conditions, respectively, are in general "additive" and depend on the moduli and volume fraction of each component.

Initial calculations assuming *isostrain* conditions and k_1=2 in both MI-P and MI-N composites, resulted in $\frac{\Omega}{b} \approx 38.5$ MPa, which is in excellent agreement with the findings

described in Chs. 4 and 5. However, further calculations assuming *isostress* conditions and k_1=2 in both MI-P and MI-N composites, resulted in $\Omega/b \approx 250$ MPa. Obviously, according to the results discussed in Ch. 5 and those of Refs. [45, 57], this value cannot be correct because it is neither in agreement with Ω/b values of Ti_2AlC nor with Mg. Therefore, the KNE model can numerically predict what stress or strain conditions are governing the MAX-metal composite samples at the microscale, if a reasonable picture of the behavior of its constituents is available.

More importantly, in-depth knowledge of the true texture, as explained above, is required in order to determine, more accurately, the fraction of the material capable of withstanding applied stresses and consequently the strains induced in the sample. It is hereby acknowledged that more work is needed to fully understand the behavior of Mg-Ti_2AlC composites, and to further develop the KNE microscale model for such solids.

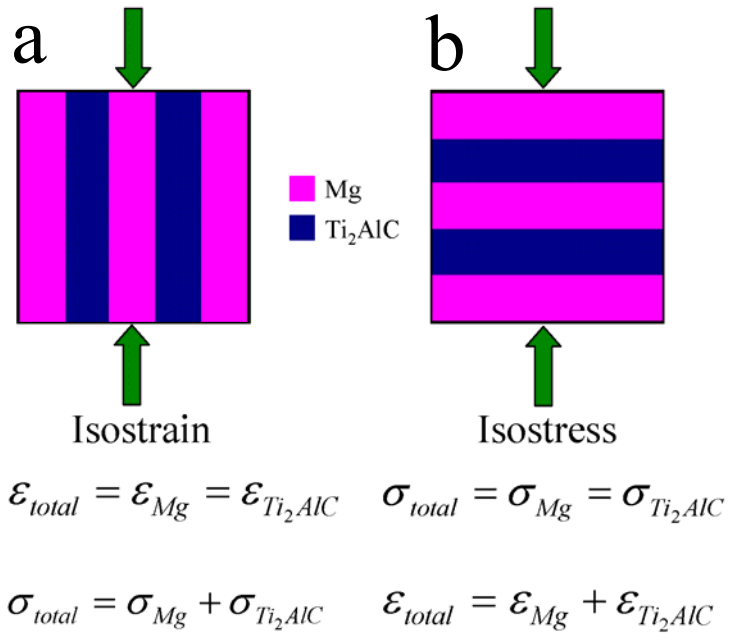

Figure 7-1: Schematic of, (a) isostrain, and, (b) isostress conditions in Mg-Ti_2AlC composites showing strain and stress continuity across the constituent phases.

7.3.3. Fabrication and Mechanical Properties of AZ31B-Ti_2AlC composites

We attempted to fabricate Ti_2AlC reinforced composites by MI using AZ31B Mg alloy. The UCS and $\overline{E}$ were measured to be 870±20 MPa (Figure 7.2) and 100±4 GPa, respectively. These results are noteworthy because usually the addition of metallic phases to binary carbides and nitrides decreases the strength [107]. The strength values achieved here by the addition of 50 vol. % AZ31B Mg alloy to Ti_2AlC are the highest ever reported for a Mg-based composite with 50 vol.% Mg. The fact that the average UCS of the latter is slightly higher than its monolithic counterpart, Ti_2AlC, is remarkable.

The $\overline{E}$ values obtained here are ~ 30% higher than those of the pure Mg-Ti_2AlC composites; an enhancement that could be attributed to the presence of AZ31B alloy as opposed to pure Mg and more importantly, the nanocrystalline nature of the matrix.

For cyclic compression tests, five cycles are obtained at each load (Figure 7.3). For the most part, the first cycles were very slightly open, registering a plastic strain of the order of ~ 0.01%.

The results obtained here could be important research directions for the future to understand the kinking non-linear elasticity of these composites.

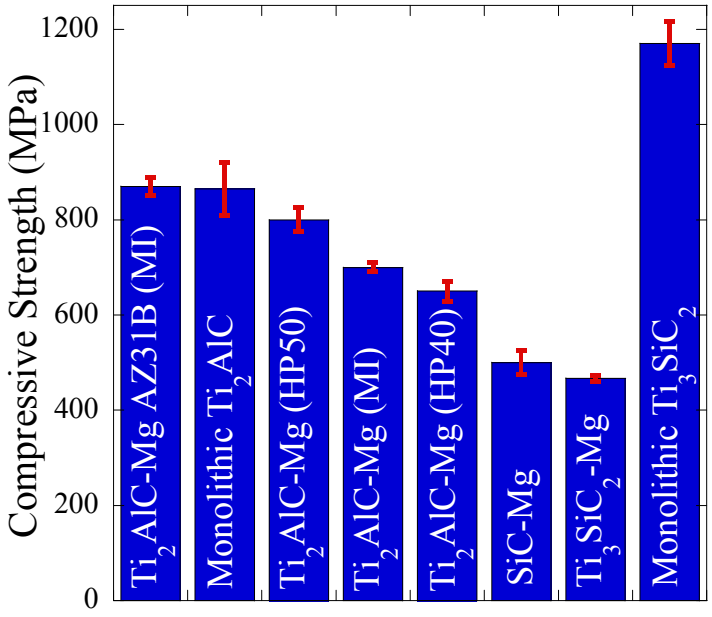

Figure 7-2: Plot of ultimate compressive strength (UCS) values of all materials tested in this work compare to Mg-Ti_2AlC AZ31B alloy composite.

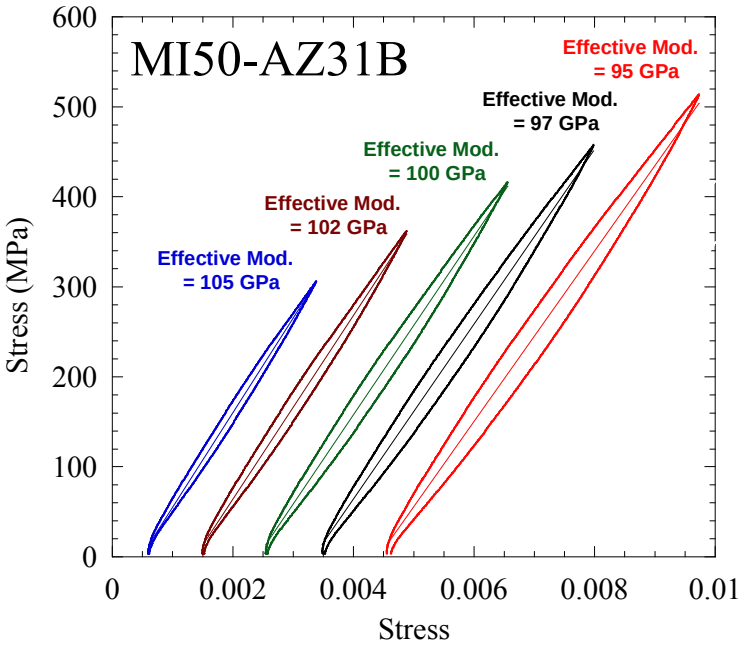

Figure 7-3: Typical compressive stress-strain curves of Mg-Ti_2AlC AZ31B alloy composite; only one cycle per load is shown and the curves are shifted horizontally for clarity.

7.3.4. Nano- and Macro- Mg Crystal Growth

The current thesis showed that solids such as Ti_2AlC-nc Mg composites are of great importance and the study of the formation of a nanocrystalline metal matrix from its melt, may not only lead to new applications, but its study should enhance our understanding of the behavior of a new class of composites with exceptional properties.

Throughout this research, we developed a simple technique (Figure 7.4) to grow Mg crystals on a variety of substrates such as alumina (Figure 7.5a), titanium foil (Figure 7.5b) and vanadium foil (Figure 7.5c and 7.5d). These crystals can be grown by a simple evaporation-condensation technique from molten Mg. Interestingly, in some cases, e.g. on vanadium foils, abnormal growth of Mg from the surface of these single crystals led to the formation of 3D *starfish* nanocrystals (Figure 7.5 e and f). Also on the surface of V, Nb and Ta, nanocrystalline Mg particles were formed in addition to the abnormal growth of Mg crystals (Figure 7.5g).

These discoveries are not only fascinating, but also are of some importance because the formation of Mg single crystals using the simple techniques mentioned above can be utilized in understanding the mechanical properties of Mg with robust techniques such as nanoindentation.

Recently, Basu *et al.* [204] have described a new constant-stress, spherical nanoindentation technique to study the creep of brittle crystals such as ZnO single crystals (Figure 7.6).

They claim that this method can be used to quantify other time dependent mechanical properties, such as fatigue and subcritical crack growth, at the submicron, and

even nanoscale. Syed *et al*. have done extensive study on indentation creep on the nanometer scale on single-crystal indium, tungsten and gallium arsenide [205]. Zhou *et al*. investigated micro/nano indentation hardness of aluminum and silicon single crystals [206]. Liu *et al*. investigated nanoindentation on copper single crystals [207]. Also recently it has been shown by Kim *et al.* that the mechanical properties such as yield strength at the nanoscale depends strongly on sample size and not on the initial dislocation density, which is substantially different from that of the bulk metals [208].

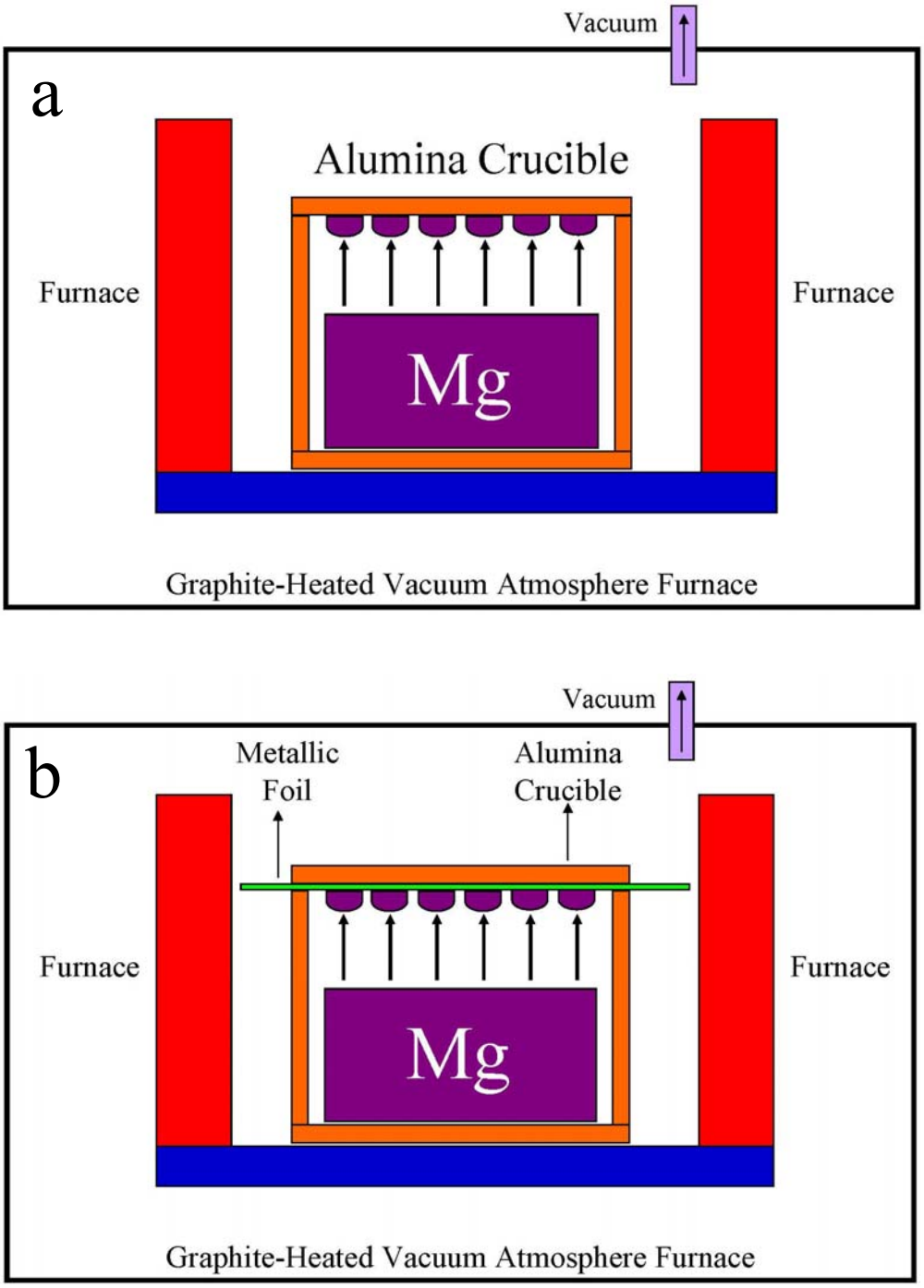

Figure 7-4: Schematic of the evaporation-condensation technique to make Mg single crystals and nano-Mg coatings on the surface of (a) alumina, (b) metallic films.

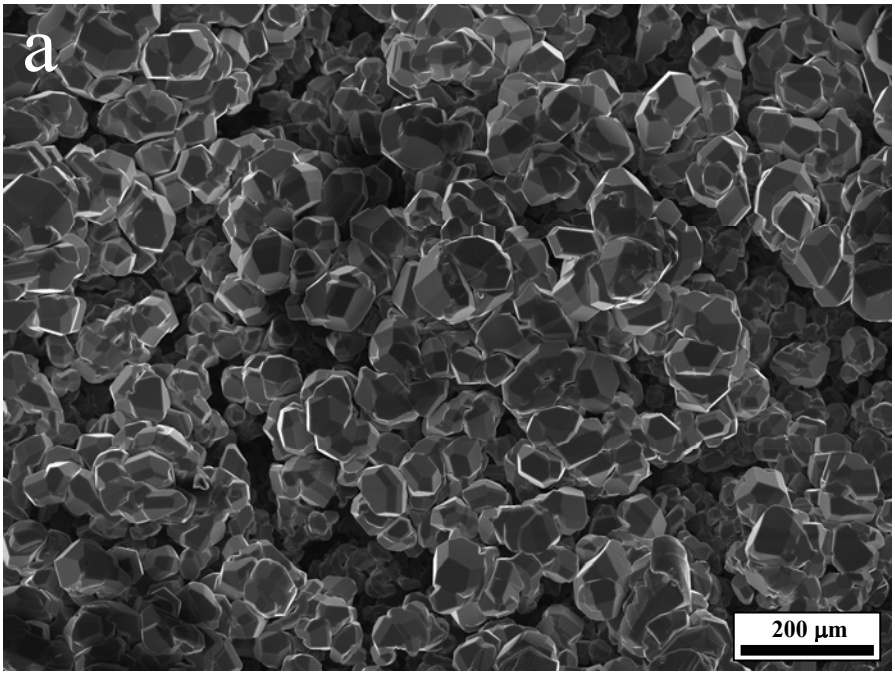
a
200 µm

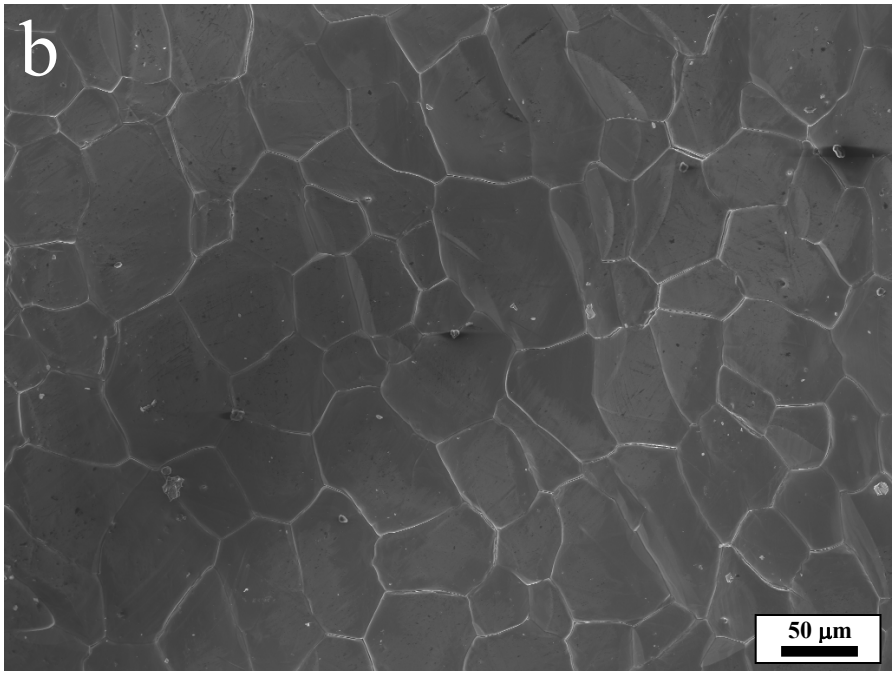
b
50 µm

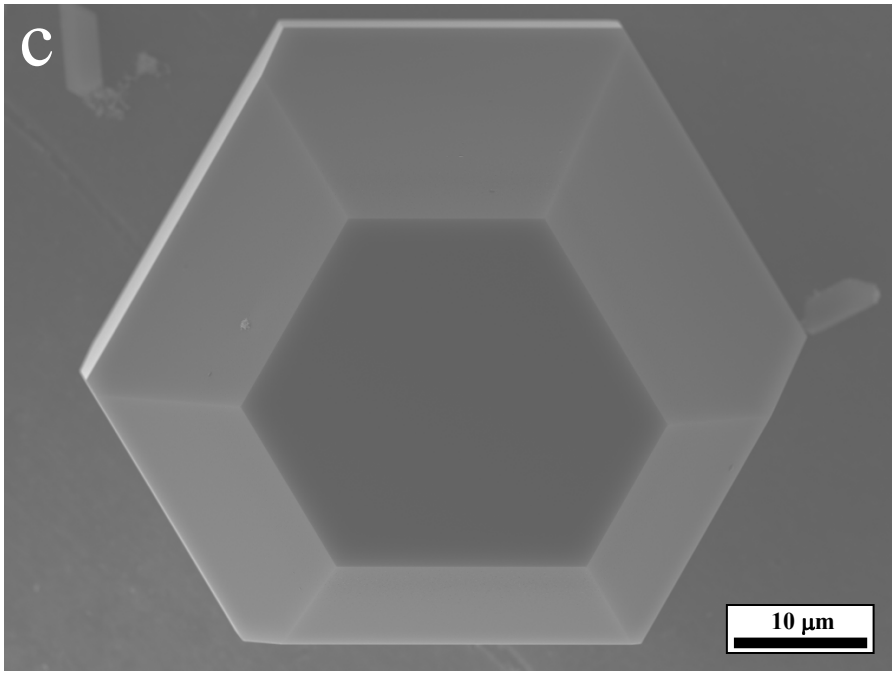
c
10 µm

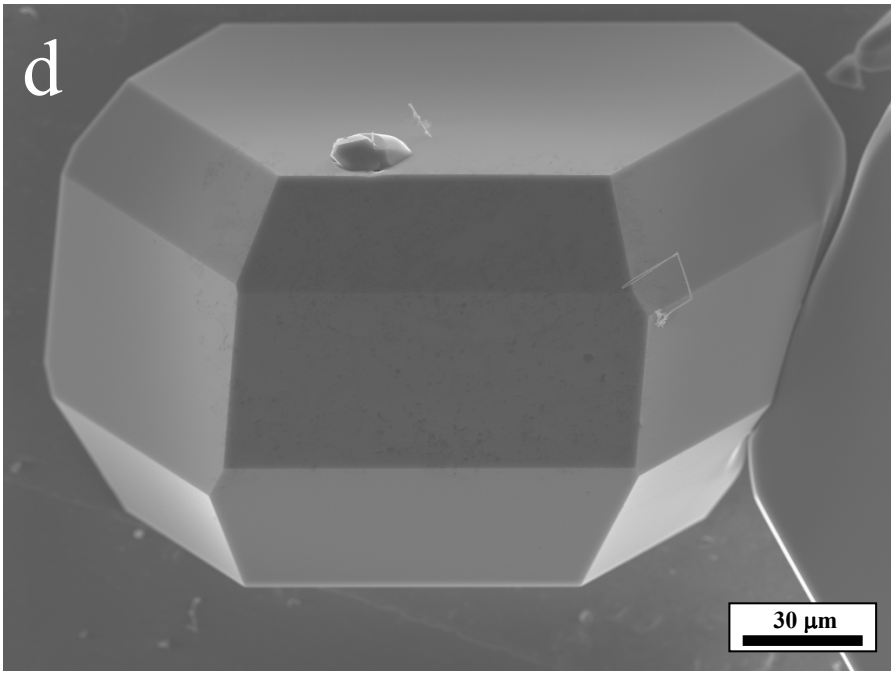
d
30 µm

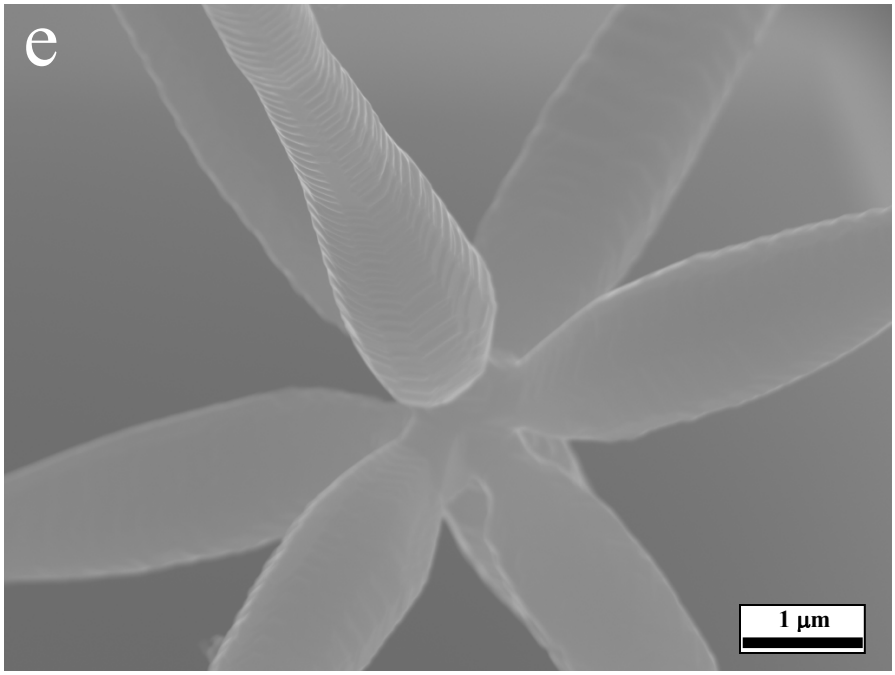
e
1 μm

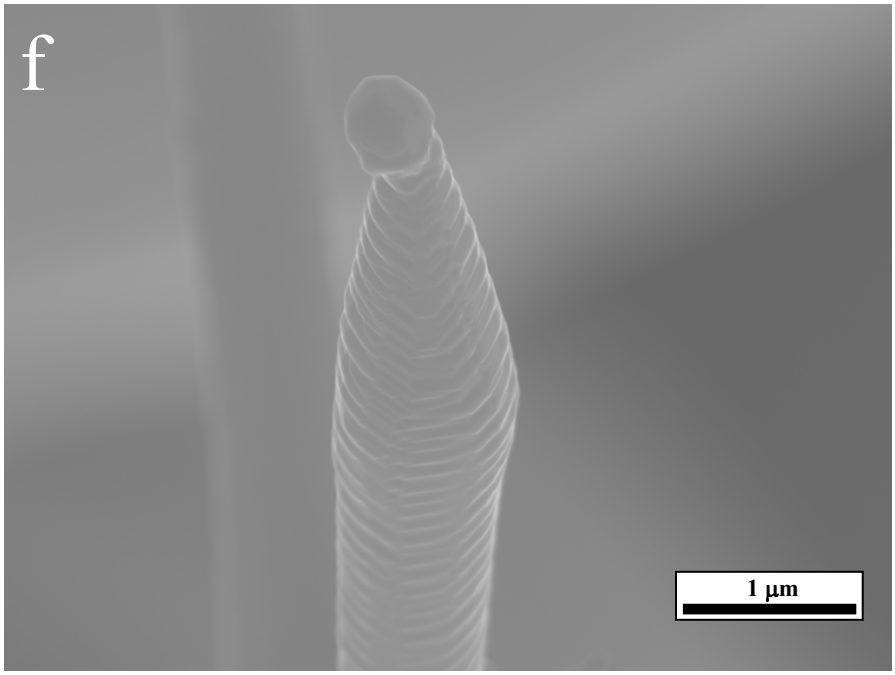
f
1 μm

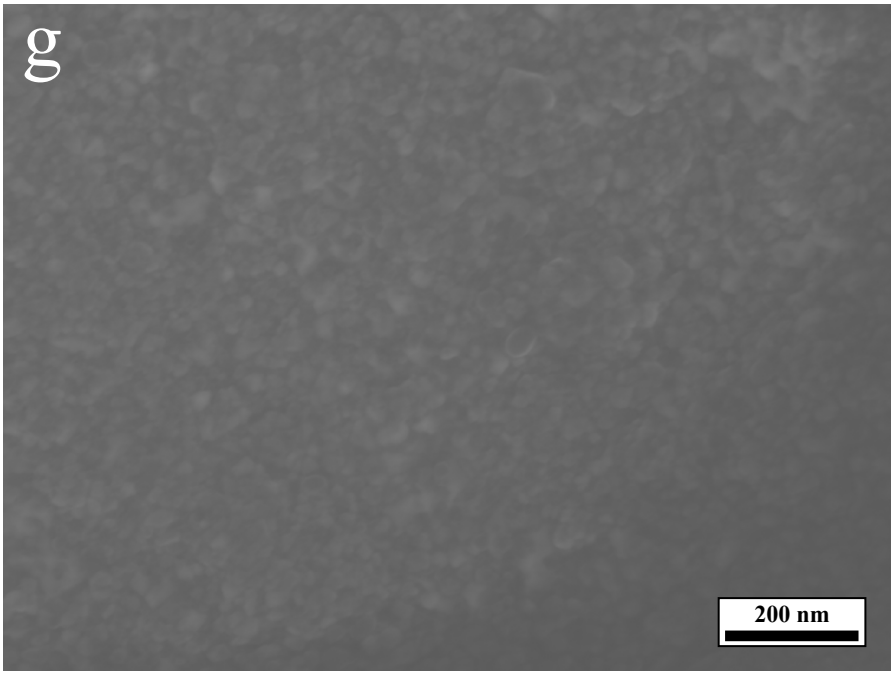

Figure 7-5: Mg crystals grown on a) alumina, b) titanium foil, c and d) vanadium foil; e and f) 3D starfish Mg nanocrystals grown on vanadium foil; g) nanocrystalline Mg formed on the surface of Nb film.

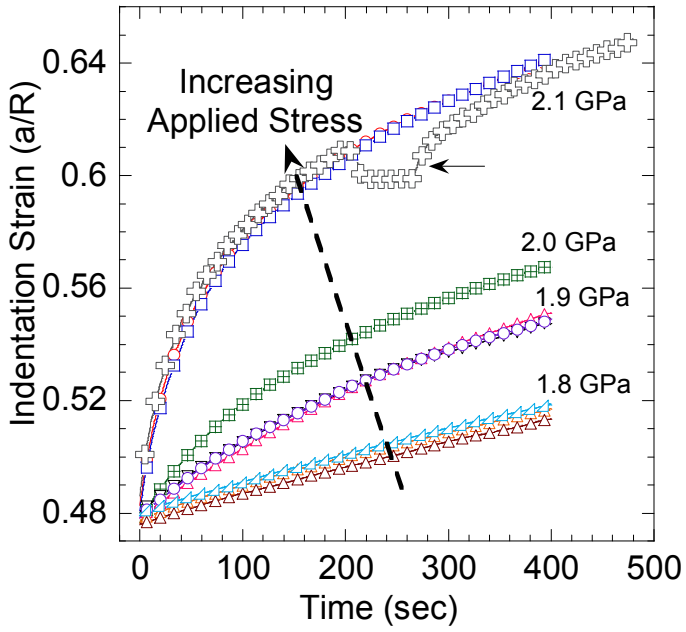

Figure 7-6: Time dependence of nano-indentation strain at stresses shown for ZnO single crystals. Horizontal arrow points to a run that was interrupted for 50 s, 200 s into the creep run [204].

As far as we are aware, there has not been any work done on nanoindentation creep and/or mechanical properties of Mg single crystals at the nanoscale. During our initial attempts, we have shown that nanoindentation experiments (Figure 7.7) on Mg single crystals grown on alumina substrates up to stress levels of the order of ~ 1 GPa agree favorably with what is known in the literature. More importantly, cyclic nanoindentation loadings have shown the formation of fully reversible, hysteretic stress-strain loops, consistent with our results on bulk Mg [58, 80]. These results are in excellent agreement with the work of Zhou *et al*. [209] that was performed on bulk Mg.

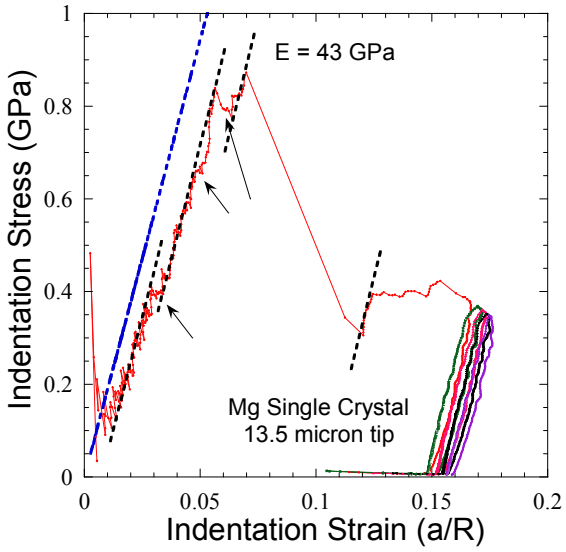

Figure 7-7: Spherical nanoindentation stress-strain results on Mg single crystals.

While each of these individual avenues of research is sufficiently broad and challenging, the overlap between these projects comprises an intriguing and coherent perspective that is beneficial to the MAX phase research group.

Appendix A : On the Synthesis and Mechanical Properties of Ti_2SC

AA.1. Introduction

The $M_{n+1}AX_n$ (MAX) phases are layered hexagonal solids with two formula units per unit cell, in which near close-packed layers of M are interleaved with layers of pure group A-element, with the X-atoms filling the octahedral sites between M layers. Titanium sulfur carbide (Ti_2SC) is a member of this new class of ternary carbides [8, 210]. Like the others, the unit cell of Ti_2SC is hexagonal (space group $D^4_{6h} - P6_3/mmc$). At *1.122 nm,* its c-lattice parameter is the lowest of all MAX phases [210]. Because of this low value - partially attributable to the small diameter of S - it was postulated that Ti_2SC could possibly exhibit unusual mechanical properties as compared to the other known MAX phases [8].

There has been reports on its electronic, thermal, magnetic, and elastic properties [211]. The room temperature thermal conductivity (≈ 60 W/mK) is the highest of any MAX phase measured to date. The Young's, shear, and bulk moduli, determined from ultrasonic measurements, are 290, 125, and 145 GPa, respectively [211]. The electrical conductivity is metallic-like and equal to $1.9\times10^6\ \Omega^{-1}m^{-1}$ at room temperature. Its Debye temperature is 765 K [211]. The bulk modulus, calculated, using the Birch-Murnaghan equation of state, is 191±3 GPa [212] which is comparable to those of Ti_2AlC, Nb_2AlC and V_2AlC. It has also been shown that the tribological properties of Ti_2SC against alumina are excellent over the 25 to 550°C range [213].

In this chapter we report on the synthesis and mechanical properties of fully dense polycrystalline Ti_2SC samples with two different grain sizes, for the first time.

AA.2. Experimental Procedures

Phase-pure -325 mesh Ti_2SC powders (3-ONE-2, Voorhees, NJ) were HPed in a graphite-heated, vacuum atmosphere HP (Series 3600, Centorr Vacuum Industries, Somerville, MA). The powder was poured and wrapped in graphite foil, which in turn was placed in a graphite die and heated at 10°C/min until the target temperatures were reached. The samples were held for ~ 5 h, at 900°C, 1100°C, 1250°C, 1350°C or 1500°C. A load, corresponding to a stress of ~ 45 MPa, was applied at 500°C and maintained throughout the entire process. Some samples HPed at 1500°C, were further annealed for 20 h at 1600°C under an Ar atmosphere in a tube furnace in order to increase their grain size. The density was measured using Archimedes method in ambient temperature water. To prevent water from penetrating into the pores, the samples were coated with a thin layer of grease.

Powders, obtained by drilling near the center of the samples, were placed in a diffractometer (Model 500D, Siemens, Karlsruhe, Germany) and their spectra were collected at a step scans of 0.02 2θ and a step time of 1 s. Scans were made with Cu Kα radiation (40 KV and 30 mA). Silicon powder was added as an internal standard.

The microstructures of mounted and polished samples were observed using a field emission SEM (FEI/Phillips XL30, Hillsboro, OR) and OM (Olympus PMG-3, Tokyo, Japan). The samples were polished with diamond solutions down to 1 μm, followed by a final surface finish with a colloidal silica suspension. Etching was carried out for 10 s with a 1:1:1 (volume) H_2O:HNO_3:HF etchant solution.

Compressive strength measurements were performed using a hydraulic testing machine (MTS 810, Minneapolis, MN) on small 3×3×3 mm^3 cubes at room temperature. The cubes were EDMed. Six samples were tested. All compression tests were performed in load-control mode at a loading rate of 54 MPa/s. EDMed cylinders, 9.7 mm in diameter and 31 mm high, were used to carry out cyclic compression tests. The strains were measured by a capacitance extensometer (MTS, Minneapolis, MN) with a 1 % range attached directly onto the specimen surface.

The nanoindenter (XP System, MTS, Oak Ridge, TN) used in this work was equipped with a CSM attachment. All tests were carried out with a load rate over load factor of 0.1. The harmonic displacement for the CSM was 2 nm with a frequency of 45 Hz. A diamond spherical tip with radius of 13.5 μm was used.

The V_H - measured using a LECO-M400 (LECO Corp. St. Joseph, MI) - were determined by averaging at least 40 measurements on different samples at 2, 3, 5 and 10 N. The indentation time was set to be 15 s per indent. The V_H values were measured at Oak Ridge National Laboratory (Wilson-Tukon 2100, Instron, Norwood, MA). The results are an average of 4 indents at each loads of 50, 100, 200 and 300 N. The V_H were carried out on both HPed and annealed samples.

We also attempted, unsuccessfully, to densify the powder by HIPing at 1500 °C and 1600 °C, under a pressure of 150 MPa and a time of 5 h. In all cases the resulting samples were ~ 30 vol. % porous in their center, and ringed with a thin layer (~1 mm) of dense material. And whereas these samples were not characterized, their lattice parameters were measured (see below). To obtain powders from these samples their surfaces were initially

ground to remove the glass that was utilized for HIPing. After mounting and polishing that revealed the dense outer layer and the porous core, which were readily observable by naked eye, powders were carefully ground from both regions using a metal file.

Typically, as a result of high damage tolerance in MAX phases, it is quite difficult to cause cracks to emanate from the corners of Vickers indentations [74]. Because Ti_2SC is more brittle (see below) cracks do emanate, which in turn allows for an estimation of the fracture toughness, K_{1c}. Measured crack lengths are correlated to K_{1C} through a semi-empirical relationship [214-216]:

$$K_{1c} = X(\frac{E}{V_H})^{\frac{1}{2}} \frac{P}{a^{\frac{3}{2}}} \qquad \text{(Eq. A.A.1)}$$

where P is the applied load, E is the Young's modulus, a is the radial crack length and X is a constant (0.016).

AA.3. Results and Discussion

In a typical XRD pattern (Figure AA.1a) of a sample HPed at 1500°C, no peaks other than those associated with Ti_2SC, anatase and Si (used as an internal standard) were observed. Table AA.1 is a summary of our data and those reported by Kudielka *et al.* [217] for Ti_2SC and Horn *et al.* [218] for anatase; the agreement is excellent. The *a* and *c* lattice parameters calculated herein, 3.205±0.002 Å and 11.208±0.004 Å, respectively, are comparable to those reported by Kudeilka and Rhode [217], (3.21 Å and 11.2 Å) and Nowotny [210] (3.216 Å and11.22 Å). Note peak at 25.251 was identified as the anatase (1 0 1) peak. Table AA.2 lists the lattice parameters and unit cell volumes calculated for

different samples processed under various conditions. Based on these results we conclude that the a and c lattice parameters are, respectively, 3.205±0.002 Å and 11.208±0.004 Å.

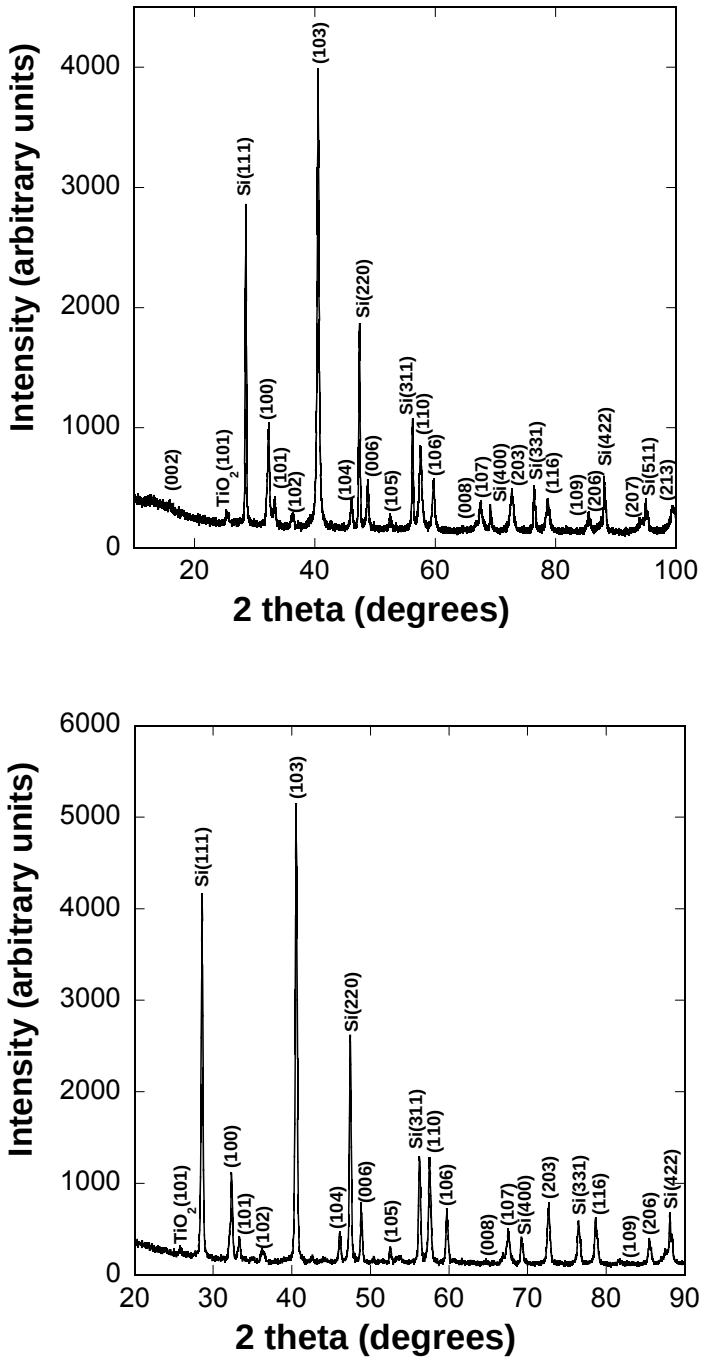

Figure AA.1: Indexed X-ray diffraction pattern of Ti_2SC after, a) HPing at 1500°C for 5 h, and b) annealing the same sample at 1600°C for 20 h.

Table AA.1: Summary of the XRD data measured in this work and those measured by Kudielka and Rhode [217].

hkl	2θ	2θ [219]	Intensity	Intensity [217]
(0 0 2)	15.806	15.841	4	2
(1 0 1)‡	25.251‡	25.209	..	anatase
(1 0 0)	32.344	32.244	22	23
(1 0 1)	33.318	33.229	7	5
(1 0 2)	36.246	35.966	5	3
(1 0 3)	40.548	40.491	100	100
(1 0 4)	46.100	46.035	9	7
(0 0 6)	48.841	48.790	15	16
(1 0 5)	52.497	52.455	6	3
(1 1 0)	57.532	57.480	25	19
(1 0 6)	59.708	59.684	13	14
(0 0 8)	66.893	66.763	4	2
(1 0 7)	67.558	67.527	9	11
(2 0 3)	72.687	72.545	15	18
(1 1 6)	78.675	78.690	12	13
(1 0 9)	85.499	85.387	8	7
(2 0 6)	87.587	87.493	5	4
(1 1 8)	93.980	93.796	4	3
(2 0 7)	94.505	94.498	4	5
(2 1 3)	99.398	99.400	13	14

‡: 2θ of the 100 peak associated with anatase

Table AA.2: Lattice parameters and unit cell volume of various samples after various processing parameters.

Processing Parameters*	*a* lattice parameter (Å)	*c* lattice parameter (Å)	Unit cell volume (Å^3)
Bulk powder	3.205	11.210	99.75
HP-900˚C	3.209	11.205	99.73
HP-1100˚C	3.206	11.207	99.79
HP-1350˚C	3.208	11.206	99.77
HP-1500˚C	3.203	11.217	99.67
HP-1500˚C→ A-1600˚C	3.208	11.201	99.83
CIP→ HIP-1500˚C (Dense skin)	3.203	11.212	99.73
CIP→ HIP-1500˚C (Porous core)	3.205	11.210	99.62
PS-1500˚C→ HIP-1500˚C (Dense skin)	3.204	11.201	99.62
PS-1500˚C→ HIP-1500˚C (Porous core)	3.204	11.208	99.73
PS-1600˚C→ HIP-1500˚C (Dense skin)	3.204	11.206	99.64
PS-1600˚C→ HIP-1500˚C (Porous core)	3.205	11.210	99.72
Average	3.206	11.208	99.72
Standard Deviation	0.002	0.004	0.06

*HP: Hot pressing; HIP: Hot isostatic pressing; CIP: Cold isostatic pressing; PS: Pressureless sintering; A: Annealing

The average unit cell volume is 99.71±0.06 $Å^3$. Given that there are no systematic variations between the lattice parameters and processing conditions, we conclude that this compound is quite stable and most probably a line compound. This is especially true given that the lattice parameters of the as-received powders and those of the HPed samples are - within the experimental scatter - identical.

Figure AA.2 shows the effect of HPing temperature on density. The porosity of the samples decreased from 40 vol. % at 900°C, to 20 vol. % at 1250°C; at 1500°C the samples were fully dense.

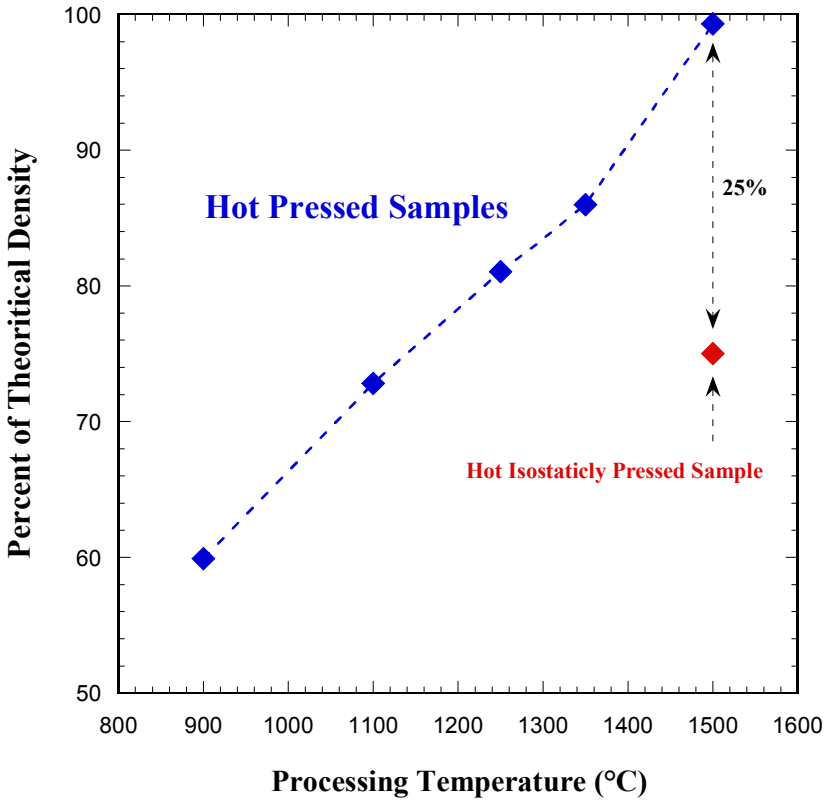

Figure AA.2: Evolution of density versus processing temperature for Ti_2SC.

The measured density at 1500°C was ~ 99 % of theoretical. As noted above, the HIPed samples were ~ 30 vol.% porous. The reason for this state of affairs is not entirely clear; however, it is reasonable to assume that some dissociation of the compound - into a gaseous phase, occurs at the high HIPing temperatures - somehow prevents densification. Why this does *not* result in a change in the lattice parameters (Table AA.2), can be either because the gas is reabsorbed upon cooling or the amount of gas needed to prevent densification is small enough as to not alter the chemistry of the samples. It is worth noting that EDS analysis of the HPed samples showed that the concentration of Ti (~ 67.5±2.5 at. %) and S (32.5±2.5 at. %) are, within the experimental scatter, consistent with the 2:1 ratio expected.

SEM and OM micrographs of fractured and polished surfaces of a sample HPed at 1500°C, shown in Figures AA.3a and AA.3b, respectively, confirm its fully dense nature and the fact that the grains are in the 2-4 μm range. A typical backscattered SEM micrograph of a polished fine-grained sample (FG), shown in Figure AA.3c, shows the presence of two regions: a bright region corresponding to Ti_2SC and a dark minority region. The total volume fraction of the dark areas - identified by XRD to be anatase and confirmed by EDS - was estimated from image analysis to be 6±4 vol.%. Oxygen in the original powder is the most likely source of contamination. Upon heating, the oxygen reacts with Ti and forms TiO_2; why anatase forms instead of rutile in unclear.

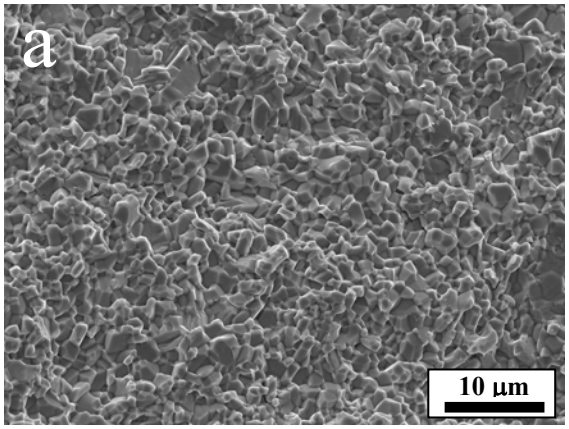
a
10 µm

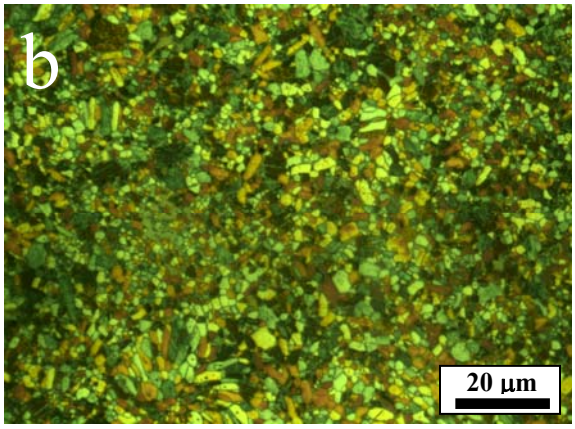
b
20 µm

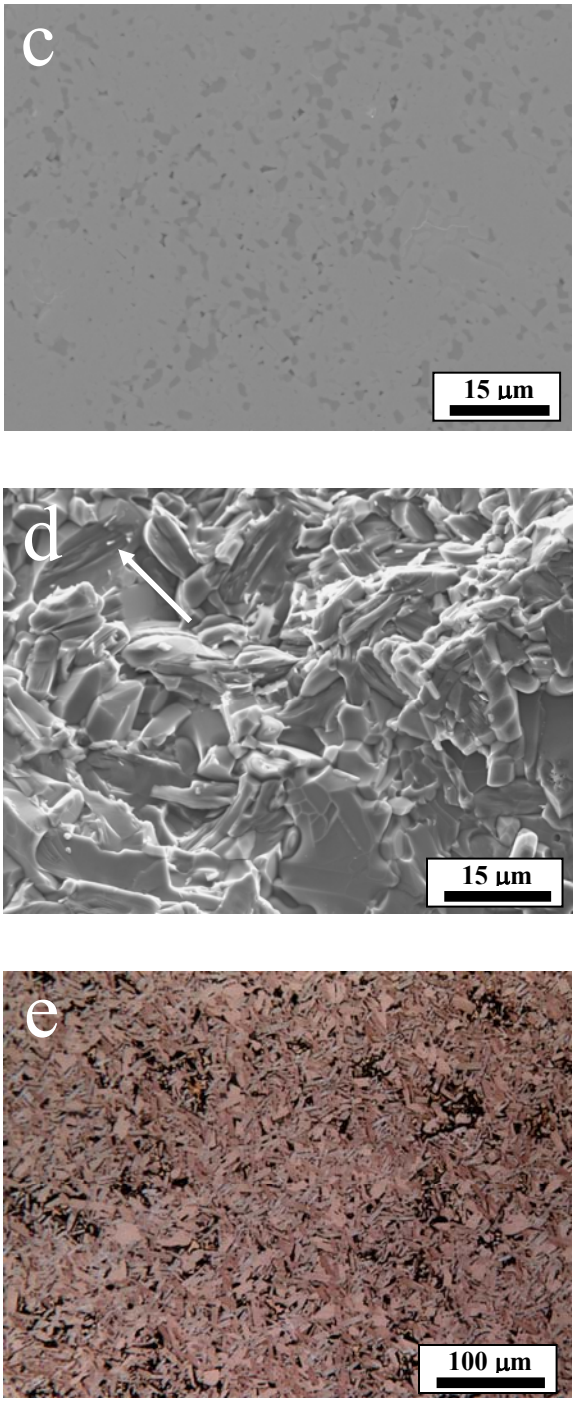

Figure AA.3: a) SEM micrograph of fractured surface of a sample HPed at 1500°C, b) Polished and etched optical micrograph of the same sample, c) backscattered SEM micrograph of polished fine-grained sample; the dark areas are an impurity phase identified as anatase, d) fractured surface of the sample HPed at 1500°C followed by heat treatment at 1600°C for 20 h and, e) polished and etched optical micrograph of the same sample.

Annealing these samples at 1600 °C for 20 h increases the grain size to the 10-20 μm range and increases their aspect ratio (Figures AA.3d and AA.3e). The high temperatures and long times needed to grow the grains imply an exceptionally stable microstructure, consistent with the thermal stability of this compound alluded to above and to those of other MAX phases such as Nb_2AlC [220]. A typical XRD pattern of the annealed sample is shown in Figure AA.1b.

And while the micrograph shown in Figure AA.3a does not show the layered nature of the compound, the fractured surface of the annealed sample (Figure AA.3d) reveals it. In the coarse-grained (CG) or annealed samples, the fracture mode becomes partially transgranular (shown by arrows in Figure AA.3d) instead of intergranular in the fine-grained (FG) samples (Figure AA.3a).

Like all MAX phases characterized to date, Ti_2SC is readily machinable. A manual hack-saw, with no lubrication or cooling, was sufficient to cut it. Because of its excellent electrical conductivity, it is also easily EDMed.

Like all other MAX phases characterized to date [146], the hardness values are initially high, decrease with increasing applied load, but then asymptote at relatively higher loads (Figure AA.4).

Why the hardness for the FG samples increases slightly at the highest load is not understood. What is obvious, however, is that the HPed samples, with their finer microstructure, are harder than their coarser-grained counterparts. The scatter in the results is typical of other MAX phases and is a result of the presence of only two independent basal slip systems [17, 74, 146].

Typical SEM micrographs of Vickers indentation marks formed under forces of 10 N, 50 and 300 N for the CG samples are shown, respectively, in Figures AA.5a-c; the corresponding micrographs for the FG samples are shown in Figures AA.5d and e. A comparison of these micrographs reveals that, like other MAX phases examined to date [17, 24, 29, 49, 220], no cracks are observed to emanate from the corners of the Vickers indentations of the CG samples, even at the highest loads (Figures AA.5a-c). This damage tolerance is a hallmark of the MAX phases and results from the activation of basal slip.

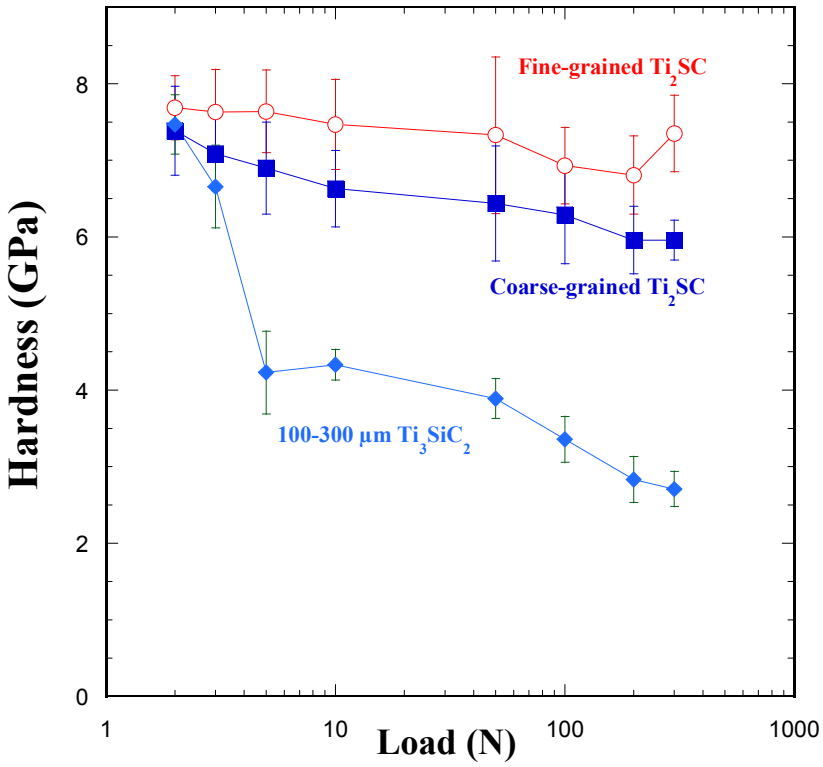

Figure AA.4: Semi-logarithmic plot of V_H versus indentation load for fine and coarse grained Ti_2SC. Also included are the results for Ti_3SiC_2 with a grain size in the 100-300 µm range for the sake of comparison [8].

Of the various energy absorbing mechanisms responsible for this damage tolerance - first described for Ti_3SiC_2[17] - only the pile-up of material around the indenter is readily observed but only when loaded to 10 N (Figure AA.5a).

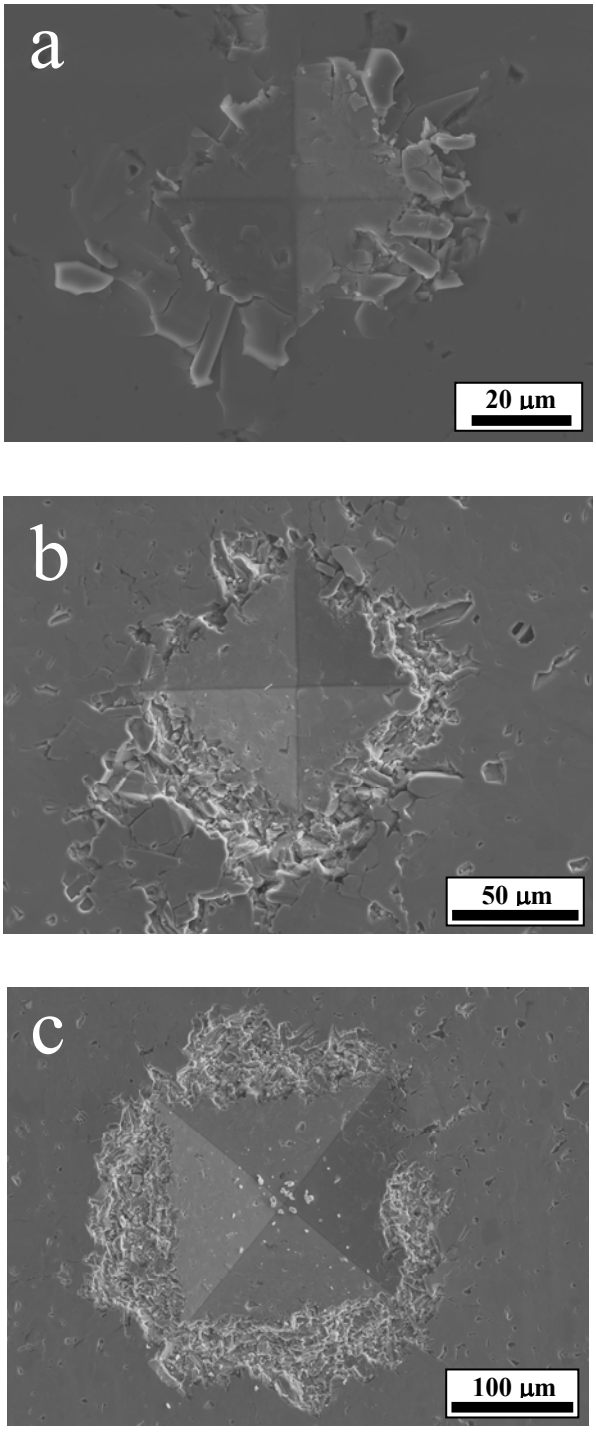

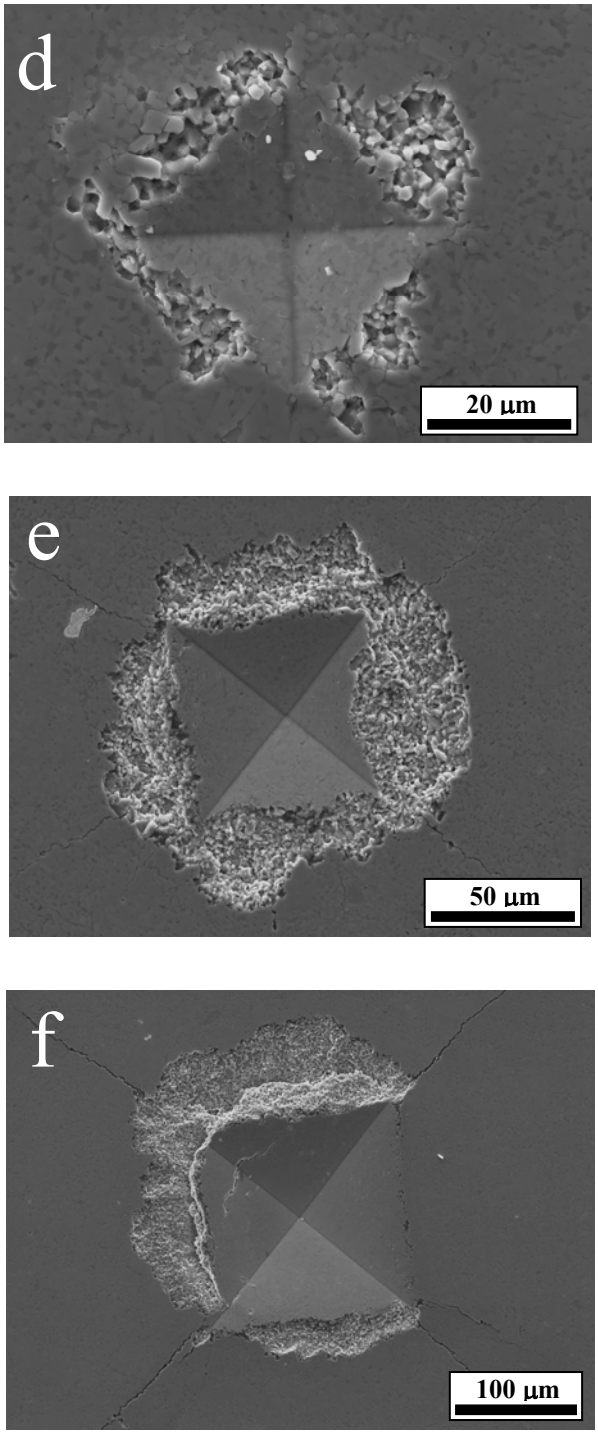

Fig. AA.5: SEM micrographs of Vickers indentations of, a) CG sample at, 10 N, b) 50 N and c) 300 N. FG sample at d) 10 N, e) 50 N and f) 300 N.

After loading to 50 and 300 N (Figures AA.5b and AA.5c) these pileups are less clear, most probably because of the flaking off of the topmost grains Also in agreement with previous work, no cracks emanate at the corners of the indents even at highest loads.

The indents in the FG samples (Figures AA.5d, e and f) are similar their CG counterparts in that little pile-up of material is apparent around the indentations. Most interestingly, and unusual for the MAX phases, is the presence of cracks emanating from the corners of the 50 and 300 N indents (Figures AA.5e and f), clearly indicating that the FG samples are more brittle than their CG-counterparts. The primary energy dissipation mechanism in the MAX phases is kinking, a form of buckling [52, 53, 56, 57, 221]. It follows that since kinking is easier in CG samples, they are less brittle than their FG counterparts.

The brittleness is also manifested by the substantial fraction of grains around the indents that seem to have flaked off as a result of the indentation (compare the micrographs in Figure AA.5).

Because the V_H values of TiO_2 (10±0.1 GPa [182]) is slightly higher than the hardness values reported herein it is reasonable to assume that the hardness of phase-pure Ti_2SC would have been lower than those reported herein. However, we have reported elsewhere [112] that the presence of small volume fractions of hard impurity phases in a MAX-phase matrix affect the hardness values, only slightly and only if they are present in large volume fractions. Therefore we believe that effect of the ~ 6 vol. % TiO_2 present in our microstructures on hardness is small.

The fracture toughness, K_{Ic}, of the FG samples was found to increase with load from ~ 4 to 6 MPa√m as the Vickers force was increased from 50 to 300 N, respectively (Figure AA.6). This reason for the increase is not entirely clear, but could possibly be related to the strong R-curve behavior exhibited by the MAX phases [222]. The average ultimate compressive strength of the six samples loaded to failure was 1.4±0.2 GPa. None of the samples exhibited plastic deformation before failure, which was brittle in nature.

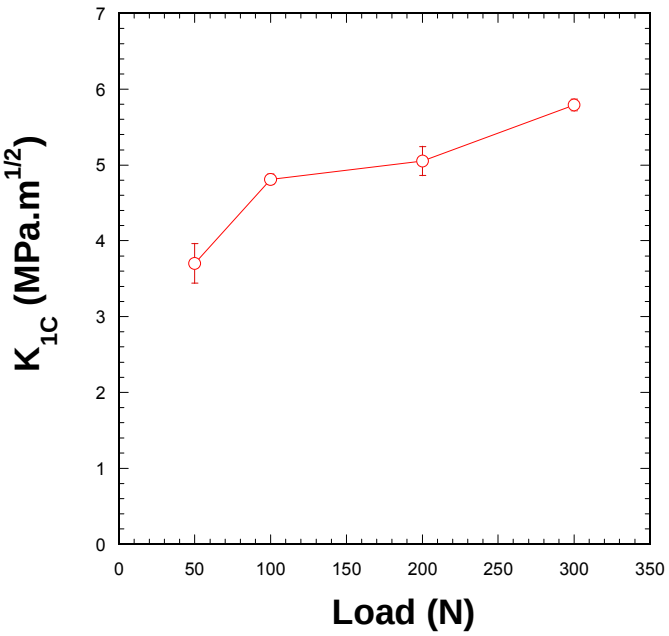

Figure AA.6: Fracture toughness calculated from Vickers indents as a function of applied indentation load for fine-grained Ti_2SC.

The average ultimate compressive strength of the six samples loaded to failure was 1.4±0.2 GPa. None of the samples exhibited plastic deformation prior to failure, which was brittle in nature.

Figure AA.7a and AA.7 shows a typical stress-strain curve of a FG and CG samples loaded to ≈ 55 % of the failure stress. Unlike other known MAX phases to date, the behavior was fully elastic till failure. For the sake of comparison, the behavior of a fine-grained Ti_3SiC_2 under cyclic compression is shown on the same figure [56]. In other words, there was no evidence for the formation of incipient kink bands typical of other MAX phases [28, 57]. We have argued in several papers that the loading–unloading stress–strain curves of MAX phases outline nonlinear, fully reversible, strain-rate independent, reproducible, closed hysteretic loops whose shape and extent of energy dissipated are strongly influenced by grain size, with the energy dissipated being significantly larger in coarse-grained solids [57, 74]. The reason why no loops are observed here is not clear, but must be partially related to FG microstructure. These comments notwithstanding, it is hereby acknowledged that other factors, such as solid solution or precipitation hardening may be at play.

At 316±2 and 310±3 GPa, the Young's modulus of FG and CG Ti_2SC – determined from Figure AA.7 by linear extrapolation of stress-strain data obtained directly from uniaxial compression test - is one of the highest reported for a M_2AX compound and rivals that of Ti_3SiC_2. These values are ~ 8 % higher than the one measured from ultrasonic experiment [212]. With a measured density of 4.59 Mg/m^3, the specific stiffness of Ti_2SC is slightly lower than those of Ti_3SiC_2 or Si_3N_4.

It is worth noting that loops were observed under repeated spherical nanoindentations loadings (Data Courtesy of Dr. Sandip Basu). Figure AA.8 shows the nanoindentation stress-strain curve results on a single spot after 8 indentation cycles. The presence of fully reversible hysteretic loops with the exception of the first loop that is

always open proves that the mechanical energy is dissipated. As we have argued in several previous papers, this is the signature of the formation of IKBs. More importantly, the nanoindentation stress-strain curves are in excellent agreement with our V_H results. Figure AA.9 show the SEM micrograph of the indent mark formed under spherical indenter. Pile-up of material around the indenter is readily observed.

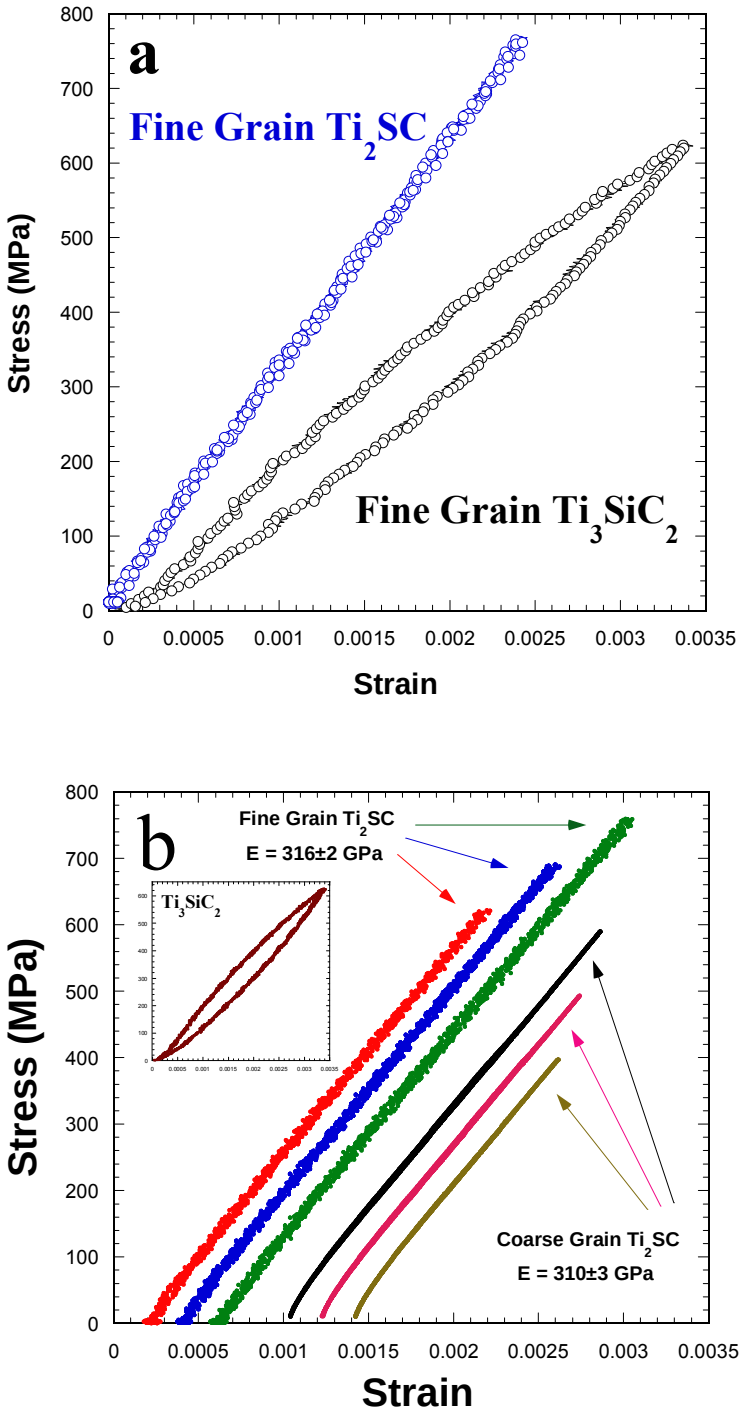

Figure AA.7: (a) Stress-strain curve in compression of fine-grained Ti_2SC sample loaded to 55 % of the failure stress; Also shown is a typical curve for Ti_3SiC_2 with comparable (3-5 μm) grain size for the sake of comparison; (b) Stress-strain curve in compression of coarse-grained Ti_2SC sample loaded to 55 % of the failure stress; Also shown is a typical curve for the fine-grained Ti_2SC and Ti_3SiC_2 (inset) for the sake of comparison.

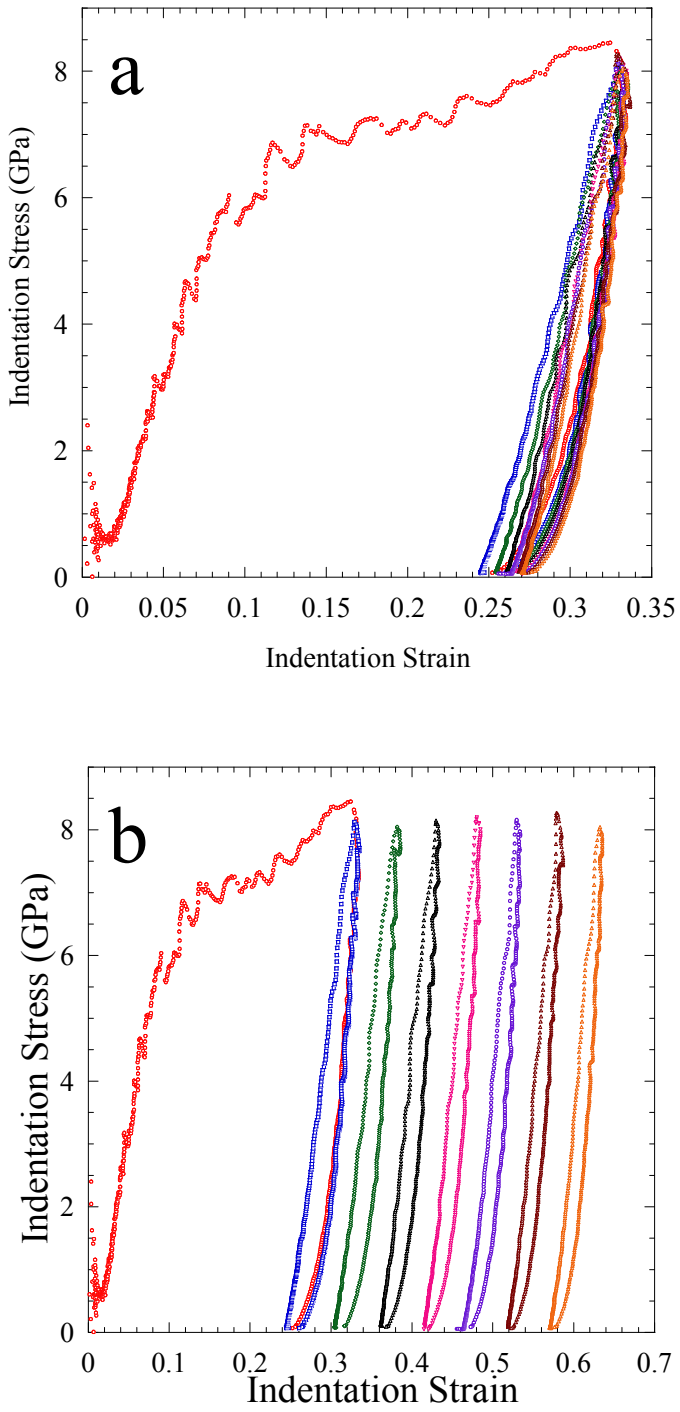

Figure AA.8: (a) Nanoindentation stress-strain curves obtained from a single spot after 8 indentation cycles for FG Ti_2SC indicating the presence of fully reversible hysteretic loops with the exception of the first loop that is always open; (b) the same loops obtained in (a) shifter horizontally for clarity.

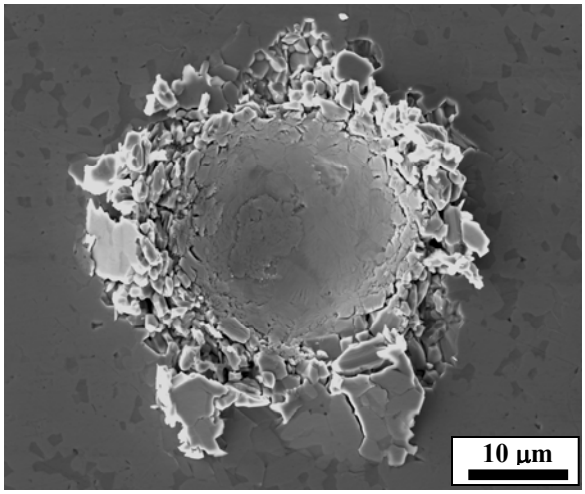

Figure AA.9: SEM micrograph of the indent formed under spherical nanoindenter on FG Ti_2SC; pile-ups around the indentation mark are obvious.

AA.4. Summary and Conclusions

Fully dense samples of Ti_2SC were fabricated, for the first time, by HPing its powders at 1500 °C for 5 h under a stress of 45 MPa. The fully dense samples had a grain size of 2-4 μm. Annealing increased the grain size to 10-20 μm range and increased their aspect ratio. Lattice parameter calculations showed that Ti_2SC is stable up to 1600°C. Unlike other MAX phases this ternary is relatively hard with V_H of ~ 8±2.

Even at a stress of 760 MPa under cyclic compression, there was no evidence for the formation of incipient kink bands and fully reversible hysteresis loops. One reason could be the small grain size. Loops were observed under repeated spherical nanoindentations; these results will be published elsewhere. With a Young's modulus of ~ 314 GPa, this material is quite stiff and with a measured density of 4.59 Mg/m^3, its specific stiffness rivals that of Ti_2AlC, and Si_3N_4. The high Young's modulus and high compressive strength together with relatively low density and relative ease of

machinability of Ti_2SC is an unusual combination that is useful whenever high specific stiffness and relative ease of machinability are required.

The V_H was a weak function of grain size and decreased slightly with increased load. Damage mechanisms around indentation marks are different for the CG and FG samples. Due to the brittleness of FG samples, cracks emanated from corners of indentation marks, when the load was >10 N; no cracks were observed in the CG samples even at the highest applied load being 300 N. Therefore, the fracture toughness of the FG samples is apparently lower as compared to CG samples.

Appendix B : On the Isothermal Oxidation of Ti_2SC in Air

AB.1. Introduction

In Appendix A, we have reported on the synthesis, microstructural characterization and mechanical properties of Ti_2SC in detail. Elsewhere, we have reported on thermal expansion and stability of Ti_2SC powders in air and Ar atmospheres using high temperature XRD [223]. Based on the result of that work, Ti_2SC is stable in Ar atmosphere up to ≈ 400ºC; above this temperature, it dissociates into TiS_2. With little anisotropy in thermal expansion, its volumetric thermal expansion was calculated to be 25.2×10^{-6} $ºC^{-1}$. In air, at 400°C, the powders start to oxidize into anatase, which, in turn transforms into rutile at higher temperatures. This work was qualitative and carried out on powders.

This section is the first work on the oxidation of bulk Ti_2SC samples, thus, it is useful to briefly review the oxidation kinetics and morphology of the oxide phases that form after long-term oxidation of other Ti-containing MAX phases in air.

When polycrystalline samples of Ti_3SiC_2, Ti_3SiC_2 – 30 vol % TiC and Ti_3SiC_2 – 30 vol % SiC are oxidized in air in the 900-1400°C range, the scales that formed were dense, adherent and resistant to thermal cycling. The oxidation mostly resulted in a duplex oxide layer (an inner TiO_2/SiO_2 layer and an outer rutile layer) and the kinetics are initially parabolic, but then become linear at longer times [18, 37, 224].

The oxidation of $Ti_{n+1}AlC_n$ ternaries in the 800-1100°C range resulted in a rutile layer in which some Al is dissolved [225]. It has also been shown that subtle changes in chemistry can result in the formation of pure Al_2O_3 layers. For example, Sundberg *et al.*

[9] have shown that Ti_2AlC forms an excellent Al_2O_3 layer that is exceedingly protective, even under intense thermal cycling. Zhou *et al.* also reported the formation of dense protective alumina layers on the surfaces of Ti_3AlC_2 [226] and Ti_2AlC [227] when oxidized in air. When the Ti_2AlC and $Ti_2AlC_{0.5}N_{0.5}$ solid solution are oxidized in air, the oxidation products are comprised of a duplex oxide layer of rutile-based solid solution and Al_2O_3. In the 1000-1100°C temperature range and for short times (≈ 20 h) the oxidation kinetics is parabolic. At 900°C, the kinetics are quasi-linear and up to 100 h the outermost layers that form are almost pure rutile, dense and protective [225]. In $Ti_4AlN_{2.9}$ and Ti_3AlC_2, at short times (<10 h) the oxidation kinetics are parabolic in the 800-1100°C temperature range but become linear at longer times. The scales that form are comprised mainly of a rutile-based solid solution and some Al_2O_3 [225].

In Ti_3GeC_2 and $Ti_3(Ge_{0.5}Si_{0.5})C_2$, at 800°C and higher, the oxide layers formed are not protective and the oxidation kinetics are linear. At higher temperatures, GeO_2 whiskers, visible to naked eye, form on the surface of the Ti_3GeC_2 [228].

Herein, we report on the isothermal oxidation behavior of bulk Ti_2SC samples in air in the 500°C to 800°C temperature range. From a technological point of view, it is crucial to determine whether the oxidation kinetics remain parabolic or become linear. More importantly, given that the oxidation products of both C and S are gases, it was postulated that its oxidation behavior may be considerably different from other Ti-containing MAX phases.

AB.2. Experimental Procedures

Processing details are fully reported in Appendix A. The oxidation study was carried out using a D-101 CAHN thermobalance (Thermo Electron Co., Waltham, MA). The resolution of our balance was 0.1 mg. Rectangular specimens ($4\times4\times10$ mm^3) were machined out of the bulk hot pressed samples using a precision diamond blade. All sides of the samples were polished up to 1200 grit SiC paper. The samples were placed in an alumina crucible that was hung by a platinum wire to the balance. The samples were oxidized in air at 500, 600, 700 and 800°C for various times that ranged from 50 h to 300 h.

At 700°C after 300 h, the experiment was followed by cyclic oxidation where the sample was cooled in the furnace to room temperature and heated up again to 700°C six consecutive times. The signal collected from the thermobalance was smoothed by signal averaging over the entire run in order to reduce the noise. The latter was done by KalidaGraph software, in which a Stineman function was applied.

For calibration purposes, 5 small $4\times4\times4$ mm^3 EDMed cubes were oxidized in air at 500, 600 and 700°C for 300 h. Samples' weights were measured by a HR-202i Analytical Balance (A&D Weighing, San Jose, CA) with a resolution of 0.01 mg, before and after oxidation. These results were used to calibrate the thermobalance data for accuracy when needed, since the noise level in the latter was sometimes high.

We also carried out a thermogravimetric thermal analysis, TGA, measurement in air on bulk samples in a simultaneous TGA-DTA, differential thermal analysis unit (2960 SDT, TA Instruments, New Castle, DE) with a highly precise, horizontal dual-balance, in

which the exhaust gas port was connected to a mass spectrometer (Benchtop Thermostar, Pfeiffer Vacuum Inc., Nashua, NH) for analysis of the gases evolved during the experiment. The heating rate in this experiment was 20°C/min.

XRD patterns of the oxidized surface were obtained using a diffractometer (Model 500D, Siemens, Karlsruhe, Germany). The spectra were collected at a step scans of 0.02 2θ and a step time of 1 s.

The microstructure of the samples was observed using a field emission SEM (Zeiss Supra 50VP, Germany) after cross-sectioning, mounting and polishing the oxidized samples with diamond solutions down to 1 μm.

AB.3. Results and Discussion

Figure AB.1 shows the XRD patterns of the oxide scales formed at 500 and 800°C. The patterns at 600 and 700°C are similar to those at 800°C and are not shown. A single rutile layer was found to be the reaction product at all temperatures. This is not too surprising given that the oxidation products of both C and S are gases (see below) and consistent with the results on Ti_2SC powders [223]. Note that Ti_2SC peaks exist only at 500°C, because at 2-3 μm, the rutile layer formed is quite thin.

Figure AB.2 shows the weight gain due to oxygen uptake in the TGA/mass spectrometer. These results unambiguously show that the weight gain starts at ≈ 600 °C, SO_2 and CO_2 are evolved at ≈ 900 °C.

We take the lag between the temperature at which oxidation commences and time SO_2 and CO_2 are evolved to indicate that the latter only start evolving after the oxide

layer thickness reaches a critical value and/or the pressure of the gases is high enough to – cause fissures, pores and/or microcracks. Such a conjecture is also consistent with the fact that the kinetics starts off parabolic, but then become linear after longer times (see below).

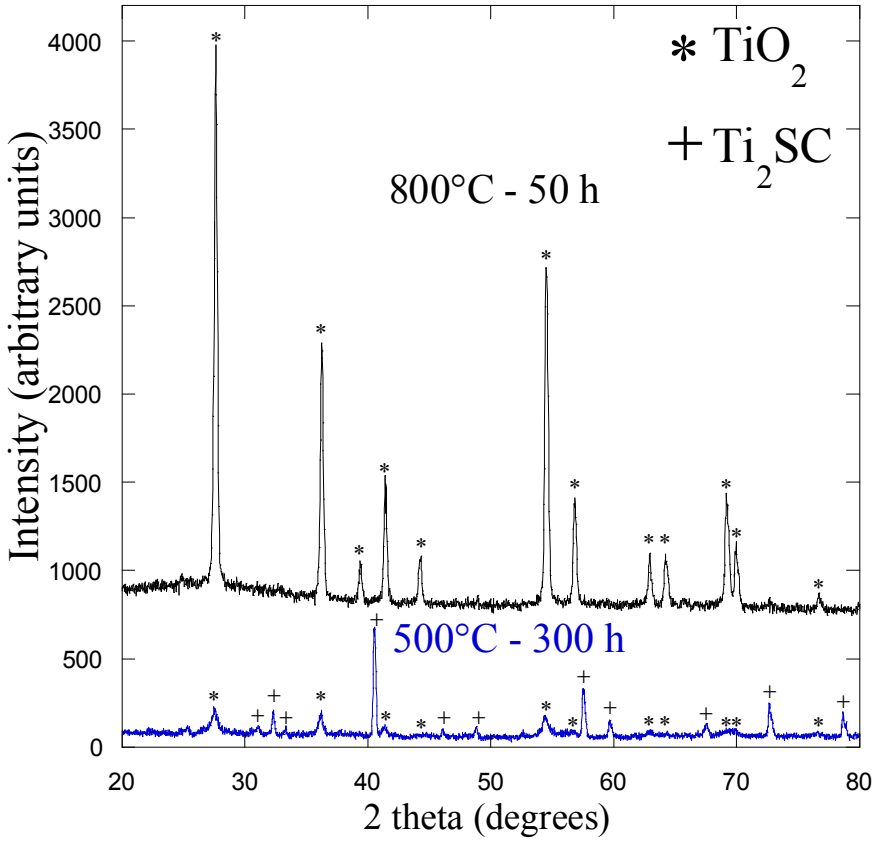

Figure AB.1: XRD patterns of bulk Ti_2SC samples oxidized in air at 500 and 800°C for 300 and 50h respectively. In all cases, rutile is the oxidation product phase. Because at 500°C, the rutile layer formed is quite thin, peaks belonging to Ti_2SC are observed.

Based on these and the XRD results there is little doubt that the oxidation reaction of Ti_2SC in air is given by:

$$Ti_2SC + 4O_2 \rightarrow 2TiO_2 + SO_2 + CO_2 \qquad \text{(Eq. A.B.1)}$$

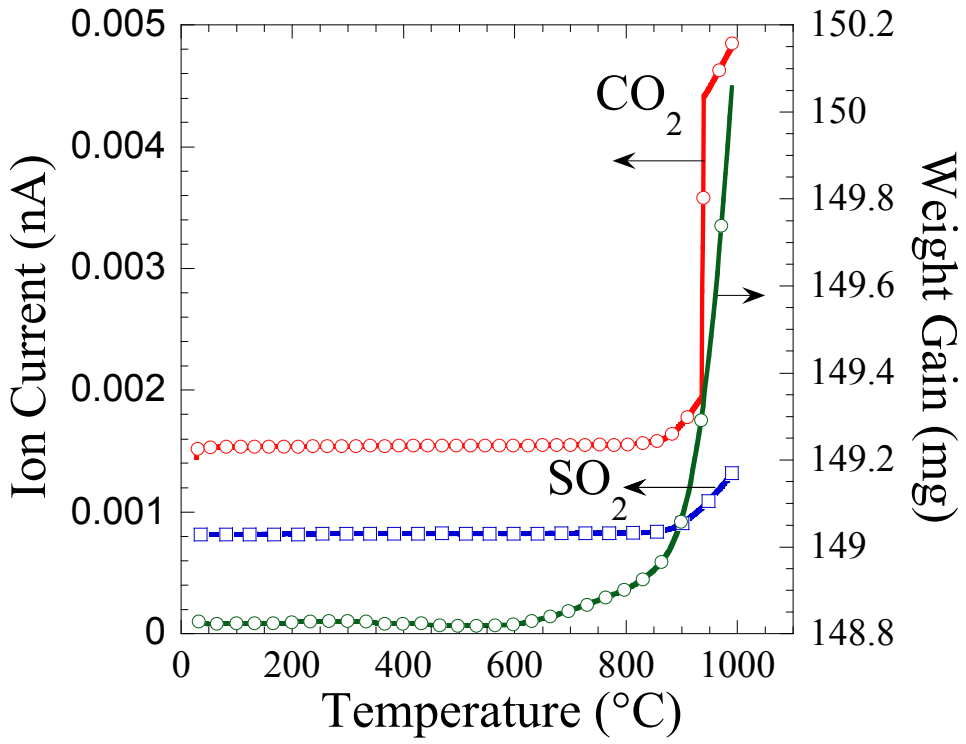

Figure AB.2: Temperature dependencies of weight gain (right axis) and composition (left axis) of gases evolved during simultaneous TGA/DTA oxidation of bulk Ti_2SC samples heated at 20°C/min in air. At about 900°C, a clear signal for the evolution of CO_2 and SO_2 was obtained.

We suppose we cannot claim with certainty that S and C diffuse out, since they can diffuse out as SO_2 or CO_2. Whether the Ti diffuses out, or the oxygen diffuses in, is less clear, but based on our previous work it is reasonable to assume that both diffuse [37]. These comments notwithstanding, it is hereby acknowledged that more work is needed to better delineate the sequence of events that result in gas evolution.

The time dependency of the weight gain, Δw, that occurs during the oxidation of Ti_2SC in air is shown in Figure AB.3a, based on which it is clear that at 800°C the

oxidation rate is quite high - i.e. catastrophic.

At 600 and 700°C, however, the oxidation kinetics are initially parabolic up to ~ 50 h; at t > ~ 50 h the oxidation kinetics become linear. It is only at 500°C that - after an initial parabolic regime up to ~ 50 h (inset of Figure AB.3a) - the weight gain appears to saturate. Clearly, these results will limit the use of Ti_2SC components in air to temperatures, not much higher than 500°C.

The weight gain, Δw, that occurs during the oxidation was converted to an oxide thickness, Δx (see below), and the results are plotted in Figure AB.3b, together with the oxide thicknesses measured directly in the SEM. The weight gain associated with reaction 1 is ≈ 21% and thus to convert the Δw results shown in Figure AB.3a to Δx, the former is multiplied by 1.87×10^{-3} (Appendix A). Possible reasons for the discrepancies observed in Figure AB.3b between the SEM results and those obtained by converting Δw to Δx at 600, 700 and 800°C are discussed below.

The oxidation of 1 mole of Ti_2SC results in 2 moles of rutile (Eq. AB.1), which translates to a weight gain of 0.02 kg/mole of Ti_2SC. The molar volume of fully dense rutile is assumed to be 18.7 cm^3/mole. The thickness of 2 moles of rutile formed, when extended over 1 m^2, is $2\times18.7\times10^{-6} = 3.74\times10^{-5}$m. It follows that when converting weight gains per m^2 to oxide thickness in m, the former is to be multiplied by: $3.74\times10^{-5}/0.02 = 1.87\times10^{-3}$m/kg/$m^2$.

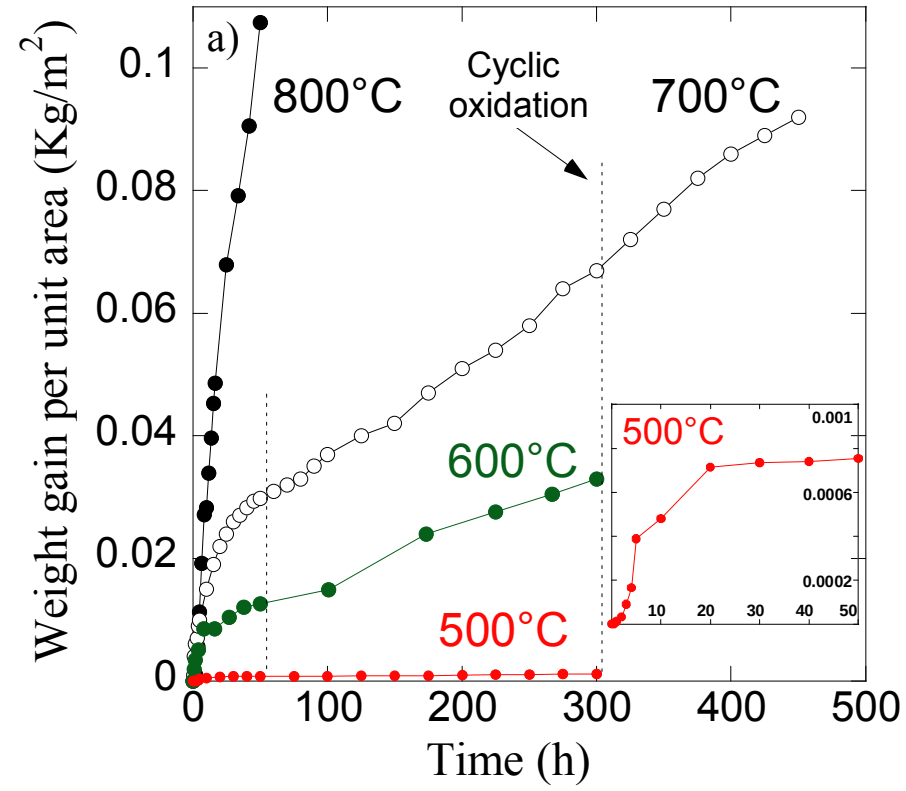
a)
800°C
Cyclic
oxidation
700°C
600°C
500°C
500°C
Weight gain per unit area (Kg/m^2)
Time (h)
0
0.02
0.04
0.06
0.08
0.1
0
100
200
300
400
500
0.001
0.0006
0.0002
10
20
30
40
50

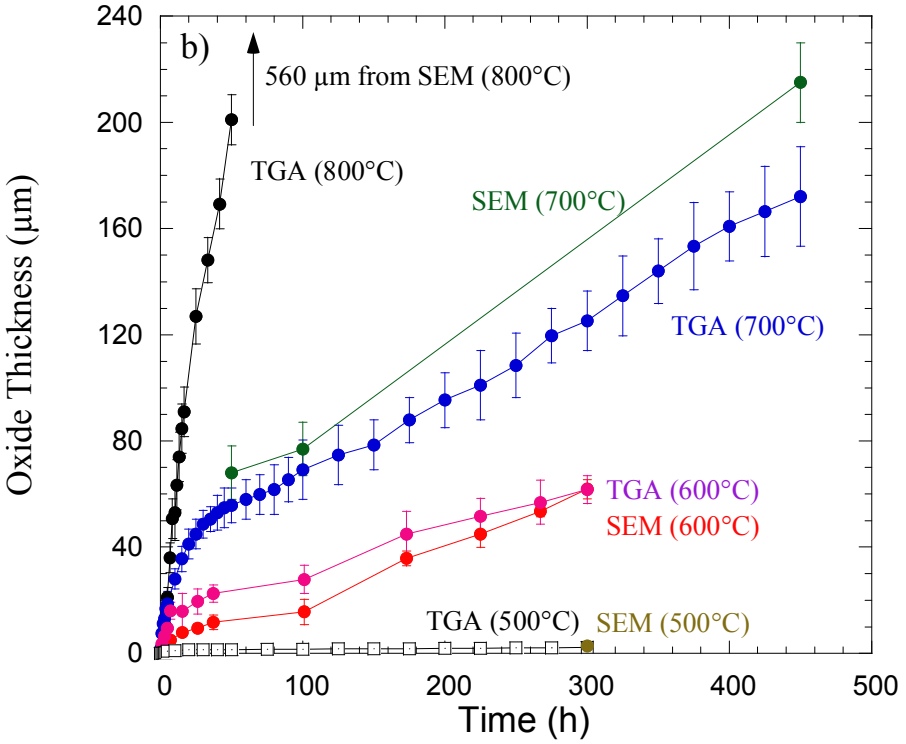
b)
560 µm from SEM (800°C)
TGA (800°C)
SEM (700°C)
TGA (700°C)
TGA (600°C)
SEM (600°C)
TGA (500°C)
SEM (500°C)
Oxide Thickness (µm)
Time (h)
0
40
80
120
160
200
240
0
100
200
300
400
500

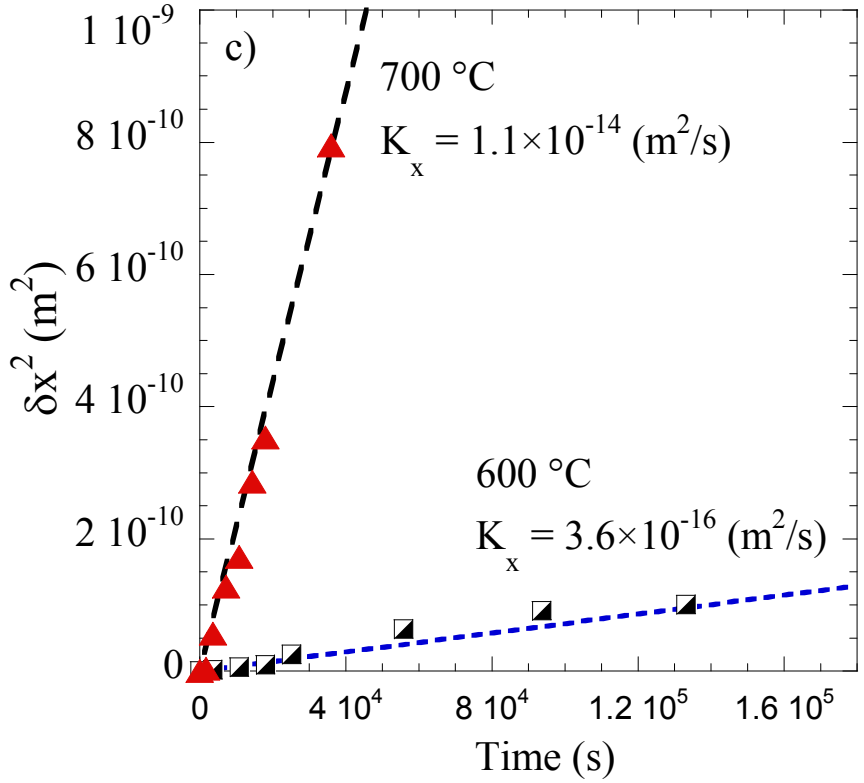
c)
700 °C
$K_x = 1.1\times10^{-14}$ (m^2/s)
600 °C
$K_x = 3.6\times10^{-16}$ (m^2/s)
δx^2 (m^2)
1 10^{-9}
8 10^{-10}
6 10^{-10}
4 10^{-10}
2 10^{-10}
0
0
4 10^4
8 10^4
1.2 10^5
1.6 10^5
Time (s)

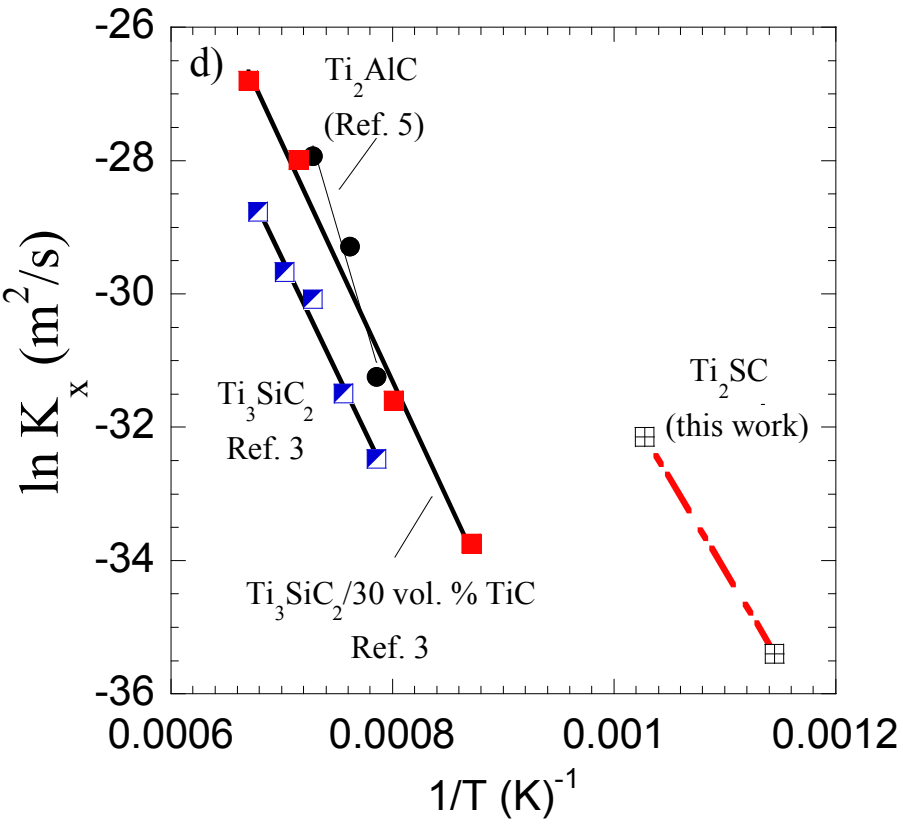
d)
Ti$_2$AlC
(Ref. 5)
Ti$_3$SiC$_2$
Ref. 3
Ti$_3$SiC$_2$/30 vol. % TiC
Ref. 3
Ti$_2$SC
(this work)
ln K_x (m^2/s)
-26
-28
-30
-32
-34
-36
0.0006
0.0008
0.001
0.0012
1/T (K)$^{-1}$

Figure AB.3: a) Weight gain, normalized by surface area, as a function of time and temperature for Ti_2SC. At 700°C after 300 h, the sample was cycled 6 times for a total of ≈ 150 h. Inset shows weight gain at 500°C for the first 50 h only; b) Comparison of oxide thickness, Δx, calculated from the weight gains assuming reaction 1 and those measured directly in the SEM. c) Plot of Δx^2 vs. time for first 50 h of oxidation at 600 and 700°C; the 700°C data were determined from the results shown in b (see below); c) Arrhenius plot of K_x. Also shown are the results for Ti_2AlC [225], Ti_3SiC_2, Ti_3SiC_2-30 vol. % TiC and Ti_3SiC_2-30 vol. % SiC [37].

To try and explore the nature of the rate limiting step during early oxidation of Ti_2SC, the time dependencies - up to 50 h only - of Δx^2 of the oxide layer at 600 and 700°C are plotted in Figure AB.3c. The linear relationship, obvious in Figure AB.3c, implies that:

$$\Delta x^2 = 2K_x t \qquad \text{(Eq.A.B.2)}$$

where $K_x(m^2/s)$, is the parabolic rate constant [182]. From these results, K_x at 600 and 700°C are calculated to be 3.6×10^{-16} and 1.1×10^{-14} m^2/s, respectively.

When these two data points are plotted on an Arrhenius plot (Figure AB.3d) it is clear that the parabolic rate constant for Ti_2SC is roughly an order of magnitude faster than that reported in previous works [37, 223, 225, 229]. The reasons for this state of affairs could be related to either the fact that the layers, even at short times, are not fully dense (see below) and/or aliovalent impurities, such as Fe present in the initial powders (long collection time energy dispersive spectroscopy indicated about 2 wt % Fe [230]), create vacancies on the oxygen or titanium sublattices, thereby enhancing the rate limiting step, which is believed to be ionic diffusion in the rutile layer [37, 225, 229].

The fact that the activation energy for the two data points obtained here is nearly

identical to that of previous work [37], strongly suggests the latter explanation. This conclusion is similar to, and consistent with, the fact that the initial oxidation kinetics of the $Ti_{n+1}AlC_n$ compounds are faster than those of Ti_3SiC_2 due to the presumed formation of oxygen vacancies when Al ions are dissolved in the rutile layer [225, 229].

Figure AB.4 shows typical secondary electron SEM image of the oxide layer formed on the surface after oxidation at 500°C for 300 h. The inset shows a backscattered electron SEM image of the same sample, clearly showing a contrast between the rutile layer and the underlying substrate.

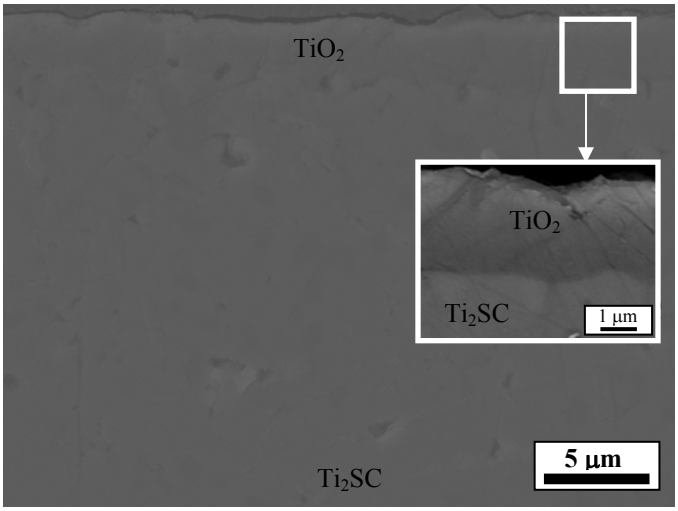

Figure AB.4: Secondary electron SEM micrograph of the oxide layer formed at 500 °C after 300 h in air. Inset shows a backscattered SEM image of the same sample.

Figures AB.5, AB.6 and AB.7 show typical secondary electron SEM images of the oxide layers formed on the surface at 600, 700 and 800°C, for various times, respectively.

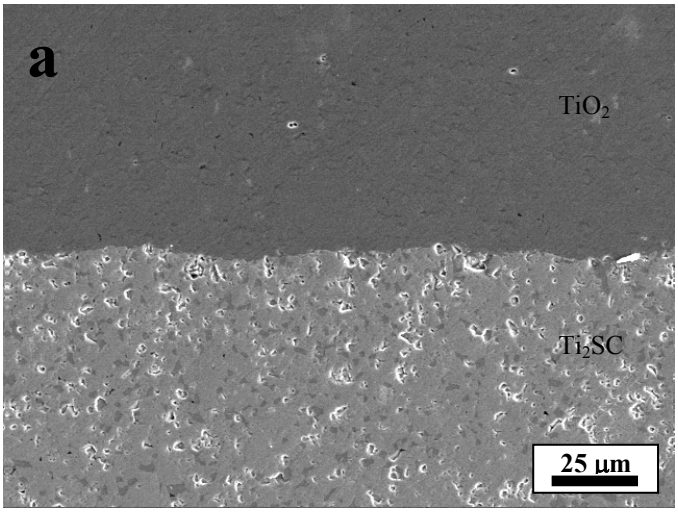
a
TiO_2
Ti_2SC
25 µm

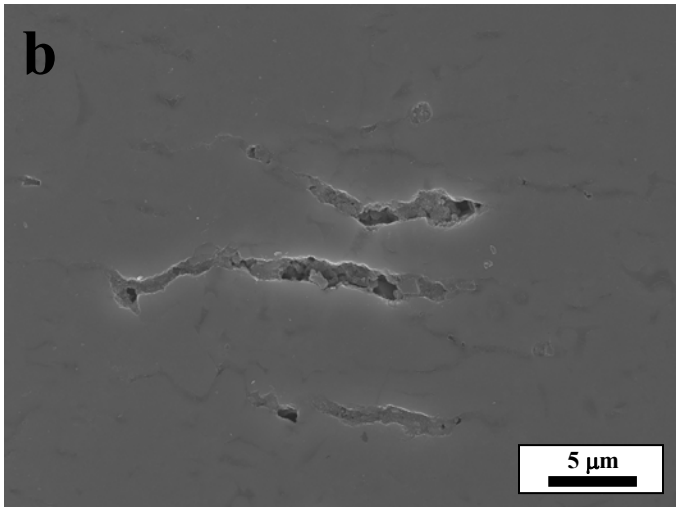
b
5 µm

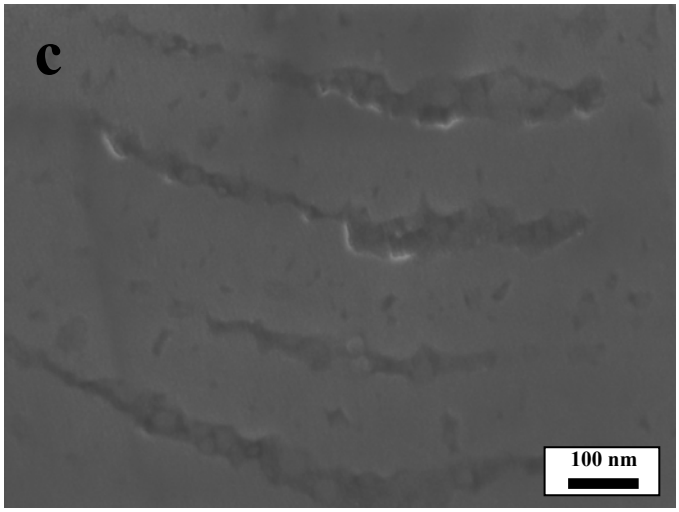

Figure AB.5: SEM micrographs of oxide layers formed at 600°C after 300 h in air, a) at low magnification; b and c) at higher magnifications showing the presence of mesopores and microcracks shown by arrows.

From these micrographs it is obvious that:

1) At 500°C, the oxide layer (Figure AB.4) did not flake off, but remained adherent, dense, apparently crack free and protective and was significantly thinner than the oxide layers formed at the higher temperatures explored herein.

2) The oxide layers formed on the surface after oxidation at 600°C for 300 h (Figure AB.5a) and at 700°C for 500 h (Figure AB.6a) - did not flake off either and remained adherent to the Ti_2SC substrate. At higher magnifications, however, the SEM images show the presence of mesopores and microcracks throughout the oxide layers formed at 600°C (Figures AB.5b and AB.c) and 700°C (Figure AB.6b to AB.d). Note that after 300 h oxidation at 700°C, the sample was cycled 6 times from room temperature to 700 °C.

3) The oxide layer formed after oxidation at 800°C for 50 h (Figure AB.7a) is quite thick and did not adhere to the substrate. Here again, at higher magnifications, mesopores and microcracks (Figure AB.7b to AB.d) were present throughout the oxide layer, but at a volume fraction that was significantly higher than samples oxidized at 700 and 600°C. It is believed that at higher temperatures, the evolved SO_2 and CO_2 gases can expand relatively more compared to 500 °C, therefore this pressure creates internal pathways in the form of porosity and microcracks, leading to dense oxide layer only in the latter.

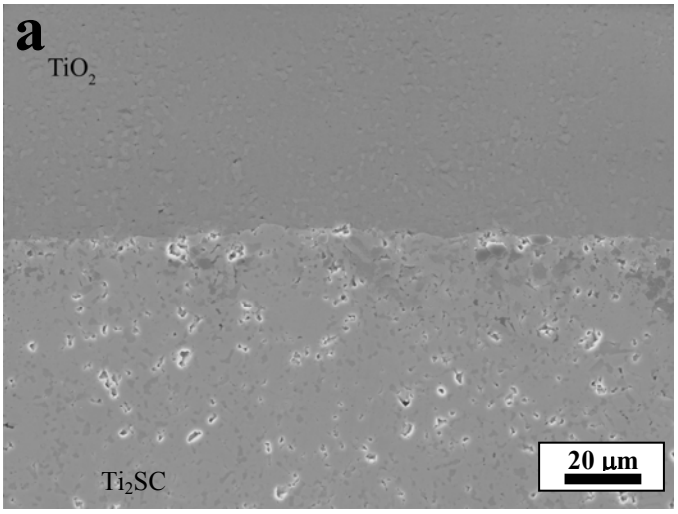

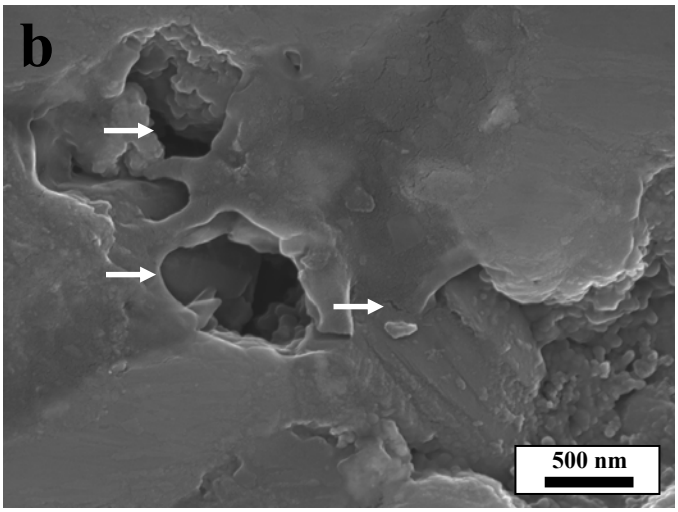

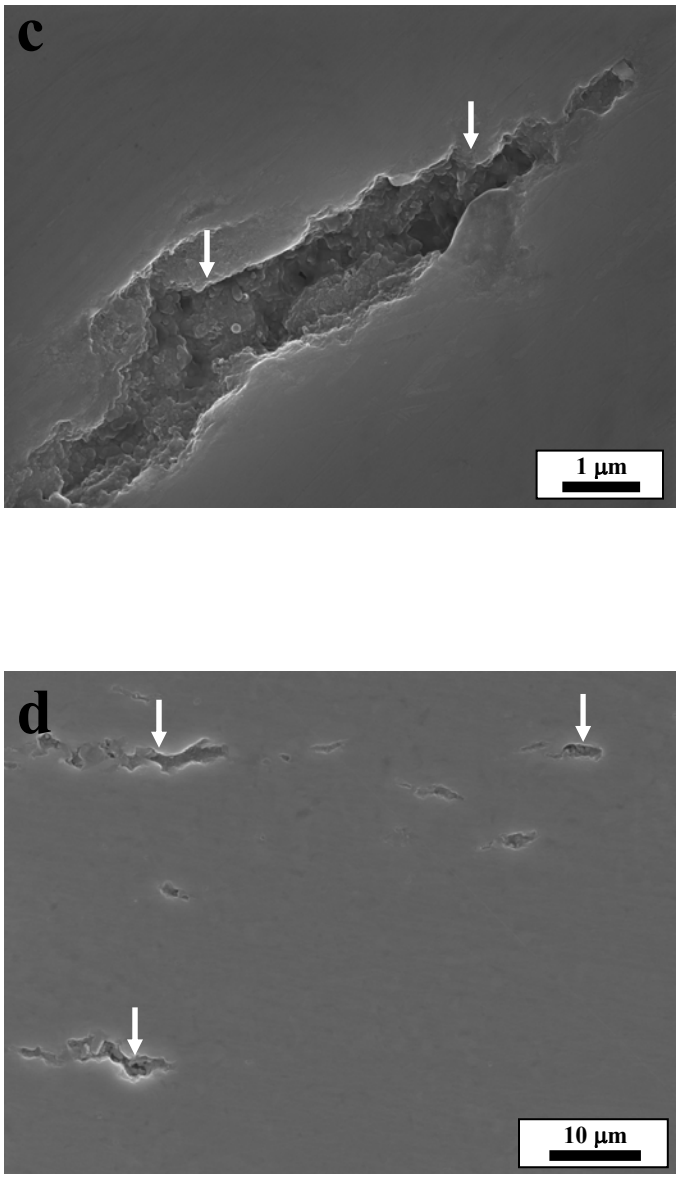

Figure AB.6: SEM micrographs of oxide layers formed at 700°C after 500 h in air, a) at low magnification; b and c) at higher magnifications showing the presence of mesopores and microcracks shown by arrows.

With this information, the reasons for the discrepancies alluded to earlier become more transparent. The oxide layers formed at 600, 700 and 800°C, after an initial 50 h period, are not fully dense, which would explain the change in kinetics from parabolic to

linear. At 800°C, the volume fraction of cracks and pores are sufficiently high that the scale appears thicker than it should be based upon the weight gain.

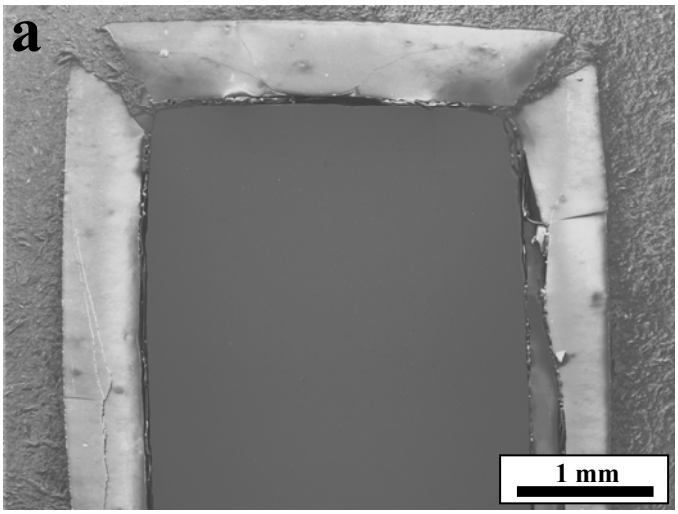

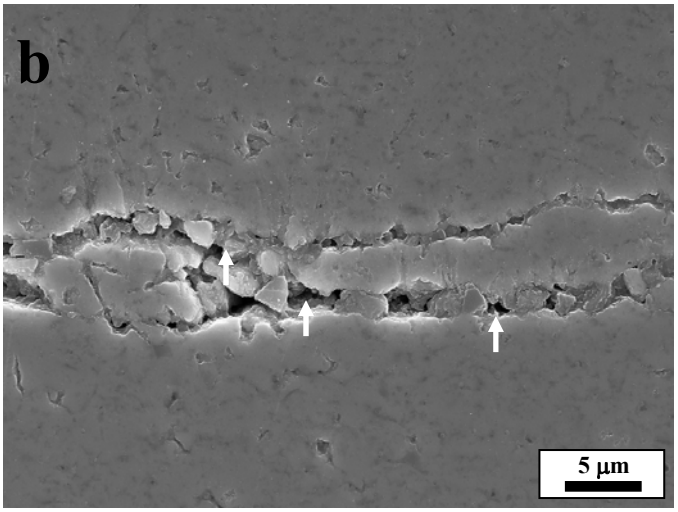

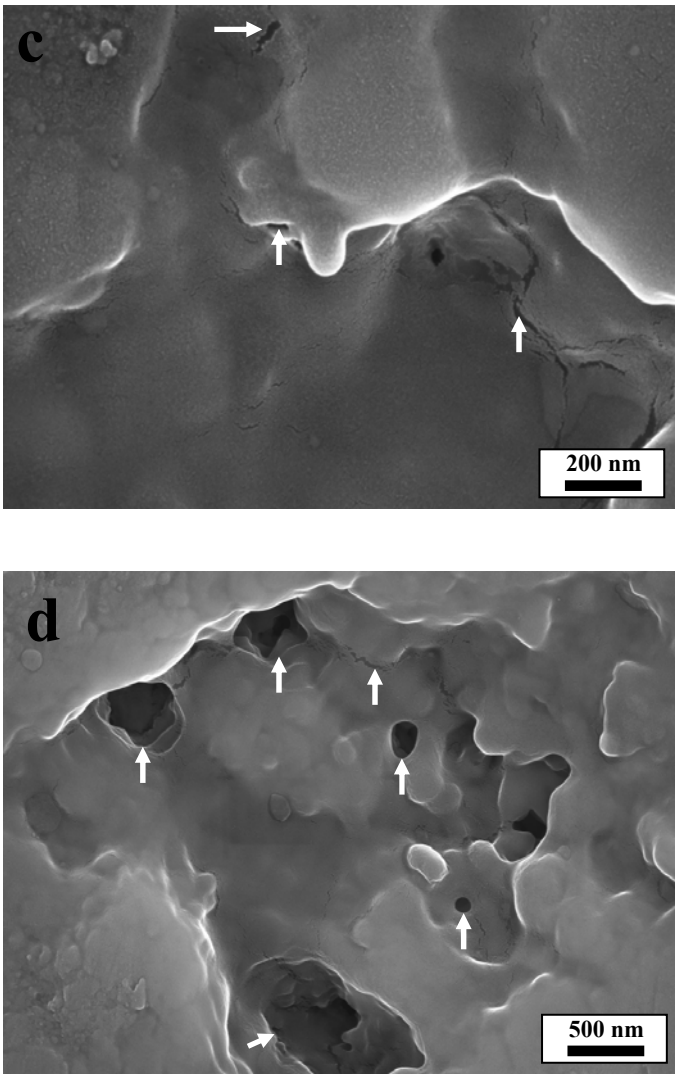

Figure AB.7: SEM micrographs of oxide layers formed at 800°C after 50 h in air, a) at low magnification; b and c) at higher magnifications showing the presence of mesopores and microcracks shown by arrows. Note that volume fraction of the latter is significantly greater than those formed at lower temperatures.

AB.4. Summary and Conclusions

The oxidation product of bulk Ti_2SC samples, at all temperatures tested is a single rutile scale, SO_2 and CO_2. The oxidation reaction is thus: $Ti_2SC + 4O_2 \rightarrow 2TiO_2 + SO_2 + CO_2$. At 800°C, the oxide layer was thick, easy to flake off and not protective, resulting in catastrophic oxidation. At lower temperatures, the oxide scales were adherent to the surface and, at least at 700°C, resistant to spalling after 6 heating and cooling cycles. At 600 and 700°C and up to ~ 50 h, the kinetics is initially parabolic, before becoming linear. The reason for the transition is believed to be the formation of pores and microcracks in the rutile layer at longer times. It is only at 500°C that the weight gain reaches a plateau at longer soaking times (t > 50 h). It follows that the maximum use temperature for Ti_2SC in air will be in the vicinity of 500°C. Based on the results of this work we conclude that the oxidation occurs by the outward diffusion of C and S. At this point it is not clear whether the Ti diffuses out and/or the O diffuses in. Based on pervious works, however, it is reasonable to assume both ions are counterdiffusing.

Appendix C : On the Synthesis and Mechanical Properties of Cr_2GeC

AC.1. Introduction

The ternary carbide, Cr_2GeC, is a MAX phase [8, 210]. Like the others, its unit cell is hexagonal (space group $D^4_{6h} - P6_3/mmc$), with unit cell parameters, a = 2.954 Å and c = 12.08 Å. This phase was first discovered by Jeitschko *et al.* in 1963 [231]. As far as we are aware, with the exception of two recent papers [232, 233] , there are no reports in the literature on its synthesis or characterization in bulk. In one of the papers [232] we measured the functional dependences of its lattice parameters to quasi-hydrostatic pressures of the order of 50 GPa and found it to be high (182±2 GPa); no phase transformations were observed. We also reported [233] on the thermal expansion, measured by XRD, in the 25-800°C temperature range. The TEC, for the a-axis, α_a, was $(12.9\pm0.1)\times10^{-6}$ °C^{-1}; that of the c-axis, α_c, was $(17.6\pm0.2)\times10^{-6}$ °C^{-1}.

Our ultimate goal is to understand the chemistry-microstructure-property relationships of the potentially technologically important MAX phases. To achieve this goal we are using a multipronged approach that includes synthesis and characterization, as well as *ab initio* calculations. It is only when the latter are mature and reliable enough will we be able to design materials by "computer". This is particularly crucial in the case of the MAX phases because of the almost innumerable number of possible solid solution combinations. A requisite first step to accomplish our goal is to understand the behavior of the end members.

In this chapter, we report, for the first time, on the synthesis and characterization of predominantly single-phase, bulk, dense polycrystalline samples of Cr_2GeC. We also

show that this carbide is a kinking nonlinear elastic solid and apply our KNE model [59] to analyzing the cyclic compressive stress-strain curves obtained.

AC.2. Experimental Procedure

Powders of Cr (99% pure, -325 mesh, Alfa Aesar, Ward Hill, MA), Ge (99% pure, -325 mesh, Cerac, Milwaukee, WI) and C (99.0% pure, - 300 mesh, Alfa Aesar, Ward Hill, MA) were stoichiometrically weighed, ball milled in a plastic container with alumina balls for 24 h, and then dried under a mechanical vacuum for 24 h at 180 °C. The powder mixture was then poured and wrapped in graphite foil, placed in a graphite die and heated, under vacuum, at 10°C/min - in a graphite-heated HP (Series 3600, Centorr Vacuum Industries, Somerville, MA) – up to 1350°C and held at that temperature for 6 h. A load, corresponding to a stress of ~ 45 MPa, was applied at 600°C and maintained throughout the run. Powders, obtained by drilling near the center of the samples, were placed in an X-ray diffractometer, XRD, (Model 500D, Siemens, Karlsruhe, Germany) and their spectra were collected, using Cu Kα radiation (40 KV and 30 mA) at step scans of 0.02 2θ and a step time of 1 s. Si powder was added as an internal standard.

The samples' densities were measured using Archimedes' method in ambient temperature water or, by dividing their weight by their volume, if they were regularly shaped. The microstructures were observed in a field emission SEM, (Zeiss Supra 50VP, Germany) after cross-sectioning, mounting and polishing with a diamond solution down to 1 μm, followed by a surface polish with a colloidal silica suspension.

The V_H was measured using a LECO-M400 (LECO Corp. St. Joseph, MI, USA) hardness tester. The microhardness values were calculated by averaging at least 20

indentations at any given load. The macrohardness was measured using a LECO-V1000 (LECO Corp. St. Joseph, MI, USA) hardness tester. The results of the latter are an average of 4 indents each at loads of 20, 50, 100 or 200 N.

The room temperature compressive strengths were measured using a hydraulic testing machine (MTS 810, Minneapolis, MN) on small $3\times3\times3$ mm^3 cubes. Six cubes were EDMed and compressed in load-control mode at a loading rate of 54 MPa/s. EDMed, cylinders, 9.7 mm in diameter and 31 mm high, were used to carry out the cyclic compression tests. The strains were measured by a capacitance extensometer (MTS, Minneapolis, MN) with a 1 % range, attached directly onto the specimen surface.

The elastic properties were determined with an ultrasonic echo-pulse technique with a RAM 5000 system from Ritec. The time of flight of a 15-MHz tone burst produced by a lithium niobate transducer was measured by heterodyne phase sensitive detection. For the ultrasonic measurements cylinders, 8 mm in diameter and 14 mm high, were used. Salol© compound was used to bond the ultrasonic transducer to the sample. Room temperature Young's, E, and shear, G, moduli were calculated from independent measurements of the longitudinal, v_l, and shear, v_s, sound velocities, assuming an isotropic media. These results were then used to calculate the bulk moduli, B, and Poisson's ratio, ν.

AC.3. Results and Discussion

AC.3.1. X-Ray Diffraction and Microstructural Results

In a typical indexed XRD pattern (Figure AC.1), no peaks other than those associated with Cr_2GeC and eskolaite, Cr_2O_3, were observed. Table AC.1 summarizes our data and those of Jeitschko *et al.* [231]. At 2.952±0.002 Å, 12.108± 0.004 Å and 91.35±0.06 $Å^3$, the *a*, *c* lattice parameters and unit cell volume our results are in good agreement with those previously reported, [231] viz. 2.951 Å, 12.08 Å and 91.08 $Å^3$, respectively.

To determine whether the hot pressing resulted in preferred orientations we measured the ratio of the XRD peak intensities of the (002) and (103) planes, both parallel and perpendicular, to the direction of hot pressing and found them to be, within the experimental scatter, identical. It thus appears that the hot pressing did not result in preferred orientations.

The measured density was ~ 98 % of theoretical (6.88 Mg/m^3), and consistent with the SEM micrographs in which no porosity was observed. A typical fractured surface SEM micrograph (Figure AC.2a) clearly shows that the fracture mode is transgranular.

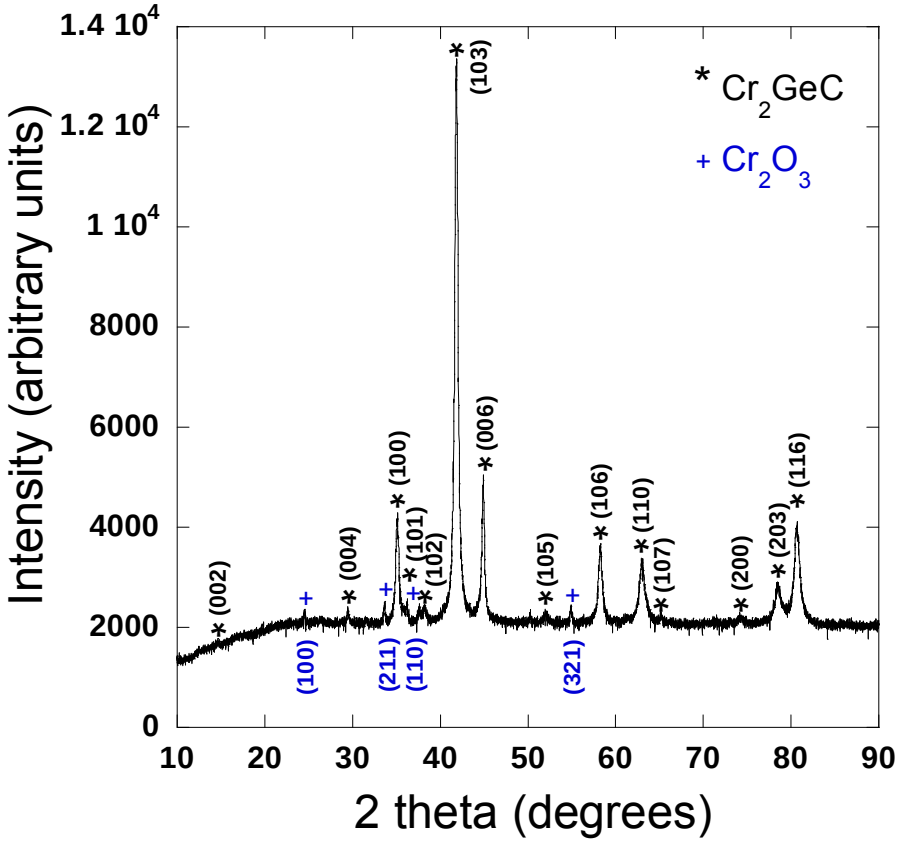

Figure AC.1: Indexed XRD pattern of Cr_2GeC synthesized at 1350°C by reactive HPing; impurity phase observed in the pattern is eskolaite.

From the micrograph the grain diameter is estimated to be 20±10 μm. The grain thickness, which is the dimension that is relevant to our model, viz. 2α, is 10±5 μm. To obtain this value, the thicknesses of 10 grains exposed on the fractured surface were averaged. The inset is the same micrograph at higher magnifications showing the nano-laminate nature of the material.

Table AC.1: Summary of the XRD data measured in this work and those measured by Jeitschko *et al.* [231].

hkl	2θ (this work)	2θ [231]	Intensity (this work)	Intensity [231]
(0 0 2)	14.640	14.703	5	10
(1 1 0)	24.532	24.573	..	eskolaite
(0 0 4)	29.589	29.655	5	10
(2 1 1)‡	33.689	33.675	..	eskolaite
(1 0 0)	35.081	35.079	40	50
(1 0 1)	35.860	35.877	5	10
($\bar{1}$ 1 0)	36.258	36.337	..	eskolaite
(1 0 2)	38.263	38.252	15	20
(1 0 3)	41.838	41.846	100	100
(0 0 6)	44.894	45.068	50	50
(1 0 5)	51.998	52.006	5	10
(3 2 1)	54.865	54.982	..	eskolaite
(1 0 6)	58.252	58.316	40	50
(0 0 8)	61.389	61.390	1	2
(1 1 0)	62.975	62.964	30	60
(1 0 7)	65.160	65.135	1	5
(1 1 4)	71.033	71.030	1	5
(2 0 0)	74.082	74.132	5	20
(2 0 1)	74.285	74.541	1	5
(2 0 2)	76.434	76.084	1	5
(2 0 3)	78.492	78.459	40	80
(1 1 6)	80.658	80.678	40	100

‡: 2θ of the most intense peak associated with eskolaite

Typical secondary and backscattered electron SEM images of a polished sample, seen in Figures AC.2 c and d, respectively, show the presence of two regions: a bright region corresponding to Cr_2GeC and a dark minority region. The total volume fraction of the dark areas was estimated, from image analysis, to be 6±2 vol. %. EDS analysis (O: ~ 62±3 at. %; Cr: 38±3 at. %) confirmed this to be the phase identified in the XRD spectra to be eskolaite. Oxygen in the original powder is the most likely source of this

contamination. Upon heating, the oxygen most probably reacts with the Cr to form Cr_2O_3. Fig. AC.2b shows a small grain of Cr_2O_3 positioned at a triple point of the Cr_2GeC grains.

We reported elsewhere [112] that the presence of hard impurity phases in MAX-phase matrices only influence the mechanical properties if they are present in large volume fractions. Therefore it is reasonable to believe that the effect of the ~ 6 vol.% eskolaite present in our microstructure on properties is small.

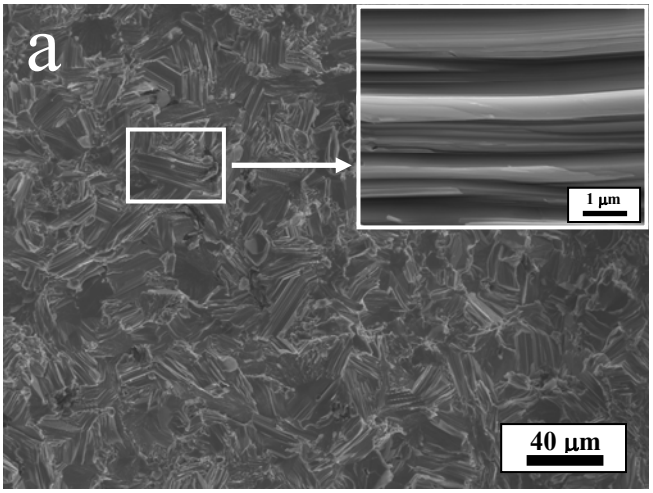

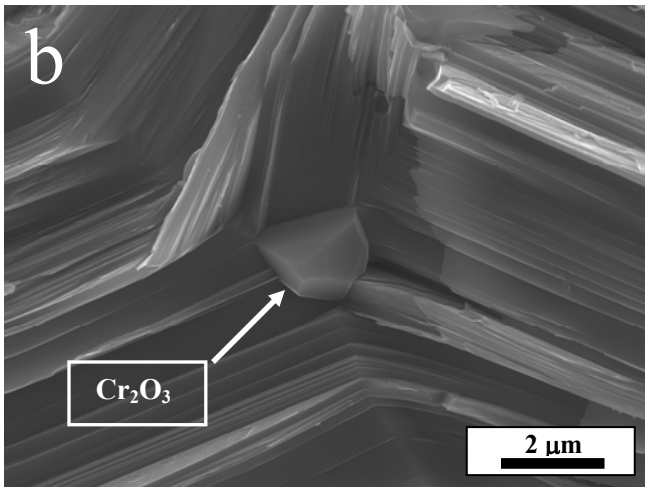

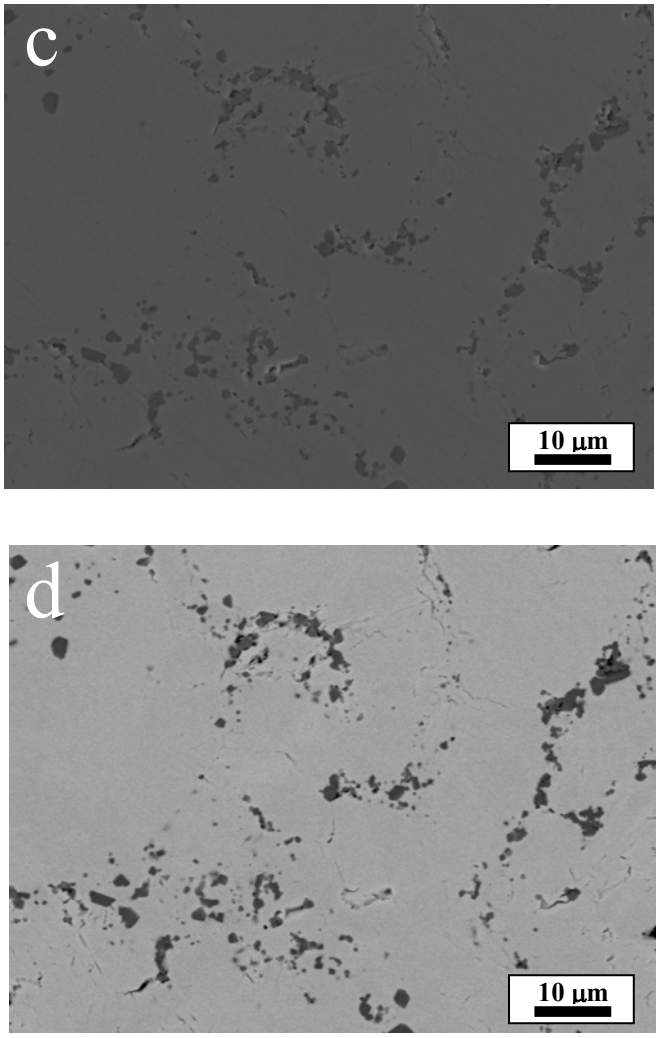

Figure AC.2: a) SEM micrograph of a fractured surface of a sample HPed at 1350 °C for 6 h; inset shows nanolaminate nature of the solid; b) small grain of Cr_2O_3 positioned at a triple point of the Cr_2GeC grains, c) polished backscattered SEM, and, d) secondary electron SEM micrograph of the same sample; dark areas are eskolaite.

AC.3.2. Machinability

Not surprisingly, and similar to all MAX phases characterized to date, Cr_2GeC is readily machinable using a manual hack-saw with no lubrication or cooling. Because of its conductivity, it can also be readily EDMed.

AC.3.3. Vickers Hardness

When the effect of indentation loads - ranging from 1 to 200 N - on the Vickers hardness values is plotted on a semi-log plot (Figure AC.3) it is clear that - like most other MAX phases characterized to date [146] - they are initially high, decrease, and then asymptote to a steady state Vickers hardness of 2.5±0.1 GPa at the higher loads. The scatter in the results is typical of other MAX phases, and reflects the presence of only two independent basal slip systems [17, 74, 146].

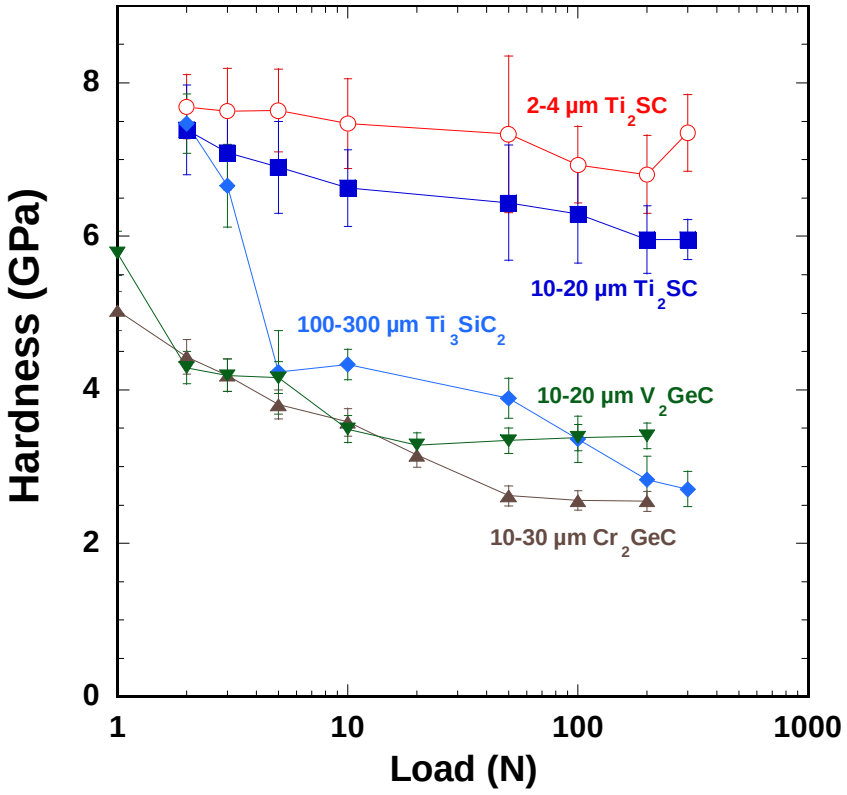

Figure AC.3: Semi-logarithmic plot of Vickers micro- and macrohardness versus indentation load for Cr_2GeC. Also shown are the results for V_2GeC, Ti_2SC and Ti_3SiC_2 for the sake of comparison.

Also included in Figure AC.3, for the sake of comparison, are the Vickers hardness results of V_2GeC, Ti_2SC [27] and Ti_3SiC_2 [21] from which it is obvious that the hardness of Cr_2GeC is one of the lowest reported so far for a MAX phase.

Typical SEM micrographs of Vickers indentation marks formed under loads of 10 N and 200 N are shown, respectively, in Figures AC.4a and 5b. Like other MAX phases [17, 24, 29, 49, 220] no cracks are observed to emanate from the corners of the Vickers indentations, even at 200 N.

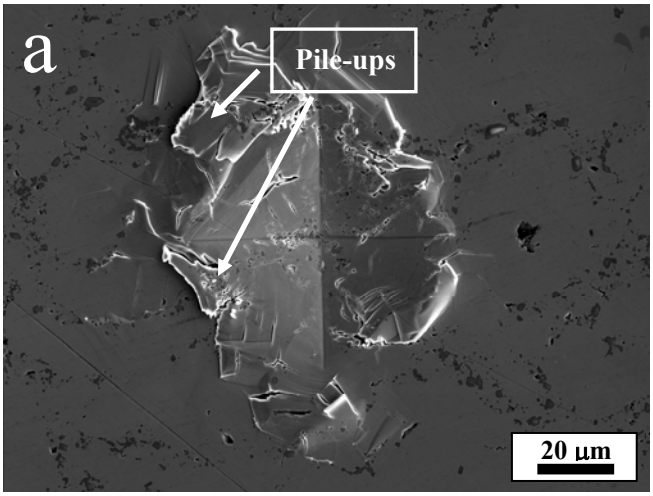

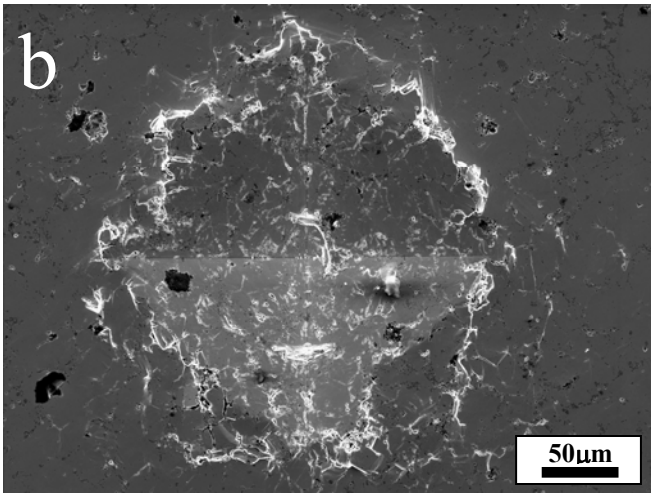

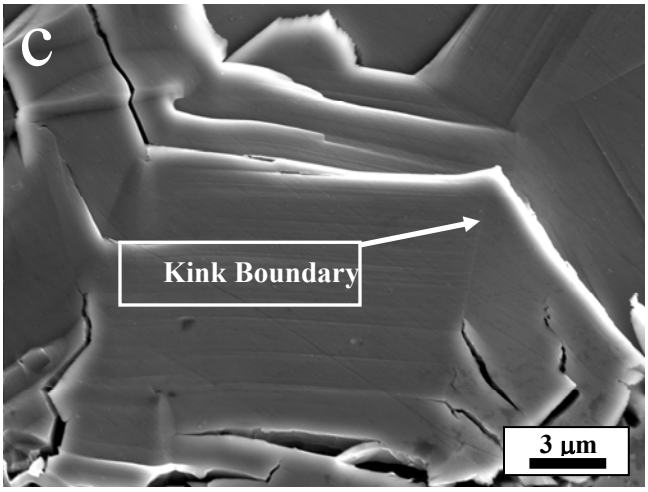
c
Kink Boundary
3 μm

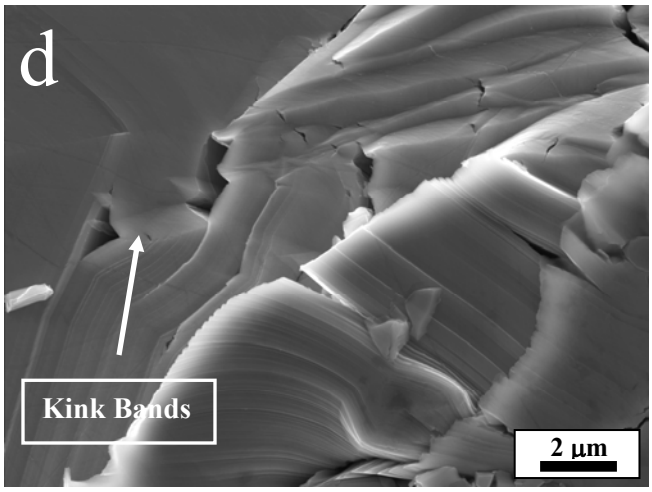
d
Kink Bands
2 μm

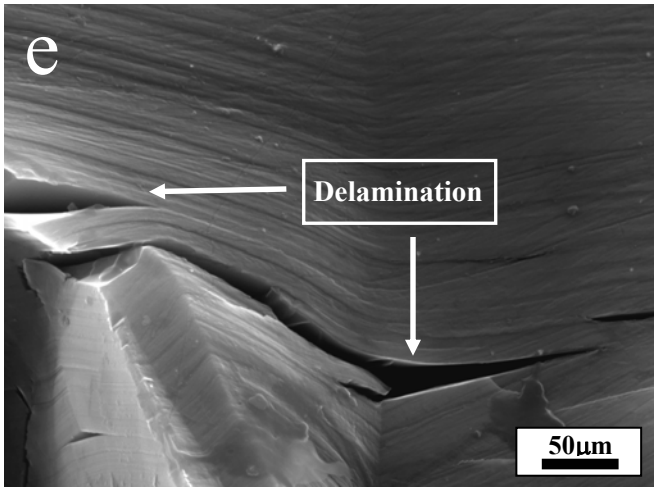

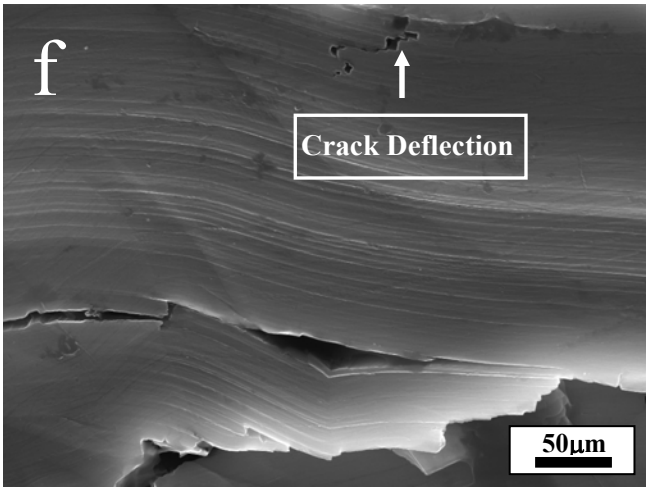

Figure AC.4: SEM micrographs of Vickers indentations at, a) 10 N, and b) 200 N; c, d, e and, f) SEM micrographs showing kink bands, crack bridging, crack deflection and delamination under, and around, indentation marks at 10 N.

Also like other MAX phases, a distinct pile-up of material around the indentation marks - due to the push out of grains for which the resolved shear stress along their basal planes exceeded the CRSS - is observed [17].

As importantly, kink bands, crack bridging, crack deflection and delaminations, first documented for Ti_3SiC_2 [17], are all readily observed around the indentation marks (Figures AC.4c, d, e and f).

Hence the damage tolerance can be attributed to the ability of the material to confine the extent of damage to a rather small area around the indentations due to the aforementioned energy absorbing mechanisms. The importance of such high damage tolerance in practical applications cannot be overemphasized.

AC.3.4 Compression Test Results

The average ultimate compressive stress of the 6 samples tested was 750±25 MPa. Figure AC.5 shows typical stress-strain curves obtained when a sample was cyclically loaded up to ≈ 75 % of the failure stress; the curves are shifted horizontally for clarity. The straight lines are the expected linear elastic response had kinking not occurred and the slopes correspond to the Young's modulus of ~ 245 GPa. Clearly, Cr_2GeC forms, fully reversible, reproducible, closed hysteretic loops under compression. As we have argued before, this is the signature of the formation and annihilation of IKBs [25, 52, 53, 55, 56, 58, 62, 234]. According to our KNE model, plots of W_d vs. σ^2, W_d vs. ε_{NL} and ε_{NL} vs. σ^2 should result in straight lines, as observed in Figures AC.6a and b, respectively. With R^2 values greater than 0.97, these results are in good agreement with our KNE model.

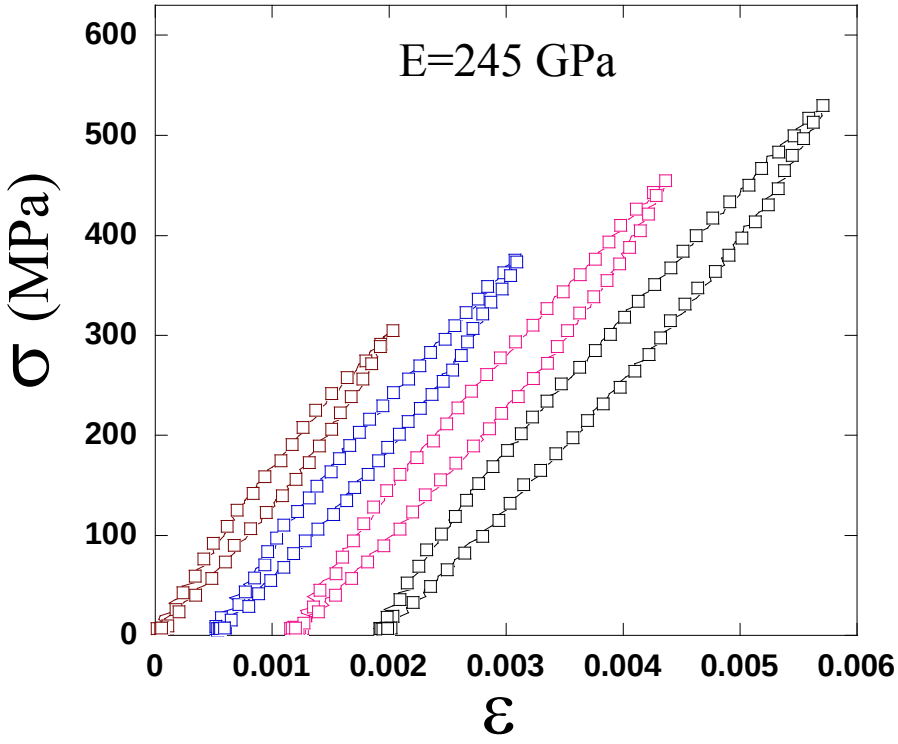

Figure AC.5: Typical compressive stress-strain curve up to 75 % of the failure stress; loops are shifted horizontally for clarity.

From the slope of the line in Figure AC.6b, Ω/b, or the CRSS, is calculated to be ~ 22 MPa, a value in line with those determined for Ti_2AlC and Ti_3AlC_2, viz. 24 and 36 MPa, respectively [235]. The threshold stress σ_t, determined from Figure AC.6a, is ~ 90 MPa. This value is lower than that of the 170 MPa for Ti_2AlC, or the 245 MPa in Ti_3AlC_2 with comparable grain sizes [45].

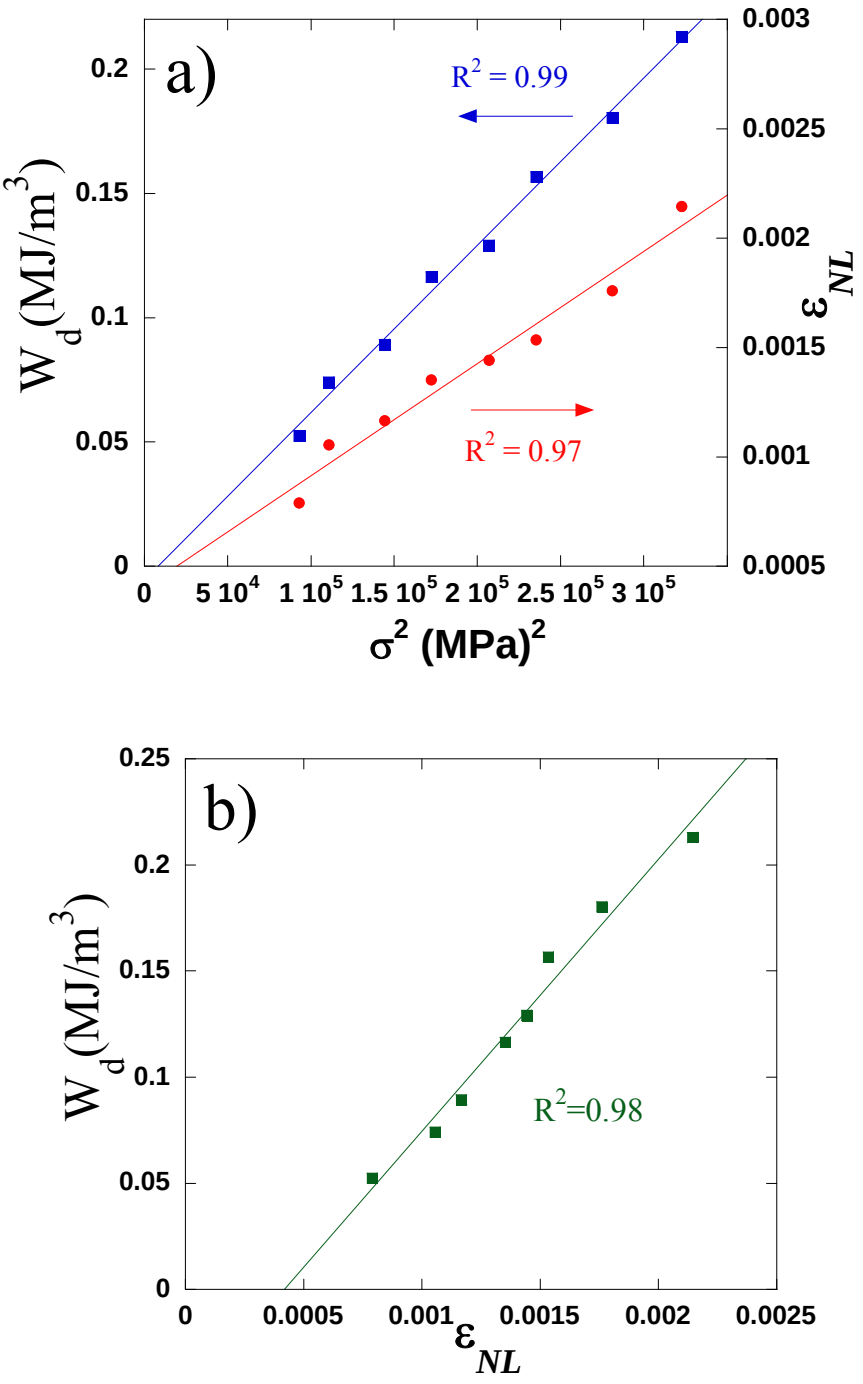

Figure AC.6: Plots of, a) W_d and ε_{NL} vs. σ^2 and, b) W_d vs. ε_{NL}; Note R^2>0.97.

The calculated values of N_k and ρ at 525 MPa are 5.3×10^{14} m^{-3} and 1.7×10^{13} cm^{-2}, respectively. The shear modulus and Poisson's ratio were measured ultrasonically (see below). The Burgers vector, b, is the *a* lattice parameter and the critical kinking angle, γ_c, is $\approx$ 0.06, assuming that local stress needed to nucleate an IKB is $\approx$ G/30 and the measured Poisson's ratio of 0.29 (see below) [53, 58].

Table AC.2: Summary of G, b, experimentally measured 2α and σ_t, Ω/b, N_k and ρ of Cr_2GeC and those of Ti_2AlC [45] and Ti_3AlC_2 [45] for the sake of comparison.

	G (GPa)	**ν**	**b (Å)**	**2α (μm)**	**σ_t (MPa)**	**Ω/b (MPa)**	**N_k $(m)^{-3}$**	**ρ (m^{-2})**
Cr_2GeC	80	0.29	2.95	10±5	90	22	5.3×10^{14}	1.7×10^{13}
Ti_2AlC [45]	119	0.2	3.00	7	170	24	7.3×10^{15}	4.2×10^{13}
Ti_3AlC_2 [45]	124	0.2	3.00	7	244	36	1.8×10^{16}	3.9×10^{13}

Table AC.3: Elastic properties of Cr_2GeC measured by ultrasonic echo-pulse technique.

Density (Mg/m^3)	v_l (m/s)	v_s (m/s)	E (GPa)	G (GPa)	B (GPa)	Debye T (K)	ν
6.88	6300	3422	245	80	165	580	0.29

Kink bands, with very sharp radii of curvature, are readily observed on the fractured surfaces of Cr_2GeC (Figure AC.7). Based on these micrographs and the evidence mentioned above, it is not unreasonable to assume that they were preceded by IKBs.

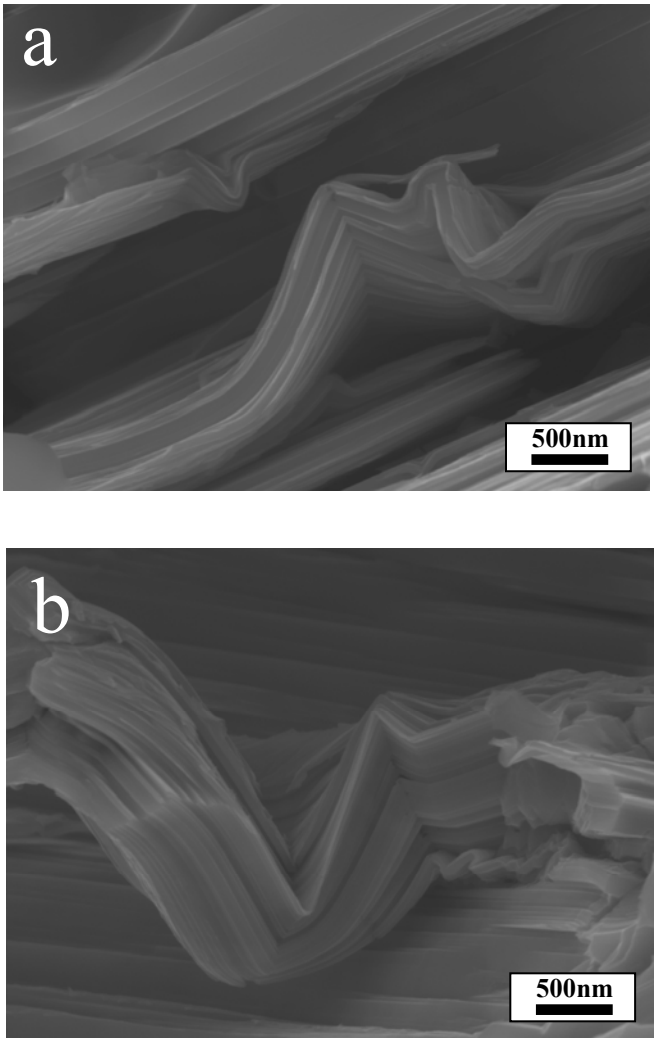

Figure AC.7: SEM micrographs of kink bands with very sharp radii of curvature on the fractured surface of Cr_2GeC.

AC.3.5 Elastic properties

The elastic properties measured by ultrasound are shown in Table AC.3. Young's and shear moduli are lower than those for other MAX phases. For many KNE solids, compression and/or tensile test underestimate the elastic moduli as a result of the nonlinear strain associated with IKB development [56, 58].

The same is shown here; Young's modulus measured using this technique - 245±3 GPa - is higher than the 200 GPa measured from Figure 6. The shear modulus and Poisson's ratio were measured to be 80 GPa and 0.29, respectively. For reasons that are not entirely clear, the latter is significantly higher than most Poisson's ratios measured to date on other MAX phases that cluster around 0.2 or slightly lower. The ultrasonic Debye temperature is estimated to be 580 K.

AC.4. Summary and Conclusions

Fully dense, readily machinable bulk samples of Cr_2GeC were synthesized by hot pressing Cr, Ge and C powders at 1350°C for 6 h, under a stress of 45 MPa. No peaks other than those associated with Cr_2GeC and eskolaite were observed; the latter had a total volume fraction of 6±2 vol. %. With a grain size of 20±10 μm, the steady state Vickers hardness was ~ 2.5±0.1 GPa. The ultimate compressive strength was 750±25 MPa; failure was brittle. At 245 GPa, Young's modulus measured by ultrasound was larger than the 200 GPa measured from the stress-strain curves. At 80 GPa, the shear modulus was relatively low for a MAX phase.

When loaded cyclically, nonlinear, fully reversible, reproducible, closed hysteretic stress-strain loops that dissipated ~ 20 % of the mechanical energy, presumably due to the formation and annihilation of IKBs, were formed. Therefore, Cr_2GeC is a KNE solid and its response to cyclic loading can be described by our recently developed microscale model. Based on that model, the critical resolved shear stress of the basal plane dislocations responsible for the IKBs is estimated to be ≈ 22 MPa.

References

[1] Barsoum MW, Ali M, El-Raghy T. Processing and Characterization of Ti_2AlC, Ti_2AlN, and$Ti_2AlC_{0.5}N_{0.5}$. Met. Mat. Trans. A 2000;31A:1857.

[2] Barsoum MW, Brodkin D, El-Raghy T. Layered Machinable Ceramics for High Temperature Applications. Scripta Materialia 1997;36:535.

[3] Barsoum MW, El-Raghy T. Synthesis and Characterization of a Remarkable Ceramic: Ti_3SiC_2. J. Amer. Cer. Soc 1996;79:1953.

[4] Barsoum MW, El-Raghy T. Room-Temperature Ductile Carbides. Met. Mat. Trans. A 1999;30A:363.

[5] Barsoum MW, Farber L, El-raghy T. Dislocations, Kink Bands, and Room-Temperature Plasticity of Ti_3SiC_2. Met. Mat. Trans. A 1999;30A:1727.

[6] Barsoum MW, Zhen T, Kalidindi SR, Radovic M, Murugaiah A. Fully reversible, dislocation-based compressive deformation of Ti_3SiC_2 to 1 GPa. Nat. Mate. 2003;2:107.

[7] Barsoum MW, El-Raghy T. The MAX phases: Unique new carbide and nitride materials - Ternary ceramics turn out to be surprisingly soft and machinable, yet also heat-tolerant, strong and lightweight. American Scientist 2001;89:334.

[8] Barsoum MW. The $M_{N+1}AX_N$ Phases: a New Class of Solids; Thermodynamically Stable Nanolaminates. Prog. Solid State Chem 2000;28:201.

[9] Sundberg M, Malmqvist G, Magnusson A, El-Raghy T. Alumina Forming High Temperature Silicides and Carbides. Ceramics International 2004;30:1899.

[10] Barsoum MW. Physical Properties of the MAX Phases. In: K. H. J. Buschow RWC, M. C. Flemings, E. J. Kramer, S. Mahajan and P. Veyssiere, editor. Encyclopedia of Materials Science and Technology. Amsterdam: Elsevier, 2006.

[11] Barsoum MW, Brodkin D, El-Raghy T. Layered Machinable Ceramics For High Temperature Applications. Scrip. Met. et. Mater. 1997;36:535.

[12] Barsoum MW, El-Raghy T. Synthesis and Characterization of a Remarkable Ceramic: Ti_3SiC_2. J. Amer. Cer. Soc. 1996;79:1953.

[13] Barsoum MW, El-Raghy T. Room Temperature Ductile Carbides. Metallurgical and Materials Trans. 1999;30A:363.

[14] Barsoum MW, El-Raghy T, Rawn CJ, Porter WD, Wang H, Payzant A, Hubbard C. Thermal Properties of Ti_3SiC_2. J. Phys. Chem. Solids 1999;60:429.

[15] Scabarozi TH, Amini S, Leaffer O, Ganguly A, Gupta S, Tambussi W, Clipper S, Spanier JE, Barsoum MW, Hettinger JD, Lofland SE. Thermal expansion of select $M_{n+1}AX_n$ (M = early transition metal, A = A group element, X = C or N) phases measured by high temperature x-ray diffraction and dilatometry. Journal of Applied Physics 2009;105:013543.

[16] Barsoum MW. The Mn+1AXn Phases and Their Properties. Ceramics Science and Technology 2009;2.

[17] El-Raghy T, Zavaliangos A, Barsoum MW, Kalidindi SR. Damage Mechanisms Around Hardness Indentations in Ti_3SiC_2. J. Amer. Cer. Soc. 1997;80: 513.

[18] Barsoum MW, El-Raghy T, Ogbuji L. Oxidation Behavior of Ti_3SiC_2 in the Temperature Range of 900–1400°C. J. Electrochem. Soc. 1997;144:2508.

[19] Barsoum MW, El-Raghy T. A Progress Report on Ti_3SiC_2, Ti_3GeC_2 and the H-Phases, M_2BX. J. Mater. Synth. Process. 1997;5:197.

[20] Barsoum MW, Yaroschuck G, Tyagi S. Fabrication and Characterization of M_2SnC (M = Ti, Zr, Hf and Nb). Scr. Mater 1997;10:1583.
[21] Low IM, Lee SK, Lawn B, Barsoum MW. Contact Damage Accumulation in Ti_3SiC_2. ,J. Amer. Cer. Soc.
1998;81:225.
[22] Farber L, Barsoum MW, Zavaliangos A, El-Raghy T, Levin I. Dislocations and Stacking Faults in Ti_3SiC_2. J. Am. Ceram. Soc. 1998;81:1677.
[23] El-Raghy T, Barsoum MW. Processing and mechanical properties of Ti_3SiC_2: part I: reaction path and microstructure evolution. . J. Amer. Cer. Soc. 1999;82: 2849.
[24] El-Raghy T, Barsoum MW, Zavaliangos A, Kalidindi SR. Processing and mechanical properties of Ti_3SiC_2: II, effect of grain size and deformation temperature. J. Amer. Cer. Soc. 1999;82 2855.
[25] Barsoum MW, Farber L, El-Raghy T, Levin I. Dislocations, Kink Bands and Room Temperature Plasticity of Ti_3SiC_2. Met. Mater. Trans. 1999;30A:1727.
[26] Wang XH, Zhou YC. Oxidation behavior of Ti3AlC2 at 1000-1400 °C in air. Corrosion Science 2003;45:891.
[27] Amini S, Barsoum MW, El-Raghy T. Synthesis and mechanical properties of fully dense Ti_2SC. Journal of the American Ceramic Society 2007;90:3953.
[28] Amini S, Zhou A, Gupta S, De Villier A, Finkel P, Barsoum MW. Synthesis and elastic and mechanical properties of Cr2GeC. Journal of Materials Research 2008;23:2157.
[29] Barsoum MW, Ali M, El-Raghy T. Processing and characterization of Ti_2AlC, Ti_2AlCN and $Ti_2AlC_{0.5}N_{0.5}$. Met Mater Trans 2000;31A:1857.
[30] Manoun B, Saxena SK, Barsoum MW. High Pressure Study of Ti_4AlN_3 to 55 GPa. Appl. Phys. Letts. 2005;86:101906.
[31] El-Raghy T, Chakraborty S, Barsoum MW. Synthesis and Characterization of Hf2PbC, Zr2PbC and M2SnC (M=Ti, Hf, Nb or Zr). J. Eur. Cer. Soc. 2000;20:2619.
[32] Tzenov N, Barsoum MW. Synthesis and characterization of Ti3AlC1.8. J. Amer. Cer. Soc. 2000;83.
[33] Manoun B, Saxena SK, El-Raghy T, Barsoum MW. High-pressure X-ray Study of Ta_4AlC_3. Appl. Phys. Lett. 2006;88:201902.
[34] Barsoum MW, Farber L, Levin I, Procopio A, El-Raghy T, Berner A. High-Resolution Transmission Electron Microscopy of Ti4AlN3, or Ti3Al2N2 Revisited
J. Amer. Cer. Soc. 1999;82:2545.
[35] Barsoum MW, El-Raghy T, Radovic M. Ti_3SiC_2: a layered machinable ductile ceramic. Interceram 2000;49:226.
[36] Barsoum MW, El-Raghy T, Ogbuji L. Oxidation of Ti_3SiC_2 in Air. J. Electrochem. Soc., 1997;144:2508.
[37] Barsoum MW, Ho-Duc LH, Radovic M, El-Raghy T. Long Time Oxidation Study of Ti_3SiC_2, Ti_3SiC_2/SiC and Ti_3SiC_2/TiC Composites in Air. J. Electrochem. Soc. 2003;150:B166.
[38] Wang XH, Zhou YC. Intermediate-temperature oxidation behavior of Ti2AlC in air. Journal of Materials Research 2002;17:2974.
[39] Wang XH, Zhou YC. High-temperature oxidation behavior of Ti2AlC in air. Oxidation of Metals 2003;59:303.

[40] Lee DB, Thuan Dinh N, Han JH, Park SW. Oxidation of Cr2AlC at 1300C in air. Corrosion Science 2007;49:3926.
[41] Zhijun L, Zhou Y, Meishuan L. Synthesis, microstructure, and property of Cr2AIC. Journal of Materials Science and Technology 2007;23:721.
[42] Lee DB, Thuan Dinh N. Cyclic oxidation of Cr2AlC between 1000 and 1300C in air. Journal of Alloys and Compounds 2008;464:434.
[43] Tian W, Wang P, Kan Y, Zhang G. Oxidation behavior of Cr2AlC ceramics at 1,100 and 1,250 °C. Journal of Materials Science 2008;43:2785.
[44] Amini S, McGhie AR, Barsoum MW. Isothermal Oxidation of Ti[sub 2]SC in Air. Journal of the Electrochemical Society 2009;156:P101.
[45] Zhou AG, Barsoum MW. Kinking Nonlinear Elastic Deformation of Ti_3AlC_2, Ti_2AlC, $Ti_3Al(C_{0.5},N_{0.5})_2$ and $Ti_2Al(C_{0.5},N_{0.5})$. Sub. for pub.
[46] Nickl JJ, Schweitzer KK, Luxenberg P. Gasphasenabscheidung im Systeme Ti-C-Si. J. Less Common Metals 1972;26:335?3.
[47] Goto T, Hirai T. CHEMICALLY VAPOR-DEPOSITED TI3SIC_2. Mater. Res. Bull. 1987;22:1195.
[48] Barsoum MW. The MN+1AXN Phases: a New Class of Solids; Thermodynamically Stable Nanolaminates. Prog. Solid State Chem. 2000;28:201.
[49] Pampuch P, Lis J, Stobierski L, Tymkiewicz M. Solid Combustion Synthesis of Ti_3SiC_2. J. Eur. Ceram. Soc. 1989;5:283.
[50] El-Raghy T, Barsoum MW, Zavaliangos A, Kalidindi SR. Processing and mechanical properties of Ti_3SiC_2: II, effect of grain size and deformation temperature. J. Amer. Cer. Soc 1999;82:2855.
[51] El-Raghy T, Zavaliangos A, Barsoum MW, Kalidindi SR. Damage Mechanisms Around Hardness Indentations in Ti_3SiC_2. J. Amer. Cer. Soc 1997;80:513.
[52] Barsoum MW, Murugaiah A, Kalidindi SR, Zhen T. Kinking Nonlinear Elastic Solids, Nanoindentations and Geology. Phys. Rev. Lett. 2004;92:255508.
[53] Barsoum MW, Zhen T, Zhou A, Basu S, Kalidindi SR. Microscale Modeling of Kinking Nonlinear Elastic Solids. Phys. Rev. B. 2005;71:134101.
[54] Basu S, Zhou A, Barsoum MW. Reversible dislocation motion under contact loading in LiNbO3 single crystal. Journal of Materials Research 2008;23:1334.
[55] Basu S, Barsoum MW, Kalidindi SR. Sapphire: A kinking nonlinear elastic solid. Journal Of Applied Physics 2006;99.
[56] Barsoum MW, Zhen T, Kalidindi SR, Radovic M, Murugahiah A. Fully Reversible, Dislocation-Based Compressive Deformation of Ti_3SiC_2 to 1 GPa. Nature Materials 2003;2:107.
[57] Zhou AG, Barsoum MW, Basu S, Kalidindi SR, El-Raghy T. Incipient and Regular Kink Bands in Dense and Porous Ti_2AlC. Acta Mater. 2006;54:1631.
[58] Zhou AG, Basu S, Barsoum MW. Kinking nonlinear elasticity, damping and microyielding of hexagonal close-packed metals. Acta Materialia 2008;56:60.
[59] Zhou A, Barsoum M. Kinking Nonlinear Elasticity and the Deformation of Magnesium. Metallurgical and Materials Transactions A 2009.
[60] Barsoum MW, Zhen T, Zhou A, Basu S, Kalidindi SR. Microscale modeling of kinking nonlinear elastic solids. Phys. Rev. B 2005;71:134101.
[61] Orowan E. A Type of Plastic Deformation New In Metals. Nature 1942;149:463.

[62] Barsoum MW, Murugaiah A, Kalidindi SR, Gogotsi Y. Kink Bands, Nonlinear Elasticity and Nanoindentations in Graphite. Carbon 2004;42:1435.
[63] Barsoum SBAZMW. On Nanoindentations, Kinking Nonlinear Elasticity of Mica Single Crystals and Their Geological Implications. In Print.
[64] Basu S, Barsoum MW, Kalidindi SR. Sapphire: A kinking nonlinear elastic solid. J. App. Phys. 2006;99:063501.
[65] Basu S, Barsoum MW. Deformation micromechanisms of ZnO single crystals as determined from spherical nanoindentation stress-strain curves. Journal of Materials Research 2007;22:2470.
[66] Basu S, Barsoum MW, Williams AD, Moustakas TD. Spherical nanoindentation and deformation mechanisms in freestanding GaN films. Journal of Applied Physics 2007;101.
[67] Basu S, Zhou A, Barsoum MW. Reversible Dislocation Motion under Contact Loading in LiNbO3 Single Crystal. Journal of Materials Research Accepted.
[68] Zhou AG, Basu S, Barsoum MW. Kinking nonlinear elasticity, damping and microyielding of hexagonal close-packed metals. Acta Materialia 2008;56:60.
[69] Zhou A. Kinking Nonlinear Elasticity: Theory and Experiments. Ph.D. Thesis 2008;Drexel University
[70] Zhou AG, Brown D, Vogel S, Yeheskel O, Barsoum MW. On The Kinking Nonlinear Elastic Deformation of Cobalt. Submitted for Publication.
[71] Amini S, Ni C, Barsoum MW. Processing, microstructural characterization and mechanical properties of a Ti_2AlC/nanocrystalline Mg-matrix composite. Composites Science and Technology 2009;69:414.
[72] Amini S, Barsoum MW. On the Effect of Texture on the Mechanical Properties of Nano-crystalline Mg-Matrix Composites Reinforced with MAX Phases. Submitted for Publication 2009.
[73] Frank FC, Stroh AN. On the Theory of Kinking. Proc. Phys. Soc. 1952; 65:811.
[74] Barsoum MW, Radovic M. Mechanical Properties of the MAX Phases. In: K. H. J. Buschow RWC, M. C. Flemings, E. J. Kramer, S. Mahajan and P. Veyssiere, editor. Encyclopedia of Materials Science and Technology. Amsterdam: Elsevier, 2004.
[75] Murugaiah A, Barsoum MW, Kalidindi SR, Zhen T. Spherical Nanoindentations in Ti_3SiC_2. J. Mater. Res. 2004;19:1139.
[76] Barsoum MW, Radovic M, Zhen T, Finkel P. Dynamic Elastic Hysteretic Solids and Dislocations. Phys. Rev. Lett. 2005;94:085501.
[77] Amini S, Zhou A, Gupta S, DeVillier A, Finkel P, Barsoum MW. Synthesis and Elastic and Mechanical Properties of Cr2GeC. Journal of Materials Science 2008;In Print.
[78] Hettinger JD, Lofland SE, Finkel P, Meehan T, Palma J, Harrell K, Gupta S, Ganguly A, El-Raghy T, Barsoum MW. Electrical transport, thermal transport, and elastic properties of M_2AlC (M= Ti, Cr, Nb, and V). Physical Review B 2005;72:115120.
[79] Zhou AG, Basu B, Barsoum MW. Kinking Nonlinear Elasticity, Damping and Microyielding of Hexagonal Close-Packed Metals. Acta Mat. 2008;56:60.
[80] Zhou AG, Barsoum MW. Kinking nonlinear elasticity and the deformation of Mg. METALLURGICAL AND MATERIALS TRANSACTIONS A In print.
[81] Lazan BJ. Damping of materials and members in structural mechanics. Pergamon Press, Oxford, New York 1968.

[82] Ye HZ, Xing Yang L. Review of recent studies in magnesium matrix composites. Journal of Materials Science 2004;39:6153.
[83] Luo A, Renaud J, Nakatsugawa I, Plourde J. Magnesium castings for automotive applications. JOM 1995;47:28.
[84] Clow BB. Magnesium industry review. Advanced Materials & Processes 1996;150:2.
[85] Basu S, Aiguo Z, Barsoum MW. Reversible dislocation motion under contact loading in LiNbO3 single crystal. Journal of Materials Research 2008;23:1334.
[86] Radovic M, Barsoum MW, El-Raghy T, Seidensticker J, Wiederhorn SM. Tensile properties of Ti3SiC2 in the 25-1300C temperature range. Acta Materialia 2000;48:453.
[87] Frank FC, Stroh AN. On The Theory of Kinking. Proc. Phys. Soc., vol. 65. LONDON, 1952. p.811.
[88] Barsoum AGZMW. Kinking nonlinear elastic deformation of Ti3AlC2, Ti2AlC, Ti3Al(C0.5,N0.5)2 and Ti2Al(C0.5,N0.5). Submitted for Publication 2009.
[89] Westengen H, Bakke P. Magnesium die casting alloys for use in applications exposed to elevated temperatures: can they compete with aluminium? Materials Science Forum 2003;419-422:35.
[90] Capel H, Harris SJ, Schulz P, Kaufmann H. Correlation between manufacturing conditions and properties of carbon fibre reinforced Mg. vol. 16. London, UK: Inst. Mater, 2000. p.765.
[91] Chua BW, Lu L, Lai MO. Influence of SiC particles on mechanical properties of Mg based composite. Composite Structures 1999;47:595.
[92] Li L, Lai MO, Gupta M, Chua BW, Osman A. Improvement of microstructure and mechanical properties of AZ91/SiC composite by mechanical alloying. Journal of Materials Science 2000;35:5553.
[93] Badini C, Marino F, Montorsi M, Guo XB. Precipitation phenomena in B4C-reinforced magnesium-based composite. Materials Science & Engineering A (Structural Materials: Properties, Microstructure and Processing) 1992;A157:53.
[94] Mikucki BA, Mercer WE, II, Green WG. Extruded magnesium alloys reinforced with ceramic particles. Light Metal Age 1990;48:12.
[95] Luo A. Processing, microstructure, and mechanical behavior of cast magnesium metal matrix composites. Metallurgical and Materials Transactions A: Physical Metallurgy and Materials Science 1995;26A:2445.
[96] Saravanan RA, Surappa MK. Fabrication and characterisation of pure magnesium-30 vol.% SiCP particle composite. Materials Science & Engineering A (Structural Materials: Properties, Microstructure and Processing) 2000;A276:108.
[97] Lim S-w, Choh T. Effect of alloying elements on SiC particulate dispersion behavior in molten magnesium. Nippon Kinzoku Gakkaishi/Journal of the Japan Institute of Metals 1992;56:210.
[98] Purazrang K, Kainer KU, Mordike BL. Fracture toughness behaviour of a magnesium alloy metal-matrix composite produced by the infiltration technique. Composites 1991;22:456.
[99] Wu K, Zheng M, Yao C, Sato T, Tezuka H, Kamio A, Li DX. Crystallographic orientation relationship between SiCw and Mg in squeeze-cast SiCw/Mg composites. Journal of Materials Science Letters 1999;18:1301.

[100] Zheng M, Wu K, Yao C, Sato T, Tezuka H, Kamio A, Li DX. Interfacial bond between SiCw and Mg in squeeze cast SiCw/Mg composites. Materials Letters 1999;41:57.
[101] Wu K, Zheng M, Zhao M, Yao C, Li J. Interfacial reaction in squeeze cast SiCw/AZ91 magnesium alloy composite. Scripta Materialia 1996;35:529.
[102] Zheng M, Wu K, Zhao M, Yao C, Li J, Li D. Precipitates in aged SiCw/AZ91 magnesium matrix composite. Journal of Materials Science Letters 1997;16:1106.
[103] Kevorkijan V. Mg AZ80/SiC composite bars fabricated by infiltration of porous ceramic preforms. Metallurgical and Materials Transactions a-Physical Metallurgy and Materials Science 2004;35A:707.
[104] Dong Q, Chen LQ, Zhao MJ, Bi J. Synthesis of TiCp reinforced magnesium matrix composites by in situ reactive infiltration process. Materials Letters 2004;58:920.
[105] Kaneda H, Choh T. Fabrication of particulate reinforced magnesium composites by applying a spontaneous infiltration phenomenon. Journal of Materials Science 1997;32:47.
[106] Kevorkijan V, Kosmac T, Kristoffer K. Spontaneous reactive infiltration of porous ceramic preforms with Al-Mg and Mg in the presence of both magnesium and nitrogen - New experimental evidence. Materials and Manufacturing Processes 2002;17:307.
[107] ASM Handbooks Online. ASM Intrnational, 2008.
[108] Gupta S, Filimonov D, Palanisamy T, El-Raghy T, Barsoum MW. Ta₂AlC and Cr₂AlC Ag-based composites-New solid lubricant materials for use over a wide temperature range against Ni-based superalloys and alumina. Wear 2007;262:1479.
[109] Zhang Z, Xu S. Copper-Ti_3SiC_2 composite powder prepared by electroless plating under ultrasonic environment. Rare Metals 2007;26:359.
[110] Ngai TL, Zhiyu X, Yuanbiao W, Yuanyuan L. Studies on preparation of Ti_3SiC_2 particulate reinforced Cu matrix composite by warm compaction and its tribological behavior. Materials Science Forum 2007;534-536:929.
[111] Ngai TL, Yuanyuan L, Zhaoyao Z. A study on Ti_3SiC_2 reinforced copper matrix composite by warm compaction powder metallurgy. Materials Science Forum 2007;532-533:596.
[112] Ho-Duc LH, El-Raghy T, Barsoum MW. Synthesis and characterization of 0.3VfTiC-TiSiC2 and 0.3VfSiC Ti3SiC2 composites. J. of Alloys and Compounds 2003;350:303.
[113] Wu J, Zhou Y, Yan C. Mechanical and electrical properties of Ti2SnC dispersion-strengthened copper. Zeitschrift fuer Metallkunde/Materials Research and Advanced Techniques 2005;96:847.
[114] Kainer KU. Magnesium alloys and technology: Wiley-VCH, 2003.
[115] Decker. RF. The renaissance of magnesium. Advanced Materials & Processes 1998;154:31.
[116] Stalmann A, Sebastian W, Friedrich H, Schumann S, Droder K. Properties and processing of magnesium wrought products for automotive applications. Advanced Engineering Materials 2001;3:969.
[117] Mortensen A, Anthony K, Carl Z. Melt Infiltration of Metal Matrix Composites. Comprehensive Composite Materials. Oxford: Pergamon, 2000. p.521.

[118] Murugaiah A, Souchet A, El-Raghy T, Radovic M, Barsoum MW. Tape Casting, Pressureless Sintering and Grain Growth in Ti_3SiC_2 Compacts. J. Amer. Cer. Soc. 2004;87:550.
[119] Jeitschko W, Nowotny H, Benesovsky F. Kohlenstoffhaltige ternare Verbindungen (H-Phase). Monatsh. Chem. 1963;94:672.
[120] Kisi EH, Crossley JAA, Myhra S, Barsoum MW. Structure and Crystal Chemistry of Ti_3SiC_2. J. Phys. and Chem. of Solids 1998;59:1437.
[121] Cullity BD. Elements of x-ray diffraction. 1978.
[122] E. Brandes GBB, c. Smithells. Smithells Metals Reference Book: Oxford; Boston: Butterworth-Heinemann, 1998.
[123] Myhra S, Crossley A, Barsoum MW. Crystal chemistry from XPS analysis of carbide-derived Mn+1AXn (n=1) nano-laminate compounds. J. Phys. and Chem. of Solids 2002:811.
[124] Barsoum MW, El-Raghy T, Farber L, Amer M, Christini R, Adams A. The Topotaxial Transformation of Ti_3SiC_2 To Form a Partially Ordered Cubic $TiC_{0.67}$ Phase by the Diffusion of Si into Molten Cryolite. J. Electrochem. Soc. 1999;146.
[125] El-Raghy T, Barsoum MW, Sika M. Reaction of Al with Ti_3SiC_2 in the 800-1000 °C Temperature Range. Mater. Sci. Eng. A 2001;298:174.
[126] ASM Specialty Handbook: Aluminum and Aluminum Alloys. ASM International, 1993.
[127] Contreras A, López VH, Bedolla E. Mg/TiC composites manufactured by pressureless melt infiltration. Scripta Materialia 2004;51:249.
[128] Barsoum MW, Murugaiah A, Kalidindi SR, Zhen T, Gogotsi Y. Kink bands, nonlinear elasticity and nanoindentations in graphite. Carbon 2004;42:1435.
[129] Zhen T. Compressive Behavior of Kinking Nonlinear Elastic Solids - Ti_3SiC_2, Graphite, Mica and BN. Department of Materials Science and Engineering, vol. PhD. Philadelphia, PA 19104: Drexel University, 2004.
[130] Basu S, Barsoum MW. Deformation micromechanisms of ZnO single crystals as determined from spherical nanoindentation stress-strain curves. Journal of Materials Research 2007;22:2470.
[131] Amini S JMCG, Luke Daemen, Andrew R. McGhie, Chaoying Ni, Lars Hultman, Magnus Odén, Michel W. Barsoum. On the Stability of Mg Nanograins to Coarsening after Repeated Melting. Nano Letters Accepted for Publication.
[132] Pierson HO. Handbook of Refractory Carbides and Nitrides. Westwood, NJ: Noyes Publications, 1996.
[133] Lim SCV, Gupta M, Lu L. Processing, microstructure, and properties of Mg-SiC composites synthesised using fluxless casting process. Materials Science and Technology 2001;17:823.
[134] Hassan SF, Gupta M. Development of ductile magnesium composite materials using titanium as reinforcement. Journal of Alloys and Compounds 2002;345:246.
[135] Hassan SF, Gupta M. Development of high performance magnesium nano-composites using nano-Al2O3 as reinforcement. Materials Science and Engineering A 2005;392:163.
[136] Hassan SF, Tan MJ, Gupta M. High-temperature tensile properties of Mg/Al2O3 nanocomposite. Materials Science and Engineering A 2008;486:56.

[137] Hassan SF, Gupta M. Effect of submicron size Al2O3 particulates on microstructural and tensile properties of elemental Mg. Journal of Alloys and Compounds 2008;457:244.
[138] Hassan SF, Gupta M. Development and characterization of ductile Mg/Y2O3 nanocomposites. Transactions of the ASME. Journal of Engineering Materials and Technology 2007;129:462.
[139] Hassan SF, Gupta M. Effect of different types of nano-size oxide particulates on microstructural and mechanical properties of elemental Mg. Journal of Materials Science 2006;41:2229.
[140] Radovic M, Barsoum MW, Ganguly A, Zhen T, Finkel P, Kalidindi SR, Lara-Curzio E. On the elastic properties and mechanical damping of Ti3SiC2, Ti3GeC2, Ti3Si0.5Al0.5C2 and Ti2AlC in the 300-1573 K temperature range. Acta Materialia 2006;54:2757.
[141] Matthew FL. Composite Materials: Engineering and Science, 1994.
[142] Kooi BJ, Poppen RJ, Carvalho NJM, M. DJT, Barsoum MW. Ti3SiC2: A damage tolerant ceramic studied with nanoindentations and transmission electron microscopy. Acta Materialia 2003;51:2859.
[143] Xiu K, Jiang QC, Ma BX, Wang Y, Sui L, Shang EY. Fabrication of TiCp/Mg composites by powder metallurgy. Journal of Materials Science 2006;41:1663.
[144] Jiang QC, Wang HY, Wang JG, Guan QF, Xu CL. Fabrication of TiCp/Mg composites by the thermal explosion synthesis reaction in molten magnesium. Materials Letters 2003;57:2580.
[145] Kumashiro Y, Itoh A, Kinoshita T, Sobajima M. The micro-Vickers hardness of TiC single crystals up to 1500C. Journal of Materials Science 1977;12:595.
[146] Ganguly A, Zhen T, Barsoum MW. Synthesis and Mechanical Properties of Ti_3GeC_2 and $Ti_3(Si_xGe_{1-x})C_2$ (x = 0.5, 0.75) Solid Solutions. J. Alloys and Compounds 2004;376:287.
[147] Brown DW, Agnew SR, Abeln SP, Blumenthal WR, Bourke MAM, Mataya MC, Tome CN, Vogel SC. The role of texture, temperature, and strain rate in the activity of deformation twinning. vol. 495-497. Switzerland: Trans Tech Publications, 2005. p.1037.
[148] Agnew SR, Tome CN, Brown DW, Holden TM, Vogel SC. Study of slip mechanisms in a magnesium alloy by neutron diffraction and modeling. Scripta Materialia 2003;48:1003.
[149] Brown DW, Abeln SP, Blumenthal WR, Bourke MAM, Mataya MC, Tome CN. Development of crystallographic texture during high rate deformation of rolled and hot-pressed beryllium. Metallurgical and Materials Transactions A (Physical Metallurgy and Materials Science) 2005;36A:929.
[150] Brown DW, Agnew SR, Bourke MAM, Holden TM, Vogel SC, Tome CN. Internal strain and texture evolution during deformation twinning in magnesium. Materials Science and Engineering A 2005;399:1.
[151] Clausen B, Tome CN, Brown DW, Agnew SR. Reorientation and stress relaxation due to twinning: modeling and experimental characterization for Mg. Acta Materialia 2008;56:2456.
[152] Wang J, Zhou Y. Dependence of Elastic Stiffness on Electronic Band Structure of Nanolaminate M2AlC (M=Ti,V,Nb and Cr) Ceramics. Phys. Rev. B 2004;69:214111.

[153] Przybyla CP, Adams BL, Miles MP. Methodology for determining the variance of the Taylor factor: application in Fe-3%Si. Transactions of the ASME. Journal of Engineering Materials and Technology 2007;129:82.
[154] Justinger H, Hirt G. Estimation of grain size and grain orientation influence in microforming processes by Taylor factor considerations. Journal of Materials Processing Technology 2009;209:2111.
[155] Taylor GI. Plastic strain in metals. Institute of Metals -- Journal 1938;62:307.
[156] Radovic M, Ganguly A, Barsoum MW, Zhen T, Finkel P, Kalidindi SR, Lara-Curzio E. On the Elastic Properties and Mechanical Damping of Ti_3SiC_2, Ti_3GeC_2, $Ti_3Si_{0.5}Al_{0.5}C_2$ and Ti_2AlC in the 300-1573 K Temperature Range. Acta Mater. 2006;54:2757.
[157] Radovic M, Ganguly A, Barsoum MW. Elastic properties and phonon conductivities of Ti3Al(C0.5,N0.5)2 and Ti2Al(C0.5,N0.5) solid solutions. Journal of Materials Research 2008;23:1517.
[158] Asthana R, Rohatgi PK, Tewari SN. Infiltration processing of metal-matrix composites: a review. Processing of Advanced Materials 1992;2:1.
[159] Ibrahim IA, Mohamed FA, Lavernia EJ. Particulate reinforced metal matrix composites-a review. Journal of Materials Science 1991;26:1137.
[160] Kelly A, Mortensen A, Buschow KHJ, Robert WC, Merton CF, Bernard I, Edward JK, Subhash M, Patrick V. Composite Materials: Overview. Encyclopedia of Materials: Science and Technology. Oxford: Elsevier, 2001. p.1361.
[161] Prewo KM, Tredway WK, Buschow KHJ, Robert WC, Merton CF, Bernard I, Edward JK, Subhash M, Patrick V. Ceramic Matrix Composites: Applications. Encyclopedia of Materials: Science and Technology. Oxford: Elsevier, 2001. p.1056.
[162] Hunt Jr WH, Buschow KHJ, Robert WC, Merton CF, Bernard I, Edward JK, Subhash M, Patrick V. Metal Matrix Composites: Applications. Encyclopedia of Materials: Science and Technology. Oxford: Elsevier, 2001. p.5442.
[163] Gell M. Application opportunities for nanostructured materials and coatings. Journal of Engineering and Applied Science 1995;A204:246.
[164] Krallics G, Latysh V, Alexandrov I, Fodor A. Application of bulk nanostructured materials in medicine. Current Applied Physics 2006;6:262.
[165] Voevodin AA, Zabinski JS. Nanocomposite and nanostructured tribological materials for space applications. Composites Science and Technology 2005;65:741.
[166] Gleiter H. Nanostructured materials: state of the art and perspectives. Nanostructured Materials 1995;6:3.
[167] Lai SL, Guo JY, Petrova V, Ramanath G, Allen LH. Size-dependent melting properties of small tin particles: nanocalorimetric measurements. Physical Review Letters 1996;77:99.
[168] Gleiter H. Nanostructured materials: basic concepts and microstructure. Acta Materialia 2000;48:1.
[169] Andrievski RA. Review stability of nanostructured materials. Journal of Materials Science 2003;38:1367.
[170] Ercolessi F, Andreoni W, Tosatti E. Melting of small gold particles: mechanism and size effects. Physical Review Letters 1991;66:911.
[171] Goldstein AN, Echer CM, Alivisatos AP. Melting in semiconductor nanocrystals. Science 1992;256:1425.

[172] Sun J, Simon SL. The melting behavior of aluminum nanoparticles. Thermochimica Acta 2007;463:32.
[173] Delogu F. Thermodynamics on the nanoscale. Journal of Physical Chemistry B 2005;109:21938.
[174] Buffat P, Borel JP. Size effect on the melting temperature of gold particles. Physical Review A (General Physics) 1976;13:2287.
[175] Eckert J, Holzer JC, Ahn CC, Fu Z, Johnson WL. Melting behavior of nanocrystalline aluminum powders. Nanostructured Materials 1993;2:407.
[176] Allen GL, Bayles RA, Gile WW, Jesser WA. SMALL PARTICLE MELTING OF PURE METALS. Thin Solid Films 1986;144:297.
[177] Takagi M. Electron-diffraction study of liquid-solid transition of thin metal films. Journal of the Physical Society of Japan 1954;9:359.
[178] Sun J, Pantoya ML, Simon SL. Dependence of size and size distribution on reactivity of aluminum nanoparticles in reactions with oxygen and MoO3. Thermochimica Acta 2006;444:117.
[179] Qi WH. Size effect on melting temperature of nanosolids. Physica B: Condensed Matter 2005;368:46.
[180] David TB, Lereah Y, Deutschert G, Kofman R, Cheyssac P. Solid-liquid transition in ultra-fine lead particles. Philosophical Magazine A (Physics of Condensed Matter, Defects and Mechanical Properties) 1995;71:1135.
[181] Shi FG. Size dependent thermal vibrations and melting in nanocrystals. Journal of Materials Research 1994;9:1307.
[182] Barsoum MW. Fundamentals of Ceramics. Bristol: Institute of Physics, 2003.
[183] Solliard C. Debye-Waller factor and melting temperature in small gold particles: related size effects. Solid State Communications 1984;51:947.
[184] Zhao M, Zhou XH, Jiang Q. Comparison of different models for melting point change of metallic nanocrystals. Journal of Materials Research 2001;16:3304.
[185] Hasegawa M, Watabe M, Hoshino K. A theory of melting in metallic small particles. Journal of Physics F (Metal Physics) 1980;10:619.
[186] Hasegawa M, Watabe M, Hoshino K. Size dependence of melting point in small particles. vol. 106. Lausanne, Switzerland, 1981. p.10.
[187] Gibbs JW. The CollectedWorks of J.Willard Gibbs. New Haven: Yale University Press, 1948.
[188] Sun DY, Mendelev MI, Becker CA, Kudin K, Haxhimali T, Asta M, Hoyt JJ, Karma A, Srolovitz DJ. Crystal-melt interfacial free energies in hcp metals: a molecular dynamics study of Mg. Physical Review B (Condensed Matter and Materials Physics) 2006;73:24116.
[189] Mikami M, Nakamura S, Kitao O, Arakawa H. Lattice dynamics and dielectric properties of TiO2 anatase: a first-principles study. Physical Review B (Condensed Matter and Materials Physics) 2002;66:155213.
[190] Traylor JG, Smith HG, Nicklow RM, Wilkinson MK. Lattice dynamics of rutile. Physical Review B (Solid State) 1971;3:3457.
[191] Gaskell D. Introduction To The Thermodynamics Of Materials. New York: Taylor & Francis, 2008.
[192] Kalyanaraman R. Nucleation energetics during homogeneous solidification in elemental metallic liquids. Journal of Applied Physics 2008;104:033506.

[193] Turnbull D. Formation of crystal nuclei in liquid metals. Journal of Applied Physics 1950;21:1022.
[194] W. Kurz DJF. Fundamentals of solidification Uetikon-Zuerich, Switzerland: Trans Tech Publications, 1998.
[195] Li Z, Liu X, Jiang L, Wang S. Characterization of Mg-20 wt% Ni-Y hydrogen storage composite prepared by reactive mechanical alloying. . Int. J. Hydrogen Energy 2007;32:1869.
[196] Schlapbach L, A. Z. Hydrogen-storage materials for mobile applications. Nature 2001;414:353.
[197] Jun Y, Ciureanu M, Roberge R. Hydrogen storage properties of nano-composites of Mg and Zr-Ni-Cr alloys. Materials Letters 2000;43:234.
[198] Huhn PA, Dornheim M, Klassen T, Bormann R. Thermal stability of nanocrystalline magnesium for hydrogen storage. Journal of Alloys and Compounds 2005;404-406:499.
[199] Terzieva M, Khrussanova M, Peshev P. Hydriding and dehydriding characteristics of Mg-LaNi5 composite materials prepared by mechanical alloying. Journal of Alloys and Compounds 1998;267:235.
[200] Gross KJ, Spatz P, Zuettel A, Schlapbach L. Mechanically milled Mg composites for hydrogen storage. The transition to a steady state composition. Journal of Alloys and Compounds 1996;240:206.
[201] Zaluski L, Zaluska A, Strom-Olsen JO. Nanocrystalline metal hydrides. Journal of Alloys and Compounds 1997;253-254:70.
[202] Li Z, Liu X, Jiang L, Wang S. Characterization of Mg-20 wt% Ni-Y hydrogen storage composite prepared by reactive mechanical alloying. International Journal of Hydrogen Energy 2007;32:1869.
[203] Schlapbach L, Zuttel A. Hydrogen-storage materials for mobile applications. Nature 2001;414:353.
[204] Basu S, Radovic M, Barsoum MW. Room temperature constant-stress creep of a brittle solid studied by spherical nanoindentation. Journal of Applied Physics 2008;104.
[205] Syed ASA, Pethica JB. Nanoindentation creep of single-crystal tungsten and gallium arsenide. Philosophical Magazine A: Physics of Condensed Matter, Structure, Defects and Mechanical Properties 1997;76:1105.
[206] Zhou L, Yao Y. Single crystal bulk material micro/nano indentation hardness testing by nanoindentation instrument and AFM. Materials Science and Engineering A 2007;460-461:95.
[207] Liu Y, Varghese S, Ma J, Yoshino M, Lu H, Komanduri R. Orientation effects in nanoindentation of single crystal copper. International Journal of Plasticity 2008;24:1990.
[208] Kim J-Y, Greer JR. Size-dependent mechanical properties of molybdenum nanopillars. Applied Physics Letters 2008;93.
[209] Zhou AG, Barsoum MW. Kinking nonlinear elasticity and the deformation of Mg. METALLURGICAL AND MATERIALS TRANSACTIONS A Accepted.
[210] Nowotny H. Struktuchemie Einiger Verbindungen der Ubergangsmetalle mit den elementen C, Si, Ge, Sn. Prog. Solid State Chem. 1970;2:27.
[211] Scabarozi TH, Amini S, Finkel P, Barsoum MW, Tambussi WM, Hettinger JD, Lofland SE. Electrical, Thermal, and Elastic Properties of Ti_2SC. Sub. for pub.

[212] Kulkarni S, Vennila S, Phatak N, Saxena SK, Zha CS, El-Raghy T, Barsoum MW, Luo W, Ahuja R. Study of Ti2SC Under Compression up to 47 GPa. J. Alloy Compds. in print.
[213] Gupta S, Amini S, Filimonov D, Palanisamy T, El-Raghy T, Barsoum MW. Tribological Behavior of Ti2SC at Ambient and Elevated Temperatures. Sub. for pub.
[214] Anstis GR, Chantikul P, Lawn BR, Marshall DB. A Critical Evaluation of Indentation Techniques for Measuring Fracture Toughness. I. Direct Crack Measurements. Journal of the American Ceramic Society 1981;64:533.
[215] Kruzic JJ, Ritchie RO. Determining the toughness of ceramics from Vickers indentations using the crack-opening displacements: an experimental study. Journal of the American Ceramic Society 2003;86:1433.
[216] Wang JG, Guan Z. Indentation toughness of ceramics: A modified approach. Journal of Materials Science (USA) 2002;37:865.
[217] Kudielka R, Rhode W. Kristallgeom. Krystallphys. Kristallchem 1960;114:447.
[218] Horn M, Schwerdtfeger CF, Meagher EP. Refinement of the structure of anatase at several temperatures. Zeitschrift fuer Kristallographie, Kristallgeometrie, Kristallphysik, Kristallchemie 1972;136:273.
[219] Kudielka H, Rohde H. Z. Kristalogr. 1960;114:447.
[220] Salama I, El-Raghy T, Barsoum MW. Synthesis and mechanical properties of Nb2AlC and (Ti, Nb)2AlC. J. Alloys Compds. 2002;347:271.
[221] Zhen T. Compressive Behavior of Kinking Non-linear Elastic Solids - Ti3SiC2, Graphite, mica and BN. Department of Materials Science and Engineering. Philadelphia: : Drexel University, 2004.
[222] Gilbert CJ, Bloyer DR, Barsoum MW, El-Raghy T, Tomasia AP, Ritchie RO. Fatigue-crack Growth and Fracture Properties of Coarse and Fine-grained Ti_3SiC_2. Scripa Materialia 2000;238:761.
[223] Kulkarni SR, Merlini M, Phatak N, Saxena SK, Artioli G, Amini S, Barsoum MW. Thermal expansion and stability of Ti2SC in air and inert atmospheres. Journal of Alloys and Compounds 2009;469:395.
[224] Radhakrishnan R, Williams JJ, Akinc M. Synthesis and high-temperature stability of Ti_3SiC_2. Journal of Alloys and Compounds 1999;285:85.
[225] Barsoum MW, Tzenov N, Procopio A, El-Raghy T, Ali M. Oxidation of $Ti_{n+1}AlX_n$ where n = 1-3 and X is C, N, Part II: Experimental Results J.. Electrochem. Soc., 2001;148:C551.
[226] Wang XH, Zhou YC. Oxidation behavior of Ti3AlC2 at 1000-1400°C in air. Corrosion Science 2003;45:891.
[227] Wang XH, Zhou YC. High-temperature oxidation behavior of Ti2AlC in air. Oxidation of Metals 2003;59:303.
[228] Gupta S, Ganguly A, Filimonov D, Barsoum MW. High-temperature oxidation of Ti_3GeC_2 and $Ti_3Ge_{0.5}Si_{0.5}C_2$ in air. Journal of the Electrochemical Society 2006;153:61.
[229] Barsoum MW. Oxidation of $Ti_{n+1}AlX_n$ where n = 1-3 and X is C, N, Part I: Model". J. Electrochem. Soc. 2001;148:C544.
[230] Scabarozi TH, Amini S, Finkel P, Barsoum MW, Tambussi WM, Hettinger JD, Lofland SE. Electrical, Thermal, and Elastic Properties of Ti_2SC. Journal of Applied Physics, submitted. 2008.

[231] Jeitschko W, Nowotny H, Benesovsky F. Kohlenstoffhaltige ternare Verbindungen (V-Ge-C, Nb-Ga-C, Ta-Ga-C, Ta-Ge-C, Cr-Ga-C und Cr-Ge-C). Monatsh. Chem. 1963;94:844.
[232] Manoun B, Amini S, Gupta S, Saxena SK, Barsoum MW. On the compression behavior of Cr2GeC and V2GeC up to quasi-hydrostatic pressures of 50 GPa. Journal of Physics Condensed Matter 2007;19:456218.
[233] S. Amini THS, A. Ganguly, S. Gupta, W. Tambussi, S. Clipper, M.W. Barsoum, J.D. Hettinger, S.E. Lofland. On the Thermal Expansion of Select MAX Phases by Dilatometry and High Temperature X-Ray Diffraction.
[234] Barsoum MW. Nanoindentations of Nanolayered Or Kinking Nonlinear Elastic Solids: CRC Press., 2005.
[235] A. G. Zhou AGaMWB. Kinking Nonlinear Elastic Deformation of Ti_3AlC_2, Ti_2AlC, $Ti_3Al(C_{0.5},N_{0.5})_2$ and $Ti_2Al(C_{0.5},N_{0.5})$. Sub. for pub.

VITA

SHAHRAM AMINI

EDUCATION

2005-2009 – Drexel University, Philadelphia, PA: **Ph.D.** in Materials Science and Engineering

2000-2003 – Shiraz University, School of Engineering, Shiraz, Iran: **M.Sc.** in Materials Science and Engineering *(Distinction)*

1995-2000 – Sharif University of Technology, Tehran, Iran: **B.Sc.** in Metallurgical and Materials Engineering

RESEARCH EXPERIENCE & PROJECT MANAGEMENT

2005-2009 – Doctoral Fellow – Drexel University; *Research Experience*: Synthesis, Fabrication and Characterization of MAX Phases (Ternary Carbides and Nitrides); Fabrication & Characterization of MAXMETs: New Class of nano-crystalline Mg Matrix Composites Reinforced with MAX Phases; Ultrahigh Damping of Random and Oriented MAX Phases and MAXMETs; Oxidation Behaviour Studies of Ternary Carbides; Processing-Microstructure-Property Relationships in MAX-based metal matrix composites and MAX phases; Thermal Properties of MAXMETs

2003-2005 – Visiting Researcher – Materials Department, Queen Mary University of London, UK; *Research Experience*: Toughening of Thermosetting Composites with Thermoplastic Fibres

2001-2003 – Project Director & Principal Investigator – Joint Collaboration; Materials Research Center at SAPCO (Supplier of Peugeot Auto Parts Co.), Ministry of Metals & Industries, Ministry of Petroleum & Shiraz University; *Research Experience*: Feasibility Study of Net-shape Discontinuously Reinforced Metal Matrix Composites in Automotive Industry; Fabrication and Characterization of Al-SAFFIL and Hybrid Al-SAFFIL/SiC Composites

1999-2001 – R&D Materials Engineer – Research and Technology Development Center and Materials Research Center, SAPCO, Tehran (Part time); *Research Experience*: Utilization of Al alloys and Composites in Automotive Industry

1999-2000 – R&D Engineer – Research and Development Center, Nik-Kala Co., Tehran (Part time); *Research Experience*: Extrusion of Copper Alloy Profiles: Processing and Post-processing Optimization and Effect of Heat Treatment on Mechanical Properties; Development, Selection and Recommendation of Refractory Materials for Use in Natural Gas Heaters

1998-1999 – Internship Project Coordinator – SAPCO's Materials Research Center, Tehran (Part-time); *Research Experience*: Material Selection, Failure analysis and Modification of Fabrication Processes of Polymeric Parts of Peugeot 405

PATENTS

2008 – MAX-based Metal Matrix Composites, United States Patent and Trademark Office.

PUBLICATIONS

Peer-Reviewed Journal Articles (Sorted by Reverse Chronological Order)

2009 – S. Amini, M.W. Barsoum: On the Stability of Mg Nanograins to Coarsening after Repeated Melting, Nano Letters.

2009 – S. Amini, C. Ni, M.W. Barsoum: Processing, Microstructural Characterization and Mechanical Properties of a Ti_2AlC Nanocrystalline Mg Matrix Composite, Journal of Composites Science and Technology.

2009 – S. Amini, A. McGhie, M.W. Barsoum: Isothermal Oxidation of Ti_2SC in Air, Journal of Electrochemical Society, Journal of the Electrochemical Society.

2008 – Monika K. Drulis, H. Drulis, A. E. Hackemer, O. Leaffer, J. Spanier, **S. Amini**, M. W. Barsoum, T. Guilbert, and T. El-Raghy: On the heat capacities of Ta_2AlC, Ti_2SC, and Cr_2GeC, Journal of Applied Physics.

2008 – S. R. Kulkarni, M. Merlini, N. Phatak, S. K. Saxena, G. Artioli, **S. Amini**, M.W. Barsoum: Thermal expansion and stability of Ti_2SC in air and inert atmospheres, Journal of Alloys and Compounds.

2008 – **S. Amini**, A. Zhou, S. Gupta, A. DeVillier, P. Finkel, M. W. Barsoum: Synthesis and Elastic and Mechanical Properties of Cr_2GeC, Journal of Materials Research.

2008 – T. H. Scabarozi, **S. Amini**, O. Leaffer, A. Ganguly, S. Gupta, W. Tambussi, S. Clipper, J. E. Spanier, M. W. Barsoum, J. D. Hettinger, S. E. Lofland: On the Thermal Expansion of Select MAX Phases by Dilatometry and High Temperature X-Ray Diffraction, Journal of Applied Physics.

2008 – T. Scabarozi, A. Ganguly, J. D. Hettinger, S. E. Lofland, **S. Amini**, P. Finkel, T. El-Raghy, M. W. Barsoum: Electronic and thermal Properties of $Ti_3Al(C_{0.5},N_{0.5})_2$ $Ti_2Al(C_{0.5},N_{0.5})$ and Ti_2AlN, Journal of Applied Physics.

2008 – T. H. Scabarozi, **S. Amini**, P. Finkel, O. D. Leaffer, J. E. Spanier, M. W. Barsoum, M. Drulis, H. Drulis, W. M. Tambussi, J. D. Hettinger, S. E. Lofland: Electrical, Thermal & Elastic Properties of Ti_2SC, Journal of Applied Physics.

2007 – S. Amini, T. El-Raghy, M.W. Barsoum: Synthesis and Mechanical Properties of Fully Dense Ti_2SC, Journal of American Ceramic Society.

2007 – S. Gupta, **S. Amini**, D. Filimonov, T. Palanisamy, T. El-Raghy, M. W. Barsoum: Tribological Behavior of Ti_2SC at Ambient and Elevated Temperatures, Journal of American Ceramic Society.

2007 – B. Manoun, **S. Amini**, S. Gupta, S. Saxena, M.W. Barsoum: On the Compression Behavior of Cr_2GeC and V_2GeC up to Quasi-hydrostatic Pressures of 50 GPa, Journal of Physics Condensed Matter.

Full Text Conference Papers

2006 – S. Amini, M.W. Barsoum: Synthesis and Characterization of Fully Dense Ti_2SC, MS&T Conference, Cincinnati, Ohio.

2003 – S. Amini, S. Javadpour, S. Amini: Manufacturing, Mechanical Properties and Micro-structural Characteristics of Ceramic Preforms, 8th European Ceramic Society Conference, Turkey, Istanbul, published in Key Engineering Materials.

2003 – S. Amini, S. Javadpour, S. Amini: Manufacturing and Microstructural Characterization of A356 SAFFIL and Hybrid A356 SiC SAFFIL Composites via Squeeze Casting Process", Proceeding of the Conference of Metallurgists, Vancouver, Canada.

2003 – S. Amini, S. Javadpour: Manufacturing of Alumina Short Fibre Reinforced Aluminium Matrix Composites via Squeeze Casting, Proceeding of the Iran Foundrymen's Society, Annual Conference, Tehran.

2003 – S. Amini, "Metal Matrix Composites in the Automotive Industry; a review", Journal of the Iran Automotive Industry.

2002 – S. Amini, S. Javadpour: SAFFIL and hybrid SAFFIL SiC Preforms Produced by Spontaneous Settlement of Ceramic Phases from a Homogeneous Slurry, Proceeding of the 3rd Materials Engineering Conference, Tehran.

POSTER PRESENTATIONS

2008 – S. Amini, Microstructural Characterization and Ultrahigh Damping of a Ti_2AlC Nanocrystalline Mg-Matrix Composite, Drexel University Research Day.

2007 – S. Amini, MAXMETs: A New Class of Metal Matrix Composites, ASM Philadelphia Liberty Bell Chapter.

2007 – S. Amini, Processing and Characterization of Ti_2AlC-Mg Composites: A New Class of Metal Matrix Composites, Gordon Research Conferences, Andover, New Hampshire.

2006 – S. Amini, Synthesis and Characterization of Ti_2SC, Drexel University Research Day.

2003 – S. Amini, Manufacturing and Property Evaluation of A356 SAFFIL and Hybrid A356 SiC SAFFIL Composites via Squeeze Casting Process, Annual Conference of Metallurgists, Tehran.

2003 – S. Amini, Metal Matrix Composites Manufactured via Melt Infiltration Techniques: The Best Substitute for Cast Iron and Steel Parts in the Automotive Industry, 5th Iranian Steel Symposium, Isfahan.

INTERNATIONAL CONFERENCE PRESENTATIONS

2009 – TMS Annual Conference, San Francisco, CA: Processing, Microstructural Characterization and Mechanical Properties of a Ti_2AlC/Nanocrystalline Mg-Matrix Composite.

2009 – ACERS Conference, Daytona Beach, FL: Mg Matrix Composites Reinforced with MAX Phases.

2009 – ACERS Conference, Daytona Beach, FL: Mechanical Properties and Ultrahigh Damping of Oriented MAX Phases.

2008 – MS&T Conference, Pittsburgh, PA: Ti_2AlC/Nanocrystalline Mg-Matrix Composites.

2008 – NATAS Annual Conference, Atlanta, GA: On the Isothermal Oxidation of Ti_2SC in Air.

2007 – ACERS Annual Conference, Daytona Beach, FL: Synthesis and characterization of Cr_2GeC & Ti_2SC.

2006 – MS&T Conference, Cincinnati, OH: Synthesis and Characterization of Fully Dense Ti_2SC.

2003 – 8th European Ceramic Society Conference (ECERS), Istanbul, Turkey: Manufacturing, Mechanical Properties and Micro-structural Characteristics of Ceramic Preforms.

2003 – Conference of Metallurgists (COM), Vancouver, Canada: Manufacturing and Property Evaluation of A356 SAFFIL and Hybrid A356 SiC SAFFIL Composites via Squeeze Casting Process.

2003 – Iran Foundrymens' Society Annual Conference, Tehran: Manufacturing of Alumina Short Fibre Reinforced Aluminium Matrix Composites via Squeeze Casting.

2002 – Third Materials Science and Engineering Conference, Tehran: SAFFIL and hybrid (SAFFIL+SiC_P) Preforms Produced by Spontaneous Settlement of Ceramic Phases from a Homogeneous Slurry.

HONORS, DISTINCTIONS, CERTIFICATES, FELLOWSHIPS, AWARDS & GRANTS

2005-2009 – Graduate Research Fellowship (~$45K per annum) – Drexel University, Philadelphia, PA

2007-2009 – Material Advantage Student Chapter Travel Grant – Congressional Visit Days, Washington, DC

2009 – Graduate Division Travel Award – TMS 2009 Conference, San Francisco, CA

2008 – Outstanding Teaching Award – Drexel University, Philadelphia, PA

2008 – Thermal Analysis Forum of Delaware Valley Travel Award – NATAS, Atlanta, GA

2008 – Graduate Division Travel Award – North American Thermal Analysis Society Conference, Atlanta, GA

2007 – Graduate Division Travel Award – Solid State Studies in Ceramics (Gordon Conference), Andover, NH

2007 – Gordon Research Conference Chair Travel Award – Solid State Studies in Ceramics, Andover, NH

2006 – Honorable Mention (Oral Presentation) – Materials Science and Technology (MS&T) Conference, Cincinnati, OH

2006 – Honorable Mention (Poster Presentation) – Drexel University Research Day, Philadelphia, PA

2004 – Certificate of Graduate Residential Course – Board of Continuing Education, Cambridge University, UK

2004 – Certificate of Student Tutoring Scheme – Mulberry School for Girls, London, UK

2003 – Departmental Scholarship (£10K per annum) **–** Queen Mary University of London, London, UK

2003 – Research Grant (~ $5000) – Materials Research Center, SAPCO and Peugeot Automotive, Co., Tehran

2002 – Research Grant (~ $1000) – Ministry of Metals, Mines and Industries, Tehran

2002 – Research Grant (~ $1000) – National Iranian Oil Company and Ministry of Petroleum, Tehran

2002 – Winner of the Golden Prize for Best Paper/Presentation – 3rd Materials Science & Eng. Conference, Tehran

2001 – First Place Ranking, two consecutive years – Shiraz University Swim Team, Shiraz

LECTURING, TEACHING & INSTRUCTORSHIP EXPERIENCE *(including class size)*

2008 – Recitation Instructor – Introduction to Materials Science & Engineering, B.Sc. Course, Drexel University (60 students)

2008 – Recitation Instructor – Fundamentals of Ceramics, B.Sc. Course, Drexel University (20 students)

2007 – Substitute Lecturer – Introduction to Materials Science & Engineering, B.Sc. Course, Drexel University (300 students)

2007 – Teaching Assistant – Fundamentals of Ceramics, B.Sc. Course, Drexel University (20 students)

2005 – Teaching Assistant – Introduction to Materials Science & Engineering, B.Sc. Course, Drexel University (330 students)

2003-2005 – Mathematics Lecturer – University Foundation Program – International House London, UK (50 students)

2003-2005 – Mathematics Teacher, GCSE and A-Levels – SBK Tuition Center, UK (one-to-one tuition)

2003-2004 – Mathematics Teacher, GCSE Level – Mulberry School for Girls, London, UK (30 students)

2003-2005 – Private Mathematics Tutor – GCSE & A-Levels, London, UK (~ 10 students tutored)

2002-2003 – Recitation Instructor – Composite Materials, M.Sc. Course, Shiraz University (10 students)

2000-2003 – Laboratory Instructor – Welding and Joining Laboratory, B.Sc. Course, Shiraz University (10 students)

2000-2003 – Laboratory Instructor – Mechanical Testing Laboratory, B.Sc. Course, Shiraz University (20 students)

2000-2003 – Laboratory Instructor – Casting and Solidification Workshop, B.Sc. Course, Shiraz University (30 students)

2002-2003 – Teaching Assistant – Selection of Engineering Materials, B.Sc. Courses, Shiraz University (30 students)

2001-2002 – Teaching Assistant – Composite Materials Science & Engineering, M.Sc. Course, Shiraz University (10 students)

2001-2002 – Laboratory Instructor – Heat Treatment Laboratory, B.Sc. Course, Shiraz University (10 students)

1995-2003 – Private Tutor – Mathematics, Physics, Chemistry and English, Tehran (~ 50 students tutored)

PROFESSIONAL MEMBERSHIPS

2007-2009 – Materials Research Society (MRS)

2006-2009 – ASM, ACERS, TMS, AIST

1995-2003 – "Foundry Society", "Metallurgical and Materials Engineering Society" & "Welding and Joining Society", Iran